Final Report to the Earthquake Commission
on Project No. 01/462

Calibration of Wellington 3D ground shaking model

Martha K. Savage[1], Rafael Benites[2], Jiashun Yu[2], John Taber[3]
Shu Qin Ma[1]

8 November 2004

[1] Institute of Geophysics
Victoria University of Wellington
Box 600, Wellington, New Zealand

[2]Institute of Geological and Nuclear Sciences
69 Gracefield Road, PO Box 30-368
Lower Hutt, New Zealand

[3]Education & Outreach Program
The Incorporated Research Institutions for Seismology
1200 New York Ave. NW, Suite 800
Washington, DC 20005, USA

DIE SUCHE NACH WAHRHEIT IST KÖSTLICHER ALS DEREN GESICHERTER BESITZ.

THE PURSUIT OF TRUTH IS MORE PRECIOUS THAN THE OWNERSHIP OF THE TRUTH.

Gotthold Ephraim Lessing

ABSTRACT

This thesis calibrates the Hutt Valley section of the previously developed Wellington 3D ground shaking model, using weak motion records from seven earthquakes recorded during the Lower Hutt deployment of seismometers. The Hutt Valley section is approximately $\frac{1}{3}$ of the whole 3D model, but exhibits the highest shaking for a presumed Wellington Fault earthquake. We use 24 weak motion sites in Lower Hutt. The sites sample the full range of soil types and depths in the region, from bedrock to thick soft sediments.

In this research, the focal mechanisms of the 15 events recorded by the four portable deployments are solved by the combined amplitude ratio and first motion method, using all the available data from New Zealand Standard Network (NZSN), SNZO, and the portable deployment.

A new method named the *1D+3D hybrid modeling technique* was developed to simulate the ground motion in Hutt Valley to compare with the recorded ground shaking data from the Lower Hutt portable deployment. The method combines 1D modeling between the source and the bottom of the valley with 3D modeling from the valley bottom to the surface.

The discrete wavenumber (DWN) method and general reflection and transmission coefficient matrices are used with a 1D velocity model to calculate the stress and velocity wavefield at the bottom of the Hutt Valley sediments. A double couple, point source model with a modulated ramp time function is used as the earthquake focus in the 1D modeling. The finite difference (FD) scheme is then used with the 3D Hutt Valley shaking hazard model to calculate the velocity wavefield at the free surface of the Hutt area, using the time domain stress and velocity wavefield at the bottom of Hutt Valley sediments as input. Stress and velocity synthetics are determined at each 40 m of the grid. To compare with the observed seismogram data in the Lower Hutt deployment, the points within the model corresponding to the recording sites were selected and the velocity time series for those sites were calculated.

Through comparing the synthetic and observed ground shaking in both time and frequency do-

mains, we conclude the following:

1. The newly developed (1D+3D) forward modeling technique works. This is verified by the 1D/3D and 1D/(1D+3D) tests. However, the 40 m grid and the low surface velocities used may be too coarse for the technique to be useful beyond 2.5 Hz.

2. Using the 1D forward modeling technique alone, but with a local 1D model for each station can reproduce some of the characteristics of the ground motion observed, e.g., some of the increase of the peak ground velocity (PGV) and some of the increase duration time of basin motions relative to rock motions.

3. The (1D+3D) forward modeling technique can match more features of the ground motion observed than the 1D modeling technique. The synthetics from the (1D+3D) modeling match the recorded data better in waveform, valley resonance frequency and site response. But the (1D+3D) forward modeling technique consumes much more computational time, which may take over 100 times of the time needed by 1D modeling, and needs a more powerful computer.

4. Two ratios are obtained for calibration of the Hutt 3D shaking hazard model. One is c_{pvr}, i.e., the ratio of the measured to synthetic peak velocity; another is c_{psr}, i.e., the ratio of measured to synthetic peak spectral ratios. c_{pvr} and c_{psr} are obtained for different shaking hazard zones classified by Dellow *et al.* (1992) based on source types (dip slip and strike slip earthquakes). The ratio of the measured to synthetic peak velocity in zone 5 and basin edge averages 0.6 ± 0.3 for dip slip and 0.7 ± 0.3 for strike slip earthquakes. The ratio of the measured to synthetic peak spectral ratios in zone 5 averages 2.0 ± 0.8 for dip slip and 1.5 ± 0.9 for strike slip earthquakes. The results for the other zones are similar. Thus, the peak velocity ratios are overestimated with the Hutt 3D shaking hazard model, while the peak spectral ratios are underestimated.

CONTENTS

FIGURES

TABLES

LIST OF ACRONYMS

DWN Discrete Wavenumber

FD Finite Difference

FAS Fourier Amplitude Spectrum

FFT Fast Fourier Transform

FSR Fourier Spectral Ratio

GNS Institute of Geological and Nuclear Sciences, New Zealand

IRIS Incorporated Research Institutions for Seismology

IS Interface Source

NZSN New Zealand Standard Network

PAS Peak Fourier Amplitude Spectrum

PGV Peak Ground Velocity

PVR Peak Velocity Ratio

PSR Peak Fourier Spectral Ratio

STF Source Time Function

SAC Seismic Analysis Code

CHAPTER 1

INTRODUCTION

Significant earthquake damage has occured in Mexico City in 1985, San Francisco in 1989, Kobe, 1995 and Taipei, 1999 because of ground motion amplification generated in an alluvial basin (Borcherdt and Glassmoyer, 1992; Kawase, 1996; Kim and Roesset, 2004). Significant progress has been made in quantifying the effects of sedimentary basins on earthquake ground shaking hazard in the past ten years. Research on shaking hazard in New Zealand has focused on both the collection and analysis of ground motion data and the development of computer models of wave propagation. Data collection has included dense temporary networks of seismographs (e.g. Taber and Smith, 1992; Taber, 2000; Adams, 2000) and the Institute of Geological and Nuclear Sciences, New Zealand (GNS) permanent strong motion network (Sritharan and McVerry, 1992).

Both weak and strong motion recordings have demonstrated significant variations in ground shaking across the Wellington region. Fourier Spectral Ratios (FSRs, note that a list of acronyms used in this thesis is available on page xix) of ground shaking at a soft sediment site relative to a nearby rock site have exhibited values of up to 15 in Lower Hutt (Taber and Smith, 1992). There are large variations in ground shaking over distances as short as 100 m and there is significant variability in the relative shaking from earthquake to earthquake (Taber and Smith, 1992). This variability is due to the three-dimensional nature of the basins, the focal mechanism of the earthquake and the frequency components of the seismogram. In this thesis, I modelled the large variations in ground shaking caused by the three-dimensional nature of Hutt Valley basin by a newly developed method ((1D+3D) modelling technique), compared them to the observed data from the Lower Hutt deployment, and calibrated the Hutt 3D shaking hazard model [Chapter 7].

1.1 Prior modelling studies

Two-dimensional finite element modelling of incident *SH* waves in Hutt Valley (Adams, 2000) has sucessfully matched many features of ground shaking data collected near the edge of the valley (Osborne and Taber, 1999). The features include the observation of a *basin edge effect* similar to that seen in the Kobe earthquake (Pitarka *et al.*, 1998), which led to a zone of intense damage paralleling the basin edge, *the wedge effect* and the *Airy-phase edge effect*. The *Basin edge effect* is purely a multipathing effect, caused by the constructive interference between direct body waves and basin edge generated surface waves (Kawase, 1996). *The wedge effect* may occur in a wedge of infinite depth with no lower vertex and becomes important the shallower the edge-slope angle (Hudson, 1963). The *Airy-phase edge effect* develops when the dominant frequency of the source signal is close to the fundamental resonant frequency of the sedimentary valley (Nagano, 1998). He simulated the effect up to 5.0 Hz.

However, the 2D modelling is incomplete for the motion due to a rupture of the Wellington fault. The calculation of *SH* waves represented the out-of-plane movement, corresponding to the motion parallel to the fault. In strike-slip ruptures, the component perpendicular to the fault is the largest and it would have to be modelled with incident in-plane (*SV*) waves (Benites, personal communication). Also, focusing and scattering of waves either in-plane or out-of-plane (i.e. 3D) effects can not be accounted for in the 2D model and thus in a geologically complex region such as Wellington, (1D+3D) modelling is necessary for a realistic comparison to the data. It is called (1D+3D) modelling instead of 3D modelling in this project because no earthquake focus fell with in the Wellington 3D shaking hazard model. The wavefields must be first brought to the sediment-bedrock interface by a 1D modelling code (Benites *et al.*, 2002), then are propagated to the free surface by the 3D FD code (Olsen, 1994). This point will be described later. In addition, the 2D modelling method (Adams and Brainerd, 1997) can not estimate the shaking hazard everywhere in Hutt Valley. It can only simulate the ground motion at the sites which are located on the two profiles, one of which is situated at the western end of Hutt Valley, another in the middle of Hutt Valley.

Haines and Yu (1997) used the Riccati equation approach of 3D modelling to calculate full wavefields in a small basin near Alfredton (diameter 400-500 m). The 3D modelling successfully reproduced many of the features of the recorded ground motions, e.g., the frequency response of the basin and peak ground motion amplification. The fundamental incident wavefields they have used

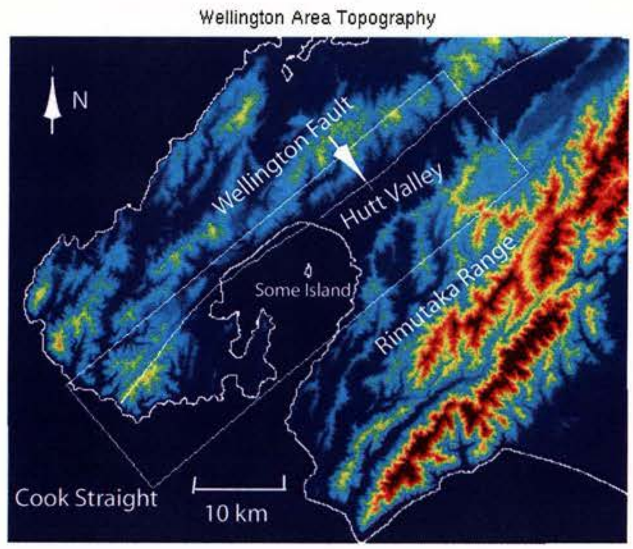

Figure 1.1 *Wellington 3D shaking hazard model location. The rectangle depicts the outline of our 3D velocity model. Also shown are the Wellington fault trace and the coastline (Benites and Olsen, 2004). Colors give elevations from sea level, from blue (sea level) to red (highest level 941 m at Rimutaka Range). Topography is mapped for clarity; it is not included in (1D+3D) modelling in Chapter 7.*

in modelling the response of Alfredton basin to incident *S* waves are plane waves with both *SH* and *SV* polarizations. Their synthesised seismograms with frequencies up to 12 Hz are in very good coincidence with observations. However due to heavy computational requirements, their technique is difficult to apply to an area as large as the Wellington region.

Olsen (1995) simulated the 3D wave propagation in the Salt Lake Basin, Utah, USA, using planar *P*-waves as incident wavefields. He concluded that amplification of ground motions tends to be greater at sites overlying the deeper parts of the basin, and the dominant contributors to amplification are the low impedance of the basin sediments, mode conversion, reverberations and scattering in the near-surface unconsolidated sediments.

1.2 Introduction to the Wellington 3D ground shaking model

Benites and Olsen (2004) initiated this study. The Wellington 3D shaking hazard model is crossed by the southernmost segments of the Wellington fault, which is about 75 km in length. Felt earthquakes frequently occur in this region. Furthermore, paleoseismic studies reveal that this is an active fault, with an almost vertical fault plane and a strike-slip focal mechanism, extending to about 20 km depth, and with a recurrence period of about 400 years for magnitude $M = 7.5$ earthquakes. It has ruptured at least twice in the past 1000 years and it ruptured most recently between 350 and 500 years ago (Van Dissen and Berryman, 1996). Recent studies of stress distributions show that the level of stress beneath Cook Strait appears to be high. Studies indicate that an earthquake of moment magnitude

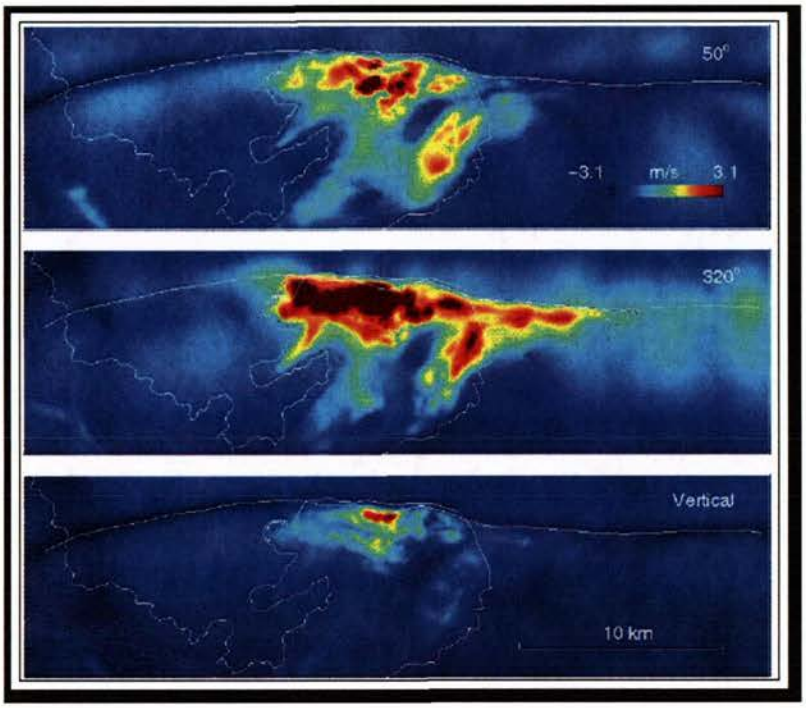

Figure 1.2 *Peak ground velocities (pgv) in the Wellington region for a rupture along the Wellington Fault starting from the south, using the Landers earthquake slip distribution. The solid line is the coast, the dotted lines mark the edge of sedimentary basins and the white line is the Wellington Fault. The strongest ground shaking is located in the Wellington Harbour and Lower Hutt Valley due to resonance caused by soft layers. The top figure represents the fault parrallel-component (azimuth 50°), the middle figure represents the fault-perpendicular component (azimuth 320°), the bottom figure represents the vertical component. Note the ground shaking along 320° (the component perpendicular to the fault) is the largest because Wellington Fault is assumed to rupture in a strike-slip fashion (Benites and Olsen, 2004).*

7.6 ± 0.3 may occur within the next few hundred years on the Wellington Fault (Van Dissen and Berryman, 1996).

The Wellington fault is embedded in a three-dimensional (3-D) stratigraphic model of the Wellington metropolitan area, generated from the integration of all available geological and geophysical (borehole, bathymetry, gravity and seismic) data (Benites and Olsen, 2004) [Figure 1.1]. The borehole positions can be found in Figure 3.6.

Surface topography and the water layer were both excluded in the simulations. The full model was discretized at 40 m spacing into 66 million grid points. Benites and Olsen (2004) modelled the strong ground motion in the Wellington metropolitan area with an assumed rupture of the Wellington Fault, starting from the Cook Strait, using the slip distribution from the Lander's earthquake in California (Wald and Heaton, 1994). They predicted that the strongest shaking will be located in Wellington

Harbour and Lower Hutt Valley due to site resonance [Figure 1.2]. The sediments in Wellington Harbour are as thick as 900 m, and those in Hutt Valley are as thick as 479 m. The peak ground velocity (PGV) on the sediment sites in Wellington Harbour and Hutt Valley reaches 3.1 m/s and is amplified 15 times compared to that on the rock site (Benites and Olsen, 2004). Both the absolute PGV and peak velocity ratio (PVR) are too large (Benites and Olsen, 2004) compared to values from similar basins in other parts of the world. The PGV on the sediment sites should be around 1.7 m/s (Benites and Olsen, 2004).

1.3 Building a small 3D shaking model

Gemini, the computer for this project, is a dual-CPU PC running Red Hat Linux 9.0. It has two AMD Athlon MP 2200 CPUs. These run at a nominal speed of 1800 MHz. Gemini has 4 GB of physical RAM installed. However, only a little over 3.6 GB of this is visible to Linux.

A small 3D shaking model called the Hutt 3D shaking model is cut out of the Wellington 3D shaking model (975 by 250 by 240 nodes, 5.6 GB memory is needed) in Chapter 2 for the (1D+3D) modelling in Chapter 7. Another reason that the whole 3D model can not be calibrated this time is that it takes the current computer too long (24 days for each run). The newly developed (1D+3D) modelling technique [Chapter 6] will be applied to the newly built Hutt 3D shaking model for the (1D+3D) synthetics. The (1D+3D) modelling technique [Chapter 6] is created by modifying and integrating Benites *et al.*'s (2002) 1D DWN modelling code and Olsen's (1995) 3D FD modelling code. The maximum frequency achieved is 2.5 Hz. The constraints on the small model are to try to keep its horizontal boundaries 1 km away from all the stations in the Lower Hutt deployment [(Taber and Smith, 1992)]. The final Hutt 3D model is $303 \times 249 \times 240$ grid points in dimension. Only 1.7 GB memory is needed. It takes the current computer 8 days for each run with the Hutt 3D model.

1.4 Determining the focal mechanisms

The focal mechanisms of 15 weak events in Greater Wellington area are determined by the amplitude ratio and first motion method (Cavill *et al.*, 1997) in Chapter 4. In addition, the focal mechanisms of the two strongest events are obtained from Webb and Anderson's (1998) study. They are for the calibration of the whole Wellington 3D shaking model. The earthquakes were selected because they were the largest events recorded on those temporary deployments. However, only the focal mechanisms of the seven events which were recorded by the Lower Hutt deployment are used in the 1D modelling [Chapter 5] and (1D+3D) modelling [Chapter 7], due to the limited computer resources available.

1.5 Studying the site effect by 1D modelling technique

The effect of sediment layering is studied by a 1D modelling technique with the individual 1D models extracted from the Hutt 3D model [Chapter 5]. The focal mechanisms determined in Chapter 4 are utilised in the 1D modelling. The results show that the 1D modelling technique can reproduce many features of ground motion at sediment sites: i.e., the amplification of peak ground velocity and the prolonged duration.

1.6 Hybrid algorithm modelling

In Chapter 6, I developed a new technique by modifying, coordinating and combining the Discrete Wavenumber (DWN) method code for 1D modelling (Benites *et al.*, 2002) and Finite Difference (FD) method code for 3D modelling (Olsen, 1995) to simulate realistic ground motion with near surface lateral heterogeneous sediment layers. It is termed "hybrid algorithm" or "hybrid technique" in this thesis.

In Chapter 7, I put the hybrid modelling algorithm into practice by modelling the ground motion with the Hutt 3D shaking model built in Chapter 2, where plenty of seismic ground motion data are available. Through comparison of the modelled ground motion data and recorded motion data, several indices are obtained for calibrating the 3D shaking hazard model.

In modelling the ground motion in Hutt Valley, first, the synthetic wavefields for both the stress and velocity are calculated [Chapter 7] at each grid point of the sediment-bedrock interface in the Hutt 3D shaking hazard model, using the 1D (the DWN) method developed originally by Benites *et al.* (2002) and revised by me for this project. Secondly, the *interface source* in the Hutt 3D model is propagated grid by grid by the FD code developed originally by Olsen (1995) and revised by me for this project. The FD method has the advantage of providing a complete solution to the ground motion modelling problem for the 3D heterogeneous medium, which has no analytical solution. The accuracy is limited only by the available grid size and time step.

CHAPTER 2

BUILDING THE HUTT 3D MODEL

2.1 The Hutt 3D shaking model

Originally, we aimed to calibrate the entire Wellington 3D shaking model. All the digital seismic data in the Greater Wellington area were collected and preprocessed for the calibration of the whole model. Due to the limitation of computer resources, we calibrated the part of the Wellington 3D model that is located in Lower Hutt, where the seismic ground motion has been measured by several portable deployments. Therefore, we built a small 3D shaking model named the Hutt 3D shaking model this time.

2.1.1 Cutting the Hutt 3D model from the Wellington 3D model

Because the project was not able to use the UCSB computer system as originally planned, the (1D+3D) modelling program was run on a smaller GNS computer. Therefore, we decided to work on only part of the Wellington 3D model. We chose to model the Lower Hutt region because it exhibits the largest amplification in the simulated Wellington fault rupture (Benites and Olsen, 2004) [Figure 1.2]. In addition, there were several dense weak motion arrays in Lower Hutt during 1990s, so that Hutt Valley has the largest ground motion database to calibrate the model. Therefore the Hutt 3D model was cut out from the Wellington 3D shaking model. The cut model is $\frac{1}{3}$ the length and the same width as the original 3D model.

The four irregular layers of sediments incorporated into the Hutt 3D model are illustrated in Figures 2.1 and 2.2. The softest has a S-wave velocity of 175 m/s, over bedrock (greywacke) with S-wave velocity of 1500 m/s, and with an assumed Poisson ratio of 0.25 [Table 2.1]. The assumed Poisson ratio of 0.25 is applied in all layers in this project for simplifying the modelling. However, it

Table 2.1
The Hutt 3D Crustal Model Specification.

layer no.	v_p(km/s)	v_s(km/s)	$\rho(g/cm^3)$	thickness(m)
layer 1	0.30	0.175	1.75	0-211
layer 2	0.52	0.3	1.80	0-70
layer 3	0.57	0.33	1.85	0-183
layer 4	0.87	0.5	1.90	0-372
layer 5	2.6	1.5	2.7	9121-9600

is likely to be much higher in the soft layers. The elastic parameters within each layer are constants, but the thickness of each layer varies through out the model. We built the Hutt 3D shaking model based on the following criteria:

1. In the horizontal plane, the edges of the Hutt 3D model were chosen to be 1 km away from all the station sites in the Lower Hutt array. The 1 km boundary zones along the four edges were padded with attenuative material (Cerjan *et al.*, 1985) to reduce artificial reflections later in the (1D+3D) modelling in Chapter 7.

2. The sediment-bedrock interface in the Hutt 3D model is 479 m deep at most. Based on the rule of thumb, $\lambda_{min} = 5\Delta h$ (Levander *et al.*, 1999), λ_{min} is the minimum wavelength that can be calculated in the FD modelling, where Δh is the grid size, which is 40 m in the Hutt 3D model. Therefore $\lambda_{min} = 200$ m in our case. Thus 9600 m (240 grid points) was chosen as the height of the Hutt 3D model, which is also the height of the Benites and Olsen's (2004) original model. So the bottom margin of the Hutt 3D model where we apply the absorbing boundary conditions is 48 λ_{min} below the deepest part of the sediment-bedrock interface.

Table 2.1 illustrates the elastic parameters used in the 3D modelling, where v_p was derived from v_s based on the assumption that $\lambda = \mu$ for the Lame parameters in the 3D medium, which is termed as Possion medium. Station locations on the surface of the Hutt 3D model in the Lower Hutt deployment are depicted in Figure 2.3. Note L17 (the southern most station), L07 (the northern most station) and L01 (the eastern most station) fall in the absorbing boundary zones, which lie within 1 km away from the respective lateral margins. L17 was one of the sites where maximum ground motion were observed in the Lower Hutt deployment [Table 3.3] since it was located in Wainuiomata basin where the sediment layer is quite soft (Taber and Smith, 1992). In Chapter 7 we will show that the synthetics from (1D+3D) modelling at L17 match the observed data poorly because it is in the absorbing boundary zone.

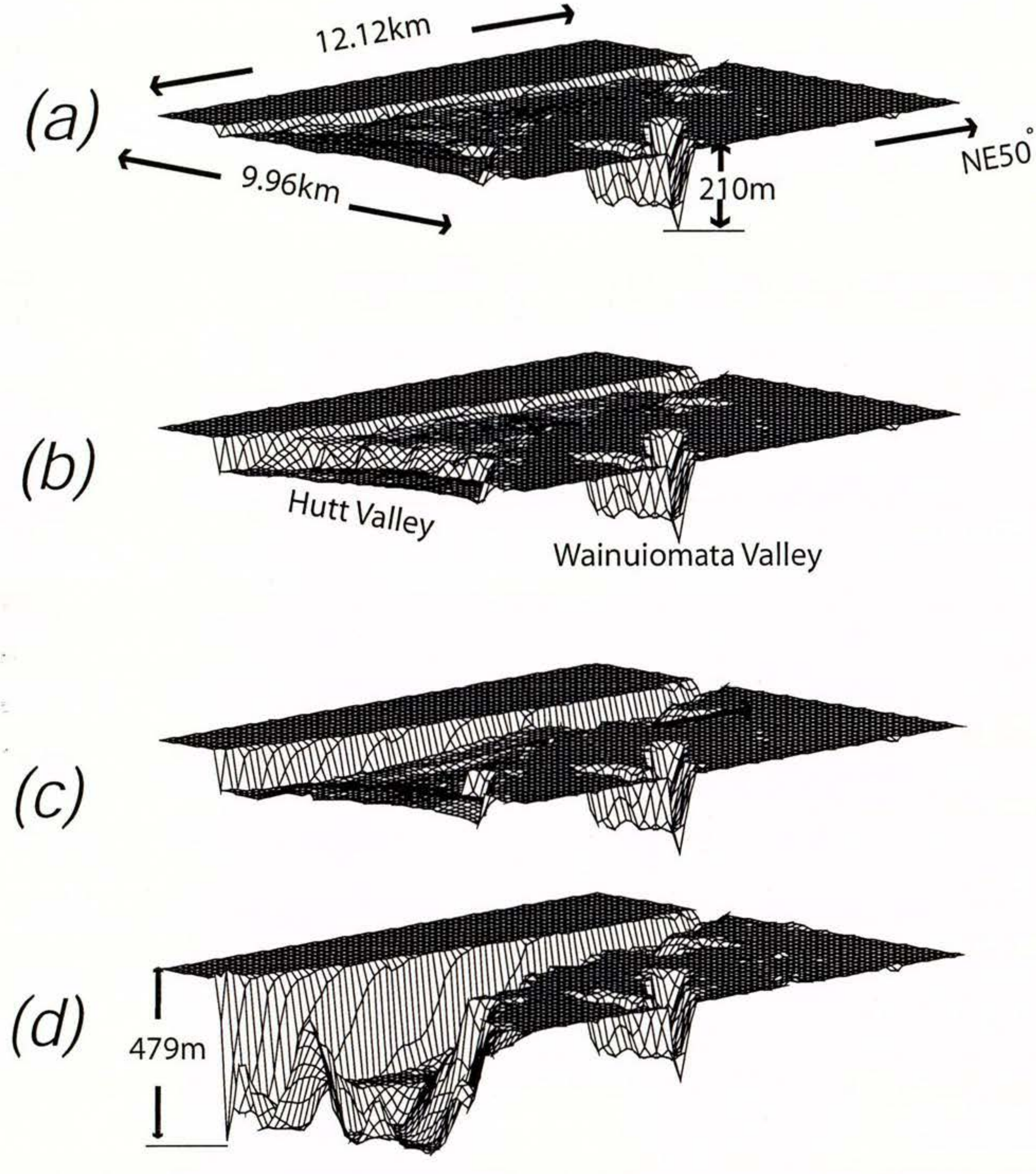

Figure 2.1 *3D perspectives of all the interfaces in the Hutt 3D shaking model. (a) The interface between the top sediment layer and the 2nd sediment layer. (b) The interface between the 2nd sediment layer and the 3rd sediment layer. (c) The interface between the 3rd sediment layer and the 4th sediment layer. (d) The interface between the 4th sediment layer and the underlying bedrock. Note that all the four sediment layers have zero thickness at the northwestern and southeastern edge of the 3D model. Note the very thick, very low velocity layer in Wainuiomata Valley.*

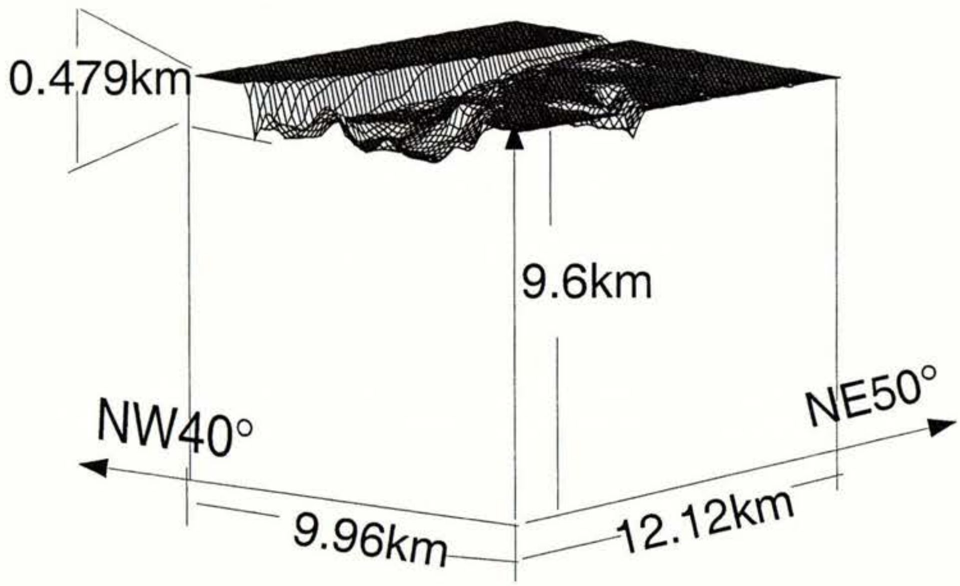

Figure 2.2 *The Hutt 3D shaking model and the geometry of Hutt Valley sediment-bedrock interface.*

2.2 Converting the layered 3D model into a gridded 3D model

The Hutt 3D model is composed of 5 irregular layers (4 sediment layers, 1 greywacke layer). The medium is homogeneous within each layer and the elastic parameters vary from layer to layer. To provide a 40 m grid for the (1D+3D) modelling, we need to define a single velocity and density in each block. A grid box may be composed of one layer to five layers. Due to conservation of travel time and conservation of mass, the elastic parameters for each grid box in the gridded 3D model are determined by the following:

$$
\begin{aligned}
\mathrm{v} &= \frac{\Delta h}{\sum_{j=m}^{n} wt_j/\mathrm{v}_j} \qquad 1 \le m \le n \le 5 \\
\rho &= \frac{\sum_{j=m}^{n} wt_j \rho_j}{\Delta h} \qquad 1 \le m \le n \le 5
\end{aligned} \tag{2.1}
$$

where Δh is the size of each grid box, which is 40 m in this case, v and ρ is the overall velocity and density of the grid box respectively, v_j is the velocity of j_{th} layer. ρ_j is the density of jth layer. wt_j is the thickness of the jth layer actually occuring within the grid box. In case the j_{th} layer does not appear in that grid box, wt_j is defined as 0 m.

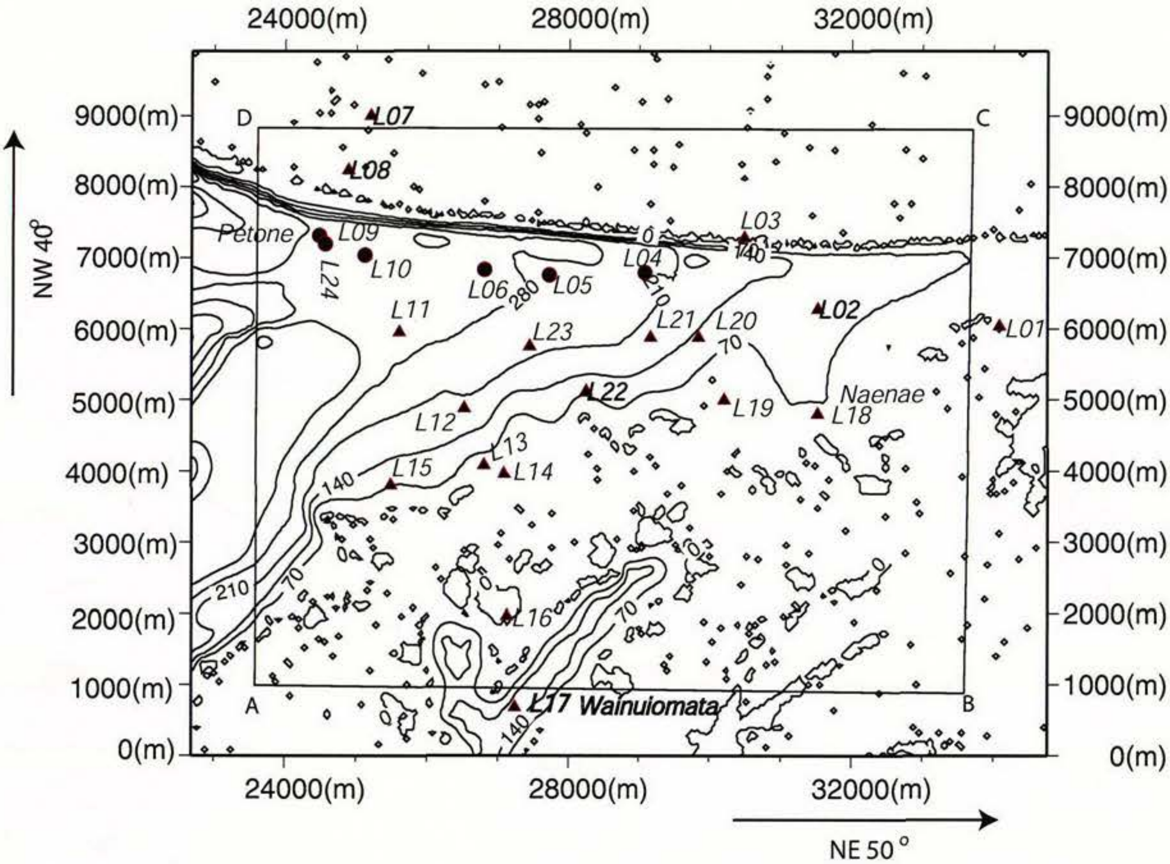

Figure 2.3 *Station locations in the Lower Hutt deployment on the surface of the Hutt 3D model. • denotes the basin edge sites, ▲ denotes the other sites. The small diamond symbols are small, isolated areas of non-zero basin thickness. Also shown are the contours of the sediment layer thickness, the contour interval is 70 m. The region between the rectangle ABCD and the Hutt 3D model margins are absorbing boundary zones for reducing artificial reflections. The Hutt 3D model ranges from 22680 m to 34760 m along $NE50°$ and 0 m to 9920 m along $NW40°$, refering to the origin of the whole Wellington 3D model. Note L01, L07 and L17 are located in the absorbing boundary zones, which are limited by the original Wellington 3D shaking hazard model.*

CHAPTER 3

DATA COLLECTION AND PROCESSING

In this Chapter, I assemble all the available seismic data, together with the corresponding instrument response. I use them in solving the focal mechanisms of the earthquakes in Chapter 4. The focal mechanisms are used in the 1D forward modelling in Chapter 5 and (1D+3D) forward modelling in Chapter 7. The collected seismic data are also used in comparison with the 1D synthetics obtained in Chapter 5 and (1D+3D) synthetics obtained in Chapter 7 to calibrate the Hutt 3D model. I removed the instrument response from the raw seismic data. I obtained the PGV (Peak Ground Velocity) for each component of each site.

3.1 Data

The following seismic data sets were collected for this study:

1. The data set from the New Zealand Standard Network (NZSN) (Maunder, 1993) and instrument response for all NZSN stations;

2. The data set from the New Zealand Strong Motion Network (Cousins, 1998);

3. The data set from SNZO (IRIS, 2004);

4. The data sets from five temporary deployments, including the Lower Hutt deployment conducted during Nov. 1990 - Feb. 1991 (Taber and Smith, 1992); the Wellington deployment conducted during Oct. 1991 - Jan. 1992 (Taber *et al.*, 1993); the Leeds Tararua deployment conducted during Jan. 1991 - Sep. 1992 (Nformi *et al.*, 1996); the broad band deployment conducted during Dec. 1997 - Jan. 1998 (Taber, 2000) and the Alicetown deployment conducted during Jan. 1999 (Osborne, 1999).

Among the data sets above, data from the Leeds Tararua deployment and SNZO were gathered for a better coverage in calculating focal mechanisms for the earthquakes captured by the Wellington deployment. The data from the other four portable deployments are for calibrating the entire 3D model. Limited by the computing ability of the Linux PC available for this project, 3D modelling is confined to Hutt Valley 3D shaking model in the current work, and therefore only the seismic data from NZSN and the Lower Hutt deployment have been exploited and analysed thoroughly. All the instrument responses involved in the above data sets are attached in Appendix A.

I do not describe in detail the data from New Zealand Strong Motion Network, the Wellington deployment, the data from the broad band deployment or the Alicetown deployment here. I have preprocessed them for the calibration of the whole Wellington 3D shaking model, and I have determined the focal mechanisms for all the events chosen to be used in calibrating the whole 3D model. However, they were not used in calibrating the Hutt 3D shaking hazard model this time. They can be analysed with the (1D+3D) modelling result from the whole Wellington model in the future once a more powerful computer becomes available.

3.1.1 NZSN Data

The spatial distribution of NZSN stations (Maunder, 1993) can be found in Figure 3.1. The NZSN data mainly consist of short period velocity data, except the data from WEL station, which is short period acceleration, and except the data from KNZ, TOZ, DSZ and MQZ after late 1998, whose seismomters are broadband sensors. The NZSN has a spacing of about 50 km, decreasing to about 20 km in the Welllington region (The Wellington Network). The sensors and recorders at short period stations are Mark Products L4-3D and EARSS respectively (Gledhill *et al.*, 1991). The sensors and recorders at broad band stations are Guralp CMG-40T and Quanterra Q4126 respectively. The sensor and recorder at the WEL station are a Kinemetrics force-balance accelerometer and an EARSS digital gain-ranging recorder.

Station MRW is near to the epicenters of the events in this study [Figure 3.1]. It is located at a critical position for calculating the focal mechanisms for this project, however, its data are clipped in most of the earthquakes studied. Thus only its first motions (which are very clear) are exploited in this situation. Only data from 3-component stations in the NZSN are used in focal mechanism calculation. Since we use the amplitude ratio method to solve the focal mechanisms, it is not necessary for us to

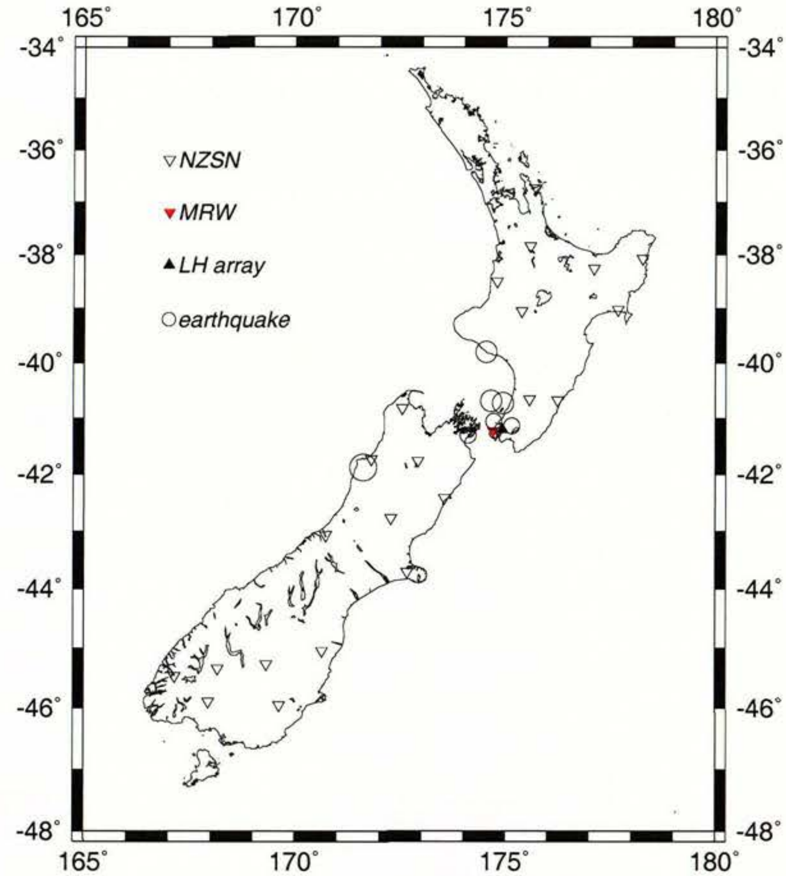

Figure 3.1 *Distribution map of three-component stations in the NZSN applied in focal mechanism solution. Earthquake locations are also included. The size of each circle represents the magnitude of the event, which ranges from 3.2 to 5.7. MRW is particularly labeled as it is at a location vital to the focal mechanism measurement, but it is clipped in all the events studied.*

know the exact value of the gain of the recorders, provided that the gains in all the three different components are identical.

3.1.2 The Leeds Tararua array

The Leeds Tararua array of 9 broad band, 3-component seismometers was deployed in Southern North Island, New Zealand from 1991 January to 1992 September. Its seismometers were Guralp CMG-3T. The array had an L shape and a station spacing of 5-10 km [Figure 3.2].

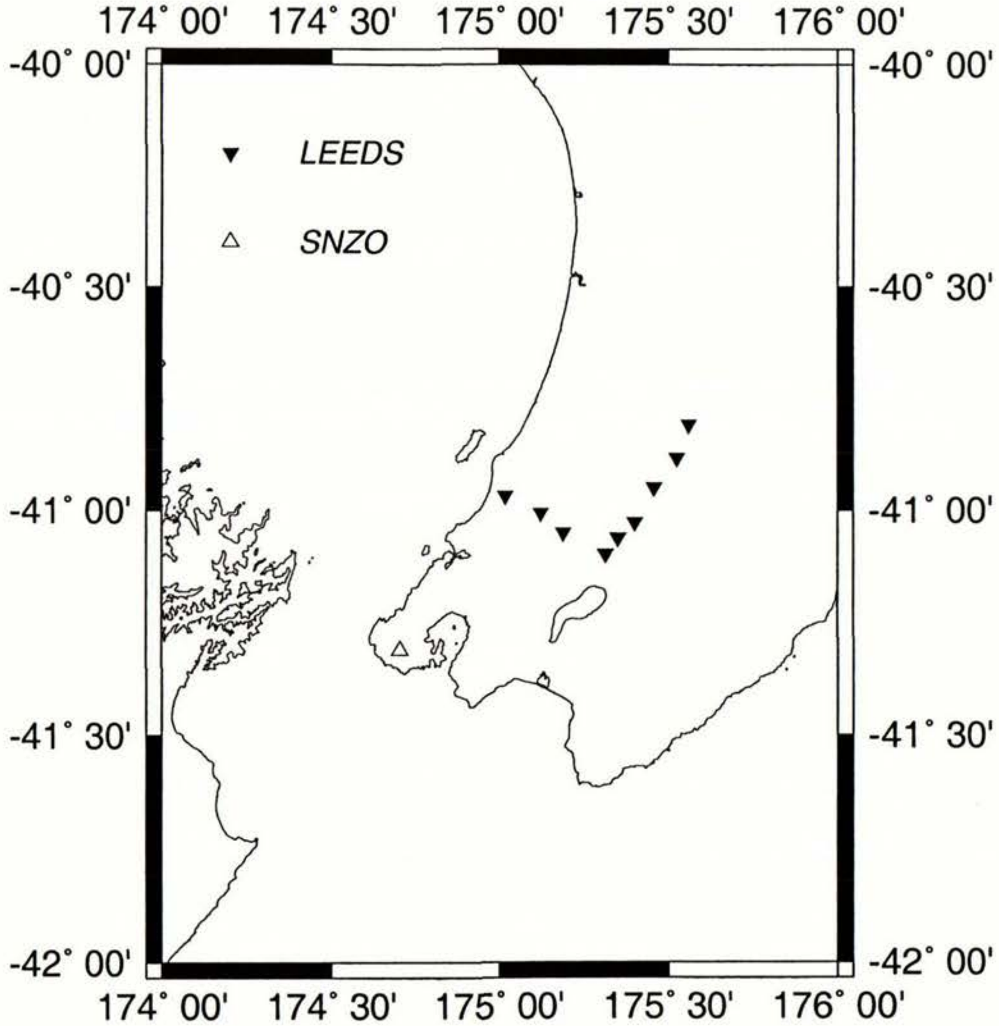

Figure 3.2 *Distribution map of the Leeds Tararua array and SNZO applied in focal mechanism solution. All the stations in this figure are broad band stations.*

3.1.3 SNZO Data

Station SNZO is a permanent station established in 1992 and operated by the Incorporated Research Institutions for Seismology (IRIS), USA. It is a very broad band velocity sensor. Its seismometer is a GeoTech KS-36000-I BD [Figure 3.2] (IRIS, 2004). Before 1997, the horizontal components were BHN and BHE, and the seimometer was located on the ground surface. After 1997, SNZO's horizontal components are BH1 (azimuth 167°) and BH2 (azimuth 257°); the seismometer is located in a borehole 98 m below the ground surface. Components were rotated to NS, EW to keep in agreement with data from the other stations before being used for focal mechanisms. The data from SNZO are of good quality because the seismometer is located in Jurassic-Permian rock so that the seismometer is not affected by the strong winds in Wellington, and its signal-noise ratio is high.

3.1.4 Data from weak motion deployments

The weak motion data set used in this study came from the Lower Hutt portable deployment, which was conducted by Taber and Smith (1992) in Nov. 1990- Feb., 1991. This deployment studied frequency dependent amplification due to site effects, as part of a microzonation survey for the Wellington Regional Council. Twenty-four sites extended 10 km up Hutt Valley from Petone foreshore. Three-component digital seismographs were installed in the study areas, with two additional sites in Wainuiomata [Figure 3.3 and Table 3.1]. The sensors and recorders are identical for all the sites. The weak motion seismometers were installed with the horizontal components oriented north and east. Five sites were located on the sides of the valley on firm soil or bedrock (L03, L07, L08, L14 and L19 [Figure 3.3]), and six sites (L04, L05, L06, L09, L10 and L24) were located on the basin edge formed by the vertical Wellington fault and Hutt Valley sediment [Figure 2.3]. The instruments were deployed primarily in two installments, with up to 18 seismographs operating at any one time [Table 3.1]. The 1 Hz natural period seismometers (Kinemetrics L4 3D) were operated with EARSS portable seismographs at a sampling rate of 100 Hz (Gledhill *et al.*, 1991).

The sites were chosen to sample the full range of soil types and depths in the region, from bedrock to thick soft sediments. The seismometers were buried just beneath the surface in soil in the backyards of private homes or placed on existing concrete slabs at private or secure public locations. Between 2 and 33 earthquakes were recorded at each site during the survey.

Data were analysed for the frequency response of wavefield sites (Taber and Smith, 1992) in a comparison study with the strong motion data recorded by the IGNS strong-motion network (Taber *et al.*, 1993). Records from seven of the earthquakes were used for the present study [Table 3.2]. Only those earthquakes which were well recored by at least 3 permanent stations in NZSN and whose focal mechanisms might therefore be solved are chosen. The chosen events must also have been well recorded at most sites in the Lower Hutt portable deployment so that their observed site effect can be used as a comparison with the simulated site effect from 1D and (1D+3D) synthetics. The events selected ranged in magnitude from 3.2 to 5.7 and were between 23 km and 285 km away from the centre of the portable array and ranged in depth from 8.3 to 104.4 km. Very few of the events were large enough to be felt in the study regions.

Unlike the gain in the instrument response for NZSN stations, which is a relative value, the gain in the header of AH files from this portable depolyment is the absolute value, which is used in calculating the PGV [Tables 3.3 and 3.4] and instrument response deconvolution [Section 3.3.1] for the comparison between the synthetics and data in Chapter 5 and Chapter 7.

The weak-motion reference sites for the Lower Hutt array are L14 and L19. L19 is used as a reference site in cases when L14 failed to record the event. L14 was located on weathered bedrock 40 m outside of the IGNS building [Figure 3.3]. L19 was located on the bedrock foundation near Naenae reservoir [Figure 3.3]. The site conditions of the other stations range from bedrock to thick soft sediments.

A description of the Lower Hutt subsurface geology can be found in Dellow *et al.* (1992). The sites will be discussed in terms of their classification within the seismic hazard microzoning of Van Dissen *et al.* (1992a) and Van Dissen *et al.* (1992b). The classification of each site is listed in Table 3.1 and is shown in Figure 3.3. Lower Hutt was divided into five zones based on the geology and measured response to strong and weak seimic shaking (Van Dissen *et al.*, 1992a). Zone 1 areas are underlain by bedrock or weathered bedrock, zone 2 areas are typically underlain by compact alluvial and fan gravel, zones 3-4 are underlain to a depth of 20 m by interfingered layers of soft sediment and compact gravel and sand, and zone 5 is generally underlain by more than 10 m of soft sediment of low shear-wave velocity. This classification is also used in the calibration of the Hutt 3D shaking hazard model [Table 7.7]. The estimated amplification of the ground motions are expected to range from none (factor of 1) for the rock sites (zone 1) to an increase in the peak ground acceleration by factors of 3 to 4 for zone 4, with a large, shallow, distant earthquake (Van Dissen *et al.*, 1992a; Van Dissen *et al.*, 1992b), and up to a factor of 18.5 for zone 5 for the mean FSR at L18 (Taber and Smith, 1992).

3.2 Instrument response

This project involves seismogram data from six different types of seismometers. They are: short period (e.g., station MNG), broad band (e.g., station TOZ), very broad band (station SNZO), velocity (e.g., station MNG) and accelerometers (e.g., station WEL).

It should be highlighted that there are two sorts of L4-3D seismometers, Mark Products L4-3D and Mark Kinemetrics L4-3D, used in this project. The instrument response of the Mark Products

Table 3.1

Station locations in the Lower Hutt deployment

Station	Address	Seismic hazard zone*	Latitude (°)	Longitude (°)	NZMGE (m)	NZMGN (m)
L01	DSIR Land Resources, Taita	1	-41.1793	174.9671	2675030	6001380
L02	20A Avalon Cres., Avalon	2	-41.1930	174.9423	2672920	5999900
L03	21 Belmont Tce, Belmont	1	-41.1925	174.9252	2671490	5999990
L04	31 Rapata Cres., LH	3-4	-41.2040	174.9162	2670700	5998730
L05	DSIR, Knights Rd, LH	5	-41.2123	174.9042	2669680	5997830
L06	46 Tama St., LH	5	-41.2173	174.8953	2668920	5997290
L07	36 Titiro Rd., Korokoro	1	-41.2120	174.8643	2666330	5997940
L08	Singers Rd., Korokoro	1	-41.2190	174.8673	2666570	5997150
L09	IBM, The Esplanade, Petone	5	-41.2277	174.8710	2666860	5996180
L10	Petone Service Ctr., 7 Britannia St.	5	-41.2260	174.8788	2667510	5996360
L11	72 Heretaunga St., Petone	5	-41.2303	174.8918	2668590	5995860
L12	Elizabeth St. Pumping Station	3-4	-41.2322	174.9087	2670010	5995610
L13	DSIR, Physical Sciences	2	-41.2360	174.9175	2670730	5995180
L14	DSIR, GNS	1	-41.2350	174.9205	2670990	5995280
L15	Shell Oil, Seaview Rd.	3-4	-41.2458	174.9075	2669870	5994110
L16	56 Meremere St., Wainuiomata	5	-41.2482	174.9368	2672320	5993790
L17	5 Miles Cres., Wainuiomata	5	-41.2563	174.9480	2673240	5992870
L18	St. Bernadettes, Naenae Rd.	2	-41.2030	174.9537	2673850	5998770
L19	Naenae reservoir	1	-41.2095	174.9402	2672700	5998080
L20	4A Trinity Ave., LH	2	-41.2055	174.9303	2671880	5998540
L21	60 Witako Ave., LH	2	-41.2098	174.9243	2671370	5998070
L22	1 Malone St., LH	2	-41.2203	174.9217	2671120	5996910
L23	13 Marie St., LH	3-4	-41.2207	174.9097	2670120	5996890
L24	8 Victoria St., Petone	5	-41.2280	174.8727	2667020	5996160

* See Section 3.1.4 for the seismic hazard zone criterion. (NZMGE,NZMGN) are the coordinates of each station in New Zealand Map Grid coordinate system. The underlined stations were deployed in the 1st deployment; the boxed stations were deployed in the 2nd deployment. The stations both underlined and boxed were in both deployments.

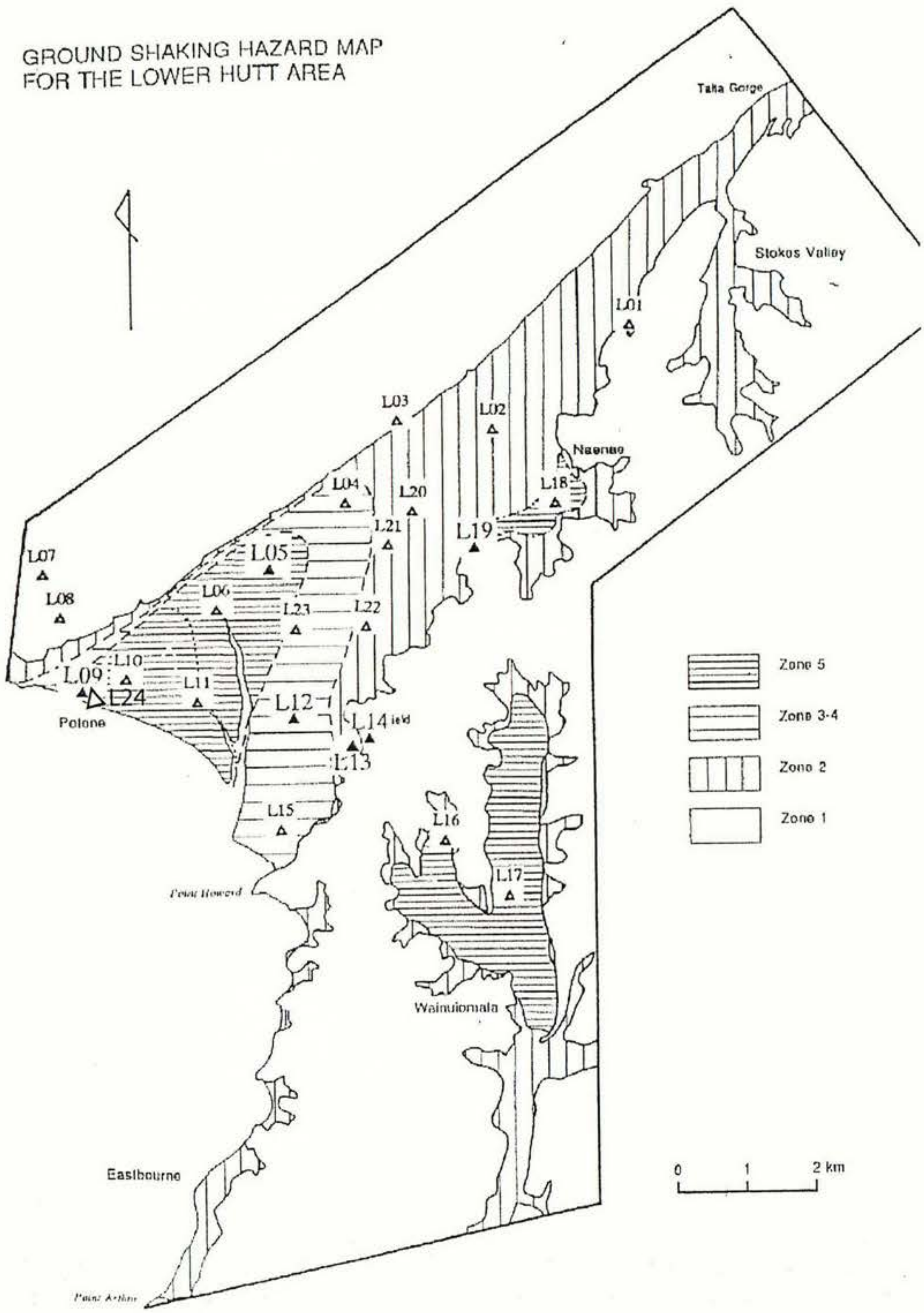

Figure 3.3 *Locations of recording sites in the Lower Hutt deployment (Taber and Smith, 1992)*

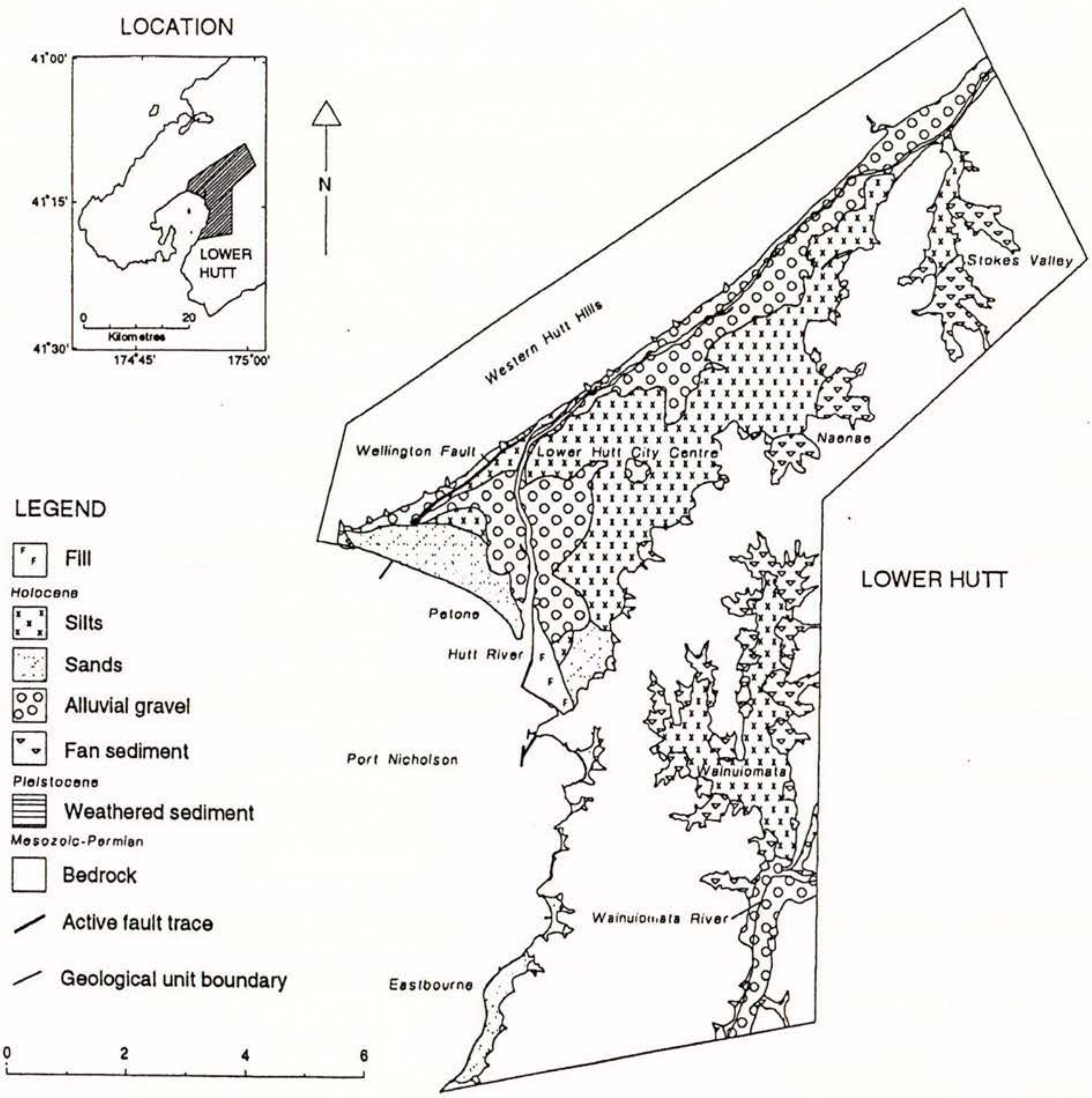

Figure 3.4 *Surface geology of the Lower Hutt Valley (Dellow et al., 1992).*

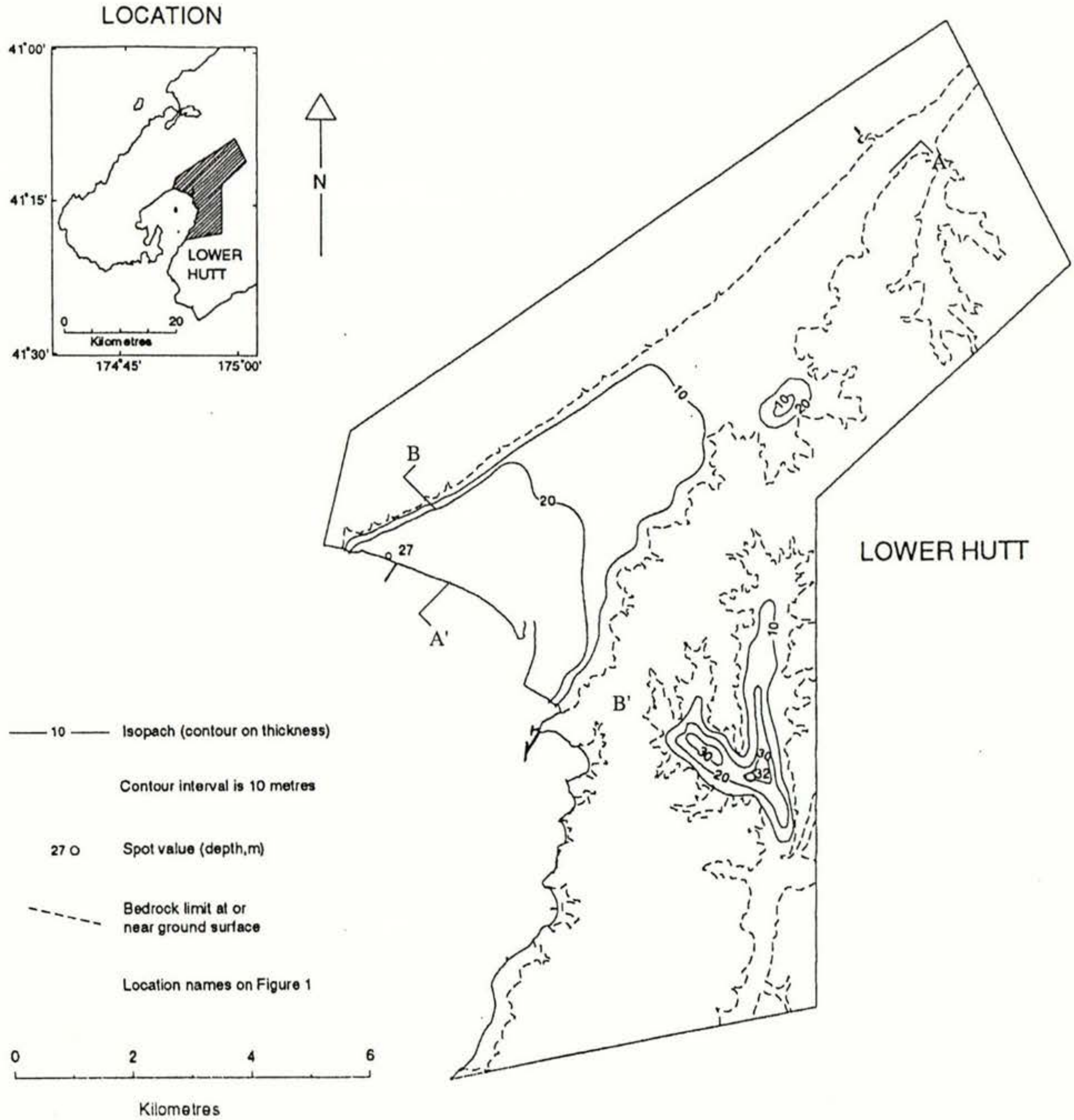

Figure 3.5 *Thickness of the soft sediments, shown by the contours (Dellow et al., 1992)*

Table 3.2

Earthquakes recorded by the Lower Hutt deployment

event	Year	Mon	Day	hour	min	Lat (°)	Long (°)	Depth (km)	Mag	Dist† (km)
1	1990	NOV	29	14	54	-39.80	174.55	104.4	4.3	144
2	1990	NOV	29	23	05	-40.69	174.66	58.9	4.5	64
3	1990	NOV	30	17	38	-40.73	174.95	16.1	4.0	56
4	1990	DEC	16	14	54	-41.14	175.16	33.0	3.2	23
5	1990	DEC	29	10	49	-41.31	174.11	48.6	3.7	68
6	1991	JAN	09	15	50	-41.06	174.73	59.9	3.6	25
7	1991	JAN	28	12	58	-41.89	171.61	8.3	5.7	285

Dist: epicentral distance from site L14

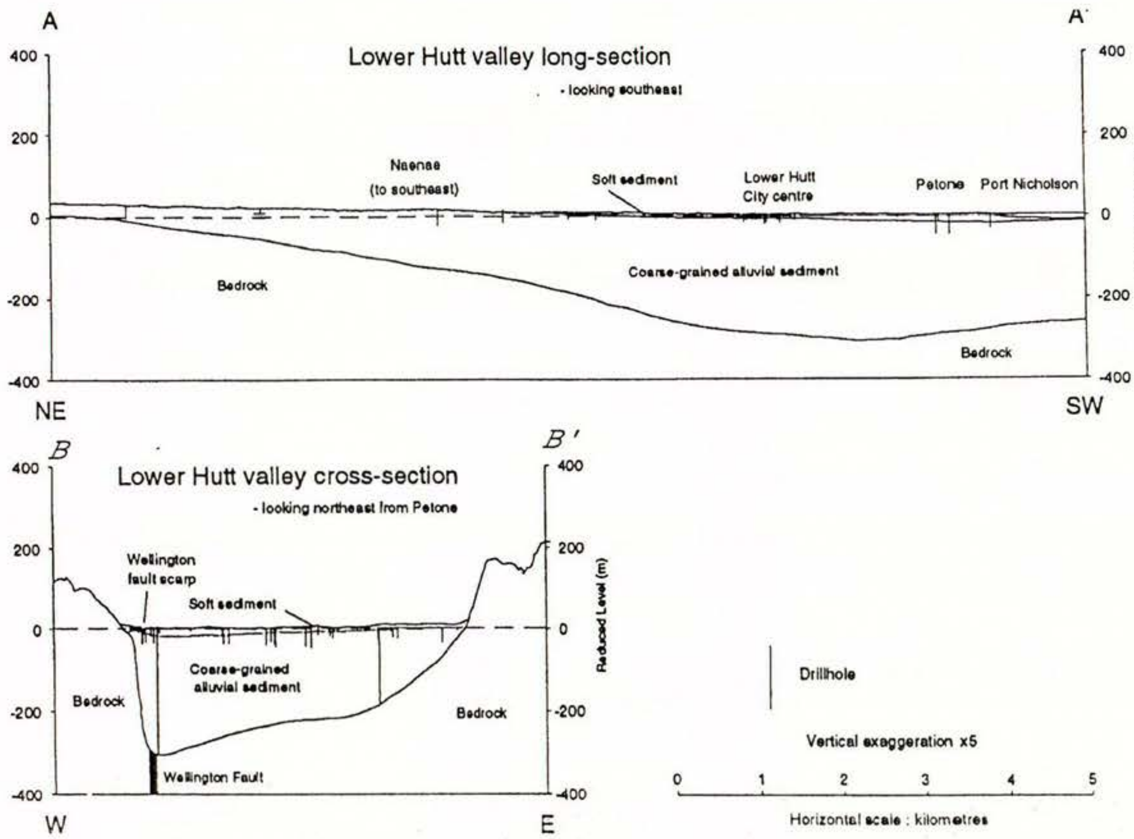

Figure 3.6 *Geological cross sections of the Lower Hutt Valley. Locations of the sections are in Figure 3.5 (Dellow et al., 1992).*

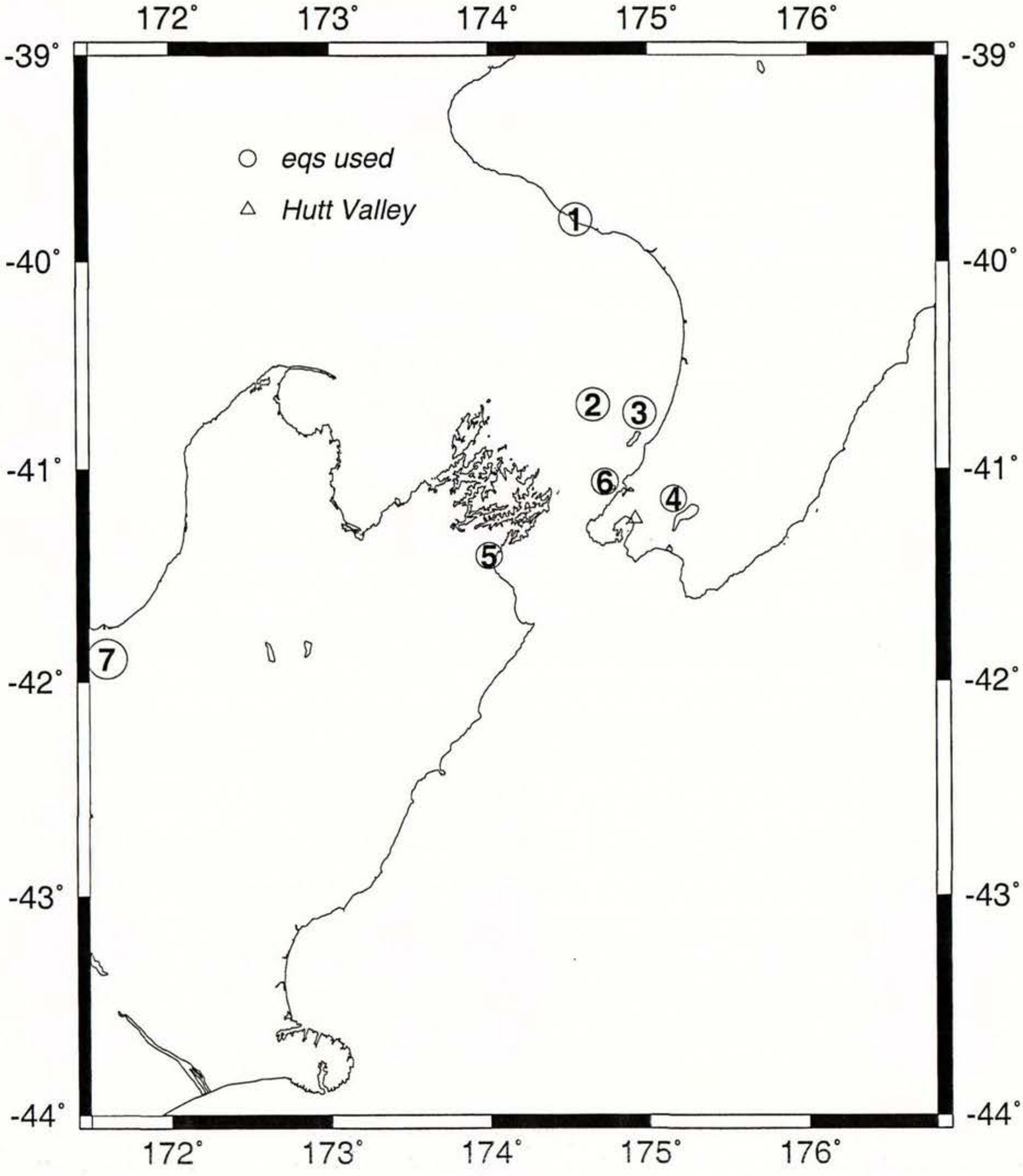

Figure 3.7 *The location of the seven earthquakes that have been selected in this study [Table 3.2]. The circles are scaled by event magnitudes, ranging from 3.2 to 5.7*

Table 3.3

Stations recording each event in the Lower Hutt first deployment and the corresponding PGV of each component (I)

Event	Lat (°)	Long (°)	Depth (km)	Mag	comp	L01	L02	L03	L04	L05	L06	L07	L08	L09	L10	L11	L12	L13	**L14**	L15	L16	L17	L18
1	-39.8	174.55	104.4	4.3		ps	ps	-	-	ps	ps	ps	ps	-	ps	-	ps	ps	ps	ps	ps	ps	-
					NS	0.52	0.36			0.23	0.21	0.31	0.29		0.14		0.18	0.21	0.35	0.19	0.52	0.80	
					EW	0.39	0.39			0.23	0.23	0.24	0.31		0.16		0.19	0.21	-	0.22	0.47	0.48	
					UD	0.24	0.21			0.10	0.14	0.31	0.16		0.10		0.10	0.24	0.26	0.15	0.27	0.31	
2	-40.69	174.66	58.9	4.5		-	ps	-	ps	-	ps	ps	ps	ps	ps	ps	-	-	ps	-	ps	-	-
					NS		2.33		1.67		2.82	1.85	2.35	2.60	2.09	2.04			1.27		3.68		
					EW		3.16		2.47		3.72	2.13	2.27	2.02	2.19	2.01			-		4.17		
					UD		3.78		1.70		1.73	2.30	1.60	3.31	1.50	2.41			0.99		1.83		
3	-40.73	174.95	16.1	4.0		ps	ps	-	ps	-	-	ps	ps	-	-	ps	ps	ps	ps	ps	ps	ps	-
					NS	3.15	2.64		2.56			1.18	1.82			1.37	1.66	2.35	1.98	1.41	4.07	4.53	
					EW	5.26	1.69		2.92			1.28	1.64			1.46	1.86	2.48	-	1.78	4.77	6.36	
					UD	2.44	2.26		2.79			0.75	1.18			1.32	0.88	1.32	2.56	1.71	1.79	2.68	
4	-41.14	175.16	33.0	3.2		ps	ps	ps	ps	ps	ps	-	ps	-	-	ps	-	-	ps	-	ps	ps	-
					NS	0.32	0.35	0.53	0.29	0.25	0.31		0.23			0.52			0.70		0.94	1.44	
					EW	0.45	0.44	0.41	0.29	0.34	0.42		0.22			0.28			0.74		0.95	0.63	
					UD	0.29	0.37	0.22	0.20	0.45	0.72		0.25			0.70			0.59		0.46	0.34	
5	-41.31	174.11	48.6	3.7		-	ps	ps	ps	-	ps	ps	-	-	ps	ps	ps	ps	ps	-	ps	-	-
					NS		0.14	0.07	0.18		0.22	0.14			0.13	0.22	0.19	0.14	0.18		0.27		
					EW		0.12	0.12	0.20		0.49	0.18			0.11	0.19	0.24	0.29	0.15		0.22		
					UD		0.27	0.13	0.11		0.36	0.11			0.87	0.10	0.17	0.15	0.26		0.18		

Note: **bold station: rock site**, underlined station: other firm sites. "ps:" p and s waves recorded, "-:" not in operation or no recording or did not work properly. There are two deployments in the survey; this is the first. Note only 18 seismographs were in operations in each deployment. The PGV is in mm/s.

Table 3.4

Stations recording each event in the Lower Hutt second deployment and the corresponding PGV of each component (II)

Event	Lat (°)	Long (°)	Depth (km)	Mag	comp	L02	L04	L05	L06	L08	L09	L11	**L14**	L15	L17	L18	**L19**	L20	L21	L22	L23	L24
6	-41.06	174.73	59.9	3.6		-	ps	ps	ps	ps	ps	ps	-	ps	-	ps	ps	ps	ps	ps	ps	-
					NS		0.61	0.95	1.02	1.56	1.31	1.14		0.96		1.01	0.54	1.12	0.82	1.90	1.23	
					EW		0.65	1.12	2.33	1.27	1.27	0.80		1.40		1.58	0.83	1.97	1.43	1.38	0.99	
					UD		1.11	1.80	3.60	1.60	3.61	2.57		2.05		0.76	0.54	1.50	1.03	1.16	1.76	
7	-41.89	171.61	8.3	5.7		ps	ps	ps	ps	ps	-	ps	ps	ps	-	ps	ps	ps	ps	ps	ps	ps
					NS	1.09	2.91	2.55	3.05	1.81		1.73	0.68	3.04		3.75	0.83	1.15	1.46	2.06	2.34	3.02
					EW	1.16	2.34	2.08	2.65	1.27		2.46	0.55	2.80		4.08	0.76	1.50	2.08	1.80.	2.17	2.54
					UD	0.62	0.74	0.90	0.88	0.83		0.90	0.37	0.83		1.71	0.44	0.57	0.68	0.87	1.08	1.88

Note:**bold station:rock site**, underlined station: other firm sites. "ps:" p and s waves recorded, "-:" no recording or not in operation. Note only 18 seismographs were in operations in each deployment. This is the second deployment. The PGV is in mm/s

L4-3D sensor with an EARSS recorder at 50 Hz sampling rate used in the NZSN, and that of the Mark Kinemetrics L4-3D with an EARSS recorder at 100 Hz sampling rate used in the Lower Hutt array, are different.

The sampling rates are 20 Hz for station SNZO, 50 Hz for short period stations in the NZSN and 100 Hz for the stations in the Lower Hutt array and the broad band stations in the NZSN. Their instrument responses vary and can be found in Appendix A.

The instrument responses from GNS were originally in two parts: the sensor's response and the recorder's response. Combining both, I got the seismograph's response. They can be found in Appendix A. Figure 3.8 shows the instrument responses of all the seismographs used in NZSN. The instrument response of the broad band seismometer Quanterra Q4126 & Guralp CMG-40T 60s is used for station KNZ, TOZ, DSZ and MQZ; that of EARSS & Kinemetrics is used for station WEL; and that of EARSS & Mark Products L4-C is used for the other stations in NZSN.

3.3 Data Processing

The seismic data was preprocessed for focal mechanism determination in Chapter 4 and for site effect studies in Chapter 5 and Chapter 7. Instrument response is removed for each seismogram, PGV is obtained for each site and data is analyzed preliminarily in this section.

3.3.1 Removing instrument response

The instrument response difference from seismometer to seismometer is considered, and the corresponding instrument response is removed from each seismogram for the focal mechanism determinations in Chapter 4 and for the subsequent FSR study in Chapter 5 and Chapter 7. Figure 3.9 demonstrates the seismogram waveforms before and after instrument response is removed in station L08 for event 1 in Table 3.2, which is equipped with the Mark Kinemetrics L4-3D seismometer and EARSS recorder (sample rate 100 Hz). The results from the instrument response deconvolution of the other seismic traces are similar.

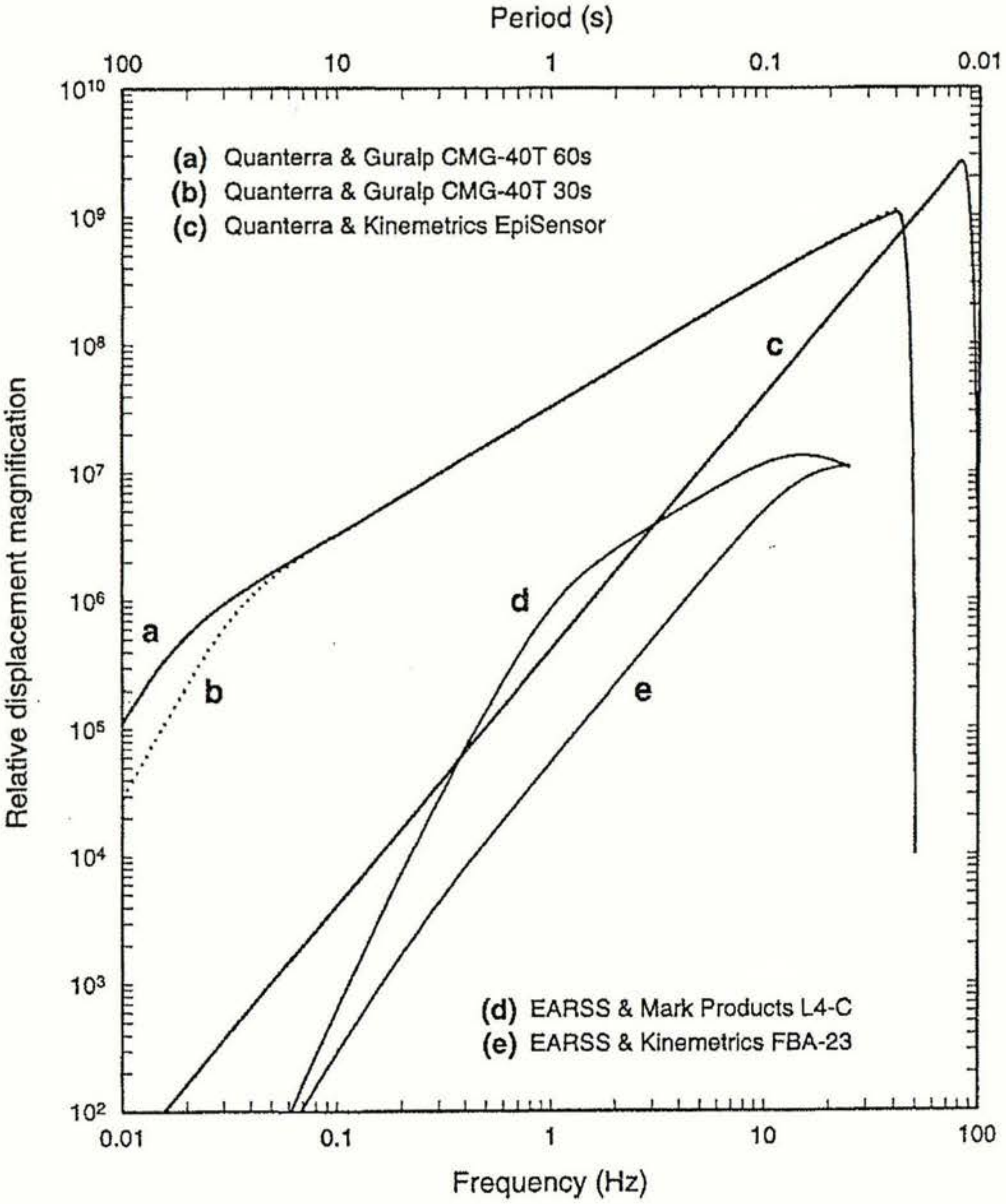

Figure 3.8 *Instrument responses of seismometers in NZSN (Maunder, 1993)*

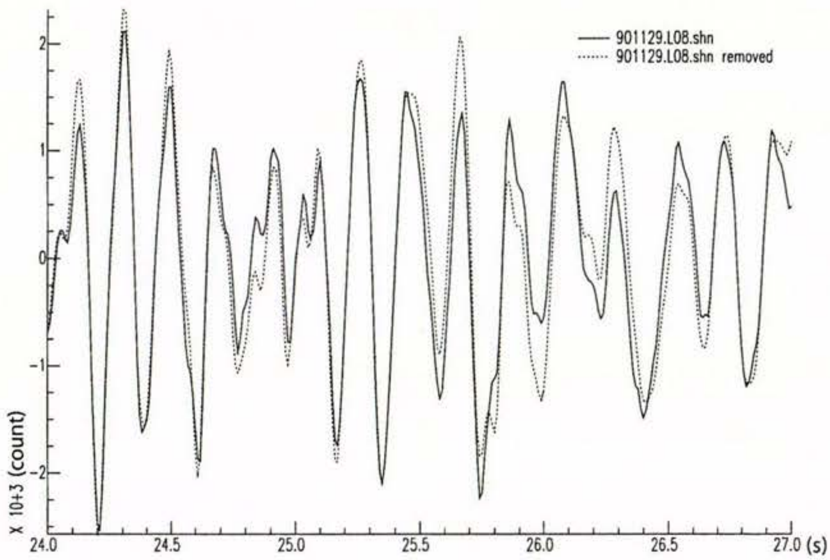

Figure 3.9 *Comparison of seismograms before and after the instrument response is removed at station L08 for event 1 in Table 3.2. The solid line is the raw data, the dotted line is the data from which the instrument response has been deconvolved (North component). The seismogram of which the instrument response is removed is normalized to the raw seismogram.*

3.3.2 Picking PGV

The PGV for the weak-motion array is picked from Seismic Analysis Code (SAC) files by a Fortran program originally written for magnitude measurement (Savage and Anderson, 1995) and is listed in Tables 3.3 and 3.4. From Figures 3.10, 3.11 and Tables 3.3, 3.4 we see that PGV varies drastically from rock station to alluvial station due to the nonlinear, frequency dependent behaviour of the sites (Taber and Smith, 1992). For example, for event 7, which is a shallow and distant event, from station L14 (rock site) to L18 (a drained and filled swamp site in Naenae), the PGV increases from 0.68 mm/s to 3.75 mm/s on the north component, from 0.55 mm/s to 4.08 mm/s on the east component, and from 0.37 mm/s to 1.71 mm/s on the vertical component. The two stations are only 4.4 km away from each other; a small distance compared to the epicentral distance of 285 km.

3.3.3 Calculating the *S* wave spectra

The *S* wave spectra for the seismic data in the portable deployments are obtained in Chapters 5 and 7 for the frequency response study. The spectra are calculated using the FFT routine in the SAC package (Tapley *et al.*, 1990).

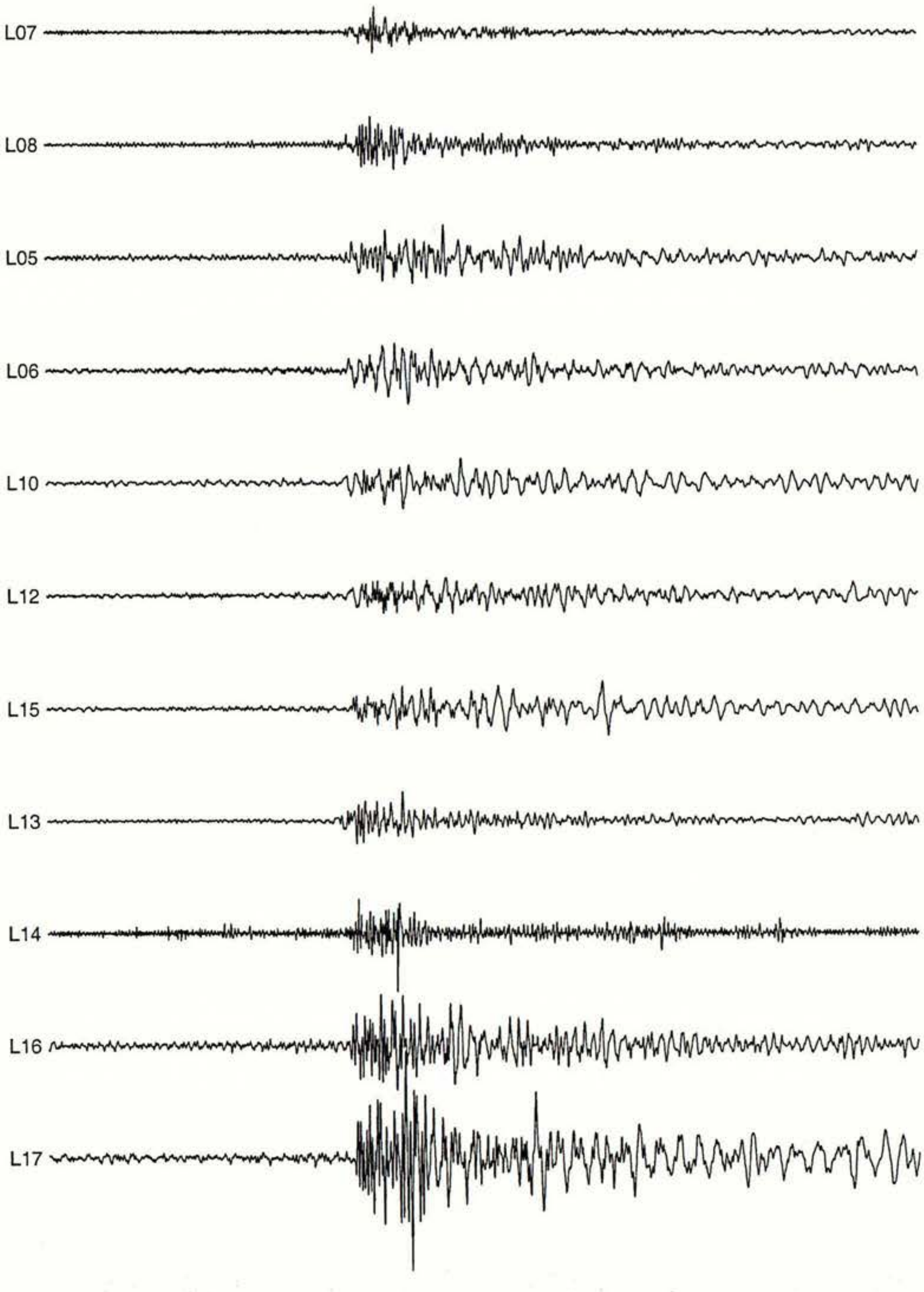

Figure 3.10 *Velocity seismograms of event 1 (north component) in Tabele 3.2 displayed roughly across Hutt Valley from L07 (a rock site) to Petone (L10) to Gracefield (L13 and L14) to Wainuiomata (L16 and L17, soft sediment sites). L17 is the station whose ground shaking is strongest among all. The maximum velocity at site L17 is 0.80 mm/s. They were normarlized by PGV of L17. The instrument response has been removed. L07, L08 and L14 are rock sites.*

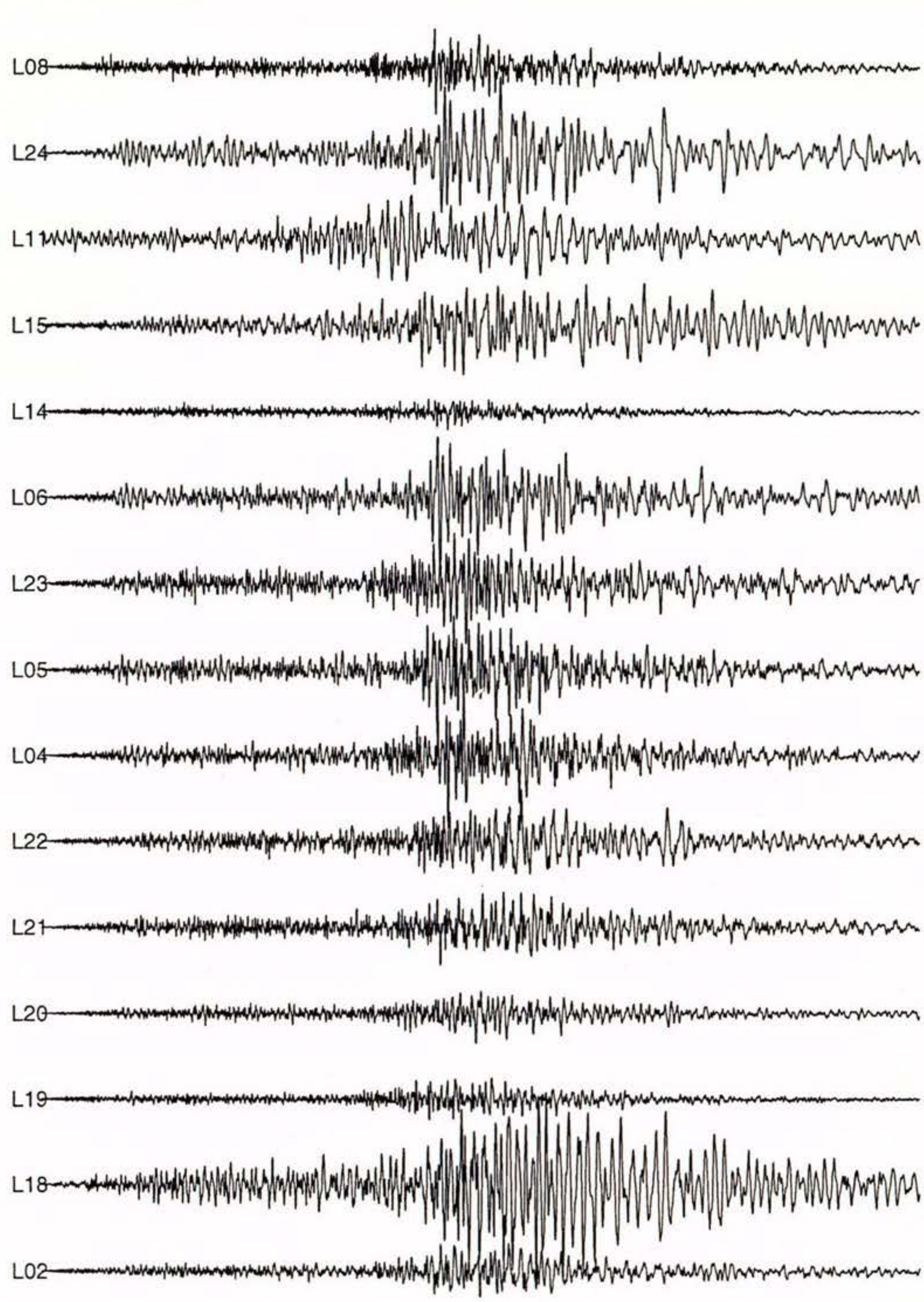

Figure 3.11 *Velocity seismograms of event 7 in Table 3.2 displayed approximately along the length of Hutt Valley (north component). The firm valley edge sites are L08, L14, and L19. There is a general decrease in amplitude when going up-valley from Petone (L24) to L02. Note the high amplitude at L18, which is located over a drained and filled swamp in Naenae. The maximum velocity at site L18 is 3.75 mm/s. They were normarlized by PGV of L18. Instrument response has been removed. L14 and L19 are rock sites.*

3.4 Data analysis

Figure 3.10 is a plot of the velocity seismograms recorded on a line of sites trending roughly across the Hutt Valley for an earthquake 144 km to the NW. The smallest amplitudes are visible at sites L07 and L08, located on rock on the west side of the valley and L14, the site used as the reference site in Chapter 5 and Chapter 7 on the east side of the valley. The initial amplitude of the shaking at the sites in the valley (L05, L06, L10, L12 and L15) is similar to or only slightly higher than at the rock sites but the shaking continues to a longer duration at the valley sites. Longer durations are due to the wave reflection by the underlying sediment layers and the scattering from the heterogeneous nature of the soft soil. Shaking duration lengthening in sediments and heterogeneities is also observed in other places around the world (Field *et al.*, 2000; Kawase, 1996). The two sites in Wainuiomata (L16 and L17) show much greater amplification of the shaking as well as increased duration.

Figure 3.11 shows the variation of shaking from the harbour to the northern extent of the array for an earthquake 285 km WSW from the sites. Other than the rock sites L08, L14 and the sediment site L18, there is a gradual decrease in amplitude from site L24 on the Petone foreshore to site L02, 5 km up the valley. Site L19 is another rock site on the east side of the valley. Site L18, which exhibits the most amplification, is located on a pocket of soft material (a drained swamp) in Naenae (Dellow *et al.*, 1992).

We selected seven events from the initial 33 by the following criteria:

1. Closer and shallower earthquakes are preferred for studying larger microzoning effects, as they cause more severe shaking hazards. The selected earthquakes ranged from 23 km to 285 km in epicentral distance and 8.3 km to 104.4 km in focal depth.

2. Among all the available events, stronger earthquakes are preferred. The selected earthquakes ranged from M_L 3.2 to 5.7. All of these events produced only weak motions at the seismographs in Lower Hutt.

3. The earthquakes which are recorded most widely by the Lower Hutt deployment are preferred. Between 11 to 16 stations recorded the selected earthquakes.

4. Only those earthquakes which have ready focal mechanism or whose focal mechanism can be calculated are selected. This requires that its waveform is recorded clearly by at least 3 NZSN

permanent stations.

The chosen seven events are listed in Table 3.2 and their corresponding spatial distribution is illustrated in Figure 3.7.

CHAPTER 4

FOCAL MECHANISM CALCULATION

4.1 Theory

There are three main methods to calculate focal mechanism solutions. They are the first motion method, the moment tensor waveform inversion method, and the combined first motion and amplitude ratio method. Note the combined first motion and amplitude ratio method is called "the amplitude ratio method" subsequently for simplification. The first motion method only makes use of the direction of the *P* first motion. It does not make use of the amplitude of the first motion, which is sensitive to the station position relative to the nodal planes (it is 0 in the *P* nodal plane and it reaches maximum in the *S* nodal plane). Therefore it needs many stations and good azimuthal coverage to constrain the nodal plane.

A dense network is required to give adequate station coverage and the event must occur within the network. New Zealand is an island country, so that the noise from sea waves and wind is strong in the seismogram. Hence the first motions of the moderate earthquakes may be buried in the noise and can not be determined. There are no ocean floor seismometers currently installed in New Zealand, so the coverage is poor. The moment tensor waveform inversion method only exploits the long period waves (i.e. about 10 - 100 s), which are fairly insensitive to complexities in the earth's structure, and makes uses of the entire waveform. It needs at least three broad band stations with good azimuthal coverage (Dreger and Helmberger, 1990; Dreger and Helmberger, 1993; Dreger and Langston, 1995; Matcham, 1999). Unfortunately, during the Lower Hutt portable array period (Nov. 1990- Feb. 1991), no broad band data are available at all. Hence the amplitude ratio method is chosen in this study for these moderately strong earthquakes.

The amplitude ratio technique (Schwartz, 1995; Matcham, 1999) uses a comparison between the

Table 4.1
Corners used in instrument response deconvolution

Instrument Type	f1	f2	f3	f4
Short Period	0.1	0.5	15	25
Broad Band	0.002	0.005	5	10

recorded waveform, and that expected from theoretical calculations. It requires fewer stations than the first motion method. The amplitude ratio depends on the anglular distance between the station and P and S nodal planes. Stations which cover $\frac{1}{2}$ quandrant in the focal sphere are enough for determining focal mechanisms with this method. The synthetics calculated in order to do this are the expected displacement seismograms from a given fault (see below for further detail). It uses a higher freqency band (1hz - 2hz in this case, in which most of the energy for local earthquakes lie) than the moment tensor inversion method, so recorded data from both short period seismometers and broad band seismometers can be utilised.

Ideally, the instrument response in a velocity or acceleration seismogram recorded by a seismometer should be removed first, then it should be converted into a displacement seismogram in order to compare with the displacement synthetics. During this procedure, a filter is implemented. The filter depends on the corners of the instrument response, and can be found in Table 4.1. f1 and f2 specify the high-pass filter and correspond to the frequencies over which the taper is applied. The taper is zero below f1 and unity above f2. f3 and f4 are analogous for the low-pass filter. The taper is unity below f3 and zero above f4. Unfortunately, a mistake in deconvolution of instrument response was discovered after the rest of the calculations were made *. One zero should have been added to the instrument response file of L4-3D from GNS for the NZSN stations. The result is that for the GNS stations, velocity seismograms rather than displacement seismograms were used. We tested this effect on two events and found the focal mechanism were not affected except for a [Table 4.3] reduction of 0.1 in ARerr (the error statistics). This is because only amplitude ratios of P/S, P/SV, P/SH and SV/SH are employed in determining focal mechanisms, and the mistakes of lacking one zero in the instrument response file are cancelled.

It is important to choose the proper filter corners because the long period ground motion will be amplified greatly during the integration.

The focal mechanism determination program was composed in SAC (Tapley *et al.*, 1990) and

*This mistake was discovered by the end of this reasearch, so there is no time to redo everything from the beginning.

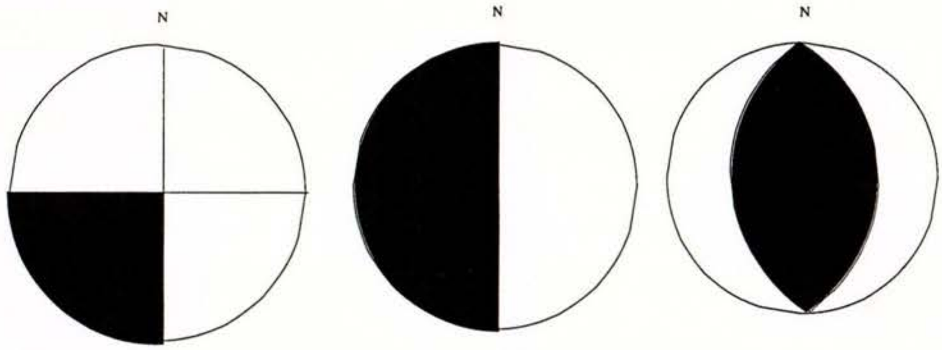

Figure 4.1 *The three fundamental faults needed to describe an arbitrary deviatoric momemt tensor (Dreger and Helmberger, 1990; Dreger and Helmberger, 1993; Dreger and Langston, 1995).*

MATLAB Version 4.2c based on the amplitude ratio technique (Schwartz, 1995); details can be found in Cavill *et al.* (1997) and Matcham (1999).

In general, the real observation $v_i(t)$ (i=1, 2, 3), which may be one of the ground displacement, velocity or acceleration, can be described as the convolution of three functions (Dreger and Helmberger, 1990; Dreger and Helmberger, 1993; Dreger and Langston, 1995) as described in equation (4.1).

$$v_i(t) = M_{jk}(t) * G_{ijk}(t) * I(t) \quad (i,j,k = 1,2,3) \tag{4.1}$$

where $M_{jk}(t)$ is the jk_{th} component in moment tensor function, $G_{ijk}(t)$ the jk_{th} component of Green functions, which is the displacement caused by the fundamental faults as shown in Figure 4.1, which includes the effect of the seismic ray path, and I(t) is the instrument response, '*' represents the convolution operator. The instrument response can be deconvolved as stated in Section 3.2 from the record. Consequently, a displacement seismogram from the pure ground motion without instrument distortion is produced. The eventual displacement seismogram, which is independent of the sensor used to record it as illustrated by equation (4.2), is used to determine focal mechanisms later.

$$u_i(t) = M_{jk}(t) * G_{ijk}(t) \tag{4.2}$$

It is unrealistic to know the exact time history of each component of the moment tensor function. To circumvent this problem, we assume the seismic source has the same fixed time history for all components, i.e. synchronous source (Dreger and Helmberger, 1990; Dreger and Helmberger, 1993; Dreger and Langston, 1995):

$$M_{jk}(t) = M_{jk}s(t) \tag{4.3}$$

where M_{jk} is the peak amplitude of the moment tensor function [equation (4.6)], s(t) is the source time function (STF). There are several options for the STF (Ben-Menahem and Singh, 1981). A ramp is chosen as the STF in focal mechanism determination. The Green functions can be obtained from the fundamental faults as shown in Figure 4.1 by the DWN method (Zeng and Anderson, 1995) using Robinson (1986) velocity model. Therefore, only M_{jk} are unknowns. M_{jk} can be determined by the amplitude ratio method through a grid search over the comparison of synthetic seismograms and observed seismograms.

4.1.1 Synthetic seismograms

I calculated the Green function based on the fundamental faults for each station in the seismic wavefield. The Green function is composed of ss_r, ds_r, dd_r, ss_t, ds_t, ss_z, ds_z and dd_z, representing radial (r), transverse (t) and vertical (z) displacements from the fundamental faults shown in Figure 4.1; where ss, ds and dd represent strike slip, dip slip and 45° dip slip faults, respectively. The displacement synthetic seismograms for any station are the linear combinations of these eight seismograms (Dreger and Helmberger, 1990; Dreger and Helmberger, 1993; Dreger and Langston, 1995).

$$\begin{aligned} \mathrm{u}_r &= A_1 ss_r + A_2 ds_r + A_3 dd_r \\ \mathrm{u}_t &= A_4 ss_t + A_5 ds_t \\ \mathrm{u}_z &= A_1 ss_z + A_2 ds_z + A_3 dd_z \end{aligned} \tag{4.4}$$

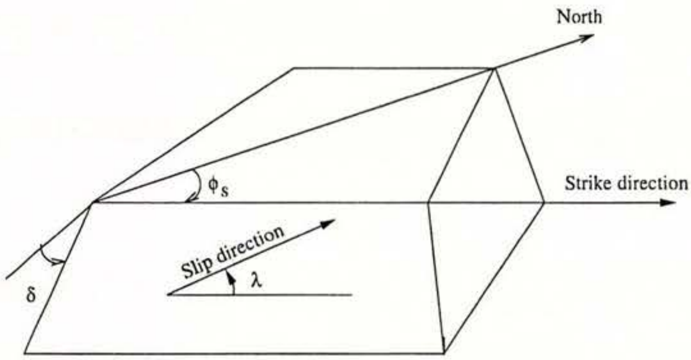

Figure 4.2 *Fault plane conventions. Definition of the fault-orientation parameters (strike ϕ_s, dip δ), and slip-direction λ (Aki and Richards, 1980). ϕ_s is measured clockwise round from north, with the fault dipping down to the right of the strike direction: $0 \le \phi_s \le 2\pi$. δ is measured down from the horizontal: $0 \le \delta \le \pi/2$.*

where A_i (i=1, 2, 3, 4, 5) are the linear functions of the independent deviatoric moment tensor elements:

$$\begin{aligned}
A_1 &= \frac{1}{2}(M_{yy} - M_{xx})cos2\theta - M_{xy}sin2\theta \\
A_2 &= M_{xz}cos\theta + M_{yz}sin\theta \\
A_3 &= \frac{1}{2}(M_{xx} + M_{yy}) \\
A_4 &= \frac{1}{2}(M_{xx} - M_{yy})sin2\theta - M_{xy}cos2\theta \\
A_5 &= M_{yz}cos\theta - M_{xz}sin\theta
\end{aligned} \tag{4.5}$$

(Dreger and Helmberger, 1990; Dreger and Helmberger, 1993; Dreger and Langston, 1995) and θ is the source-receiver azimuth (positive clockwise from the north). Note the Green function defined here is independent of the source-receiver azimuth.

Under a Cartesian coordinate system in which the x-direction is taken as positive north, y positive east and z positive downward with the origin at the epicenter, the quantities M_{ij} (i, j=x, y, z) are the components of the moment tensor **M** defined as (Aki and Richards, 1980):

$$\begin{aligned}
M_{xx} &= -M_0(\cos\lambda\sin\delta\sin 2\phi_s + \sin\lambda sin2\delta\sin^2\phi_s) \\
M_{xy} &= M_0(\cos\lambda\sin\delta\cos 2\phi_s + 0.5\sin\lambda\sin 2\delta\sin 2\phi_s) \\
M_{xz} &= -M_0(\cos\lambda\cos\delta\cos\phi_s + \sin\lambda\cos 2\delta\sin\phi_s) \\
M_{yy} &= M_0(\cos\lambda\sin\delta\sin^2\phi_s - \sin\lambda\sin 2\delta\cos^2\phi_s) \\
M_{yz} &= -M_0(\cos\lambda\cos\delta\sin\phi_s - \sin\lambda\cos 2\delta\cos\phi_s) \\
M_{zz} &= M_0\sin\lambda\sin 2\delta
\end{aligned} \tag{4.6}$$

where M_0 is the earthquake's scalar moment, ϕ_s is the fault's strike azimuth, measured clockwise from north; δ is the fault dip angle, measured from the horizontal; λ is the fault rake, the angle between the strike direction and slip (Aki and Richards, 1980). Note there are three azimuths used in this method: the azimuth of fundamental faults (0°, Figure 4.1) used when Green functions are calculated, the source-receiver azimuth (θ, equation (4.5)) used in the coeffcients A_i (i=1, 2, 3, 4, 5) and the azimuth of the focus fault (ϕ_s,equation (4.6)). The imaginary frequency technique and the DWN method are used in Green function preparation (Zeng and Anderson, 1995).

4.1.2 The amplitude ratio and first motion polarity technique

The initial steps of this technique are: the eight synthetic seismograms from the fundamental faults (Dreger and Helmberger, 1990; Dreger and Helmberger, 1993; Dreger and Langston, 1995) at each station are calculated, and the displacement synthetics are obtained from equations (4.4) and (4.5). The observed acceleration or velocity data are converted to displacement seismograms and rotated into the vertical, radial and transverse components in the cylindrical coordinate system [Figure 4.4] in order to be comparable to the corresponding displacement synthetics (Schwartz, 1995), where the 3 unknowns (ϕ_s, λ and δ) are involved.

Once this is done, a grid is constructed covering the strike, rake and dip specified. The grid area and spacing are adjustable so that an initial coarse search can be performed, followed by a finer search, covering less area. For each fault orientation, the first motion and amplitude ratios are calculated from the synthetics. The first motions in the vertical component from the data are picked by the user and P-wave and S-wave windows are also picked. The criteria for selecting the P, S windows are:

1. Only the direct arrivals P_g and S_g are wanted. The refracted arrivals P_n and S_n, which arrive earlier than P_g and S_g when the focal distance falls in a certain range and the focus is above the Moho discontinuity, are excluded.

2. For this method, only the initial part of P_g and S_g which are correlated with source parameters directly are exploited. The P_g and S_g window should stop before the arrival of the waves produced by scattering and reflection. The P_g and S_g windows are 2 s in length approximately.

3. The P first motion and window are selected in the vertical component, as P ground motion in the vertical component is clearer and stronger than that in the horizontal components. The S

window start time is selected in the tangential component to avoid mistaking the *P-S* and *S-P* conversions as *S*. *P-S* conversion are generated by the reflection when the *P* wave hits the free surface. *S-P* conversions are generated by the reflection when the *S* wave hits the free surface.

4. The first motions of P_n are used only in the case that it is not fuzzy, otherwise it will be discarded.

It is vital to pick the *P* and *S* windows properly - the focal mechanism results change drastically with the window position.

Within the given windows, the algorithm will search for the maximum amplitudes for each arrival. The results for the data are compared with the grid of synthetic results. A set of results whose errors fall within the given limits are returned for each of the techniques separately - first motions and amplitude ratios. Both sets of limits are specified as an error above the minimum error. First motion errors are simply the number of stations whose first motion polarities fall outside the respective quadrants for the given source mechanism. The amplitude ratio errors for each ratio (P/S, P/SV, P/SH and SV/SH) are the log of the ratio of measured to synthetic ratios:

$$\begin{aligned}
Err_{P/S} &= log\left(\frac{P_{data}/S_{data}}{P_{syn}/S_{syn}}\right) \\
Err_{P/SV} &= log\left(\frac{P_{data}/SV_{data}}{P_{syn}/SV_{syn}}\right) \\
Err_{P/SH} &= log\left(\frac{P_{data}/SH_{data}}{P_{syn}/SH_{syn}}\right) \\
Err_{SV/SH} &= log\left(\frac{SV_{data}/SH_{data}}{SV_{syn}/SH_{syn}}\right)
\end{aligned} \tag{4.7}$$

and the total amplitude ratio error Err_T is defined as:

$$Err_T = \sqrt{\frac{Err_{P/S}^2 + Err_{P/SV}^2 + Err_{P/SH}^2 + Err_{SV/SH}^2}{4}} \tag{4.8}$$

Those members of the grid that fall within the given error margins are returned as possible results. The best fit is given as the result with the smallest error from the amplitude ratios that falls within the set of possible results returned by the first motion polarity calculations. The amplitude ratio gridsearch is not expected to be successful for events if only one station provides amplitude ratio data (Matcham, 1999). It can give reasonable focal mechanism solutions for each event since several stations provide amplitude ratio data in this project.

4.1.3 Amplitude ratio calculation

For each position in the grid of strike, dip, rake, equations (4.4) and (4.5) are used to calculate a synthetic displacement seismogram for the vertical, radial and transverse components from the Green functions already created. In order to best represent the maximum absolute amplitude, the envelope as shown in Figure 4.4 of the signal is used to calculate the maximum amplitudes. The envelope of the signal is found using the method implemented by the SAC package (Tapley *et al.*, 1990). The envelope is the magnitude of the analytic signal by quadrature. The amplitude maxima are calculated within the P and S windows specified by the user for all the stations chosen for focal mechanism.

4.2 Data sources

The NZSN provides the bulk of the data for the focal mechanism solutions, with the addition of SNZO, and one of the temporary stations from the portable deployments to provide better azimuthal coverage for each earthquake. Not all the station data from the portable deployment are used for focal mechanisms because compared to the focal distance, those stations are close to each other. Their azimuths and take off angles to the earthquake are quite simliar to each other, and they occupy almost the same position in the focal sphere. The NZSN consisted of short period velocity seismometers mainly during the period of the Lower Hutt array, with the only exception being station WEL, which was equipped with an acceleration seismometer. The data from station WEL was fully exploited in this project due to its important position. It is located in the Wellington urban area and recorded most events clearly. All the seismographs in the Lower Hutt deployment are short period velocity seismometers, and all the 24 sites shared the same type of instrument.

Only 3-component stations are used for the amplitude ratio technique. In choosing stations for amplitude ratio, we abide by the following principles:

1. Stations with rock foundations are preferred, because the first motion at the rock site is much more clear. Moreover, ground shaking in stations located on soft layers may be amplified

Table 4.2
Robinson (1986) Wellington velocity model

Layer No.	Thickness (km)	v_p (km/s)	Q_p	v_s (km/s)	Q_s	ρ (g/cm^3)
layer 1	0.4	4.40	100.0	2.54	50.0	2.46
layer 2	4.6	5.63	100.0	3.16	50.0	2.61
layer 3	10.0	5.77	200.0	3.49	100.0	2.69
layer 4	10.0	6.39	300.0	3.50	150.0	2.76
layer 5	10.0	6.79	500.0	3.92	250.0	2.93
layer 6	10.0	8.07	1000.	4.80	500.0	3.39
layer 7	250.0	8.77	1000.	4.86	500.0	3.55

greatly and the corresponding amplitude ratio is distorted, consequently it is less reliable for focal mechanisms.

2. Close stations are prefered since the Robinson (1986) crustal velocity model [*Table 4.2*] used for focal mechanisms is derived for the Wellington area mainly and the amplitude ratio method is a method chiefly for local earthquakes.

3. Stations with some difference in azimuth and take off angle are prefered. The spatial distribution of stations can be found in Figure 3.1. This will guarantee that different positions in focal sphere relative to P and S nodal planes are represented. Station MRW is not far away from all earthquakes studied here and it recorded most of the earthquakes. Unfortunately, data from MRW are clipped for most earthquakes studied here. Only its first motion is exploited in this situation. Otherwise the amplitude ratio from MRW can improve the azimuth coverage for focal mechanisms.

4.3 Basic Processing

The data in use were stored in AH format (the data from the Lower Hutt portable deployment, the Wellington portable deployment, the Leeds Tararua portable deployment, the broad band portable deployment, the Alicetown portable deployment and SNZO) and SAC format (the data from NZSN). For the initial processing stage, all the data is converted into SAC format (Tapley *et al.*, 1990). The deconvolution of the instrument response, integration and decimation are performed by shell scripts, which invoke the SAC package. Once this stage of the process is completed, the data is converted into the Helmberger ascii format. This is a data format that consists of a file header containing the number of records, and then another header for each trace containing sampling interval and the number of points. The data follow this second header and are recorded in ascii text.

We use the Robinson (1986) Wellington regional velocity model [Table 4.2] to calculate the synthetic seismograms. It consists of seven layers with seismic wave velocity changes in the vertical direction only. The Moho velocity discontinuity is located 35 km below the free surface. In the Robinson (1986) model, the layer velocities are designed to provide a suitable contrast to represent the interface of the subduction zone formed by the collision of the Pacific plate and the Australian plate.

The synthetic Green functions are created using the method of Zeng and Anderson (1995). This code is similar in the main part to the 1D forward modelling technique for ground motion (Benites *et al.*, 2002) which will be used in Chapter 5, where the synthetic velocity seismograms are obtained and used to compare with the observed data. Both codes use travel times and thus require that the synthetics start from the event origin time. The codes use frequency-wavenumber integration to propagate the stress matrix through the layers of the model. The output of this program is first converted into SAC format, and later converted into the Helmberger ascii format by shell scripts before being compared with the recorded data.

The shell scripts for basic processing were originally developed by Dreger and Langston (1995) and then modified by Cavill *et al.* (1997), using SAC (Tapley *et al.*, 1990). The amplitude ratio and first motion polarity code was written by Cavill *et al.* (1997), using Matlab. For this technique a graphical user interface was developed by Matcham (1999) for ease of use, and to minimise the potential for mistakenly passing the wrong parameters.

4.4 Procedure

The grid calculates a matrix of the maximum amplitudes of the *P*, *SV* and *SH* waves for each point on the focal sphere for the synthetics. A similar matrix is created for the *P* first motion polarities for the synthetics. I pick *P*, *SV* and *SH* wave windows and *P* first motions for all the available stations. The picked windows are used to calculate a similar set of matrices for the data, and the columns are compared between the data and the synthetics to determine the best fault parameter solution.

I illustrate the inversion procedure using event 2 in Table 3.2 [Figures 4.3 and 4.4]. This earth-

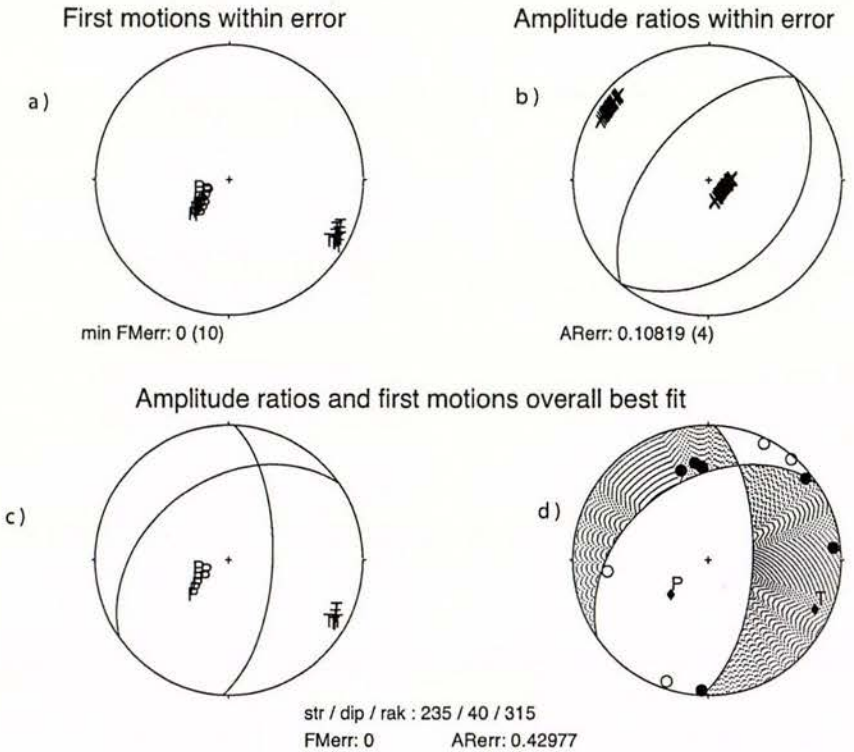

Figure 4.3 *Results of first motion and amplitude ratio fitting for event 2 in Table 3.2 (equal area, lower hemisphere projection). (a) Focal mechanism solution by first motions only. "min FMerr" represents the minimum first motion error (0 in this case) among all the first motions available (10 in this case). (b) Focal mechanism solution by amplitude ratio only. ARerr represents the minimum amplitude ratio error (0.10819 in this case) from all the stations used (4 in this case). (c) Focal mechanism solution by both. (d) The best fit focal mechanism with the first motion data overlain.*

quake is located only 64 km away from the Lower Hutt array. It is located to the north west of Wellington. No P_n and S_n appeared in any stations as the focus is below the Moho discontinuity. Displacement seismograms for the fundamental faults and distances to all stations are calculated at a depth of 59 km, assuming the GNS epicentral parameters and Robinson (1986) Wellington velocity model [Table 4.2].

Figure 4.3 demonstrates (a) all possible solutions of the T and P axes from the polarity information alone. Also demonstrated (b) are the locations of the principle axes and the nodal planes from the amplitude ratio data only. Note P and T axes are not distinguishable from amplitude ratio information. All results within the error level are displayed in (a) and (b). Plot (c) shows the results constrained by all the information from both the polarity and amplitude. The first motion results are used to discrminate P and T axes. (d) shows the best fit focal mechanism with the first motion data overlain. This is the eventual result, which will be used in the forward modelling in Chapter 5 and Chapter 7.

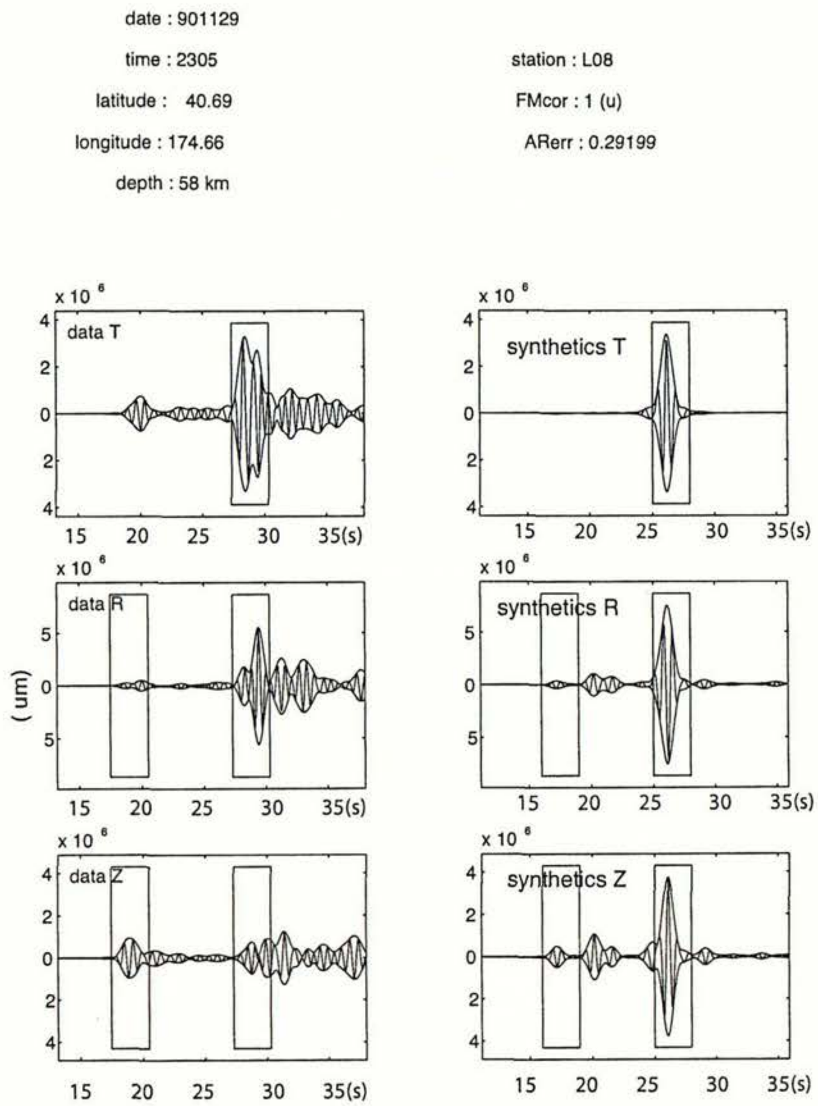

Figure 4.4 *Displacement data from L08 and the corresponding synthetics for the best fit solution for the event shown in Figure 4.3. data T and synthetics T represent the tangential component; data R and synthetics R represent the radial component; data Z and synthetics Z represent the vertical component in the cylindrical coorinate system. Note the synthetics in this figure are essentially identical to those obtained by the 1D modelling code [Figure 5.2]*

We can also see that the azimuthal coverage for this event is very good.

I describe the method by showing the steps used for station L08. The recorded data from the other stations are processed in the same way. Figure 4.4 shows the comparison between data and synthetics for the station L08, a temporary station in the Lower Hutt deployment, located to the north of Hutt Valley at a rock site.

The synthetics of L08 [Figure 4.4] are calculated in this way: once the fault farameters have been determined, the components of the focal moment tensor are derived from equation (4.6). Combining with the source-receiver azimuth θ of L08, the coefficients A_i (i=1, 2, 3) can be derived from equation (4.5). Exploiting the Green functions calculated previously (Zeng and Anderson, 1995), the synthetics are forward modelled by equation (4.4). Both the data and the synthetics were filtered by a 2nd order butterworth filter to 1 Hz-2 Hz. The data were decimated to 10 samples/s from the original 100 samples/s for the comparison with the corresponding synthetics. The corresponding waveforms are quite similar. However, there are more later arrivals in the coda of the data, probably generated by scattering, refracting and reflecting of the incident waves by the heterogeneity of the genuine medium. The *P* ground motion is 0 in the transverse component in the synthetics due to the fact that the Robinson (1986) velocity model is horizontally homogeneous, whereas the *P* ground motion is nonzero in the transverse component in the data due to the heterogeneous nature of the real crust. However, the *P* ground motion in the transverse component in the data is still much smaller than that in the radial component, which is why we pick the *S* window from the transverse component.

The entire focal sphere grid search for the amplitude ratios generates a source of error estimation [equations (4.7) and (4.8)]. The errors for all possible fault orientations are plotted against the strike, dip and rake [Figure 4.5]. This solution has a best fit of $40°/35°/90°$ (strike/dip/rake) for nodal plane I and $228°/55°/84°$ for nodal plane II. Two minima are displayed, one for the fault plane and one for its auxiliary plane. A 180° ambiguity in the rake exists due to the fact that no polarity information is used. The first motion polarity data is added to remove the ambiguity. The error plot equivalent to Figure 4.5 with the first motion data included is shown in Figure 4.6. From these plots, the user can determine the level of certainty that should be assigned to the result. In general, we find FMerr [Table 4.3] ranges from 0 to 3 and ARerr [Table 4.3] ranges from 0.09 to 0.62.

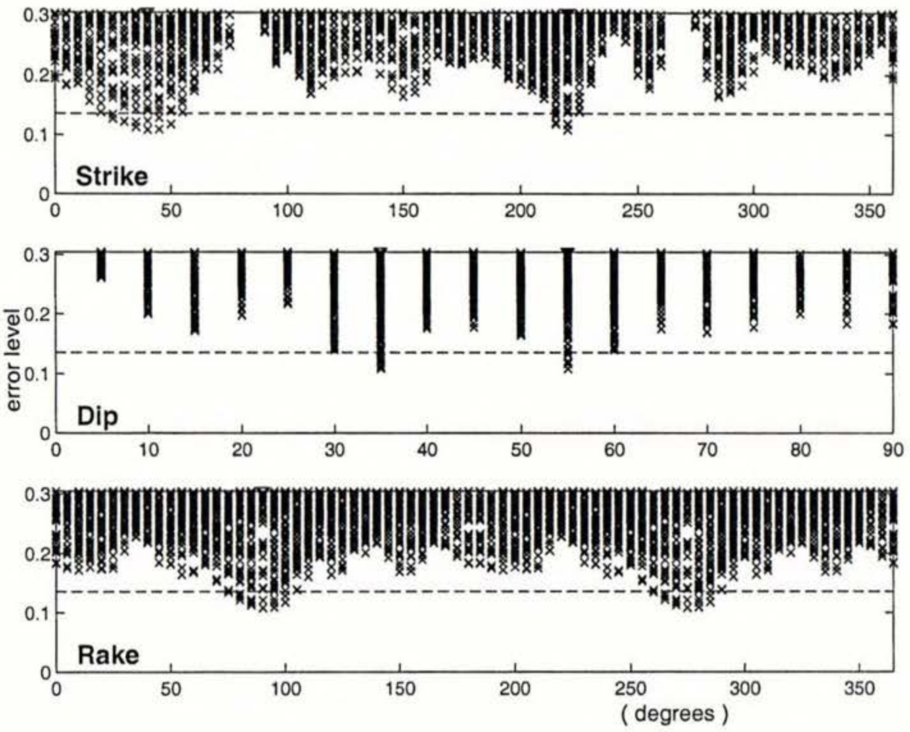

Figure 4.5 *A graphical indication of the reliability of the solution returned by the amplitude ratio grid search. This solution has a best fit of 40° / 35° / 90° (strike/dip/rake, nodal plane I). Note also the 180° ambiguity in the rake measurement due to the lack of polarity information. The dotted line shows the error above which the focal mechanism is rejected. The plot is truncated at error of 1.3 times this level.*

Table 4.3

Focal mechanisms used for 1D forward modelling in Chapter 5 and (1D+3D) forward modelling in Chapter 7.

event	Date	Time	Lat (°)	Lon (°)	Depth (km)	Mag	strike (°)	Dip (°)	Rake (°)	Dist* (km)	FMerr**	ARerr***
1	29/11/90	14:54	-39.80	174.55	104.4	4.3	55	80	245	144	0	0.31
2	29/11/90	23:05	-40.69	174.66	58.9	4.5	235	40	315	64	0	0.43
3	30/11/90	17:38	-40.73	174.95	16.1	4.0	15	20	105	56	0	0.43
4	16/12/90	14:54	-41.14	175.16	33.0	3.2	45	65	300	23	0	0.09
5	29/12/90	10:49	-41.31	174.11	48.6	3.7	60	45	300	68	0	0.33
6	09/01/91	15:50	-41.06	174.73	59.9	3.6	100	20	170	25	0	0.32
7	28/01/91	12:58	-41.89	171.61	8.3	5.7	300	50	345	285	3	0.62

*Dist: epicentral distance from site L14

**FMerr: first motion error, the number of inconsistent first motions.

***ARerr: amplitude ratio error, average of Err_T [Equation (4.8)] over all stations .

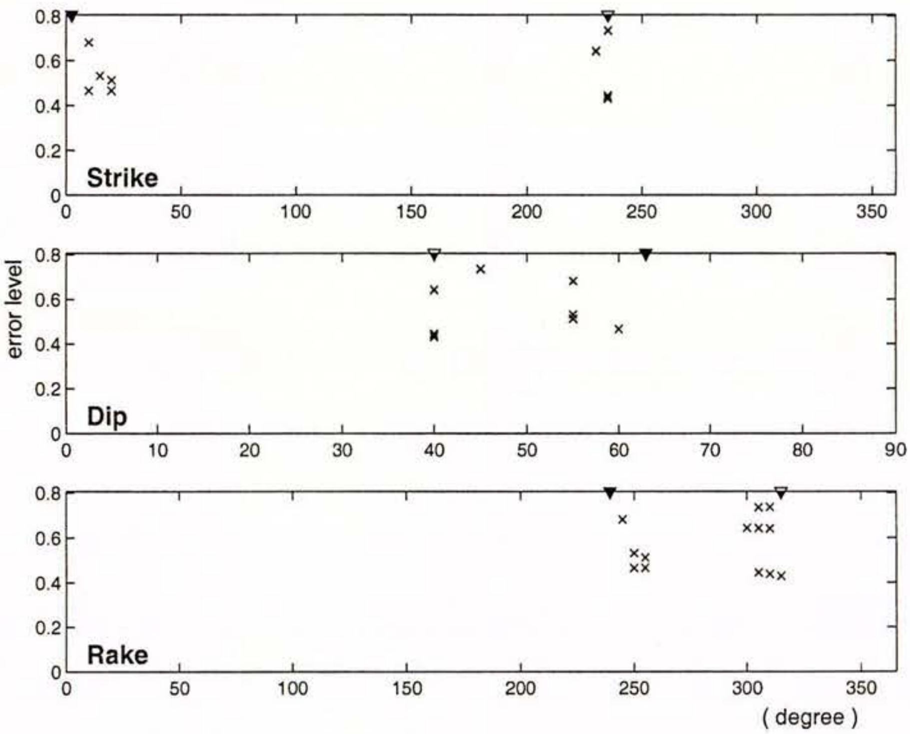

Figure 4.6 *The amplitude ratio errors of only those focal mechanisms which also agree with first motion data, from the same grid search as Figure 4.5. The single minimum in the rake plot shows the rake unambiguously now because first motion polarity data is included. The solutions (strike/dip/rake) for this event using both first motion and amplitude ratio data are 235° /40° /315° for nodal plane I and 5° /63° /240° and for nodal plane II.*

4.5 Focal mechanism results

The focal mechanisms of 15 events for calibrating of the complete Wellington 3D model have been inverted by the amplitude ratio method. However, only the focal mechanisms of those events which were recorded by the Lower Hutt Deployment are further used in modelling the (1D+3D) ground motion due to the limitation set by the present computer power available for this project. Therefore only the focal mechanisms of the seven local earthquakes for the Lower Hutt deployment are listed in Table 4.3 and shown in Figure 4.7. Table 4.3 demonstrates that the levels of first motion error range from 0 to 3 and the levels of amplitude ratio error range from 0.09 to 0.62. The locations of these seven earthquakes relative to NZSN are displayed in Figure 3.1.

All focal mechanisms measured for the other events are listed in Table B.1, Appendix B.

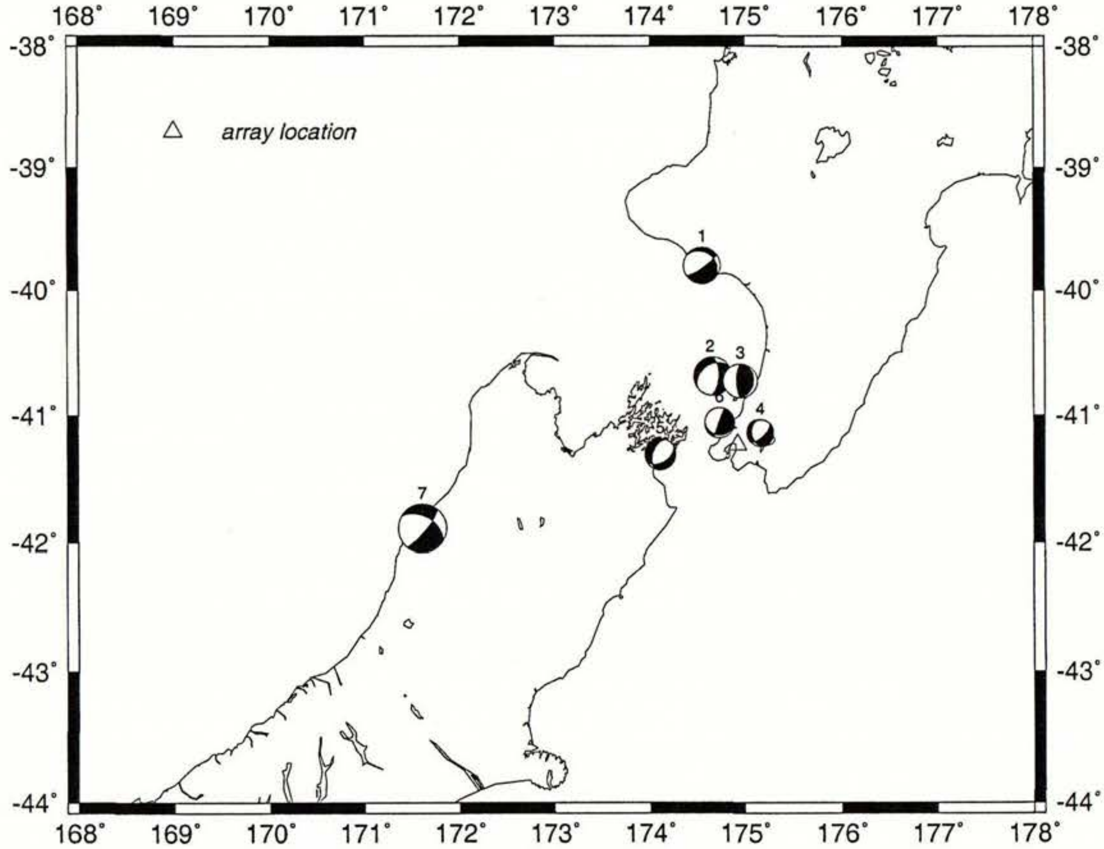

Figure 4.7 *Results of the focal mechanism determination represented as lower hemisphere beach balls at the epicenter locations. The shaded quadrants are compressional zones. All the focal mechanisms of these seven earthquakes are used in the 1D modelling in Chapter 5. Only the focal mechanisms of event 2, 3, 4 and 6 are used in the (1D+3D) modelling in Chapter 7 since they are closer to Lower Hutt.*

CHAPTER 5

1D MODELLING METHOD AND RESULT

5.1 Introduction

For our numerical calculations we use the DWN representation of the seismic wavefields generated by a double-couple point source, originally developed by Bouchon and Aki (1977). The source is embedded in a layered medium, and we use the generalised reflection/transmission coefficients (Kennett, 1983) to propagate the wavefield through the layers. This approach has also been used by Chin and Aki (1991) and Zeng and Anderson (1995). In essence, this is equivalent to representing the wavefield as a superposition of homogeneous and inhomogeneous plane waves propagating at discrete angles. The wavefield is computed at all the recorded sites of the Lower Hutt deployment described in Section 3.1.4. In the next section, I will give a brief description of the DWN method for completeness.

5.2 DWN method

We choose the geographical coordinate system of Aki and Richards (1980) in which x (North), y (East) and z (vertical, positive down) as depicted in Figure 5.1. In the absence of body forces, the elastic wave equations (Aki and Richards, 1980) for homogeneous, isotropic media can be written as follows:

$$\begin{aligned} \nabla^2\Phi - \frac{1}{\alpha^2}\frac{\partial^2\Phi}{\partial t^2} &= 0 \\ \nabla^2\vec{\Psi} - \frac{1}{\beta^2}\frac{\partial^2\vec{\Psi}}{\partial t^2} &= 0 \end{aligned} \tag{5.1}$$

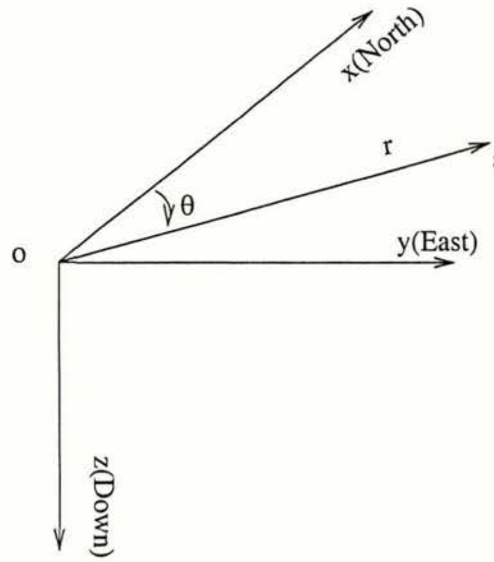

Figure 5.1 *The coordinate system used in the 1D modelling code (Benites et al., 2002). o: epicenter, s: station position. θ is the station azimuth, positive clockwise from North. r is the epicentral distance.*

where Φ represents the dilational potential and $\vec{\Psi}$ represents the shear vector potential, $\vec{\Psi} = (\Psi_x, \Psi_y, \Psi_z)$, from which the elastic motion $\vec{u} = (u_x, u_y, u_z)$ can be derived. Each of the equations (5.1) is a Helmholtz equation, or scalar wave equation. $\vec{\Psi}$ obeys the additional condition:

$$\nabla \cdot \vec{\Psi} = 0 \tag{5.2}$$

with

$$\begin{aligned} \alpha^2 &= \frac{\lambda + 2\mu}{\rho} \\ \beta^2 &= \frac{\mu}{\rho} \end{aligned} \tag{5.3}$$

α and β are the *P* and *S* velocity respectively. In addition, λ and μ are the Lamé parameters with μ the rigidity, and ρ is the medium density. The *P* wave solution is given by the scalar wave equation for Φ; the *S* wave solution is given by the vector wave equation for $\vec{\Psi}$.

In the plane of incidence, the shear vector potential can be expressed in terms of the in-plane Ψ_{SV} and out of plane Ψ_{SH} potentials (Bouchon and Aki, 1977):

$$\begin{aligned} \Psi_{SV} &= \frac{k_x}{k}\Psi_y - \frac{k_y}{k}\Psi_x \\ \Psi_{SH} &= \Psi_z - sgn(z)\frac{\gamma}{k^2}(k_x\Psi_x + k_y\Psi_y) \end{aligned} \tag{5.4}$$

where sgn represents the signum function, with

$$
\begin{aligned}
k &= \sqrt{k_x^2+k_y^2} \\
\gamma &= \sqrt{\frac{\omega^2}{\beta^2}-k^2} \\
\nu &= \sqrt{\frac{\omega^2}{\alpha^2}-k^2}
\end{aligned}
\tag{5.5}
$$

The method is extended to multiple layers following the DWN method (Bouchon and Aki, 1977; Bouchon, 1979; Chin and Aki, 1991). The potentials that represent a double couple point source for each Fourier component k (wavenumber) are:

$$
\begin{aligned}
\Phi^{\pm}(k) &= R_P^{\pm}\exp\{\pm i\nu(z-z_s)\} \\
\Psi_{SV}^{\pm}(k) &= R_{SV}^{\pm}\exp\{\pm i\gamma(z-z_s)\} \\
\Psi_{SH}^{\pm}(k) &= R_{SH}^{\pm}\exp\{\pm i\gamma(z-z_s)\}
\end{aligned}
\tag{5.6}
$$

where z_s is the depth of the point source, and $\pm$ refers to waves going up (+) and down (-) in the source layer. The coefficients $R_P^{\pm}$, $R_{SV}^{\pm}$ and $R_{SH}^{\pm}$ pertain to the radiation of P, SV and SH wavefields in cylindrical coordinates, respectively. They incorporate the values of the moment tensor and magnitude. These coefficients are (Benites *et al.*, 2002):

$$
\begin{aligned}
R_P^{+} &= M_P\{A_0J_0(kr)+A_1J_1(kr)\} \\
R_P^{-} &= M_P\{A_0J_0(kr)+A_2J_1(kr)\} \\
R_{SV}^{+} &= M_{SV}\{B_0J_0(kr)+B_2J_1(kr)\} \\
R_{SV}^{-} &= M_{SV}\{B_1J_0(kr)+B_3J_1(kr)\} \\
R_{SH}^{+} &= M_{SH}\{C_0J_0(kr)+C_1J_1(kr)\} \\
R_{SH}^{-} &= M_{SH}\{C_0J_0(kr)+C_2J_1(kr)\}
\end{aligned}
\tag{5.7}
$$

where J_0 and J_1 are the Bessel functions of order zero and one respectively, with

$$
\begin{aligned}
M_P &= \frac{iDk}{4\pi\nu L k_\beta^2} \\
M_{SV} &= \frac{iD}{4\pi L k_\beta^2} \\
M_{SH} &= \frac{iD}{4\pi L\gamma}
\end{aligned}
\tag{5.8}
$$

where D is the slip, and

$$
\begin{aligned}
A_0 &= k^2(\cos^2\theta M_{xx} + \sin 2\theta M_{xy} + \sin^2\theta M_{yy}) + \nu^2 M_{zz} \\
A_1 &= \frac{k(-\cos 2\theta M_{xx} - 2\sin 2\theta M_{xy} + \cos 2\theta M_{yy})}{r} + 2i\nu k(\cos\theta M_{xz} + \sin\theta M_{yz}) \\
A_2 &= \frac{k(-\cos 2\theta M_{xx} - 2\sin 2\theta M_{xy} + \cos 2\theta M_{yy})}{r} - 2i\nu k(cos\theta M_{xz} + \sin\theta M_{yz}) \\
B_0 &= +k^2(\cos^2\theta M_{xx} + \sin 2\theta M_{xy} + \sin^2\theta M_{yy} - M_{zz}) \\
B_1 &= -k^2(\cos^2\theta M_{xx} + \sin 2\theta M_{xy} + \sin^2\theta M_{yy} - M_{zz}) \\
B_2 &= +\frac{k(-\cos 2\theta M_{xx} - 2\sin 2\theta M_{xy} + \cos 2\theta M_{yy})}{r} - \frac{ik(2k^2 - k_\beta^2)(\cos\theta M_{xz} + \sin\theta M_{yz})}{\gamma} \\
B_3 &= -\frac{k(-\cos 2\theta M_{xx} - 2\sin 2\theta M_{xy} + \cos 2\theta M_{yy})}{r} - \frac{ik(2k^2 - k_\beta^2)(\cos\theta M_{xz} + \sin\theta M_{yz})}{\gamma} \\
C_0 &= \frac{k(M_{xx} - 2\cos 2\theta M_{xy} - M_{yy})}{2} \\
C_1 &= \frac{(-M_{xx} + 2\cos 2\theta M_{xy} + M_{yy})}{r} + i\gamma(\sin\theta M_{xz} - \cos\theta M_{yz}) \\
C_2 &= \frac{(-M_{xx} + 2\cos 2\theta M_{xy} + M_{yy})}{r} - i\gamma(\sin\theta M_{xz} - \cos\theta M_{yz})
\end{aligned}
\tag{5.9}
$$

and L represents the periodicity length for the DWN method, L is defined as follows:

$$
L = \sqrt{(\nu_p t_l)^2 - (z_s - z_o)^2} + r \tag{5.10}
$$

where θ is the azimuth angle measured from north, positive clockwise [Figure 5.1], M_{xx}, M_{xy}, M_{xz}, M_{yy}, M_{yz} and M_{zz} are the moment tensor components, as defined by equation (4.6), t_l is the total duration of the synthetic seismograms, r is the epicentral distance, and z_o is the observation depth.

Once the potentials have been calculated, the displacement and stress wavefields in the source layer can be computed from (Benites *et al.*, 2002):

$$\begin{pmatrix} u_r \\ u_z \\ \tau_{zr} \\ \tau_{zz} \end{pmatrix} = \begin{pmatrix} -ik & i\gamma & -ik & -i\gamma \\ -i\nu & -ik & i\nu & -ik \\ -2\mu\nu k & -\mu l & 2\mu\nu k & -\mu l \\ \mu l & -2\mu\gamma k & \mu l & 2\mu\gamma k \end{pmatrix} \begin{pmatrix} \Phi^- \\ \Psi^-_{SV} \\ \Phi^+ \\ \Psi^+_{SV} \end{pmatrix} \tag{5.11}$$

for *P*-*SV* waves; and

$$\begin{pmatrix} u_\theta \\ \tau_{z\theta} \end{pmatrix} = \begin{pmatrix} -ik & ik \\ \mu\gamma k & -\mu\gamma k \end{pmatrix} \begin{pmatrix} \Psi^-_{SH} \\ \Psi^+_{SH} \end{pmatrix} \tag{5.12}$$

for *SH* waves.

In equations (5.11) and (5.12), l is defined as follows:

$$l = \sqrt{2k^2 - \frac{\omega^2}{\beta^2}} \tag{5.13}$$

A modulated ramp (Ben-Menahem and Singh, 1981) will be used as STF in both Chapter 6 and Chapter 7 to calculate the stress wavefields.

In time domain,

$$f(t) = \begin{cases} 0, & (t < 0) \\ \frac{t}{T}(1 - \frac{\sin\omega_n t}{\omega_n t}), & (0 \leq t \leq T) \\ 1, & (t > T) \end{cases} \tag{5.14}$$

In the frequency domain,

$$f(\omega) = \frac{1}{\omega} \frac{\sin(\omega T/2)}{(\omega T/2)} \frac{e^{-i\omega T/2 - \pi i/2}}{1 - (\omega/\omega_n)^2} \tag{5.15}$$

The corresponding first derivative g(t) is used to compute the particle velocity. In time domain:

$$g(t) = \begin{cases} 0, & (t < 0) \\ \frac{1-\cos\omega_n t}{T}, & (0 \leq t \leq T) \\ 0, & (t > T) \end{cases} \tag{5.16}$$

In frequency domain:

$$g(\omega) = \frac{\sin(\omega T/2)}{(\omega T/2)} \frac{e^{-i\omega T/2}}{1-(\frac{\omega}{\omega_n})^2} \tag{5.17}$$

In equations (5.14), (5.15), (5.16) and (5.17), $\omega_n = \frac{2\pi n}{T}$, T is known as the rise time, and n=1, 2, 3, ...

The wavefield in cylindrical coordinates is rotated back to the geographical coordinates by:

$$\begin{aligned} u_x &= \cos\theta u_r - \sin\theta u_\theta \\ u_y &= \sin\theta u_r + \cos\theta u_\theta \\ u_z &= u_z \end{aligned} \tag{5.18}$$

5.3 Testing procedure for the 1D modelling code

The computer code incorporated in the focal mechanism determination software package used in Chapter 4 gives the synthetic seismograms on the free surface only. Benites *et al.* (2002) developed a computer code (i.e. the 1D modelling code) to calculate synthetic seismograms for displacement and the three components of the stress tensor (τ_{rz}, $\tau_{\theta z}$ and τ_{zz}) at arbitrary depths of observation, using equations (5.6), (5.7), (5.8) and (5.9) to represent the double couple point source for each wavenumber k, which can be modified to calculate the other three components of the stress tensor (τ_{rr}, $\tau_{r\theta}$ and $\tau_{\theta\theta}$). The displacement and all six components of the stress tensor are of crucial importance for the development of the (1D+3D) modelling technique of Chapter 6.

5.3.1 Tests

To test the 1D modelling algorithm by Benites *et al.* (2002), I have computed the synthetic displacement of event 2 in Table 4.3 at L08 [Figure 5.2], and compared them with the corresponding synthetics of Figure 4.4. The velocity model and all the other parameters used are the same for both calculations. The results are essentially identical.

I carried out another test by calculating the particle velocity using Robinson (1986) velocity model [Table 4.2] for a grid of 51 by 51 observation points covering an area of 51 $\times$ 51 km^2 at the free surface, i.e., the interval between the neighbouring points is 1 km. The focus is at 20 km depth right

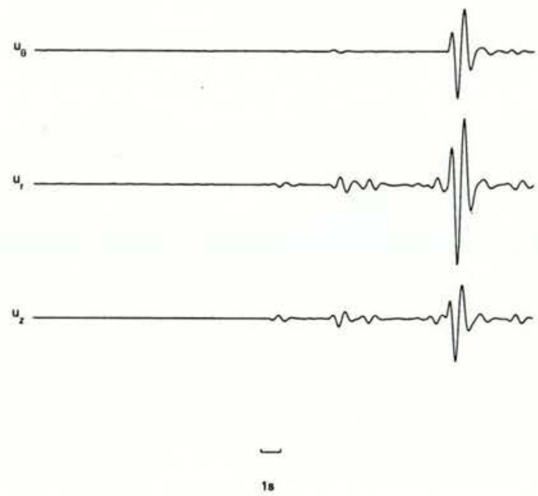

Figure 5.2 *The displacement synthetic seimogram at L08 calculated from the 1D modelling code. Note the synthetics in this figure are essentially identical to those obtained from the focal mechanism determination code in Figure 4.4. u_θ corresponds to T, u_r corresponds to R, u_z corresponds to Z. Also note only the envelope is shown in Figure 4.4 while the actual seismogram is shown in this figure, that is why partly they look different.*

below the mesh center. The focal mechanism is that of event 2 in Table 4.3.

Results are given as snapshots at 4.15 s (*P* wavefield) [Figure 5.3 (a)], 6.05 s (*S* wavefield) [Figure 5.3 (b)] and 6.55 s (*S* wavefield) [Figure 5.3 (c)]. These results convey, accurately, the values of the focal mechanism (strike 235°, dip 40° and rake 315°), showing both the left lateral and normal faulting [Figure 4.3]. From a pure strike slip rupture, we expect u_r changes drastically with azimuth; from a pure dip slip rupture, we expect u_r not to change with azimuth. In this case, we can detect some lack of azimuthal variation in the u_r component. Note that there is no *P*, only *S* waves in the 1D modelling for the u_θ component.

These two tests confirm the accuracy of the 1D modelling code developed by Benites *et al.* (2002).

5.4 Local one dimensional models

To study the effects of the sediment layers underneath each seismic station of the deployment described in Chapter 3 on the ground motion, I use a local one dimensional (1D) model for each site. The values of the elastic parameters for these local 1D models are obtained from the Lower Hutt 3D model [Figure 2.2] and listed in Tables 5.1 and 5.2. The elastic parameters of the top thin layers are important to quantify the amplification factors for frequencies of engineering interest (between 0.0

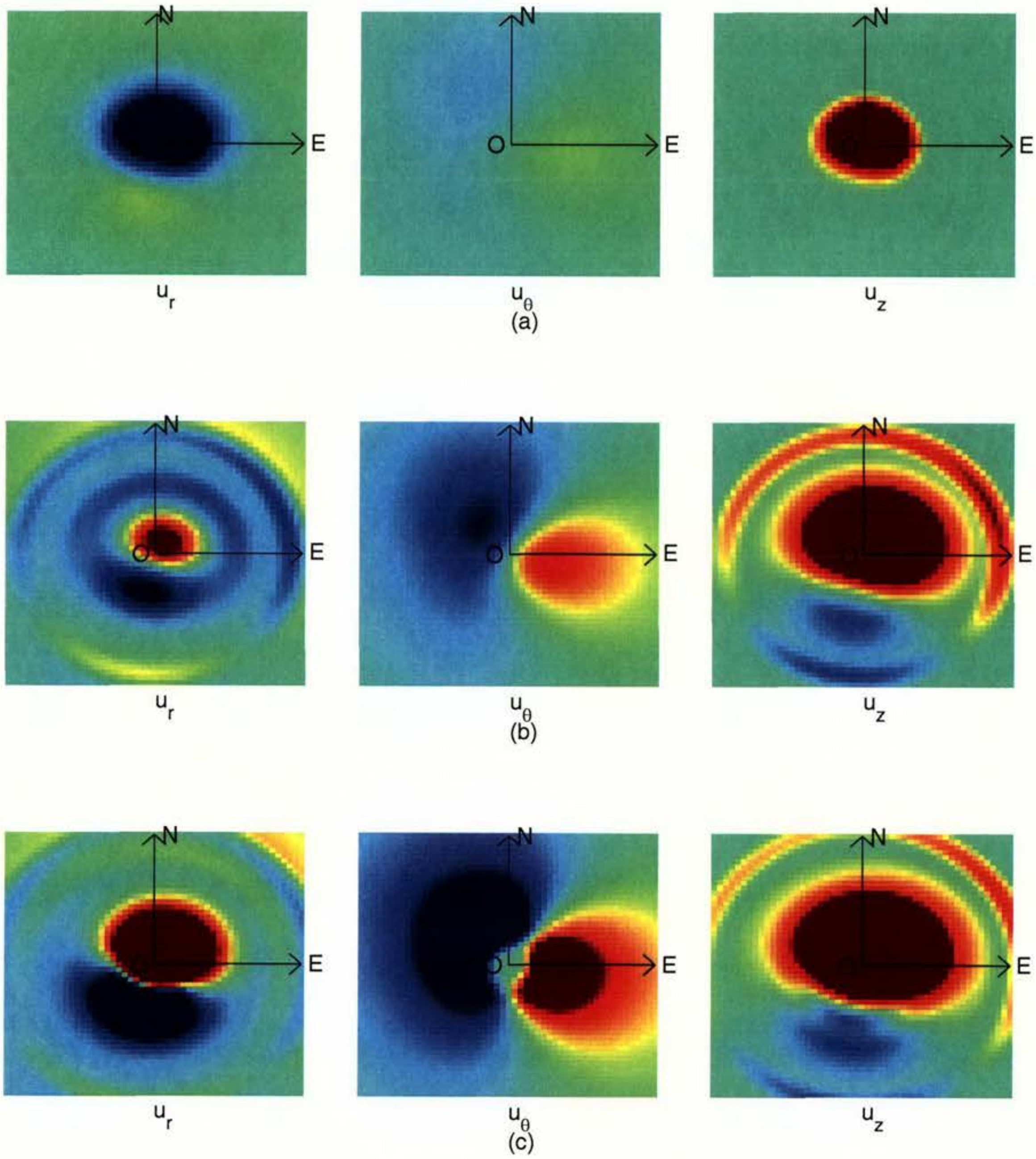

Figure 5.3 *The displacement wavefield in an area of 51 × 51 km^2, covered by a grid of 51 × 51 points at the free surface. The assumed double-couple point source is 20 km right below the center of the area. O represents the epicenter. The snapshots are for (a) at 4.15 s (P wavefield) from the event origin time, (b) at 6.05 s (S wavefield) from the event origin time, (c) at 6.55 s (S wavefield) from the event origin time. The left panel in each figure corresponds to the radial component, the center panel to the azimuthal component and the right panel to the vertical component. Note that the wavefield follows the radiation pattern. The red color represents the positive value, the blue color represents the negative value.*

Table 5.1

The top sediment layers of the 1D local model underneath each station of the Lower Hutt deployment. The values of v_p, v_s and ρ are shared by all the local models. The thickness of each layer in every local 1D model varies from station to station. The layer number increases with depth.

station name	elastic parameter	Layer 1	Layer 2	Layer 3	Layer 4	Layer 5
	v_p(km/s)	0.30	0.52	0.57	0.87	2.60
	v_s(km/s)	0.175	0.3	0.33	0.5	1.5
	$\rho(g/cm^3)$	1.75	1.80	1.85	1.90	2.7
L01(km)	↑	0	0	0	0	10.0
L02(km)	|	0.022	0.002	0.091	0	9.885
L03(km)	|	0	0	0	0	10.0
L04*(km)	|	0.024	0.003	0.028	0.169	9.776
L05(km)	|	0.022	0.002	0.053	0.173	9.75
L06(km)	|	0.025	0.009	0.055	0.214	9.697
L07(km)	|	0	0	0	0	10.0
L08(km)	|	0	0	0	0	10.0
L09(km)	|	0.036	0.012	0.057	0.215	9.68
L10(km)	|	0.031	0.003	0.071	0.201	9.678
L11(km)	layer	0.022	0.014	0.062	0.206	9.696
L12*(km)	thickness	0.020	0.004	0.042	0.129	9.805
L13(km)	|	0.005	0	0	0	9.995
L14(km)	|	0	0	0	0	10.0
L15*(km)	|	0.025	0.015	0.032	0.001	9.927
L16(km)	|	0	0	0	0	10.0
L17(km)	|	0.166	0	0	0	9.834
L18(km)	|	0.033	0.002	0.025	0	9.95
L19(km)	|	0	0	0	0	10.0
L20(km)	|	0.019	0.020	0.006	0.083	9.872
L21(km)	|	0.019	0.013	0.012	0.141	9.815
L22(km)	|	0.013	0.002	0.033	0.038	9.914
L23*(km)	|	0.020	0	0.055	0.169	9.756
L24(km)	↓	0.035	0.002	0.071	0.191	9.701

The sites labeled with * located in zone 3-4.

Hz -3.0 Hz) (Benites *et al.*, 2002).

Table 5.1 is the upper part of each local 1D model. Each layer has the same velocity, but its thickness varies from site to site [Figure 5.4]. The thicknesses of the top 5 layers all add up to 10 km. The site with the thickest soft sediments is L09, with 0.32 km. The site with the thickest top sediment layer is L17, with 0.166 km. L10 was located in the seaward end of the Lower Hutt Valley, and L17 in the Wainuiomata valley. Seven sites (L01, L03, L07, L08, L14, L16, L19) were on firm soil, i.e. with no soft sediments underneath them. L01, L19, L14 and L16 are located to the south east of Hutt Valley. L03, L07 and L08 are located towards the north west of Hutt Valley [Figure 3.3].

Table 5.2

The bottom five layers shared by all the local 1D models. The layer number increases with depth.

Parameter	Layer 6	Layer 7	Layer 8	Layer 9	Layer 10
v_p (km/s)	5.77	6.39	6.79	8.07	8.77
v_s (km/s)	3.49	3.50	3.92	4.80	4.86
$\rho(g/cm^3)$	2.69	2.76	2.93	3.39	3.35
layer thickness (km)	5.0	10.0	10.0	10.0	∞

Note that the layer 5 [Table 2.1] of "The Hutt 3D crustal model specification" has wave velocities of v_p=2.6 km/s and v_s=1.5 km/s extending to 10 km deep, which are low compared to layer 1, layer 2 and layer 3 of Robinson (1986) Wellington model [Table 4.2]. This leads to the unreasonable thickness of layer 5 in the local 1D models [Table 5.1]. This produces the sharp impedance contrast on the interface between layer 5 [Table 5.1] and layer 6 [Table 5.2] in the local 1D models. The sharp impedance contrast produces a big amplitude *SP* conversion in the local 1D synthetics [Figures 5.11, 5.12 and 5.13] later. Layer 5 in the 3D model used in the study of assumed Wellington Fault ruputure (Benites and Olsen, 2004) is 1 km thick, with Robinson (1986) velocity model below. The author of this thesis failed to keep exactly in agreement with Benites and Olsen's (2004) study. Nevertheless, the strong *SP* conversion phase [Figures 5.11, 5.12 and 5.13] introduced by the sharp impedance contrast will not affect the 1D and (1D+3D) calibration indices in this project much, since the calibration indices are ratios of sediment site over rock site. It is cancelled because it exists in the synthetics of both sediment site and the rock site.

Table 5.2 lists the values of the bottom layers in each local 1D model, from the Robinson (1986) Wellington regional 1D model.

5.5 Effect of layering

The question of why sediment layers enhance the shaking hazard can be explained using a two-layer velocity model with one sediment layer over a halfspace in Section 5.5.1 and is described in Section 5.5.2.

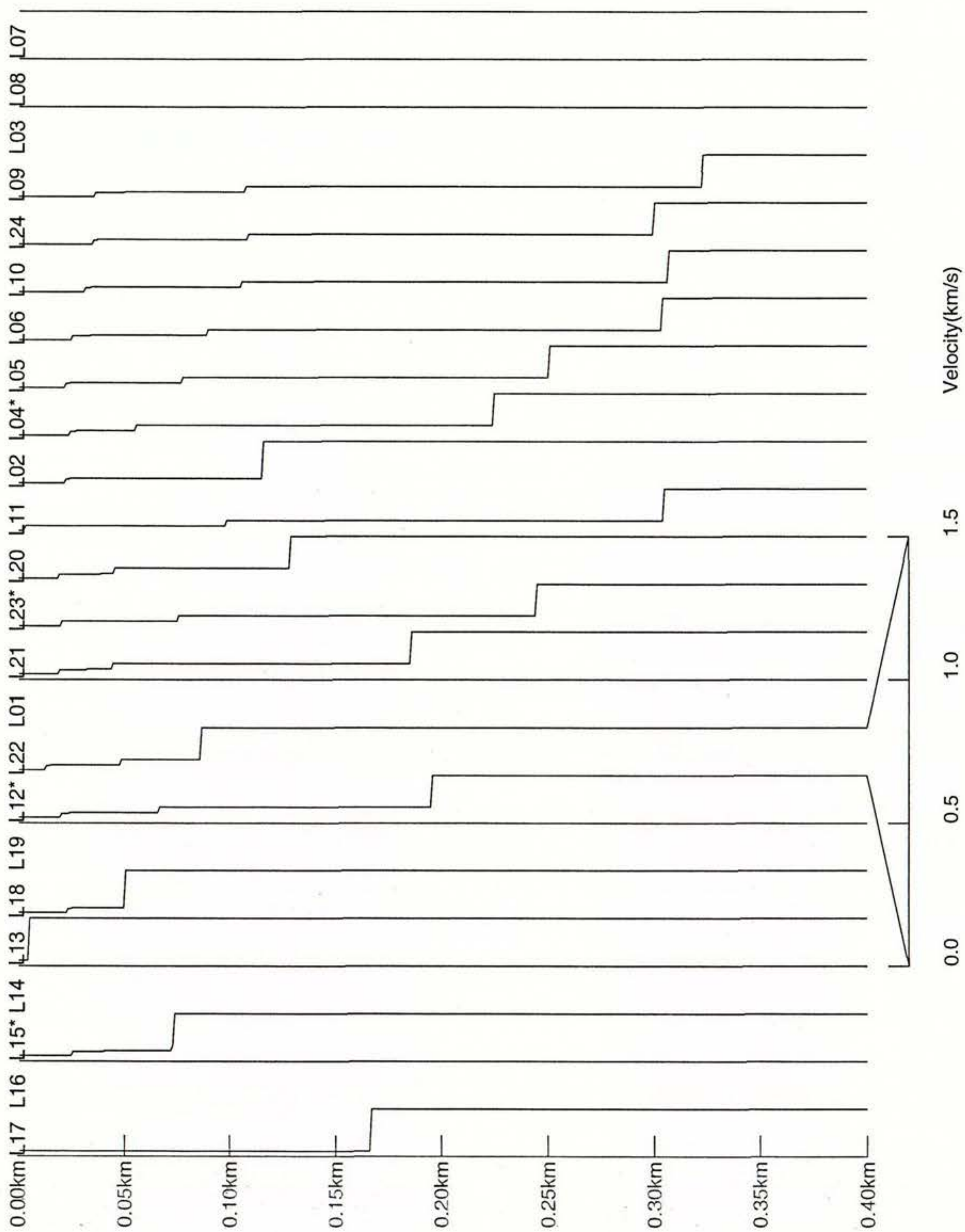

Figure 5.4 *The S wave velocity profile for the stations in the Lower Hutt deployment (Nov. 1990-Feb. 1991) extracted from the Hutt 3D model [Figures 2.1 and 2.2], arranged roughly across the valley [Figure 3.3]. The sites labeled with * located in zone 3-4.*

5.5.1 Theory

The 1D models used in synthesizing the seismograms consist of four sediment layers and six rock layers [Tables 5.1 and 5.2]. To simplify amplification calculation, all the sediment layers can be regarded as one sediment layer, and all the rock layers can be regarded as one rock layer whose *S* wave velocity is the average of the velocity of all the layers, as defined by equation (5.19):

$$\begin{aligned} h &= \sum_{i=1}^{m} h_i \\ v_s &= \frac{h}{\sum_{i=1}^{m} \frac{h_i}{v_{si}}} \end{aligned} \tag{5.19}$$

where v_{si} and h_i are the *S* wave velocity and the thickness of the ith layer, respectively; v_s is the resultant velocity of *S* wave, h the total thickness of all the layers, m is the number of sediment or rock layers (m=4 for all the soft layers, m=6 for all the rock layers). Certainly, reflections from the sediment-sediment interfaces will also contribute to the amplification, but are of secondary importance to the sediment-rock interaction.

There are two primary ways that free surface ground motions are amplified due to a 1D low velocity layer overlying a higher velocity halfspace:

1. The basic way that a low velocity layer causes amplification is due to impedance contrast between layers. Here we illustrate the amplification theory with *SH* wave only, under the particular case of incident angle 0°; the amplification theory for *SV* is similar to *SH*, but more complicated due to wave conversion. Equation (5.20) (Lay and Wallace, 1995) gives the amplitude of the low velocity relative to the halfspace:

$$\frac{A_T}{A_I} = \frac{2\rho_I v_I}{\rho_I v_I + \rho_T v_T} \tag{5.20}$$

where A_I and A_T are the amplitudes of the incident and transmitted shear waves, ρ_I and v_I are the density and shear wave velocity of the half space, ρ_T and v_T are the density and shear wave velocity of the low velocity layer. The low velocity layer will also have a lower density, therefore, $\rho_I v_I > \rho_T v_T$, which implies $A_T > A_I$. This means that the amplitude will be increased in the low velocity layer; the velocity and density contrasts decide the level of amplification.

2. Vertical resonances within a low velocity layer will also occur, where the seismic energy is repeatedly bounced off the top and bottom of the layer. The multiple-reflections between layer interfaces enhance the duration time of ground motion. This leads to much more amplification of peak FSR than the amplification of peak ground velocity in the time domain at sediment sites. This phenomena is termed the *quarter-wavelength rule* and the resonant frequency is measured by equation (5.21) (Coutel and Mora, 1998):

$$f_n = \frac{v_s(2n+1)}{4h} \quad (n = 0, 1, 2, 3, \ldots) \tag{5.21}$$

where f_n is a resonant frequency, h is the thickness of the low velocity layer, v_s is the shear wave velocity and n represents different resonant modes. The resonant frequency when $n = 0$ is called the fundamental mode frequency, that when $n = 1$ is called the 1st mode frequency, that when $n = 2$ is called the 2nd mode frequency, and so on.

5.5.2 Comparison between 1D synthetics and data

The recorded particle velocity data has been corrected for instrument response, as stated in Section 3.3.1 and bandpass filtered from 0.5 Hz to 3.0 Hz. This bandwidth includes most of the predominant frequencies of the motion so that the filtered and unfiltered waveforms are similar in amplitude and shape.

Figures 5.5, 5.6 and 5.7 show that the synthetic waveforms at L09 and L10 match that of their correponding data at the start of the *S* wave. Probably the local 1D models underneath L09 and L10 fit the true velocity structure better than those 1D models at the other sites. Generally speaking, the synthetic waveforms from each of the local 1D models does not match exactly with the corresponding data. Probably the main source of the misfit is that the structure under the receivers is much more complex than the 1D local models and that there are mutiple reflections from other layers, which could be dipping or anistropic, and that there will be scattering from various heterogeneities that can not be easily modelled. The mismatch of observed and synthetic waveforms is even worse at firm sites L16, L14, L08 and L07 [Figures 5.5, 5.6 and 5.7]. Among the many reasons for this, the dominant might be the two and three dimensional effects of structure near the receiver. As well, there might be shallower velocity structure in the real crust than the one considered here, affecting waves from different bedrock interface. We can see the subsequent pulses (e.g., R1 and R2) in the synthetic

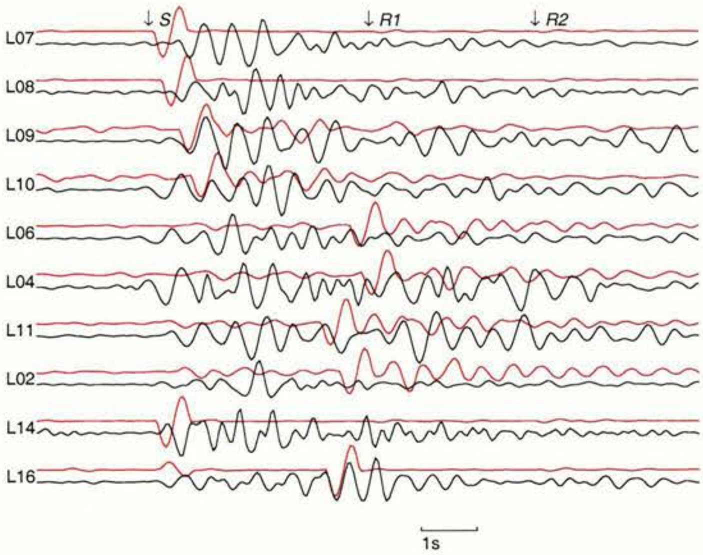

Figure 5.5 *Comparison between the synthetic and the real velocity data for event 2 in Table 4.3 (North component). The black trace of each pair is the data, the red trace of each pair is the synthetic, displayed approximately across the NW40° valley profile. Each trace is normalized by its own peak amplitude. The traces are aligned by eye on their S phase arrival. The start of the S phase and the reflecting waves from the bedrock interfaces are marked. The apparent misalignment between the synthetic and data at any station is produced because the initial S wave on either the synthetic or the data waveform is much smaller than the subsequent arrivals, so it is difficult to be seen on this scale. Site L16 is an exception for synthetics since it sits on the firm site in the Hutt 3D shaking model [Table 5.1], whereas it sits in zone 5 in the true Lower Hutt deployment [Figure 3.3].*

seismogram of L16, L14, L08 and L07, which are firm sites in the 1D models. They are the reflecting waves from different layers. They must also occur in the seismograms at the soft sites; however, they are less visible since they interfere with the other reflecting waves from sediment interfaces [Figures 5.5, 5.6 and 5.7]. Benites and Aki (1994) compared synthetics and data for a site response study as well with 2D modelling; their conclusions were in respect to basin effect and topography effect. Zeng and Anderson (1995) also compared synthetics and data for site response study, but they focused mainly on method development.

A ten second window, starting 0.5 s before the *S* wave arrival was selected from each component of a recorded data seismogram and the corresponding 1D synthetic seismogram. A 4% Hanning taper was applied to the window to reduce aliasing in Fourier transforms, which were later applied to the data to calculate Fourier amplitude spectrum (FAS). The FAS of the seismograms in Figures 5.5, 5.6 and 5.7 are shown in Figures 5.8, 5.9 and 5.10 respectively. The synthetic spectrogram from the local 1D model match fairly well with the corresponding data spectrogram, particularly in the sediment sites (L02, L11, L04, L06, L10 and L09). Note the multiple peaks in the spectrograms of both the

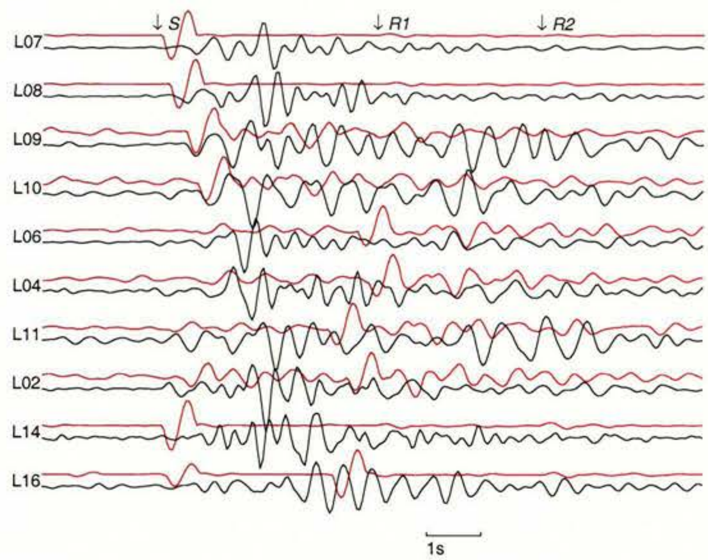

Figure 5.6 *Comparison between the synthetic and the real velocity data for event 2 in Table 4.3 (East component). The black trace of each pair is the data, the red trace of each pair is the synthetic, displayed approximately across the NW40° valley profile. Each trace is normalized by its own peak amplitude. The traces are aligned by eye on their S phase arrival. The start of the S phase and the reflecting waves from the bedrock interfaces are marked. The apparent misalignment between the synthetic and data at any station is produced because the initial S wave on either the synthetic or the data waveform is much smaller than the subsequent arrivals, so it is difficult to be seen on this scale. Site L16 is an exception for synthetics since it sits on the firm site in the Hutt 3D shaking model [Table 5.1], whereas it sits in zone 5 in the true Lower Hutt deployment [Figure 3.3].*

synthetics and the data in the sediment sites, which are generated by the different resonant modes [equation (5.21)].

To examine the effects of sediment layers on the synthetic waveforms, Figures 5.11, 5.12 and 5.13 show the whole seismograms that were studied previously with their sole *S* waves in Figures 5.5, 5.6 and 5.7 respectively. The *SP* conversion from the interface between Layer 5 and Layer 6 which is a sharp velocity contrast [Tables 5.1 and 5.2] is labelled. So is the *S* wave. The amplitude and duration of the synthetic seismogram of the sediment sites L02, L11, L04, L06, L10 and L09 are much greater compared to that from each of the rock sites L16, L14, L08 and L07. That is caused by the resonance in the sediment layer, the multiple-reflections in the top thin layers and by the combination of the multiple-reflection due to the strong velocity contrast at 10 km depth ($v_s = 1.5$ km/s and $v_s = 3.49$ km/s, respectively) [Tables 5.1 and 5.2]. There is also the multiple-reflections from the top low velocity layers. The seismic waves become postcritically reflected off the boundary at 10 km depth, and therefore most energy is reflected upward and little is transmitted into deeper layers.

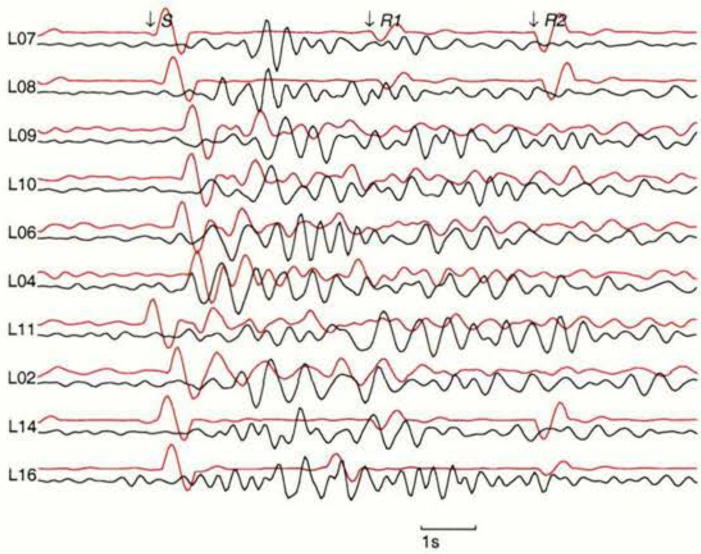

Figure 5.7 *Comparison between the synthetic and the real velocity data for event 2 in Table 4.3 (Vertical component). The black trace of each pair is the data, the red trace of each pair is the synthetic, displayed approximately across the NW40° valley profile. Each trace is normalized by its own peak amplitude. The traces are aligned by eye on their S phase arrival. The start of the S phase and the reflecting waves from the bedrock interfaces are marked. The apparent misalignment between the synthetic and data at any station is produced because the initial S wave on either the synthetic or the data waveform is much smaller than the subsequent arrivals, so it is difficult to be seen on this scale. Site L16 is an exception for synthetics since it sits on the firm site in the Hutt 3D shaking model [Table 5.1], whereas it sits in zone 5 in the true Lower Hutt deployment [Figure 3.3].*

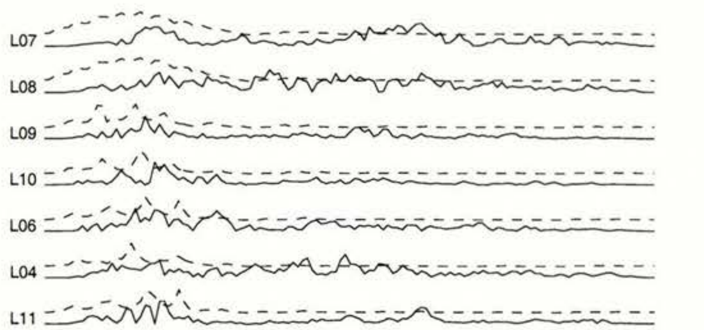

Figure 5.8 *Comparison between the spectrograms of the synthetic and the velocity data for event 2 in Table 4.3 (North component). The solid traces of each pair are the data, the dashed traces of each pair are the synthetics, displayed approximately across the NW40° valley profile. Each trace is normalized by its own spectrogram peak amplitude.*

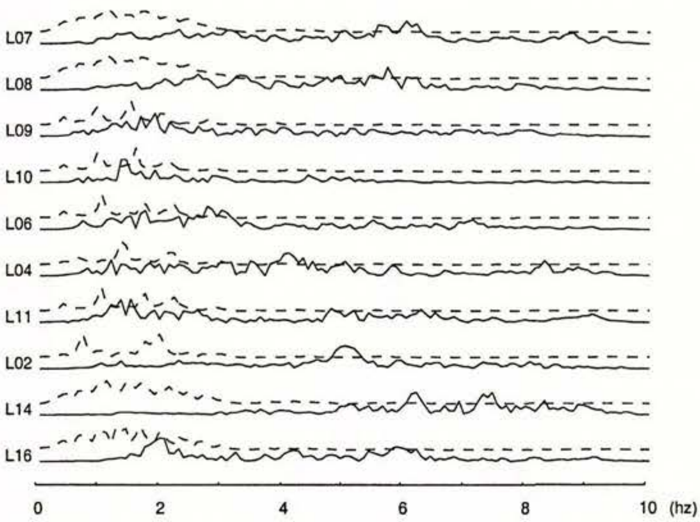

Figure 5.9 *Comparison between the spectrograms of the synthetic and the velocity data for event 2 in Table 4.3 (East component). The solid traces of each pair are the data, the dashed traces of each pair are the synthetics, displayed approximately across the NW40° valley profile. Each trace is normalized by its own spectrogram peak amplitude.*

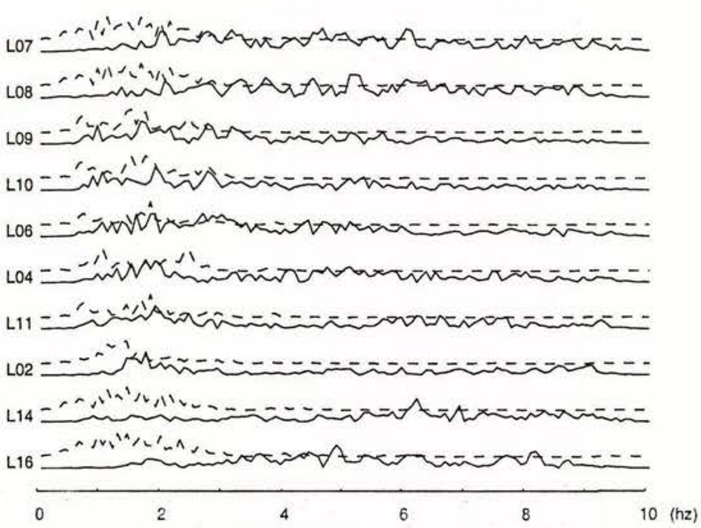

Figure 5.10 *Comparison between the spectrograms of the synthetic and the velocity data for event 2 in Table 4.3 (vertical component). The solid traces of each pair are the data, the dashed traces of each pair are the synthetics, displayed approximately across the NW40° valley profile. Each trace is normalized by its own spectrogram peak amplitude.*

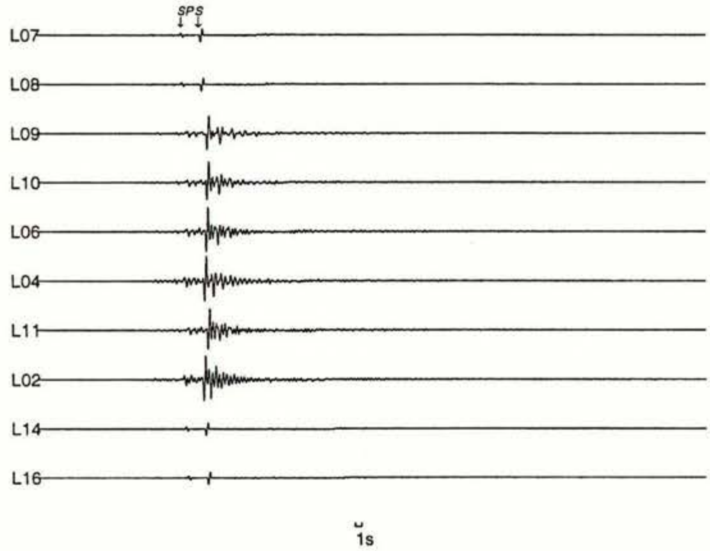

Figure 5.11 *Synthetic seismograms of event 2 in Table 4.3 (North component), displayed approximately across the NW40° valley profile. Each trace is normalized by the the maximum amplitude of the L02 trace, whose synthetic ground motion is strongest among all. SP and S denote SP conversion [Page 5.4] and S respectively.*

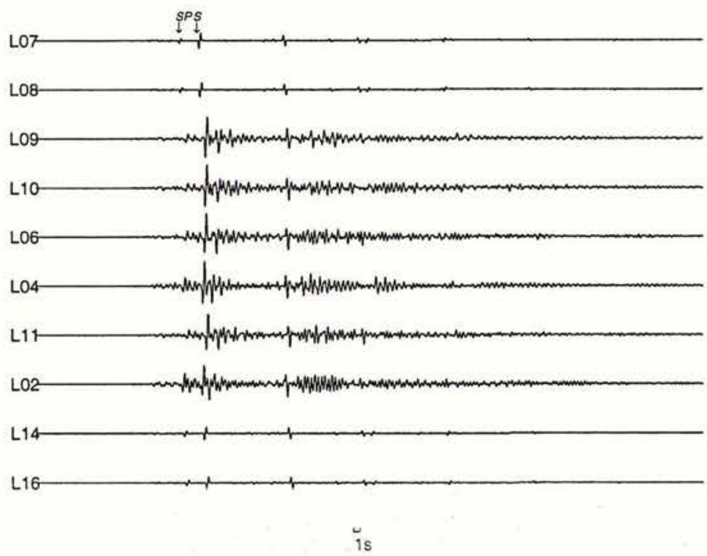

Figure 5.12 *Synthetic seismograms of event 2 in Table 4.3 (East component), displayed approximately across the NW40° valley profile. Each trace is normalized by the the maximum amplitude of the L10 trace, whose synthetic ground motion is strongest among all. SP and S denote SP conversion [Page 5.4] and S respectively.*

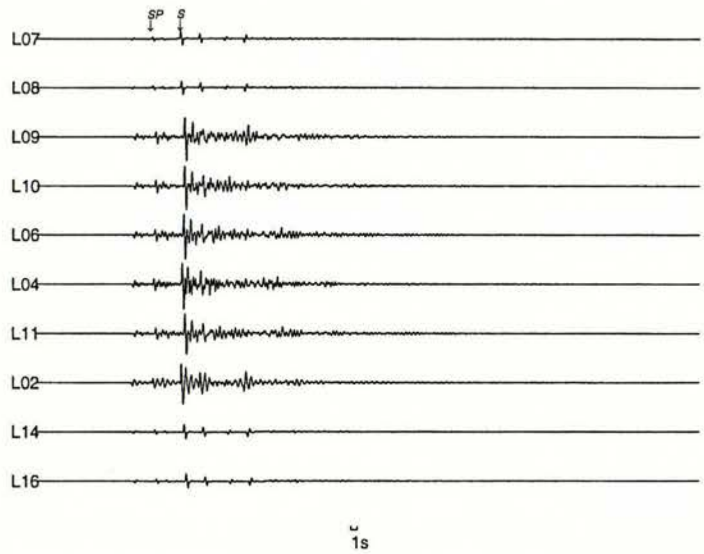

Figure 5.13 *Synthetic seismograms of event 2 in Table 4.3 (vertical component), displayed approximately across the NW40° valley profile. Each trace is normalized by the the maximum amplitude of the L10 trace, whose synthetic ground motion is strongest among all. SP and S denote SP conversion [Page 5.4] and S respectively.*

The large amplitudes and duration at L02, L11, L04, L06, L10 and L09 as compared with the rock sites suggest the effects of site resonance, whose frequency is determined by both of the thickness and S-wave velocity in the top thin layers. The frequency of oscillation for a sediment layer over a half space is related to the velocity of the material and the thickness of the sediment layer. A wave whose frequency follows the relationship of equation (5.21) will resonate in the sediment layer.

In Figures 5.8, 5.9 and 5.10, the spectrum $U(\omega)$ at each site is the product of three factors (Borcherdt and Glassmoyer, 1992):

$$U(\omega) = S(\omega)P(\omega)B(\omega) \tag{5.22}$$

where $S(\omega)$ represents the spectrum of the source, $P(\omega)$ represents the filtered spectrum of the path from the source to Hutt Valley bottom and $B(\omega)$ represents the filtered spectrum of the sediment layers. $S(\omega)$ is a constant for all the sites; for a given small earthquake, $P(\omega)$ can be considered almost the same for all sites, because the spatial extent of the array is small compared with the focal distance. Only $B(\omega)$ changes drastically from site to site, which determines the site effects. From Figures 5.14, 5.15 and 5.16 we know that the synthetic spectrum value at rock site L14 (i.e., $S(\omega)P(\omega)$) is small compared to those on the sediment sites. Hence, approximately we can think that the spectral peak

Table 5.3

Resonant frequencies observed in the data and in the synthetics

Component	f*	L02	L11	L04	L06	L10	L09
north	f_{dn}	1.7	2.0	2.0	1.6	1.9	1.7
	f_{sn}	2.0	2.3	1.5	1.7	1.6	1.6
east	f_{de}	2.3	1.6	1.2	2.8	1.4	2.0
	f_{se}	2.0	1.1	1.4	1.1	1.6	1.6
vertical	f_{du}	1.8	2.0	1.8	2.7	2.0	1.7
	f_{su}	1.5	1.9	1.1	1.9	1.8	1.6
average of	f_{da}	1.9	1.9	1.7	2.4	1.8	1.8
3 components	f_{sa}	1.8	1.8	1.3	1.6	1.7	1.6
expected from	f_r	1.8	1.6	1.3	1.6	1.6	1.5
quarter-wavelength rule	n	1	2	1	2	2	2

* f_{dn} and f_{sn} are the peak frequencies of data and synthetics along north component respectively; f_{de} and f_{se} are the peak frequencies of data and synthetics along east component respectively; and f_{du} and f_{su} are the peak frequencies of data and synthetics along vertical component respectively. f_{da} and f_{sa} are the peak frequencies of data and synthetics of the average over the three components respectively. f_r is the peak frequency from *quarter-wavelength rule*. See equation (5.21). n=0 represents the fundamental mode; n=1 represents the 1st mode; n=2 represents the 2nd mode. n varies from site to site and is chosen based on Figures 5.14, 5.15 and 5.16; the maximum peak is the nth peak at each site.

at each site in Figures 5.8, 5.9 and 5.10 represents the resonant frequency of the corresponding site. $S(\omega)P(\omega)$ is cancelled in FSR calculation in Section 5.6 later.

The resonant frequencies for the data and the synthetics from Figures 5.8, 5.9 and 5.10 can be found in Table 5.3.. They match approximately to each other. They do not match exactly because Hutt Valley structure is much more complicated than the 1D local models can represent. Figures 5.14, 5.15 and 5.16 show that most energy concentrates in the frequency band of 0.0 - 3.0 Hz. Therefore, here only the peaks below 3.0 Hz are considered. These peak frequencies are not wholely identical to the peak frequencies shown in Figures 5.8, 5.9 and 5.10. Another feature is that the synthetics' E component has many more phases than the N component [Figures 5.11 and 5.12]. This phenomena can be explained as follows: in this event, the N component is close to the radial component, while the E component is close to the transverse component. The reflection coefficient for *SH* and that for *SV* are independent from each other (Lay and Wallace, 1995). The reflection coefficient for *SH* is probably greater than that for *SV* in this particular case, so that total internal reflections happen for *SH*; moreover, possiblely the *SV* loses more energy to *SV-P* conversions.

Table 5.3 indicates that f_{da}, f_{sa} and f_r (n=1 or 2 in different sites) expected from the *quarter-wavelength rule* [equation (5.21)] are overall in agreement in all the three components; i.e., the peak

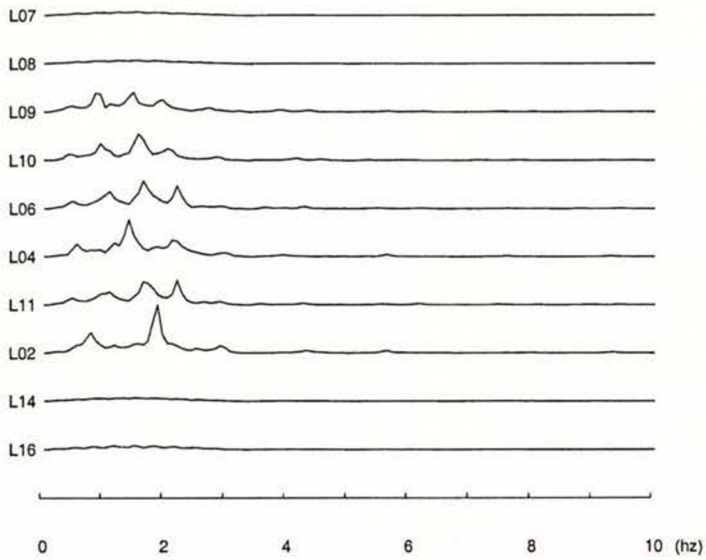

Figure 5.14 *S wave spectrograms of the synthetic seismograms of event 2 in Table 4.3 (North component), displayed approximately across the NW40° valley profile. Each trace is normalized by the maximum spectrogram's peak amplitude of the L02 trace, whose spectrogram synthetic ground motion is strongest among all.*

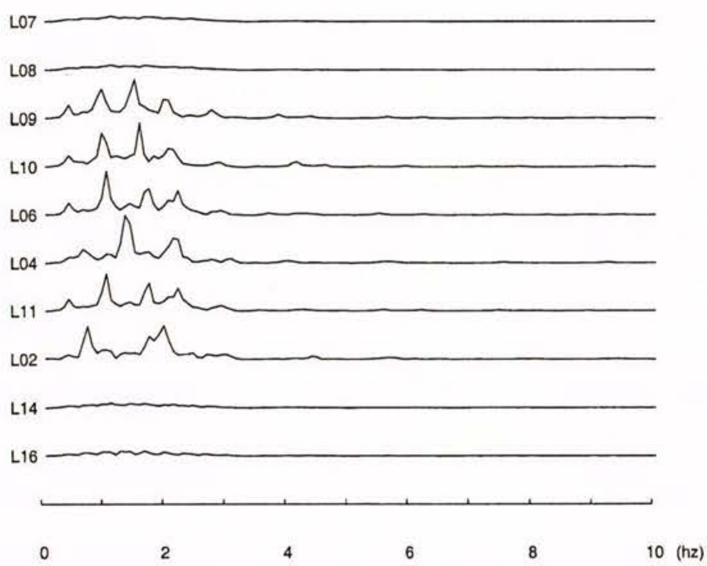

Figure 5.15 *Spectrograms of the synthetic seismograms of event 2 in Table 4.3 (East component), displayed approximately across the NW40° valley profile. Each trace is normalized by the maximum spectrogram's peak amplitude of the L04 trace, whose spectrogram's synthetic ground motion is strongest among all.*

resonant frequency from the synthetics is nearly identical to the peak resonant frequency from the *quarter-wavelength rule.*

Similarly, from south east to north west, the synthetic spectrogram's amplitude from the local 1D model is small at the beginning at the sites out of Hutt Valley (site L16, L14) [Figures 5.14, 5.15

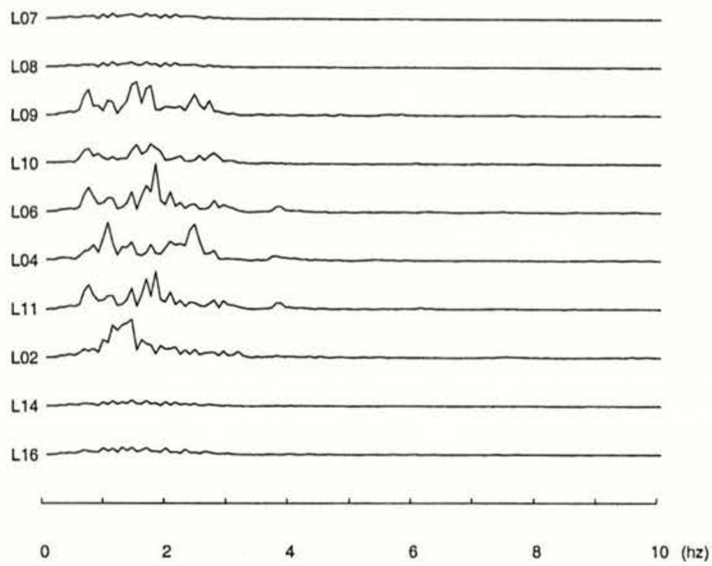

Figure 5.16 *Spectrograms of the synthetic seismograms of event 2 in Table 4.3 (Vertical component), displayed approximately across the NW40° valley profile. Each trace is normalized by the maximum spectrogram's peak amplitude of the L06 trace, whose spectrogram's synthetic ground motion is strongest among all.*

and 5.16]. It increases gradually in Hutt Valley. It reaches peak at L06. Then it starts to decay. The spectral amplitude becomes small again at the sites to the north west of Hutt Valley. There are more peaks in the spectrograms of E component than the N component. The peak amplitude of the E component is larger [Figures 5.14 and 5.15]. This is consistent with the observation that there are more reverberations in the traces of E component than in those of N component [Figures 5.11 and 5.12].

Therefore we infer that qualitively, 1D modelling can simulate the ground motion amplification in both the time domain and the frequency domain at sediment sites in Hutt Valley.

5.6 Comparison study of FSRs between data and synthetics

A sedimentary basin like Lower Hutt can resonate at particular frequencies just like a simple harmonic oscillator [equation (5.21)]. The resonance continues long after the seismic energy has been attenuated at the nearby rock site. To examine these resonances, FSRs from each site have been calculated for the data and for the synthetic seismograms from the local 1D model. Effects due to the earthquake source and variations in the path between the source and the receiver are much reduced through the uses of spectral ratios [equation (5.22)]. The FSR is strongly influenced by the duration of the shaking and is generally higher than the PVR, particularly for resonant sites when the whole Hutt Valley shakes like a harmonic oscillator. For example, for event 1 in Table 3.3 at site L17, the peak FSR was 17.5 whereas the ratio of peak ground velocity was only 2.0. All the cycles of moderate motion as shown in the seismic traces in Figures 3.10 and 3.11 may excite resonances in buildings with the same period. This is why FSR is chosen to characterize site effect instead of PVR.

Since the amplification effect is primarily in the horizontal plane, only the FSRs of the horizontal components are calculated. A 1 Hz triangular window was first employed to smooth the Fourier transform amplitudes. Then a FSR was obtained from dividing each spectrum by the corresponding spectrum of the reference site [Figure 5.17]. Usually the reference site was L14. L19 was used as reference site in case L14 failed to record an event.

The limits outside which the FSRs are not applicable are determined as follows: at both high and low frequencies the amplitude spectrum of the signal approaches the spectral level of the background noise. The ratio for frequencies less than 0.5 Hz are not meaningful due to the effective response of the short period seismometers and the spectral smoothing. There is little energy for the high frequency in the synthetics [Figures 5.14, 5.15 and 5.16], so 4.0 Hz was chosen as the maximum frequency on the plots.

The FSRs for the data and 1D synthetics for one firm site (L03, located in zone 1) and three soft soil stations (L02 in zone 2; L12 in zone 3-4 and L09 in zone 5) are illustrated in Figure 5.17. Note that each site might only have recorded several among all the seven events. Those for the other firm sites located in zone 1 are similar to that of L03. Those for the other soft sites located in zone 2 are similar to that of L02, those for the other soft sites located in zone 3-4 are similar to that of L12, and those for the other soft sites located in zone 5 are similar to that of L09 except L16, as L16 sat in zone 5 in the deployment but sits on rock site in the local 1D model and Benites and Olsen (2004) 3D model. They are plotted in Appendix C. The average FSRs of the rock sites for the data are up to 3 times higher than the expected values of 1; those for the synthetics are all close to 1. As expected, generally the amplification increases from zone 1 to zone 5 for both data and synthetics.

Figure 5.18 (a) shows that the 1D synthetics can simulate the ground motion amplification in most sediment sites, but underestimate the observed ground motion amplification. The synthetic FSRs at L16, L17, L18 and L24 are much lower than their corresponding data FSRs. Perhaps the problem lies in that the Hutt 3D shaking hazard model does not include low enough velocities in the upper layer

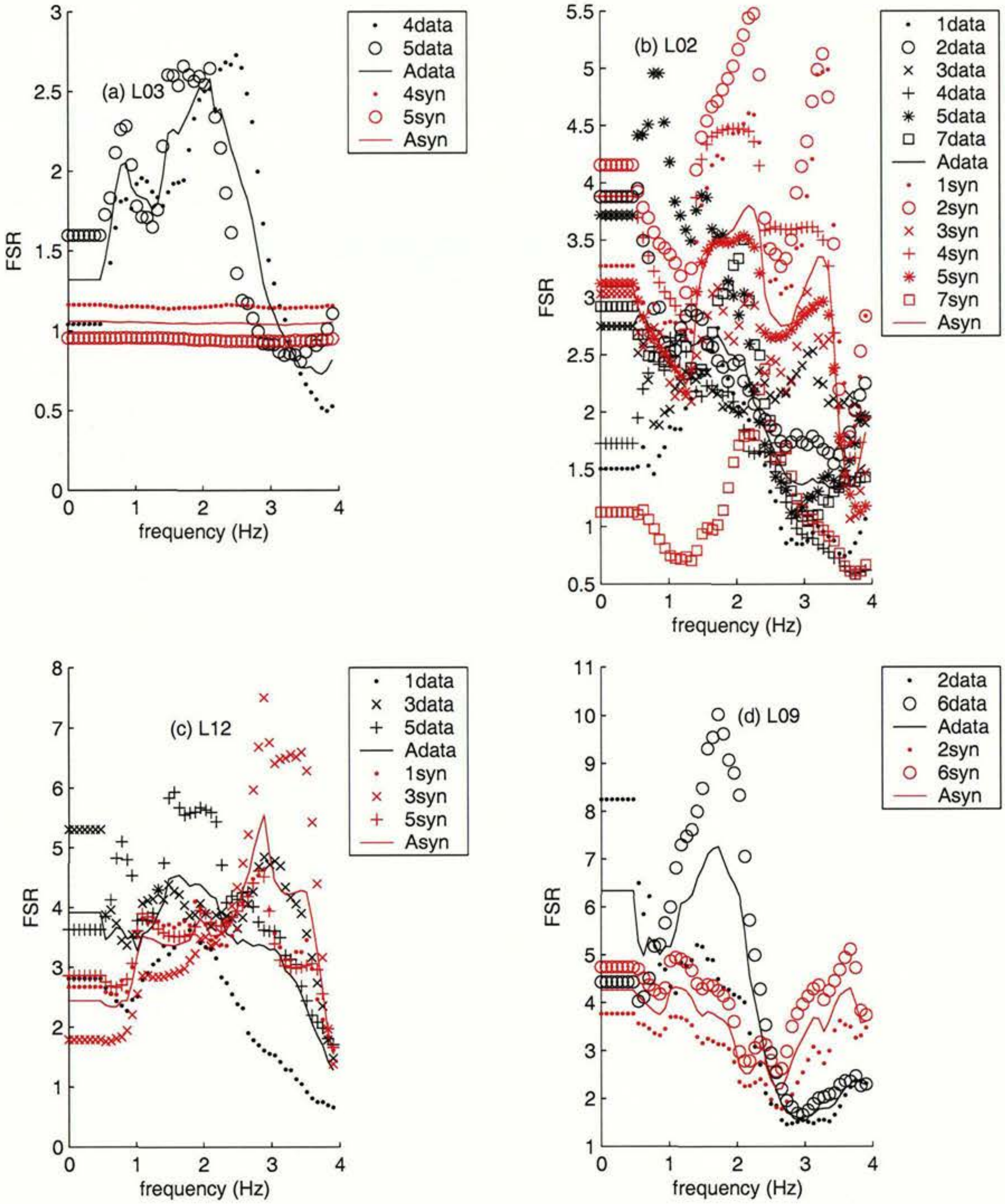

Figure 5.17 *Comparison between FSRs of data and synthetic in the horizontal components for all events for site L03, L02, L12 and L09. The solid line is the average over all events. "4data" and "4syn" represent the data's and synthetic's FSR, respectively, for event 4 in Table 3.2 respectively. Other symbols are analogous. "Adata" and "Asyn" represent the avearage of data FSR and the avearage of synthetic FSR, respectively.*

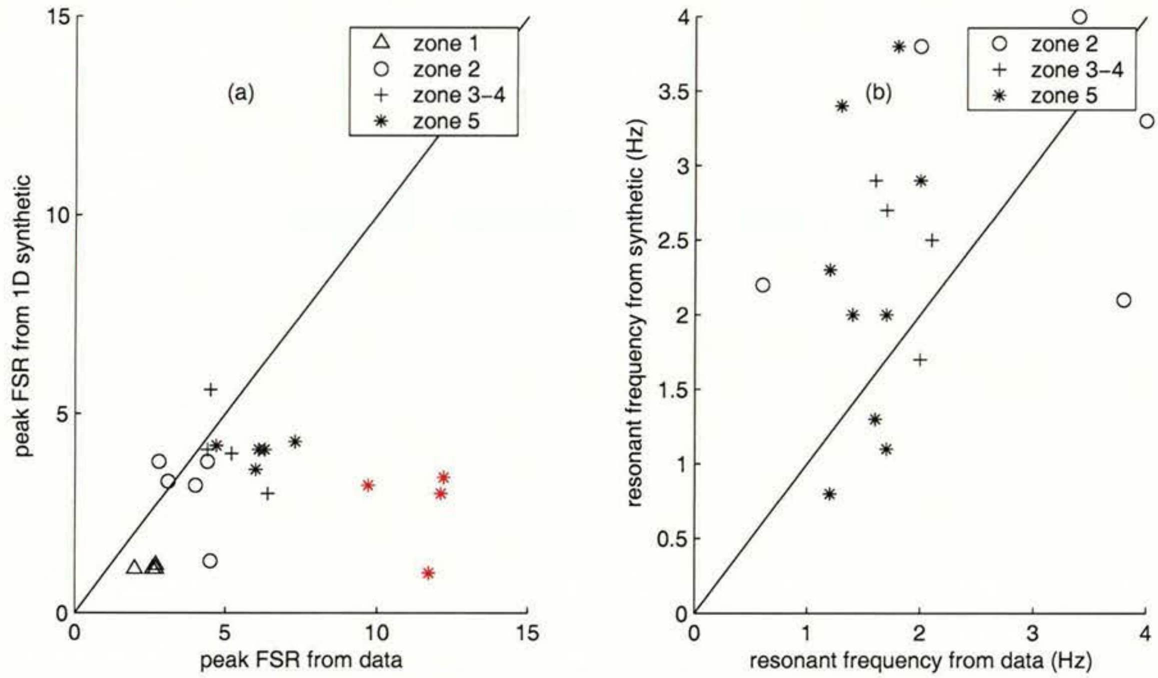

Figure 5.18 *The correlation relationship between data and synthetics. (a) The correlation relationship between maximum FSR from data and that from synthetic. The line is $y = x$. The red symbols represent L16, L17, L18 and L24, respectively, which are discussed specificlly in Page 75. (b) The correlation relationship between resonant frequency from data and that from synthetic. There is no resonant frequency from the synthetics for the firm sites in zone 1 [Figures 5.17 (a) and C.1], so zone 1 is not included in (b). The line is $y = x$. See Page 20 for zone classification.*

at these local sites. It even suggests that there may be a much larger variation in velocity in the real upper layer than is in the model. Figure 5.18 (b) shows the resonant frequencies from synthetics in zone 3-4 match those from the data better than in the other zones. This implies that the thickness and velocity of the sediment layer are better known for zone 3-4 than in the other zones in the Hutt 3D shaking hazard model.

Equation (5.23) gives the correlation coefficient (Dixon and Massey, 1969) between (X,Y):

$$\mathrm{corr}(X,Y) = \frac{\sum_{i=1}^{n}(x_i - \overline{x})(y_i - \overline{y})}{\left[\sum_{i=1}^{n}(x_i - \overline{x})^2 \sum_{i=1}^{n}(y_i - \overline{y})^2\right]^{1/2}} \tag{5.23}$$

where (x_i, y_i) represents the data's and the synthetic's maximum FSR respectively at i_{th} site; or the data's and the synthetic's resonant frequency respectively at i_{th} site. $\overline{x}$ and $\overline{y}$ represent the corresponding average. $\mathrm{corr}(X,Y)$ is called the correlation coefficient.

From equation (5.23), the correlation coefficients are calculated based on 19 of all the 24 sites for the average of all the seven events. Site L14 is excluded because it is used as the reference site; sites L16, L17, L18 and L24 are also excluded (the red symbols in Figure 5.18) since their synthetic FSRs are much lower than their data FSRs, which probably imply that there are much lower velocities underneath the true sites than given in the local 1D models:

$$\begin{aligned} \mathrm{corr}_a(X,Y) &= 0.64 \\ \mathrm{corr}_f(X,Y) &= 0.56 \end{aligned} \tag{5.24}$$

where corr_a and corr_f are the correlation coefficients for maximum FSR amplitude and resonant frequency respectively.

We found that:

1. The 1D synthetic FSRs match the data FSRs better in hazard zone 3-4 than in the other zones. In zone 1, the firm sites L03, L07, L08 and L19, the 1D synthetics are amplified little, whereas the data are amplified by factors of 1.8-2.7. The 1D peak FSR in most stations are lower than or equal to that in the data (L02, L04, L12, L20 are exceptions) [Figures 5.18 (a) and 5.19 (a)]. These imply that the velocity and thickness of the sediment layers of the local 1D models at zone 3-4 fit the true site structure better than those at other zones [Table 5.1 and Figure 5.4].

2. The 1D synthetic FSRs for event 7 underestimate the data FSRs greatly [Figures 5.17 (b), C.1 (c) and (d), C.2 (b), (c) and (d), C.3 (a), (b) and (c), C.4 (a), (b) and (d) and C.5 (c) and (d), Appendix C]. The Robinson (1986) Wellington velocity model is for the Wellington region mainly, so the local 1D models in this chapter apply best to earthquakes near Wellington. For an earthquake so far as 285 km like event 7 [Table 3.2], Robinson (1986) Wellington velocity model may not work properly. Perhaps that is why the ground motion from 1D synthetics is amplified much less than that from the recorded data for event 7; other reasons for one event giving spurious results could be that its focal mechanism is not exactly right.

3. The resonant frequency in the 1D synthetic FSRs is close to that in the data [Figures 5.18 (b) and 5.19 (b)]. There are no resonant frequency values in the 1D synthetic FSRs for L03, L07

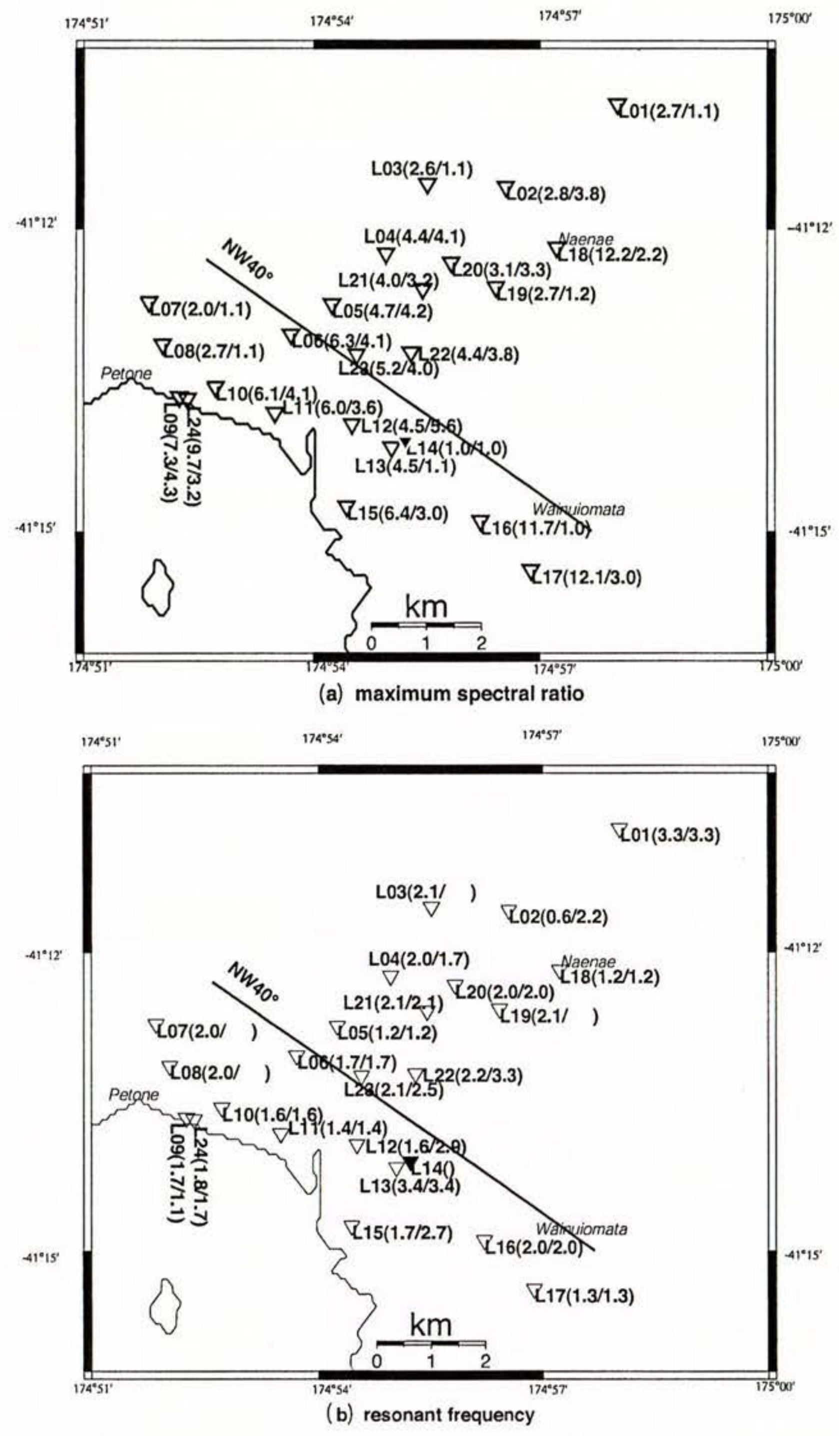

Figure 5.19 *Distribution map of the maximum value and the resonant frequency of the mean FSR for each site in Hutt Valley. (a) maximum FSR value. (b) resonant frequency. Note there are no resonant frequencies from the 1D synthetics for the stations in zone 1 (L03, L07, L08 and L19). The number plotted is an average of the north and east component. The solid triangle (L14) is the reference site and thus the FSR there is 1 by definition in (a); furthermore, the resonant frequency at L14 is empty in (b) since it is used as reference site. The left value is from the data, the right value is from 1D modelling. See also Figure 5.18 (a) and (b).*

and L19 since no sediment layers occur in their velocity models.

5.7 Summary

From the analysis and comparison of 1D synthetics and data, the following conclusions are reached:

1. A too sharp velocity contrast between Layer 5 and Layer 6 [Tables 5.1 and 5.2] generates a strong *SP* conversion [Figures 5.11, 5.12 and 5.13]. This leads to the reduction of PGV and peak Fourier amplitude spectrum (PAS) at each site. However, this will not affect the FSR and resonant frequency much since effects due to the path between the source and the receiver are much reduced through the uses of spectral ratios.

2. The 1D modelling method can simulate the ground motion amplification on most of the sediment sites; however, generally, the FSRs from the 1D synthetics underestimate the ground motion amplification compared to those from the recorded data [Figure 5.18 (a)]. This is particularly true for zone 5. The correlation coefficient between the synthetic maximum FSR and the observed maximum FSR is $\mathrm{corr}_a(X,Y) = 0.64$.

3. The 1D modelling method can predict a fairly good resonant frequency for most of sediment sites [Figure 5.18 (b)]. The correlation coefficient between the synthetic resonant frequency and the observed resonant frequency is $\mathrm{corr}_f(X,Y) = 0.56$.

4. The 1D synthetics for L16 and L17 simulate the corresponding data poorly. Ground motion is amplified greatly in the data but it is amplified little in the corresponding 1D synthetics. In the real portable deployment, L16 and L17 were located on the Wainuiomata valley. In the Wellington 3D shaking hazard model, L16 sits on rock site, i.e., there is no sediment layers underneath L16. The velocity v_s in the sediment layer under L17 is 175 m/s. Perhaps that is much larger than the real *S*-wave velocity in Wainuiomata valley, which is close to 80 m/s (Chávez-García *et al.*, 1999). That is why the 1D synthetics in L16 and L17 can not match their corresponding data reasonably.

The method of synthetic seismogram calculation with local 1D models extracted from the Hutt 3D model presented in this Chapter gives a primitive way of estimating shaking hazard in Hutt Valley. However, there is a range of the ground motion amplification in the recorded data caused by

2D and 3D effects. 1) Abrupt velocity increase between the alluvial valley and the surrounding rock environments can trap seismic energy and generate amplification. 2) Scattering produced by lateral heterogeneity of the true crust causes amplification. 3) Topographic effects occur in hilly and mountainous areas can cause amplification (Geli *et al.*, 1988). 4) Focusing effects of deep structures such as buried basins or folded structures can lead to amplifications at the free surface (Hartzell *et al.*, 1997). These have partly answered why the peaks in the spectrum of the real data in Lower Hutt exhibits more complexity than that of the 1D synthetics. In a local geological area like Hutt Valley, 1) and 2) seem to affect the recorded data largely, the sediment sites here may amplify the ground motion more than those in a plain. It is likely that the synthetics from (1D+3D) modelling in Chapter 7 will be able to simulate the amplification in the data better than that from 1D modelling.

CHAPTER 6

DEVELOPMENT OF THE HYBRID (1D+3D) MODELLING TECHNIQUE

The aim for this project is to calibrate the Wellington 3D shaking hazard model with the recorded data. To do so, it is necessary to develop a new modelling technique by modifying and combining the 1D modelling technique (Benites *et al.*, 2002) and the 3D modelling technique (Olsen, 1994) together, which is termed as *(1D+3D) hybrid modelling technique*. To do this, we put the ground motion wavefield at each grid point of Hutt Valley bottom, calculated by the 1D modelling technique as an incident wavefield into the 3D model, so that the ground motion can be propagated through sediment layers before arriving at the free surface. The key problems in developing (1D+3D) hybrid modelling technique are:

1. Modifying the 1D code by DWN method to get all the components of the stress tensor and all the components of the velocity vector into a Cartesian coordinate system.

2. Modifying the 3D FD code to read in the ground motion at Hutt Valley bottom from the 1D code.

6.1 Modifying the 1D code for this project and test

I calculated all the components of the stress tensor and velocity vector in Cartesian coordinate system by modifying the 1D code, which is input into the 3D FD code in the 2nd step of (1D+3D) modelling.

6.1.1 Development of 1D code involving some algebra and programming

Originally, the 1D code from Benites *et al.* (2002) gave the velocity vector (v_r, v_θ, v_z) and three components of the stress tensor (τ_{rz}, $\tau_{\theta z}$ and τ_{zz}) in the cylindrical coordinate system. But all the components of the stress tensor (τ_{xx}, τ_{yy}, τ_{zz}, τ_{xy}, τ_{xz} and τ_{yz}) and the velocity vector (v_x, v_y, v_z) in the valley bottom are needed as incident wavefield for the 3D FD code to satisfy the equations of motions and the initial conditions. Furthermore, the stress tensor and velocity vector used as the input for the 3D code are in a Cartesian system. The velocity vector rotation from cylindrical coordinate system to Cartesian coordinate system has been presented in Page 58. In this chapter, I develop the 1D code a further step to compute the stress tensor from the displacements. The components are imposed at each grid cell that intersects the bottom of the Hutt Valley, i.e., at a single grid point in this thesis. Instability may result if any source is imposed over too short a distance in any direction, with grid dispersion resulting. In the future, we may try to impose the *interface source* over a volume of considerable size, a source containing $6 \times 6 \times 6$ grid points at least to match the span of the fourth-order spatial and second-order temporal finite difference.

First, I obtained the other 3 stress tensor components (τ_{rr}, $\tau_{r\theta}$ and $\tau_{\theta\theta}$) by the following method:

In cylindrical coordinates, the stress tensor can be derived from the displacements (Aki and Richards, 1980):

$$\tau_{rr} = (\lambda+2\mu)\frac{\partial u}{\partial r} + \lambda(\frac{\partial v}{r\partial\theta} + \frac{u}{r}) + \lambda\frac{\partial w}{\partial z} \tag{6.1a}$$

$$\tau_{\theta\theta} = \lambda\frac{\partial u}{\partial r} + (\lambda+2\mu)(\frac{\partial v}{r\partial\theta} + \frac{u}{r}) + \lambda\frac{\partial w}{\partial z} \tag{6.1b}$$

$$\tau_{zz} = \lambda\frac{\partial u}{\partial r} + \lambda(\frac{\partial v}{r\partial\theta} + \frac{u}{r}) + (\lambda+2\mu)\frac{\partial w}{\partial z} \tag{6.1c}$$

$$\tau_{r\theta} = \mu(\frac{\partial u}{r\partial\theta} - \frac{v}{r} + \frac{\partial v}{\partial r}) \tag{6.1d}$$

$$\tau_{rz} = \mu(\frac{\partial u}{\partial z} + \frac{\partial w}{\partial r}) \tag{6.1e}$$

$$\tau_{\theta z} = \mu(\frac{\partial v}{\partial z} + \frac{\partial w}{r\partial\theta}) \tag{6.1f}$$

where u, v and w are the displacements along unit vectors $\vec{e}_r$, $\vec{e}_\theta$ and $\vec{e}_z$ respectively. τ_{rz}, $\tau_{\theta z}$ and τ_{zz} have been given by the DWN method in the original 1D code [equation (5.11)]. Note that $\tau_{r\theta}$ is within the plane $\vec{e}_r\vec{e}_\theta$, i.e. it does not depend on derivatives with z. Derivatives $\frac{\partial u}{\partial r}$, $\frac{\partial u}{\partial\theta}$, $\frac{\partial v}{\partial r}$ and $\frac{\partial v}{\partial\theta}$ can be obtained from the expressions for u and v [equations (5.11) and (5.12)].

τ_{rr} and $\tau_{\theta\theta}$, which both involve $\frac{\partial w}{\partial z}$, must be propagated through the layers. Since τ_{zz} also involves $\frac{\partial w}{\partial z}$, rearranging (6.1c) we get:

$$\frac{\partial w}{\partial z} = \frac{1}{\lambda + 2\mu}[\tau_{zz} - \lambda(\frac{\partial u}{\partial r} + \frac{\partial v}{r\partial\theta} + \frac{u}{r})] \tag{6.2}$$

so this problem is solved.

Taking advantage of the relationships (Boas, 1966):

$$\begin{aligned} J_2(x) &= 2J_1(x) - xJ_0(x) \\ \frac{dJ_0(x)}{dx} &= -J_1(x) \\ \frac{dJ_1(x)}{dx} &= \frac{J_1(x) - xJ_2(x)}{x} \end{aligned} \tag{6.3}$$

where $J_0(x)$, $J_1(x)$ and $J_2(x)$ are the Bessel functions of order zero, one and two respectively, the derivatives of displacement radiation factors for a double-couple point source are derived from equation (5.7):

$$\begin{aligned} \frac{\partial R_P^+}{\partial r} &= M_P\{AS_0J_0(kr) + AS_2J_1(kr)\} \\ \frac{\partial R_P^-}{\partial r} &= M_P\{AS_1J_0(kr) + AS_3J_1(kr)\} \\ \frac{\partial R_P^+}{\partial\theta} &= M_P\{AS_4J_0(kr) + AS_5J_1(kr)\} \\ \frac{\partial R_P^-}{\partial\theta} &= M_P\{AS_4J_0(kr) + AS_6J_1(kr)\} \\ \frac{\partial R_{SV}^+}{\partial r} &= M_{SV}\{BS_0J_0(kr) + BS_2J_1(kr)\} \\ \frac{\partial R_{SV}^-}{\partial r} &= M_{SV}\{BS_1J_0(kr) + BS_3J_1(kr)\} \\ \frac{\partial R_{SV}^+}{\partial\theta} &= M_{SV}\{BS_4J_0(kr) + BS_6J_1(kr)\} \\ \frac{\partial R_{SV}^-}{\partial\theta} &= M_{SV}\{BS_5J_0(kr) + BS_7J_1(kr)\} \\ \frac{\partial R_{SH}^+}{\partial r} &= M_{SH}\{CS_0J_0(kr) + CS_2J_1(kr)\} \\ \frac{\partial R_{SH}^-}{\partial r} &= M_{SH}\{CS_1J_0(kr) + CS_3J_1(kr)\} \\ \frac{\partial R_{SH}^+}{\partial\theta} &= M_{SH}\{CS_4J_0(kr) + CS_5J_1(kr)\} \\ \frac{\partial R_{SH}^-}{\partial\theta} &= M_{SH}\{CS_4J_0(kr) + CS_6J_1(kr)\} \end{aligned} \tag{6.4}$$

where M_P, M_{SV} and M_{SH} can be found in Section 5.8.

$$
\begin{aligned}
AS_0 &= kA_1 \\
AS_1 &= kA_2 \\
AS_2 &= -kA_0 - \frac{k(-\cos 2\theta M_{xx} - 2\sin 2\theta M_{xy} + \cos 2\theta M_{yy})}{r^2} - \frac{A_1}{r} \\
AS_3 &= -kA_0 - \frac{k(-\cos 2\theta M_{xx} - 2\sin 2\theta M_{xy} + \cos 2\theta M_{yy})}{r^2} - \frac{A_2}{r} \\
AS_4 &= k^2(-sin2\theta M_{xx} + 2cos2\theta M_{xy} + sin2\theta M_{yy}) \\
AS_5 &= \frac{k}{r}(2sin2\theta M_{xx} - 4cos2\theta M_{xy} - 2sin2\theta M_{yy}) - 2i\nu k(sin\theta M_{xz} - cos\theta M_{yz}) \\
AS_6 &= \frac{k}{r}(2sin2\theta M_{xx} - 4cos2\theta M_{xy} - 2sin2\theta M_{yy}) + 2i\nu k(sin\theta M_{xz} - cos\theta M_{yz}) \\
BS_0 &= kB_2 \\
BS_1 &= kB_3 \\
BS_2 &= -kB_0 - \frac{k}{r^2}(-cos2\theta M_{xx} - 2sin2\theta M_{xy} + cos2\theta M_{yy}) - \frac{B_2}{r} \\
BS_3 &= -kB_1 + \frac{k}{r^2}(-cos2\theta M_{xx} - 2sin2\theta M_{xy} + cos2\theta M_{yy}) - \frac{B_3}{r} \\
BS_4 &= k^2(-sin2\theta M_{xx} + 2cos2\theta M_{xy} + sin2\theta M_{yy}) \\
BS_5 &= -BS_4 \qquad (6.5) \\
BS_6 &= \frac{k}{r}(2sin2\theta M_{xx} - 4cos2\theta M_{xy} - 2sin2\theta M_{yy}) + \frac{i}{\gamma}k(2k^2 - k_\beta^2)(sin\theta M_{xz} - cos\theta M_{yz}) \\
BS_7 &= \frac{k}{r}(-2sin2\theta M_{xx} + 4cos2\theta M_{xy} + 2sin2\theta M_{yy}) + \frac{i}{\gamma}k(2k^2 - k_\beta^2)(sin\theta M_{xz} - cos\theta M_{yz}) \\
CS_0 &= kC_1 \\
CS_1 &= kC_2 \\
CS_2 &= -kC_0 + \frac{M_{xx} - 2cos2\theta M_{xy} - M_{yy}}{r^2} - \frac{C_1}{r} \\
CS_3 &= -kC_0 + \frac{M_{xx} - 2cos2\theta M_{xy} - M_{yy}}{r^2} - \frac{C_2}{r} \\
CS_4 &= 2ksin2\theta M_{xy} \\
CS_5 &= \frac{-4sin2\theta M_{xy}}{r} + i\gamma(cos\theta M_{xz} + sin\theta M_{yz}) \\
CS_6 &= \frac{-4sin2\theta M_{xy}}{r} - i\gamma(cos\theta M_{xz} + sin\theta M_{yz})
\end{aligned}
$$

where θ is the azimuth angle from north, positive clockwise [Figure 5.1]. $A_0, A_1, A_2, B_0, B_1, B_2, B_3, C_0, C_1, C_2$ can be found in equation (5.9).

Next, I rotated the stress tensor from the cylindrical coordinate system to the Cartesian coordinate system.

To perform the rotation, the Jacob rotation matrix T and reverse Jacob rotation matrix T^{-1} (Boas, 1966) are used, which are as follows:

$$T = \begin{pmatrix} cos\theta & sin\theta & 0 \\ -sin\theta & cos\theta & 0 \\ 0 & 0 & 1 \end{pmatrix} \tag{6.6}$$

$$T^{-1} = \begin{pmatrix} cos\theta & -sin\theta & 0 \\ sin\theta & cos\theta & 0 \\ 0 & 0 & 1 \end{pmatrix} \tag{6.7}$$

The stress tensor in the Cartesian coordinate system is obtained from that in the cylindrical coordinate system by:

$$\begin{pmatrix} \tau_{xx} & \tau_{xy} & \tau_{xz} \\ \tau_{yx} & \tau_{yy} & \tau_{yz} \\ \tau_{zx} & \tau_{zy} & \tau_{zz} \end{pmatrix} = T^{-1} \begin{pmatrix} \tau_{rr} & \tau_{r\theta} & \tau_{rz} \\ \tau_{\theta r} & \tau_{\theta\theta} & \tau_{\theta z} \\ \tau_{zr} & \tau_{z\theta} & \tau_{zz} \end{pmatrix} T \tag{6.8}$$

6.1.2 Testing the modified 1D code

To check that the 1D code was modified successfully, the stress components for τ_{rr}, $\tau_{r\theta}$ and $\tau_{\theta\theta}$ as a function of distance along the surface of the mesh were plotted in Figures 6.1 (a), (b) and (c). The epicenter is used as the origin of the coordinate system.

To test the stress tensor, we use a half space homogeneous velocity model, and a simple focal mechanism: pure strike-slip, vertical fault, with $\phi_s = 0°$, $\delta = 90°$ and $\lambda = 0°$ [figure 4.2 and equation (4.6)]. The focus is 9 km right below the center of the 51 by 51 mesh.

From Figure 6.1 (a) we see the nodal planes of τ_{rr} and $\tau_{\theta\theta}$ are along NS and EW respectively, which is identical to the nodal planes of the focal mechanism used. We also see that $\tau_{r\theta}$'s nodal planes are along 45° direction and 135°, which are 45° away from the nodal planes of the focal mechanism used. That is exactly what the radiation factors for stress are expected in equation (6.4). From the derivatives of displacement radiation factors in equation (5.7) and (5.9) we get the result that τ_{rr} and

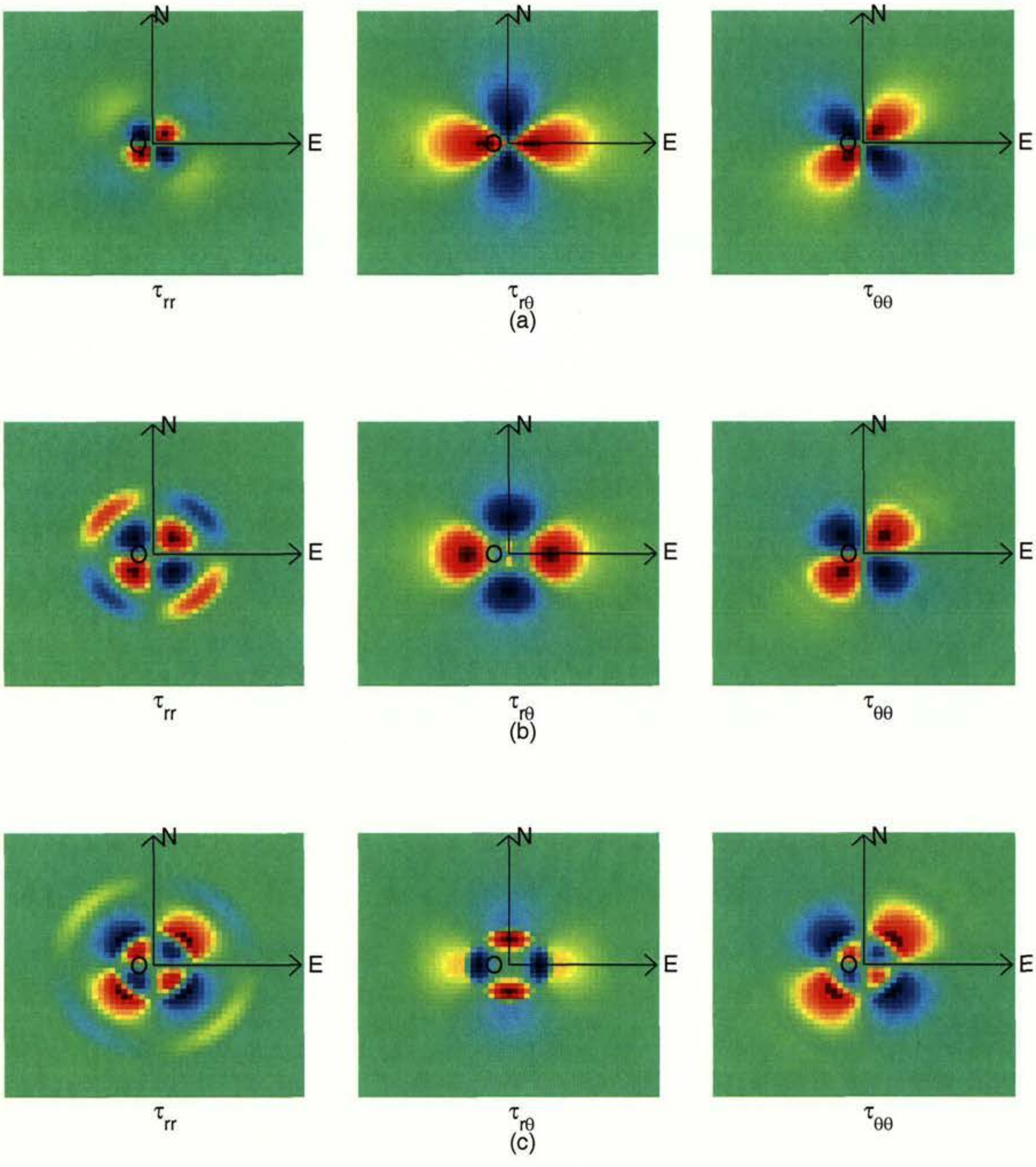

Figure 6.1 *The stress wavefield in an area of 51 × 51 km^2, covered by a grid of 51 × 51 points at the free surface. The assumed double-couple point source is 9.0 km right below the center of the area. O represents the epicenter. The snapshots are for (a) at 1.25 s (P wavefield) from the event origin time, (b) at 1.95 s (P wavefield) from the event origin time, (c) at 2.45 s (S wavefield) from the event origin time. The left panel in each figure corresponds to τ_{rr}, the center panel to $\tau_{r\theta}$ and the right panel to $\tau_{\theta\theta}$. The red color represents the positive values, the blue color represents the negative values. Note that the wavefield follows the radiation pattern.*

$\tau_{\theta\theta}$ are 0 in the nodal planes, and $\tau_{r\theta}$ is 0 along the planes which are 45° to the nodal planes. Figures 6.1 (b) and (c) are the radiation pattern for another two subsequent moments to show the evolution of the wavefield with time.

6.2 Methodology of the 3D FD

The 3D FD code is based on the equations of motions and the constitutive laws.

6.2.1 Theory

The 3D FD code was originally composed by Olsen (1994). In a 3D Cartesian system with x axis horizontal and positive to the east, y axis horizontal and positive to the north, z axis vertical and positive upwards, the equations of motions are (Levander, 1988):

$$\begin{aligned} \rho\frac{\partial \mathrm{u}_t}{\partial t} &= \frac{\partial \tau_{xx}}{\partial x}+\frac{\partial \tau_{xy}}{\partial y}+\frac{\partial \tau_{xz}}{\partial z} \\ \rho\frac{\partial \mathrm{v}_t}{\partial t} &= \frac{\partial \tau_{yx}}{\partial x}+\frac{\partial \tau_{yy}}{\partial y}+\frac{\partial \tau_{yz}}{\partial z} \\ \rho\frac{\partial \mathrm{w}_t}{\partial t} &= \frac{\partial \tau_{zx}}{\partial x}+\frac{\partial \tau_{zy}}{\partial y}+\frac{\partial \tau_{zz}}{\partial z} \end{aligned} \tag{6.9}$$

and the constitutive laws for an isotropic medium are:

$$\begin{aligned} \tau_{xx} &= (\lambda+2\mu)\frac{\partial \mathrm{u}}{\partial x}+\lambda\frac{\partial \mathrm{v}}{\partial y}+\lambda\frac{\partial \mathrm{w}}{\partial z} \\ \tau_{yy} &= \lambda\frac{\partial \mathrm{u}}{\partial x}+(\lambda+2\mu)\frac{\partial \mathrm{v}}{\partial y}+\lambda\frac{\partial \mathrm{w}}{\partial z} \\ \tau_{zz} &= \lambda\frac{\partial \mathrm{u}}{\partial x}+\lambda\frac{\partial \mathrm{v}}{\partial y}+(\lambda+2\mu)\frac{\partial \mathrm{w}}{\partial z} \\ \tau_{xy} &= \mu(\frac{\partial \mathrm{u}}{\partial y}+\frac{\partial \mathrm{v}}{\partial x}) \\ \tau_{xz} &= \mu(\frac{\partial u}{\partial z}+\frac{\partial w}{\partial x}) \\ \tau_{yz} &= \mu(\frac{\partial \mathrm{v}}{\partial z}+\frac{\partial \mathrm{w}}{\partial y}) \end{aligned} \tag{6.10}$$

where u, v and w are the displacement components in $\vec{x}$, $\vec{y}$ and $\vec{z}$, u_t, v_t and w_t are the particle velocities, τ_{ij} are the stresses. λ, μ and ρ can be found on Page 54. The compressional velocity α and the shear velocity β are in equation (5.3).

$$
\begin{aligned}
\tau_{xz} &= 0 = \mu(\tfrac{\partial u}{\partial z} + \tfrac{\partial w}{\partial x}) \\
\tau_{yz} &= 0 = \mu(\tfrac{\partial v}{\partial z} + \tfrac{\partial w}{\partial y}) \\
\tau_{zz} &= 0 = \lambda\tfrac{\partial u}{\partial x} + \lambda\tfrac{\partial v}{\partial y} + (\lambda + 2\mu)\tfrac{\partial w}{\partial z}
\end{aligned}
\qquad (6.11)
$$

The horizontal derivatives pose no problem. Olsen (1994) assumed appropriate symmetry for the stress components at the free surface and extended the grid two nodes above it. He used the boundary conditions to solve for the vertical derivatives and satisfy the free-surface condition. The other boundaries at the grid periphery are coded to satisfy the Clayton-Engquist A1 absorbing condition (Clayton and Engquist, 1977). To further reduce artificial reflections, the boundaries of the model are padded with a zone of attenuative material (Cerjan *et al.*, 1985). In this study, 25 grid points (1 km) in each of the boundaries of the Hutt 3D model are padded.

A staggered grid is used to solve the 3D elastic equations of motion [equations (6.9), (6.10) and (6.11)] (Levander, 1988) for the FD grid, where the simulated state variables (the velocities v_x, v_y and v_z, the stress tensor τ_{xx}, τ_{yy}, τ_{zz}, τ_{xy}, τ_{xz} and τ_{yz}) are spatially staggered from one another (Levander, 1988). The accuracy is fourth-order in space and second-order in time.

The configuration of a given virtual node and the coordinate system of the oringinal 3D FD code are illustrated in Figure 6.2. τ_{nn} corresponds to the normal stresses (i.e., τ_{xx}, τ_{yy} and τ_{zz}). All other variables are spaced 1/2 grid point from the others.

In the 3D FD code, at the source site, the relationship among stress rate, focal moment tensor and velocity STF is as follows (Olsen, 1994):

$$
\begin{aligned}
\frac{\partial \tau_{xx(xs,ys,zs,t)}}{\partial t} &= -0.5M_{xx}S(t) \\
\frac{\partial \tau_{xy(xs,ys,zs,t)}}{\partial t} &= -0.5M_{xy}S(t) \\
\frac{\partial \tau_{xz(xs,ys,zs,t)}}{\partial t} &= -0.5M_{xz}S(t) \\
\frac{\partial \tau_{yy(xs,ys,zs,t)}}{\partial t} &= -0.5M_{yy}S(t) \\
\frac{\partial \tau_{yz(xs,ys,zs,t)}}{\partial t} &= -0.5M_{yz}S(t) \\
\frac{\partial \tau_{zz(xs,ys,zs,t)}}{\partial t} &= -0.5M_{zz}S(t)
\end{aligned}
\qquad (6.12)
$$

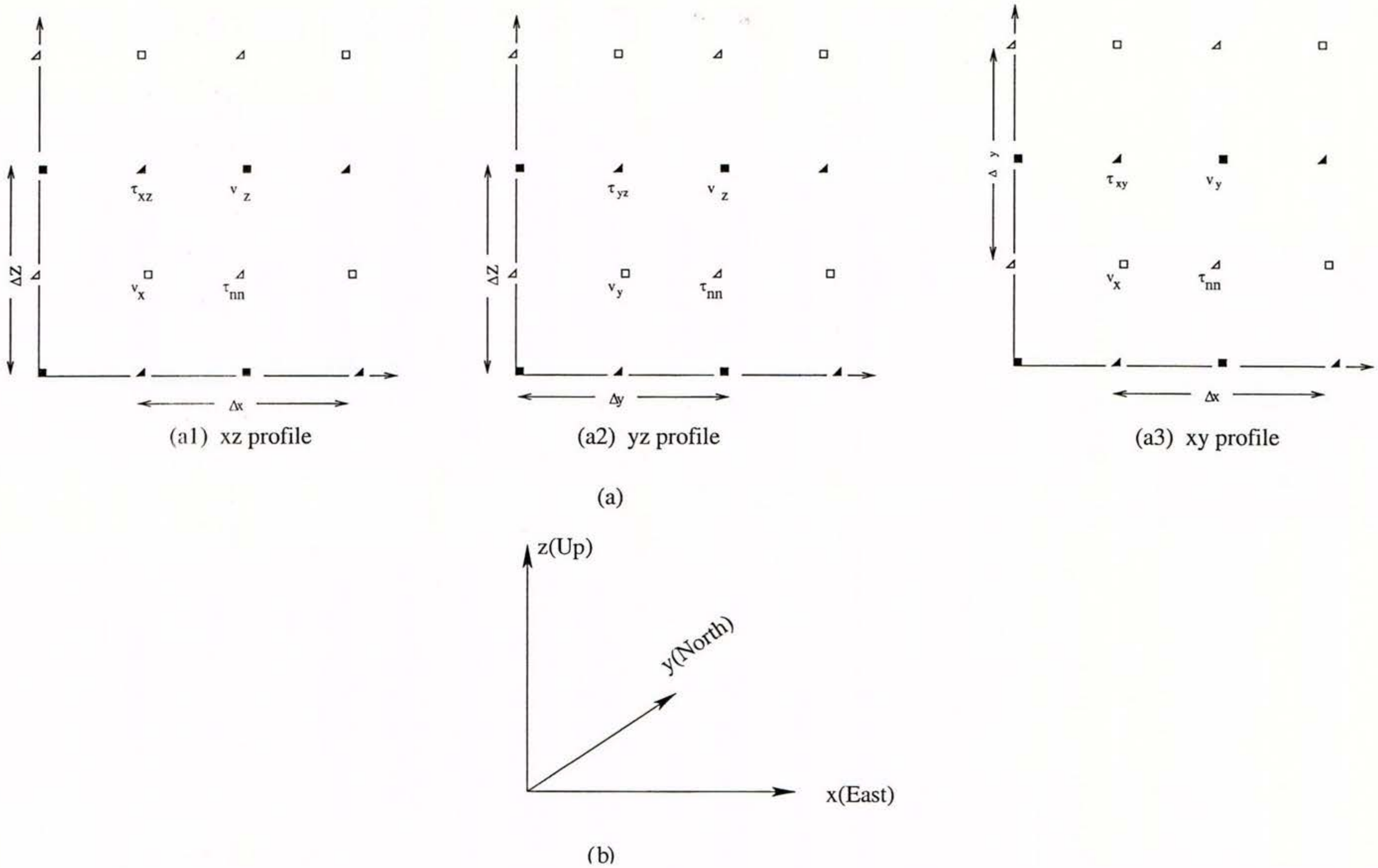

Figure 6.2 *The configuration of a given virtual node and the coordinate system of the 3D FD code. (a) Configuration: v_x is considered the reference point for each virtual node, all the other variables are staggered by $\frac{1}{2}$ grid point from this reference point. (b) Coordinate system of the 3D FD code*

where τ_{ij} (i, j=x, y, z) is the ijth component in the stress tensor, M_{ij} (i, j=x, y, z) is the corresponding component in the focal moment tensor [equation (4.6)] and S(t) is coded as the velocity STF [equation (5.16)]. (xs,ys,zs) is the grid point for the source site. The original 3D FD code for this project is not exactly the same one which Olsen (1995) used for the 3D wavefield simulation at Salt Lake Basin. Instead, a double couple point source is imposed in the program, whereas Olsen (1995) used a planar P-wave implemented in a plane near the free surface edge of the model as the source in his study at Salt Lake Basin. He chose a velocity Ricker wavelet as the STF since that contained the frequency band needed by his study.

6.2.2 The stability criterion

FD computations require determinations of spatial and temporal sampling criteria. Spatial sampling is generally chosen to avoid grid dispersion in solutions. Subsequently, the temporal sampling is chosen to avoid numerical instability.

The temporal sampling (Δt) required by the stability criterion in the 3D fourth order FD method is as follows (Lines *et al.*, 1998):

$$\begin{aligned} \Delta t_0 &= \frac{\Delta h}{2 v_{pmax}} \\ \Delta t &\leq \Delta t_0 \end{aligned} \tag{6.13}$$

where Δt_0 is called *stability limit*, and v_{pmax} is the maximum P wave velocity in the Hutt 3D model; Δh is the length of the grid box in the 3D model.

6.3 Tests

To understand the output of the 3D FD code, two tests are carried out as follows:

6.3.1 Test 1

The moment tensor of an explosion source is:

$$\begin{pmatrix} M_{xx} & M_{xy} & M_{xz} \\ M_{yx} & M_{yy} & M_{yz} \\ M_{zx} & M_{zy} & M_{zz} \end{pmatrix} = \begin{pmatrix} 1 & 0 & 0 \\ 0 & 1 & 0 \\ 0 & 0 & 1 \end{pmatrix} \tag{6.14}$$

The wavefields in the vertical profile from an explosion source are calculated, the velocity modulated ramp function [equation (5.16)] with a rise time of 0.5 s is used in this calculation. Several snapshots are displayed in Figure 6.3 (a), (b) and (c). The cube model is composed of 101 by 101 by 100 grid points, and the assumed source is located at the grid point of (51,51,50), i.e. the centre of the cube model.

In a homogeneous medium, an explosion source generates *P* waves, which propagate concentrically. When the *P* wavefront arrives at the free surface, it is reflected and part of the *P* wave is converted into a *SV* wave. Figure 6.3 (a), (b) and (c) show how the seismic waves generated by the explosion source and the reflected seismic waves propagate. Note that theorically, in a homogeneous medium, along xz profile, v_y should be 0. However, v_y is not exactly 0 from the FD code due to the noise from the numerical computational nature of the FD method. Nevertheless, it is much smaller than v_x and v_z.

6.3.2 Test 2

The 3D FD code is further tested by the 1D DWN code. This test is also called the 1D/3D test in this project.

A *test 3D Hutt model* and a *1D homogeneous model* are used in this test and in the later test of Section 6.5. It is called *test 3D Hutt model* here because it shares the same dimensions with the real *Hutt 3D shaking hazard model*, which are 303 × 249 × 240 grid points. The difference between them lies in that the *test 3D Hutt model* is a homogeneous model. The elastic parameters used in the *test 3D Hutt model* and the *1D homogeneous model* are $v_p = 2.6$ km/s, $v_s = 1.5$ km/s and $\rho = 2.74\ g/cm^3$, exactly same as the elastic parameters of the bedrock layer in the real *Hutt 3D shaking hazard model.*

The 1D DWN modelling code and 3D FD modelling code use completely different numerical

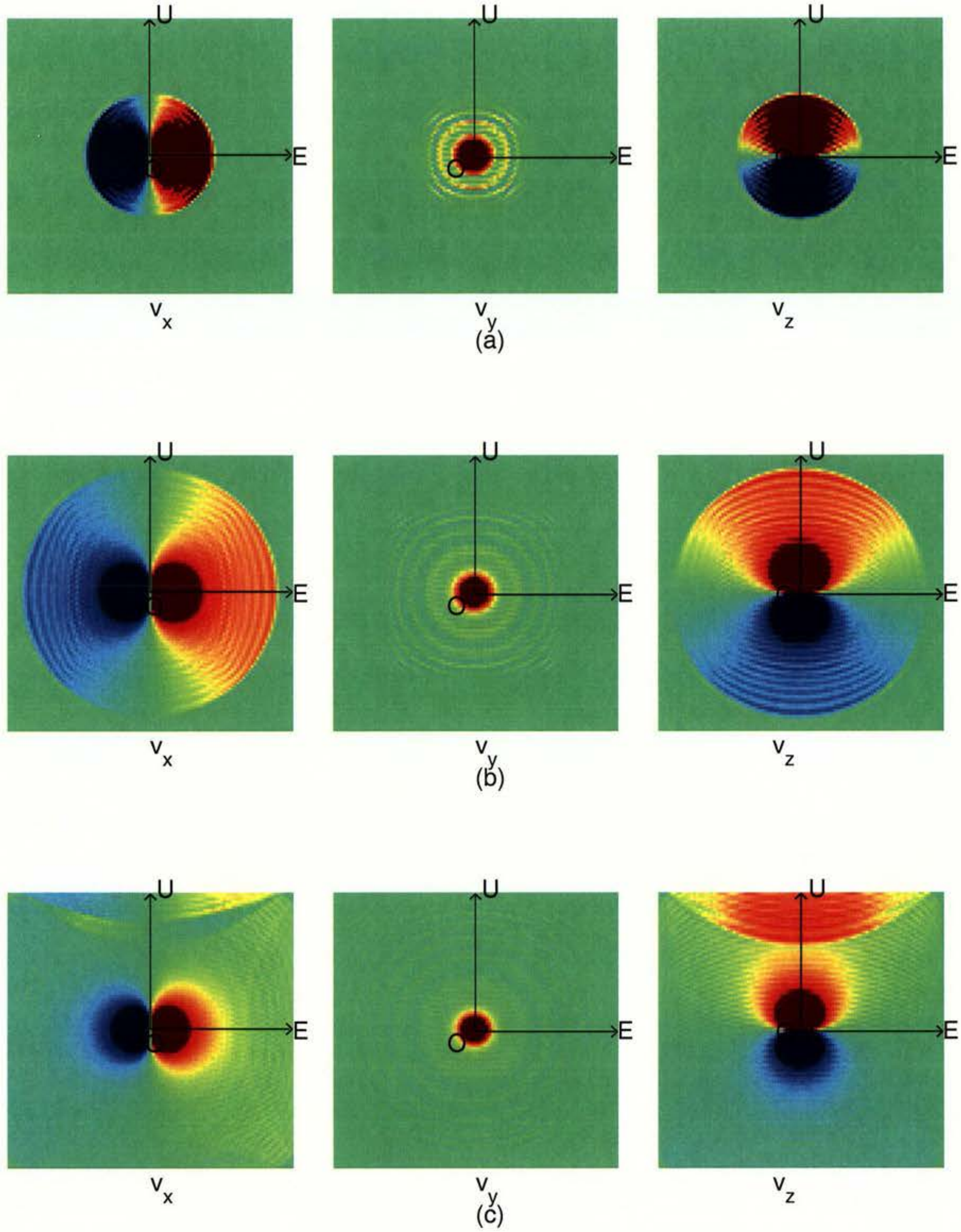

Figure 6.3 *The velocity wavefield for an explosion source in the 3D constant model. This is along the cross-section of $y = y_s$ ((x_s, y_s, z_s) is the source location in the 3D model). "U" represents vertical axis, "E" represents EW axis. O represents the epicenter. The snapshots are for (a) at 0.375 s (P wavefield) from the event origin time, (b) at 0.75 s (P wavefield) from the event origin time, (c) at 1.125 s (P wavefield) from the event origin time. The left panel in each figure corresponds to the east component (v_x), the center panel to the north component (v_y) and the right panel to the vertical component (v_z). Red and blue signify positive and negative vaules respectively. Note that the wavefield follows the radiation pattern of an explosion source. Also note the reflections from the free surface in (c).*

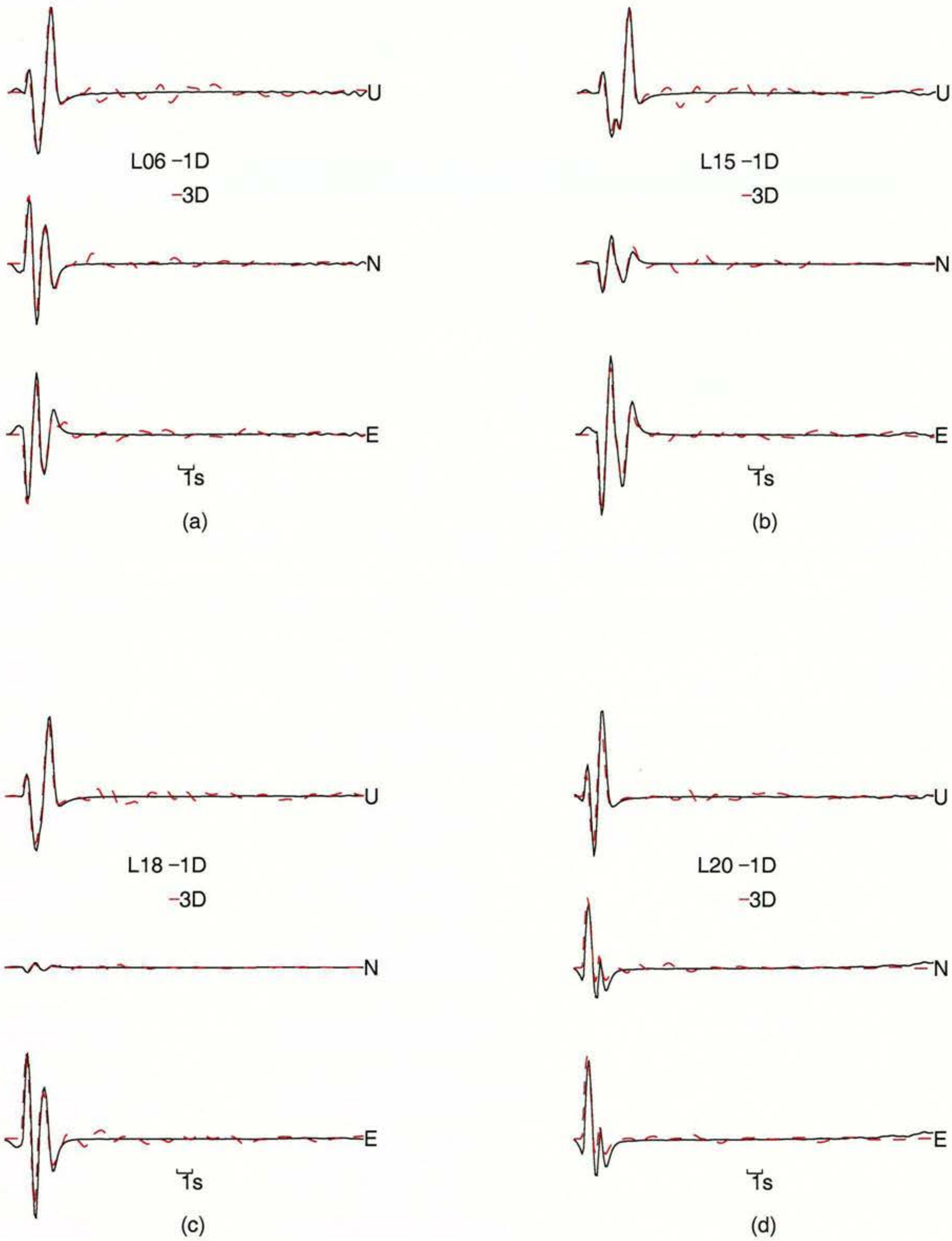

Figure 6.4 *Comparisons of 1D synthetics (black solid) and 3D (red dashed) synthetics from an explosion source. Each component of the 1D and 3D synthetics is normalized by the maxima of the synthetics at the corresponding station. Both the 1D velocity model and 3D velocity model are uniform. (a) L06 station, the maxima is from the 3D synthetics of U component. (b) L15 station, the maxima is from the 1D synthetics of U component. (c) L18 station, the maxima is from the 3D synthetics of U component. (d) L20 station, the maxima is from the 3D synthetics of U component.*

methods. The former uses DWN method, while the latter uses FD method. The FD method is a numerical scheme developed from the first-order system of hyperbolic elastic equations of motion and constitutive laws expressed in particle velocities and stresses. To examine the fidelity of solutions generated with the 3D code, I compare FD solutions with the solutions from the 1D DWN method code in a uniform elastic half-space. I put an explosion point source in the lateral centre of the test 3D Hutt model, but at only 0.48 km depth, which is the maximum depth of Hutt Valley sediment-bedrock interface used as the *interface source* in the (1D+3D) modelling, Chapter 7; 3D synthetics from 13 different stations in all the four quadrants are obtained. The FD scheme was run at 43% of the *stability limit* [equation (6.13)] and the source pulse had a rise time of 1 s. Independently, I put the exact same source in the 1D homogeneous model, and obtained synthetics from the 1D DWN method code at the identical sites.

Horizontal and vertical motion seismograms from four sites representing different quadrants are shown in Figures 6.4 (a), (b), (c) and (d). The 1D/3D plots for the synthetic seismograms from the other nine sites are similar to Figures 6.4 (a), (b), (c) and (d) and are not displayed here. For all traces in the different quadrants, the FD solutions are in excellent agreement with the 1D solutions in polarity, waveform and periods, suggesting that the 3D FD forward modelling code works properly. Note the late noise in the 3D synthetics after the *P* wave in the 1D synthetics stops. That is produced by dispersion from the numerical computational method and artificial reflections from the artificial boundaries. The long period noise averages about 5% of signal amplitude.

A 1 km zone adjacent to each artificial boundary is padded with absorbing materials, but the artificial reflections are not completely absorbed. I also calculated the 3D synthetics and 1D synthetics at a focal depth of 4.84 km (located at the geometry centre of the 3D model) and 7.64 km (located nearby at the bottom of the absorbing boundary zone of the 3D model) respectively. The results indicate that when the seismic focus is deeper, the long period noise caused by the artificial reflections from the bottom boundary will increase. That is why the Hutt 3D model is constructed to be much thicker than the thickness of the sediment layers.

6.4 Modifying the 3D FD code for the (1D+3D) modelling technique

Originally, the 3D FD code from Olsen (1995) is for a double couple, point source located in the center of the 3D model. The source for the modified 3D FD code in this study is a different one; it is situated at the bottom of Hutt Valley. The wavefields in the 1D model are brought to the interface between the sediment and the underlying bedrock in the 3D model by the 1D code, then they start to propagate in the 3D model. The wavefields created by the 1D code at the irregularly curved interface work as the source in the 3D code, therefore it is called the *interface source* in this study. *Interface source* is a key term introduced by (1D+3D) modelling technique. So I modified the source section to read the seismograms at Hutt Valley bottom from the first step of the hybrid technique modelling (the 1D modelling).

Note in case the thickness of the soft layer is 0 m [Figure 2.2], the corresponding free surface serves as the *interface source*. When the *interface source* is imposed at the surface in rock regions,its amplitude is doubled. The *interface source* at the free surface still acts as a surface reflector. Surface waves develop at the surface *interface source*. These are based on the fact that when the *interface source* is imposed at the free surface in rock regions, simply z_o = 0 km (z_o: observation depth) is assumed in those grid points in the first step of (1D+3D) modelling, therefore the *interface source* at the free surface inherits all the properties of the free surface in the 1D modelling (Benites *et al.*, 2002).

One difficult problem I have handled is the coordinate system. To read the seismograms from the 1D modelling step, I obtained the relationship between the stress tensor in the coordinate system of the 3D modelling code and that in the coordinate system of the 1D modelling code, and the relationship between the velocity vector in the coordinate system of the 3D modelling code and that in the coordinate system of the 1D modelling code [see below, equation (6.15)] and inserted them in the modified 3D code. Another minor modification I have done to the 3D code is to replace the original velocity model with Hutt Valley velocity model.

The following five changes were made to the original 3D FD code:

1. I modified the source subroutine to read the stress and velocity wavefield in Hutt Valley bottom created by the modified 1D modelling code.

2. I modified the model subroutine to read in Hutt Valley 3D shaking model. In addition, I modified the units used in the original 3D FD code to keep consistent with the 1D code. All the elastic parameters in the 3D model share the same unit to the corresponding elastic parameters in the 1D model to keep in accordance to each other.

3. I met the need required by the *stability criterion* [equation (6.13)] with a linear interpolation

technique. In the particular case of Hutt Valley 3D velocity model, $v_{pmax} = 2.6$ km/s, $\Delta x = \Delta y = \Delta z = 0.040$ km. So it is required that $\Delta t \leq \Delta t_0 = 0.0080$ s to follow that criterion. A value of $\Delta t = 0.0035$ s was used previously by Benites and Olsen (2004) in the modelling of the strong motion from the Wellington fault rupture and thus also was employed by me. There are 253 by 199 grid points in Hutt Valley bottom. If the wavefield in each grid point in Hutt Valley bottom is calculated with a time interval of $\Delta t = 0.0035$ s in the first step of 1D modelling, it will cost the Linux computer 20 days to calculate a time series of 51.2 s in the the first step of (1D+3D) modelling only. To analyse the site effect caused by the 3D model, 12.8 s of the *S* wave seismogram is needed for each site [Chapter 7]. A time series of 51.2 s is the minimum value of seismogram length based on the focal distance in the earthquakes used. It is too time consuming to use 0.0035 s in the first step of (1D+3D) modelling for the input wavefield; besides the data filesize will be as huge as 33 GB, which is too large for the Linux computer to handle.

Therefore a linear interpolation trick is used. Since the engineering seismologists are mainly interested in the seismic wave frequencies below 2.5 Hz, I calculate the wavefields by the 1D code with a time interval of 0.2 s only, and the 1D synthetics wavefields are interpolated linearly in the 3D code so that the sampling rate becomes as small as 0.0034 s for the FD calculation. Note the seismograms created by linear interpolation for Hutt Valley *interface source* to work as the incident wavefield for the second stage of (1D+3D) modelling are an approximation to the genuine seismograms from the first stage of (1D+3D) modelling. Within each quarter period, the waveform can be approximated as a line and hence can be sampled as densely as needed.

4. I transformed the stress tensor and velocity vector from the coordinate system of the 1D DWN code into the coordinate system of the 3D code. Since the 1D DWN code uses a coordinate system with x positive north, y positive east, z positive down and the 3D FD code uses a coordinate system with x postive east, y positive north, z positve up, the following relationships are used in reading the wavefield in the 3D FD code from the 1D DWN code:

$$
\begin{aligned}
\tau_{3Dxx} &= \tau_{1Dyy} \\
\tau_{3Dxy} &= \tau_{1Dxy} \\
\tau_{3Dxz} &= -\tau_{1Dyz} \\
\tau_{3Dyy} &= \tau_{1Dxx} \\
\tau_{3Dyz} &= -\tau_{1Dxz} \\
\tau_{3Dzz} &= \tau_{1Dzz} \\
v_{3Dx} &= v_{1Dy} \\
v_{3Dy} &= v_{1Dx} \\
v_{3Dz} &= -v_{1Dz}
\end{aligned}
\tag{6.15}
$$

where τ_{3Dxx}, τ_{3Dxy}, τ_{3Dxz}, τ_{3Dyy}, τ_{3Dyz} and τ_{3Dzz} are the components of the stress tensor in the 3D coordinate system, v_{3Dx}, v_{3Dy} and v_{3Dz} are the components of the velocity vector in the 3D coordinate system, τ_{1Dxx}, τ_{1Dxy}, τ_{1Dxz}, τ_{1Dyy}, τ_{1Dyz} and τ_{1Dzz} are the components of the stress tensor in the 1D coordinate system, v_{1Dx}, v_{1Dy} and v_{1Dz} are the components of the velocity vector in the 1D coordinate system.

5. To reduce the possibility of introducing noise and save computational time, the original 3D FD code are modified to read the *interface source* wavefields from the very beginning of *P* wave; since the wavefields from the modified 1D modelling start from the event origin time, therefore the part of the *interface source* wavefields before *P* wave arrives is chopped off for the revised 3D FD modelling.

There is one major difference between the modified 3D code and the original 3D code in the source section: in the original 3D code, only the components of the stress tensor are employed for the double couple point source; in the modified 3D code, the components of both stress tensor and velocity vector are employed. This is an important feature for the *interface source* [Section 6.5] compared to the double couple point source.

One alternate way for the (1D+3D) modelling technique is: using velocity wavefield in Hutt Valley bottom as incident wavefield only. The experiments show that the noise in the corresponding 1D/(1D+3D) test is smaller than using both stress and velocity as incident wavefield, since the stress components are from the spatial derivative of displacements and lead to more numerical instability. However, physically, both stress and velocity work as incident wavefields at the *interface source*, as is required by the equations of motion together with the boundary conditions and the initial conditions. The velocity vector is served as the only input in case the source is a plane wave (Olsen, 1995). The stress tensor is served as the only input in cases in which the source is a rectangle fault, the inhomogeneous slip distribution along the fault is considered and the fault is within the 3D model (Benites and Olsen, 2004; Olsen, 2001). In the rest of this (1D+3D) modelling study, both stress tensor and velocity vector are input in the *interface source*.

6.5 Test on the (1D+3D) modelling technique

This test is called 1D/(1D+3D) test in this study.

To test the technique, I use the *test 3D Hutt model* and the *1D homogeneous model* as stated in Section 6.3.2. Note that the (1D+3D) model formed in this test is still a half space model since the same elastic parameters are shared by the separate 1D model and the separate 3D model. There is no genuine "sediment site" in the test 3D model at all. These terms are borrowed and used here because the distance between "rock site" and the *interface source* is zero; whereas the distance between "sediment site" and the *interface source* is not zero.

I set a double couple, point source right below the center of the test Hutt 3D model. The focus is 11 km deep, only 1.4 km below the bottom margin of the 3D model.

First, I propagated the seismic wavefields by the modified 1D code to each grid in Hutt Valley bottom. Using these seismic wavefields in the test Hutt Valley bottom as the *interface source* in the modified 3D code, the stress and velocity fields were then propagated to the free surface of the test Hutt 3D model. The same 13 sites in the Lower Hutt deployment chosen in Section 6.3.2 were also used for the 1D/(1D+3D) test here. They represented different distances to the *interface source*. The corresponding velocity synthetics were output from the modified 3D code. These velocity seismograms used for comparison were calculated by the 1D code independently.

Only the figures of four sites in different quadrants are displayed here. Figures 6.5 (a), (b), (c) and (d) are the comparison and contrast of the synthetics from 1D modelling and (1D+3D) modelling at the four sites. We can see that the initial *P* and *S* waveforms from 1D and (1D+3D) at the four sites were quite close to each other. Figure 6.5 (a) illustrates that the initial pulse of the 1D synthetic and (1D+3D) synthetic of L09 match each other fairly well. L09 is only 1.9 km away from the 3D model lateral boundary, which is one of the closest stations to the 3D model lateral boundary among all the 24 stations in the Lower Hutt deployment, and only 0.9 km away from the 3D model absorbing boundary zone; in addition, L09 is 0.32 km above the *interface source*, and is one of the stations furthest from the *interface source*. All these factors may lead to the consequence that the discrepancy between (1D+3D) synthetics and 1D synthetics for L09 may be the one of the worst in

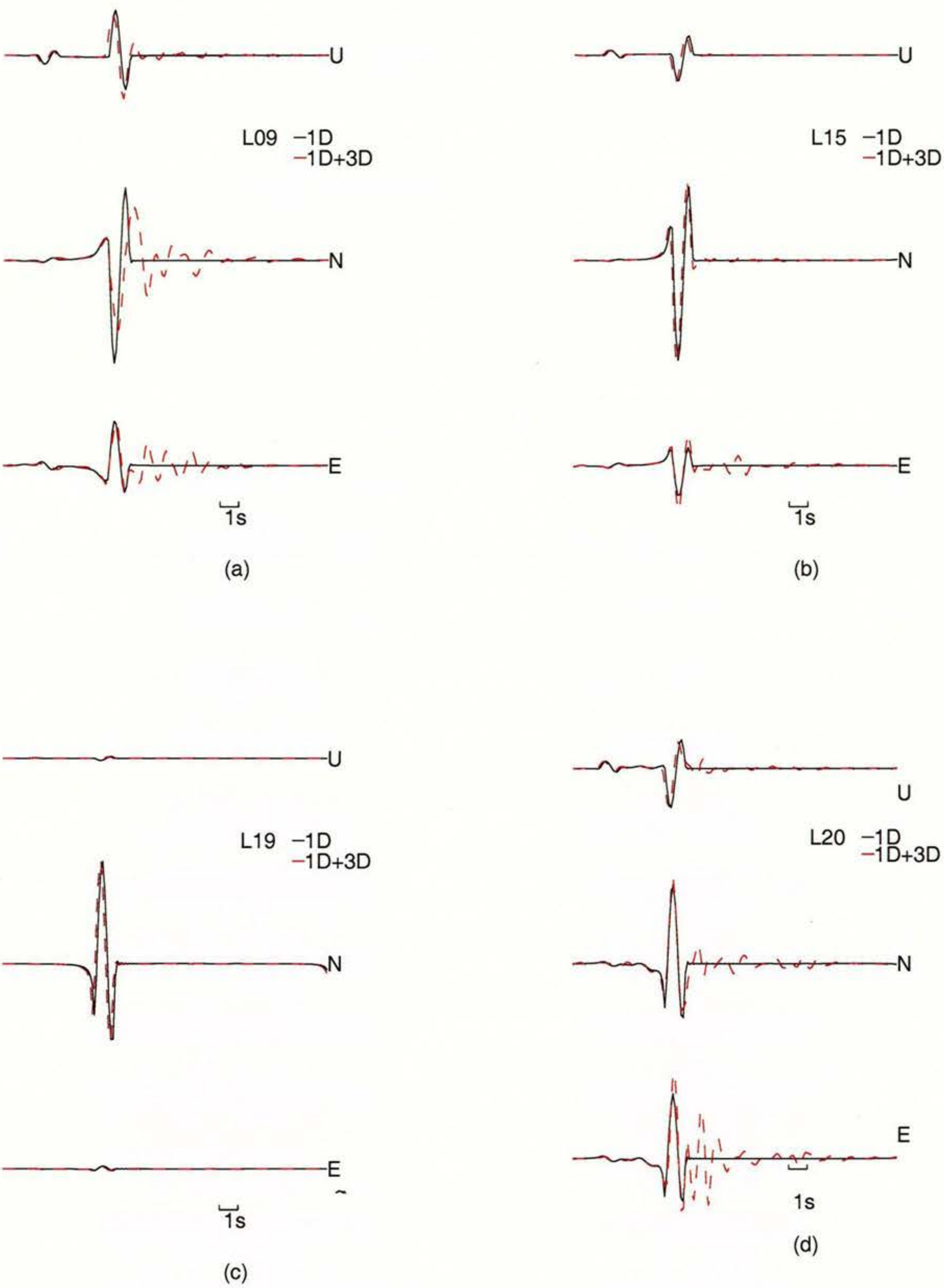

Figure 6.5 *A comparison of whole seismograms between 1D synthetic (black solid) and (1D+3D) synthetic (red dashed). $v_p = 2.6$ km/s, $v_s = 1.5$ km/s in both the 1D and 3D models. True amplitude traces are shown. (a) L09 station. (b) L15 station. (c) L19 station. (d) L20 station. No genuine "sediment site" really exists in the test 3D model. The distance between "rock site" (L19) and the interface source is zero; wheras the distance between "sediment site" (L09, L15 and L20) and the interface source is not zero.*

all the Lower Hutt deployment. However, the traces of (1D+3D) synthetics and 1D synthetics at L09 match fairly reasonably. This demonstrates that it is enough to reduce artificial reflections from the 3D Hutt Valley model boundary by choosing its boundary 1 km away from all the stations in the portable delpoyment and padding the 1 km zones close to the artificial boundaries of the model with attenuative material (Cerjan *et al.*, 1985). The plots from all the other nine sites are similar. The (1D+3D) results are nearly identical to the corresponding 1D result in all the 13 sites, that is exactly what we have expected. This convinces us that the revision of the 3D code is successful; moreover, it shows that the newly developed (1D+3D) modelling technique works properly.

Figure 6.5 (a) and (d) show that noise exist in the (1D+3D) synthetics at the deepest "sediment sites" (e.g., L09). Probably it is caused by grid dispersion; instabilities have a longer way to propagate to the free surface since the *interface source* is deeper there. Tests show that those later artifacts decrease with a longer rise time of the ramp source and higher velocities of test (1D+3D) model. This is because the wavelength increases with a longer source time and higher velocities of test (1D+3D) model, which leads to the reduction of grid dispersion effect. Those later artifacts decay as well when only a velocity vector is employed as input in the *interface source*, since the components of stress tensor are proportional to the spatial derivatives of the displacements, which introduce instability. It also probably can be reduced by changing the grid size to a smaller value and laterally enlarging the test 3D model. I wanted to confirm this by experiment but could not since there is not enough common block memory in the computer available. It is analyzed quantitively in Section 6.6.

6.6 Error analysis on the (1D+3D) modelling technique

Theoretically, in a homogeneous medium, the seismogram from (1D+3D) modelling should be exactly identical in waveform and amplitude to that from 1D modelling only, if the 3D test model is infinitely large in vertical dimension and lateral dimensions and if the grid size in the 3D test model is infinitesimal. However, it is impossible to build a 3D model infinitely large in dimensions and infinitesimally small in grid size. The test 3D model employed here is exactly the same size as the real Hutt 3D shaking model I worked on. To see the expected errors introduced by the (1D+3D) modelling technique, I studied the discrepancies between the synthetics from (1D+3D) modelling and sole 1D

Table 6.1

Error analysis derived from the comparison study between (1D+3D) modelling and 1D modelling based on half space models.

"soil classification"	error index	average error value*	range of error values
"zone 1"	e_{pv}	0.01	0.006-0.012
	e_{ps}	0.01	0.006-0.012
"zone 2"	e_{pv}	0.06	0.03-0.08
	e_{ps}	0.11	0.08-0.14
"zone 3-4"	e_{pv}	0.08	0.06-0.11
	e_{ps}	0.13	0.09-0.15
"zone 5"	e_{pv}	0.09	0.06-0.13
	e_{ps}	0.14	0.09-0.16

"soil classification", "zone 1", "zone 2", "zone 3-4" and "zone 5" here are not true soil classification as illustrated in Figure 3.3. There is no sediment site in the test 3D model at all. I borrowed these terms and used them here because the distance between "rock site" and the *interface source* is zero; wheras the distance between "sediment site" and the *interface source* is not zero. The medium parameters in each grid box are the same. The test 3D model is a constant model.

modelling with a half space model by two indices e_{pv} and e_{ps}, which is defined as follows:

$$\begin{aligned} e_{pv} &= \frac{1}{n}\sum_{i=1}^{n}\left[\frac{1}{3}\left(\sum_{j=1}^{3}\left|1-\frac{pv(1D+3D)_{ij}}{pv1D_{ij}}\right|\right)\right] \\ e_{ps} &= \frac{1}{n}\sum_{i=1}^{n}\left[\frac{1}{3}\left(\sum_{j=1}^{3}\left|1-\frac{ps(1D+3D)_{ij}}{ps1D_{ij}}\right|\right)\right] \end{aligned} \qquad (6.16)$$

where $pv(1D+3D)_{ij}$ and $pv1D_{ij}$ are the PGV of (1D+3D) synthetics and 1D synthetics at the ith station, jth component respectively; $ps(1D+3D)_{ij}$ and $ps1D_{ij}$ are the PAS of (1D+3D) synthetics and 1D synthetics at ith station, jth component respectively. || denotes absolute value. n is the number of stations in each zone.

The results are illustrated in Table 6.1.

In Table 6.1, e_{pv} is the average error of PVR between (1D+3D) synthetics and 1D synthetics in all the sites in each "zone" used in the (1D+3D) test; e_{ps} is the average error of PAS ratio between (1D+3D) synthetics and 1D synthetics in all the sites in each "zone" used in the (1D+3D) test. Table 6.1 shows that the error introduced by the (1D+3D) hybrid modelling method is 1% in "zone 1", and it approaches 14% in "other zones". This error level is not large. e_{ps} is always larger than e_{pv} in each zone, i.e., the PGV from (1D+3D) synthetic fit that from the 1D synthetic better than the PAS. From the viewpoint of theory, the (1D+3D) synthetics lack the high frequencies presented in the 1D

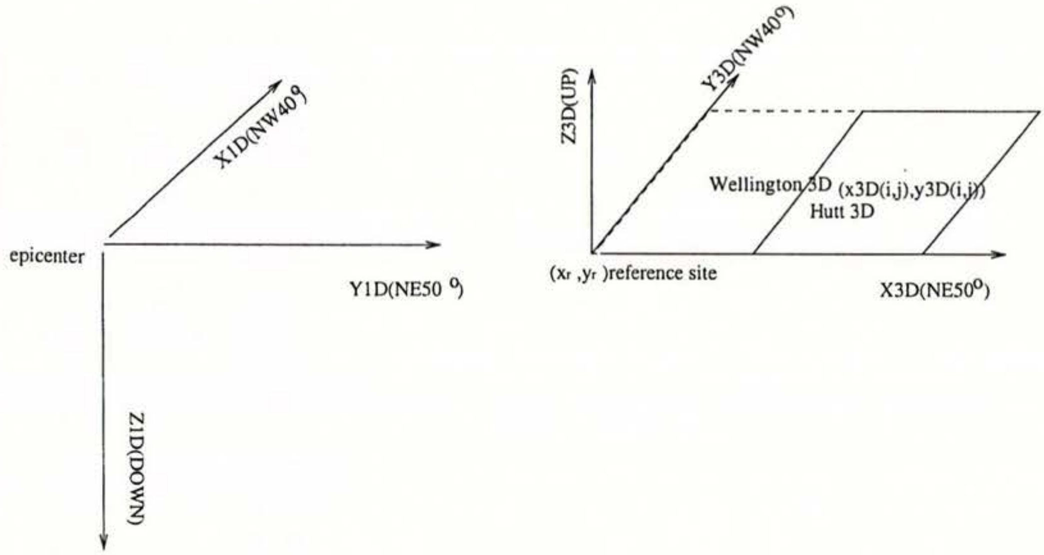

Figure 6.6 *The coordinate systems used in the final 1D and 3D code of (1D+3D) modelling technique*

synthetics due to that it is band limited, hence the (1D+3D) PGV is expected to be always smaller than the corresponding 1D PGV. However, in this (1D+3D) test, the (1D+3D) synthetics are limited in band up to 7.5 Hz, which is far above the maximum frequency (2.5 Hz) under study. So that drawback does not affect the case presented here. The reason that PAS is worse lies in that PGV uses the main waveform, which fits nicely, while PAS includes the artifact due to grid dispersion [Figure 6.5].

6.7 Some further work on the coordinate systems

To this point, the 1D/3D and 1D/(1D+3D) tests were performed in the coordinate systems of the original 1D code and 3D code. However, the true Hutt Valley 3D model strikes $NE50°$, so in the final 1D code, a coordinate system of x_{1D}=$NW40°$, y_{1D}=$NE50°$ and z_{1D}=positive down is used, and in the final 3D code, a coordinate system of x_{3D}=$NE50°$, y_{3D}=$NW40°$ and z_{3D}=positive up is used. For each earthquake, the epicenter is the origin of the final 1D coordinate system [Figure 6.6]. The start point of Wellington 3D shaking hazard model is the origin of the final 3D coordinate system [Figure 6.6]. It is point (x_r, y_r, z_r) and is called the reference site.

The coordinate of each (i,j) grid point in the 3D model Hutt Valley bottom used in the 1D code are:

$$
\begin{aligned}
x_{1D}(i,j) &= y_{3D}(i,j) + x_r \\
y_{1D}(i,j) &= x_{3D}(i,j) + y_r \\
z_{1D} &= -z_{3D}(i,j) + z_r
\end{aligned}
\tag{6.17}
$$

where (x_{3D}(i,j), y_{3D}(i,j), $z_{3D}(i,j)$) are the coordinate of the (i,j) grid point in the 3D Hutt Valley model coordinate system, (x_r, y_r, z_r) is the origin of the eventual 3D coordinate system. (x_r, y_r, z_r) are calculated by the following formula:

$$
\begin{aligned}
x_r &= rcos\theta_1 \\
y_r &= rsin\theta_1 \\
z_r &= 0
\end{aligned}
\tag{6.18}
$$

where r is the distance between the reference site and the epicenter, and θ_1 is the "azimuth" of the reference site in the eventual 1D coordinate system. $z_r = 0$ means that both the origins of the eventual 3D coordinate system and the origin of the eventual 1D coordinate system are located at the free surface. The "azimuth" here is the azimuth angle to $NW40°$, not to the real north. Moreover, the fault "azimuth" θ_1 (relative to $NW40°$) in the eventual 1D coordinate system is related with the real fault azimuth θ_0 (relative to north) by $\theta_1 = \theta_0 + 40°$.

Correspondingly, in the eventual 3D code, for the purpose of comparing with the real data from the portable deployment later in Chapter 7, I get the EW component, NS component and vertical component ground motion by rotating back:

$$
\begin{aligned}
v_E &= v_x cos(\theta_2) - v_y sin(\theta_2) \\
v_N &= v_x sin(\theta_2) + v_y cos(\theta_2) \\
v_U &= v_z
\end{aligned}
\tag{6.19}
$$

where $\theta_2 = 40°$, which is the angle between x axis in the eventual 3D code and east direction.

CHAPTER 7

(1D+3D) MODELLING RESULT AND ANALYSIS

In this Chapter, I simulate the (1D+3D) synthetics at the recorded sites in the Lower Hutt deployment by the technique developed in Chapter 6. I compare the data, 1D synthetics and (1D+3D) synthetics. I calculate the corresponding 1D calibration ratios to calibrate the PVR and peak Fourier spectral ratio (PSR) from the local 1D models, and also calculate the corresponding (1D+3D) ratios to calibrate the PVR and PSR from the Hutt 3D shaking hazard model.

7.1 Application of the (1D+3D) code

In the (1D+3D) forward modelling, both the 1D velocity model (a new one, partly different from Robinson (1986) Wellington velocity model; see below Table 7.1) and the Hutt 3D shaking hazard model are involved.

The new 1D velocity model used in the first step of calculating the (1D+3D) synthetics [Table 7.1] is formed by replacing the layers in the top 10 km of the Robinson (1986) velocity model [Table 4.2] with the elastic parameters of the bottom layer in the Wellington 3D shaking hazard model [Table 2.1]. As discussed above (Page 62), the velocity is unrealistically low in the models used in Chapter 5 and this Chapter in the lower 9 km. This causes arrival times mismatch, which is one reason we

Table 7.1

The 1D velocity model used in the first step of calculating the (1D+3D) synthetics

Parameter	Layer 1	Layer 2	Layer 3	Layer 4	Layer 5	Layer 6
Layer thickness(km)	10	5.0	10.0	10.0	10.0	∞
v_p(km/s)	2.6	5.77	6.39	6.79	8.07	8.77
v_s(km/s)	1.5	3.49	3.50	3.92	4.80	4.86
$\rho(g/cm^3)$	2.7	2.69	2.76	2.93	3.39	3.35

Table 7.2

(1D+3D) modelling parameters used in this study. n_c is the number of time steps chopped off before P wave arrives in the interface source wavefield.

parameter	value
Spatial discretization (m)	40
Temporal discretization in the 1_{st} step of (1D+3D) modelling (Δt s)	0.2
Temporal discretization in the 2_{nd} step of (1D+3D) modelling (s)	0.0034
linear interpolation factor from the 1_{st} step to the 2_{nd} step (n)	58
v_{pmin} in the 3D section (km/s)	0.30
v_{smin} in the 3D section (km/s)	0.175
ρ_{min} in the 3D section (g/cm^3)	1.75
v_{pmax} in the 3D section (km/s)	2.60
v_{smax} in the 3D section (km/s)	1.5
ρ_{max} in the 3D section (g/cm^3)	2.7
Number of grid points along azimuth 50°	303
Number of grid points along azimuth 320°	249
Number of grid points along vertical	240
Number of grid points padded with attenuative material along each artificial edge	25
Number of time steps in the 1_{st} step of (1D+3D) modelling	256
Number of time steps in the 2_{nd} step of (1D+3D) modelling	14819-n_c
Simulation time (s)	51.2-$\frac{n_c \Delta t}{n}$
Temporal discretization output from the 2_{nd} step (s)	0.2

align the traces by their *S* arrivals,.

The parameters used in the (1D+3D) modelling are shown in Table 7.2.

The (1D+3D) synthetics of four earthquakes were calculated by the (1D+3D) modelling technique developed in Chapter 6. They are event 2, 3, 4 and 6 in Table 4.3 respectively. The magnitudes are $M_L = 4.5$, $M_L = 4.0$, $M_L = 3.2$ and $M_L = 3.6$, respectively. The distances from site L14 are 64 km, 56 km, 23 km and 25 km respectively. The focal depths are 58.9 km, 16.1 km, 33.0 km and 59.9 km respectively. The focal mechanisms are predominantly normal faulting, thrust faulting, normal faulting and strike slip respectively. Among the 24 stations in the portable deployment, 23 stations recorded at least one of these four earthquakes. The 23 stations have sampled all the types of soil and covered Hutt Valley well. Only one station (site L24) missed all four events.

The 1D code calculates seismograms of 51.2 s length, up to 2.5 Hz at each 40 m grid point at Hutt Valley bottom. Both stress and velocity seismograms are calculated, then they are input into the 3D code as the incident wavefield. The synthetic seismic wavefield propagates grid by grid through the equation of motion in the 3D code and eventually approaches the free surface of the 3D model. The data and the 1D synthetic all are decimated to a time interval of 0.2 s and filtered to 2.5 Hz to be

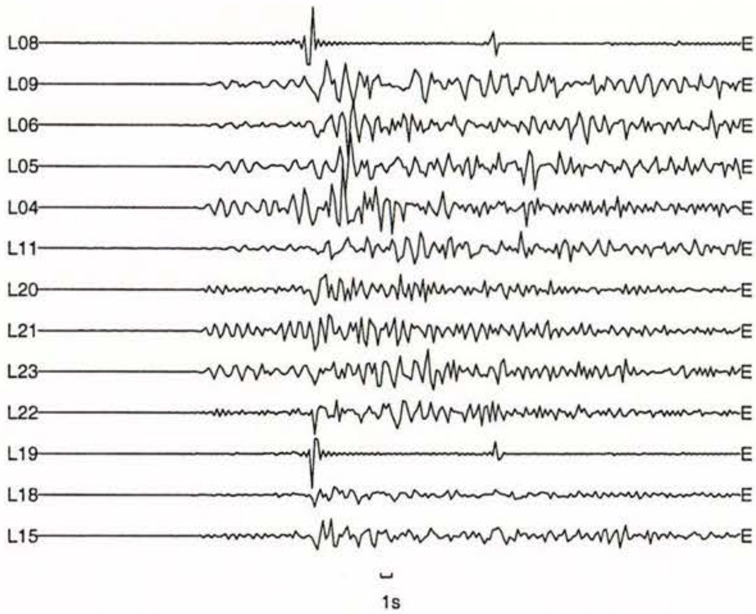

Figure 7.1 *(1D+3D) synthetic seismograms of event 6 in Table 4.3 (east component), displayed approximately across the NW40° valley profile. Each trace is normalized by the maximum peak amplitude of the strongest trace (L04 in this case).*

comparable to the (1D+3D) synthetics.

Figures 7.1, 7.2 and 7.3 show that the peak amplitude of (1D+3D) synthetic ground motions on sediment sites (e.g., L09) are amplified heavily compared to those on rock sites (e.g., L19); moreover, the ground motion on sediment sites last much longer compared to those on rock sites. As expected, the *P* wave ground motion is stronger in the vertical component than in the horizontal components. Note the ringy, beating vertical signal at L18 [Figure 7.3], which was located at Naenae basin. Naenae is a very low velocity hole surrounded by rock. Perhaps this strange signal is created by the resonance of Naenae basin, whose resonant frequency is 2.5 Hz by the *quarter-wavelength rule* [equation (5.21)], and the sediment depth is 0.06 km there.

From Figures 7.4, 7.5 and 7.6 we find the (1D+3D) synthetic waveform appears to simulate the data waveform better than the 1D synthetic waveform in all the sediment sites (e.g., L09). The (1D+3D) modelled synthetics on the sediment sites (site L05, L06, L09, L11, L18) match the durations in the data better and may exhibit some of the later arrivals. Therefore it appears that the 3D Hutt Valley velocity model can simulate the real ground motion more closely than the 1D model. This may be because it accommodates the heterogeneity structure of Hutt Valley and it can synthesize the effects of focusing and scattering of waves in a geologically complex region. However, some of the

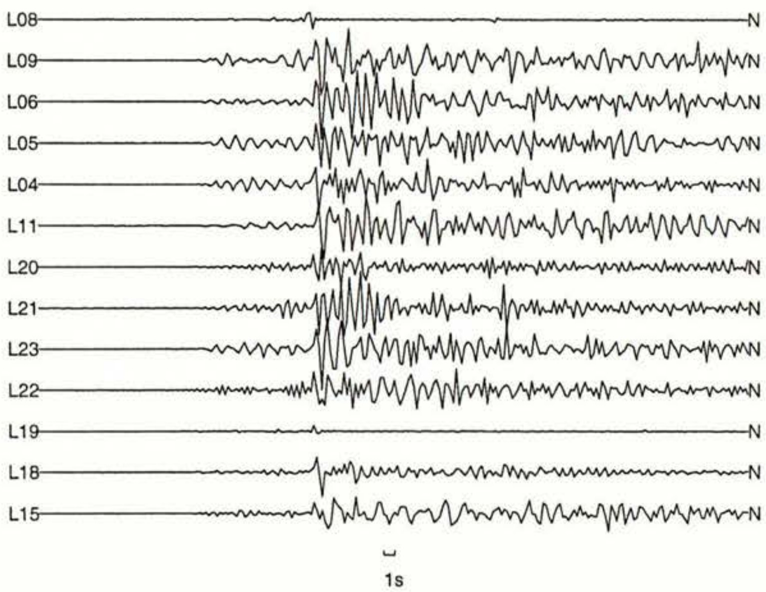

Figure 7.2 *(1D+3D) synthetic seismograms of event 6 in Table 4.3 (north component), displayed approximately across the NW40° valley profile. Each trace is normalized by the the maximum peak amplitude of the strongest trace (L21 in this case).*

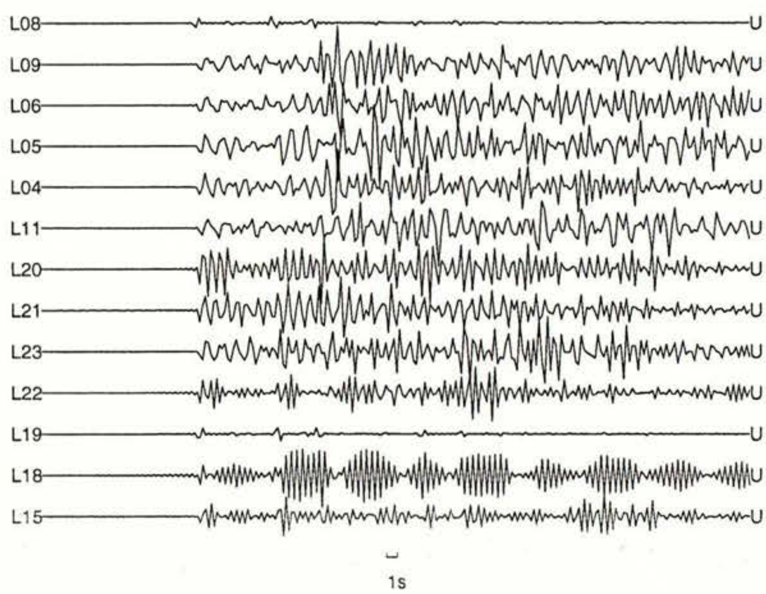

Figure 7.3 *(1D+3D) synthetic seismograms of event 6 in Table 4.3 (vertical component), displayed approximately across the NW40° valley profile. Each trace is normalized by the the maximum peak amplitude of the strongest trace (L09 in this case).*

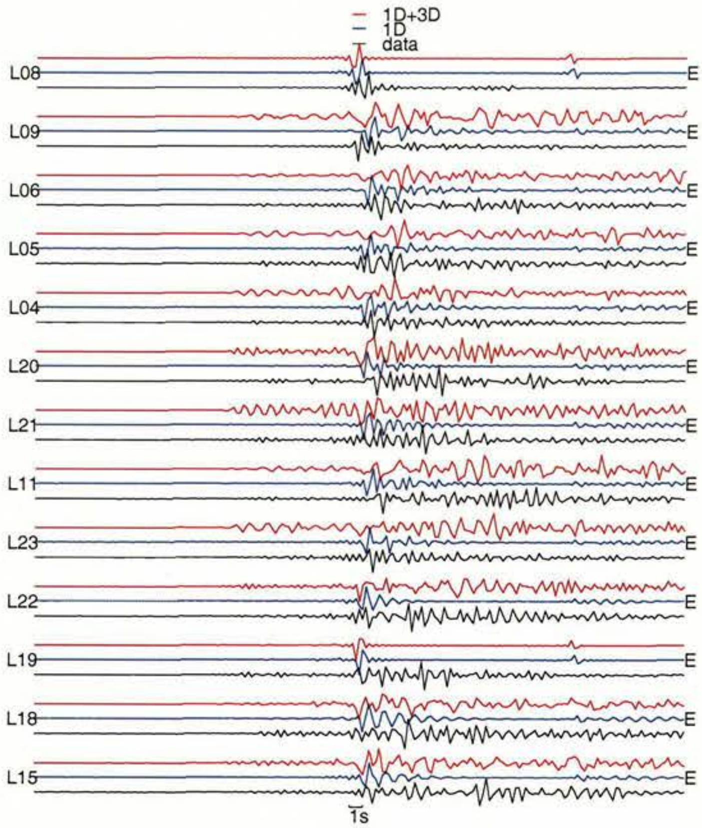

Figure 7.4 *Comparison of the data (black), 1D synthetic (blue) and (1D+3D) synthetic (red) seismograms of event 6 in Table 4.3 (east component), displayed approximately across the NW40° valley profile. Each trace is normalized by the maximum amplitude of itself. All the traces are aligned by S arrival time.*

later arrivals might be caused by the spurious noise generated by the (1D+3D) modelling technique itself [Figure 6.5 (a) and (d)].

The spectra of the data, 1D synthetics and (1D+3D) synthetics are obtained in the same way as illustrated on Page 66. Here a 12.8 s window, starting 0.5 s before the *S* wave arrival was selected from each component. The data and 1D synthetics all are redecimated so that the time interval in their time series are in accordance to that in the (1D+3D) time series.

Figure 7.7 presents the (1D+3D) synthetic spectra of event 6 in Table 4.3. It demonstrates that for each component, the spectrum amplitude at each of the sediment sites is much larger than that on rock sites.

Figure 7.8 presents the (1D+3D) synthetic seismogram and (1D+3D) synthetic spectra of event 6 in Table 4.3 at site L20, which was located on sediment near the center of the Lower Hutt 3D model. Figure 7.9 presents the (1D+3D) synthetic seismogram and (1D+3D) synthetic spectra of the

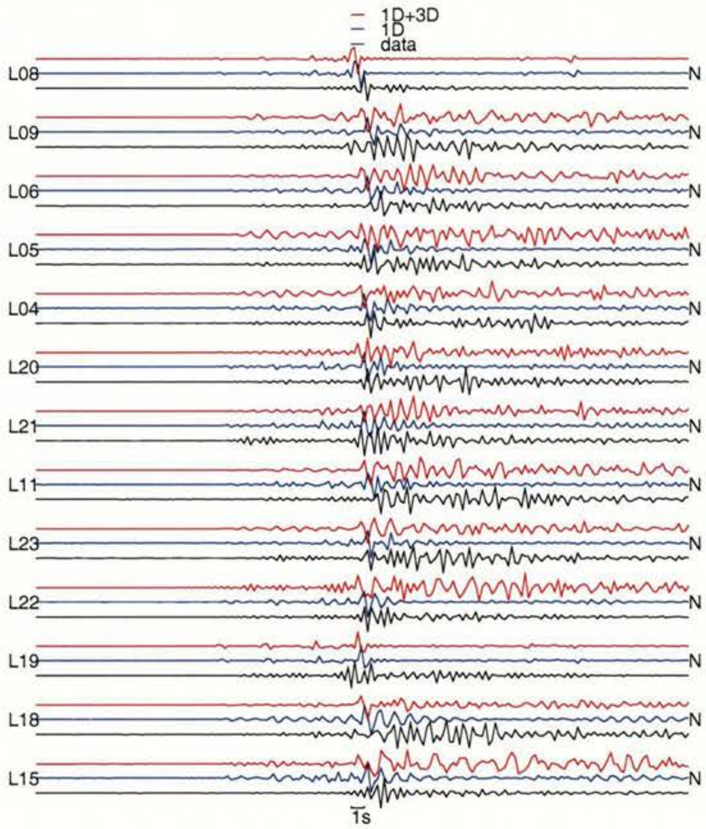

Figure 7.5 *Comparison of the data, 1D synthetic and (1D+3D) synthetic seismograms of event 6 in Table 4.3 (north component), displayed approximately across the NW40° valley profile. Each trace is normalized by the maximum amplitude of itself. All the traces are aligned by S arrival time.*

same event at site L19, which was located on rock in Naenae. At sediment sites, (1D+3D) modelling works better than 1D modelling in simulating the recorded waveform and duration time; there are more frequency contents in the (1D+3D) modelled spectrogram than the 1D modelled spectrogram. However, the noise introduced by (1D+3D) modelling technique itself may affect the waveform and spectrogram of the (1D+3D) synthetic at sediment sites [Section 6.5]. At the rock sites, (1D+3D) modelling does not work better than 1D modelling in simulating the recorded time domain waveform and duration time, or the recorded spectrogram; i.e., (1D+3D) modelling and 1D modelling are almost identical. Because the *interface source* is directly imposed at the free surface at bedrock, the (1D+3D) synthetic and the corresponding 1D synthetic are identical at the rock sites.

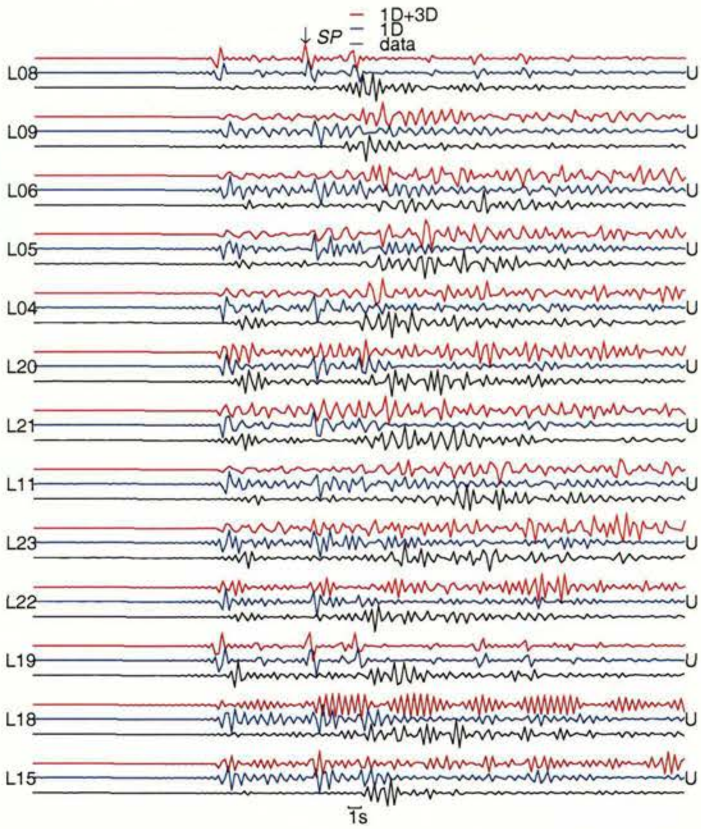

Figure 7.6 *Comparison of the data, 1D synthetic and (1D+3D) synthetic seismograms of event 6 in Table 4.3 (vertical component), displayed approximately across the NW40° valley profile. Each trace is normalized by the maximum amplitude of itself. All the traces are aligned by S arrival time. The arrow labeled with SP denotes the arrival time of S-P conversion from the interface between the bottom layer of the Hutt 3D shaking hazard model [Table 7.2] and the 2nd top layer of the 1D model [Table 7.1].*

7.2 Analysis of frequency dependent amplification

FSRs are calculated for the data, 1D synthetics and (1D+3D) synthetics. Compared to the previous FSRs in Chapter 5, the FSRs now are calculated up to lower frequency (2.5 Hz) cutoffs since the (1D+3D) synthetics are also only up to 2.5 Hz, limited by the resolution of the Hutt 3D model.

Figure 7.10 depicts the amplification by data, 1D synthetics and (1D+3D) synthetics in four sites representing all the different zones [Figure 3.3]. L03 is a "firm site" in the Hutt 3D model, yet amplification was still observed in the recorded data. L02 is located in zone 2; at frequencies greater than 1Hz, ground motion amplification from (1D+3D) modelling overestimates that from observed data and that from 1D modelling. L12 is located in zone 3-4; both synthetics underestimate ground motions. L09 is located in zone 5; ground motion amplification from (1D+3D) modelling is closer to

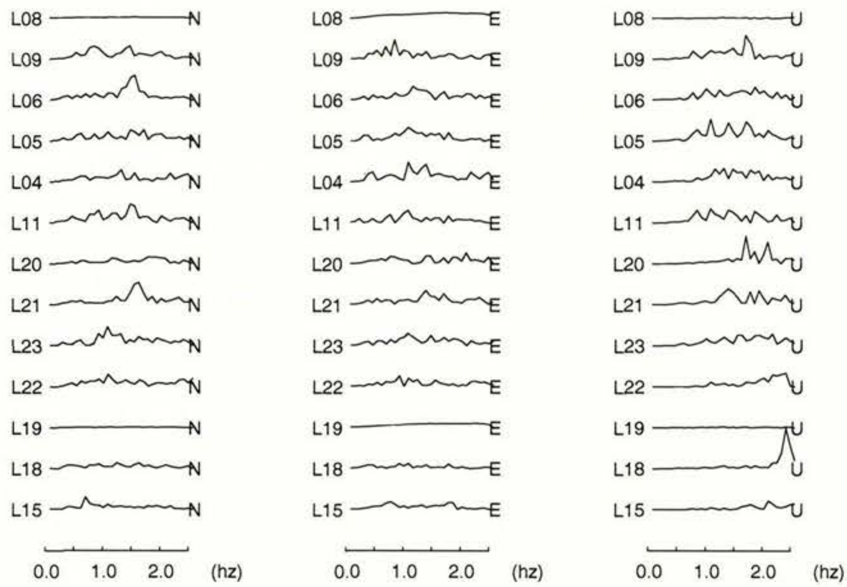

Figure 7.7 *(1D+3D) synthetic spectra of event 6 in Table 4.3, displayed approximately across the NW40° valley profile. Each trace is normalized by the maximum peak amplitude of the strongest trace. The strongest trace among all stations and all the three components is the vertical component of L18.*

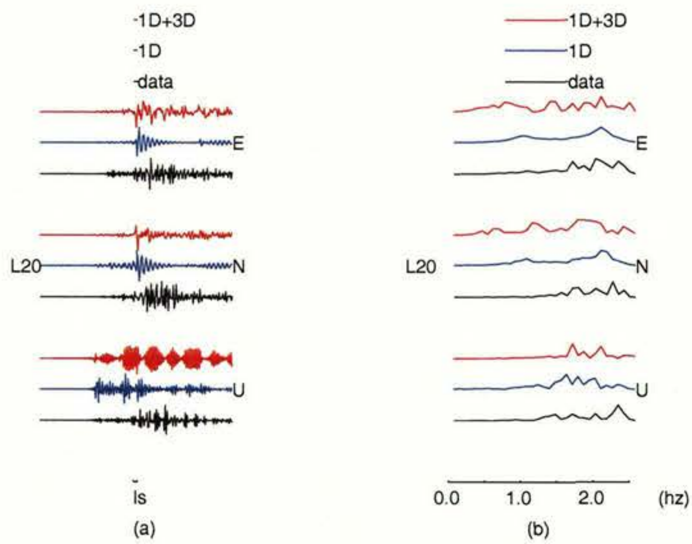

Figure 7.8 *Comparison of the data, 1D synthetic and (1D+3D) synthetic in both time domain and frequency domain of event 6 in Table 4.3 (L20, sediment site).*

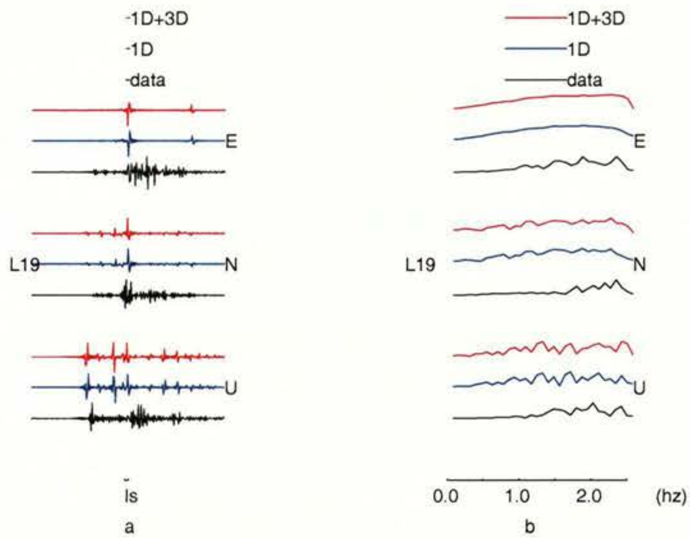

Figure 7.9 *Comparison of the data, 1D synthetic and (1D+3D) synthetic in both time domain and frequency domain of event 6 in Table 4.3 (L19, rock site).*

that from observed data than that from 1D modelling for both dip slip events and strike slip events; the ground motion amplification from (1D+3D) synthetics for the strike slip events matches that from the data well. Note that the (1D+3D) synthetics at sediment sites amplify ground motion much more than the 1D synthetics. This may be due to the fact that 1D layered velocity model can simulate amplification from the impedance contrast, multiple-bounces between the top and bottom of the soft layers and *P-S* conversion [Section 5.5.1]; whereas 3D gridded model can simulate more: it can simulate the amplification from *basin edge effect*, *wedge effect*, *Airy phase edge effect* and scattering generated by the lateral inhomogeneity [Section 1.1]. Unfortunately, the noise added to the synthetics in the procedure of using the (1D+3D) method [Figure 6.5] could also be affecting this process, so we can not make a firm conclusion this time. The results from all the other sites can be found in Appendix D.

The FSRs of the data, 1D synthetics and the (1D+3D) synthetics is shown in Figure 7.11. For three stations for dip slip events, the (1D+3D) synthetics amplify ground motion more than the 1D synthetics do on the basin edge sites, whereas the (1D+3D) synthetics do not amplify ground motion much more than the 1D synthetics do on the other sites. This suggests that the (1D+3D) synthetics may indeed be reproducing the *basin edge effect* [Section 1.1] successfully. For the one strike slip event, the (1D+3D) synthetics amplify ground motion much more than the 1D synthetics do, particularly in basin edge sites (L09, L06, L05 and L04). Figure 7.12 depicts the resonant frequencies from

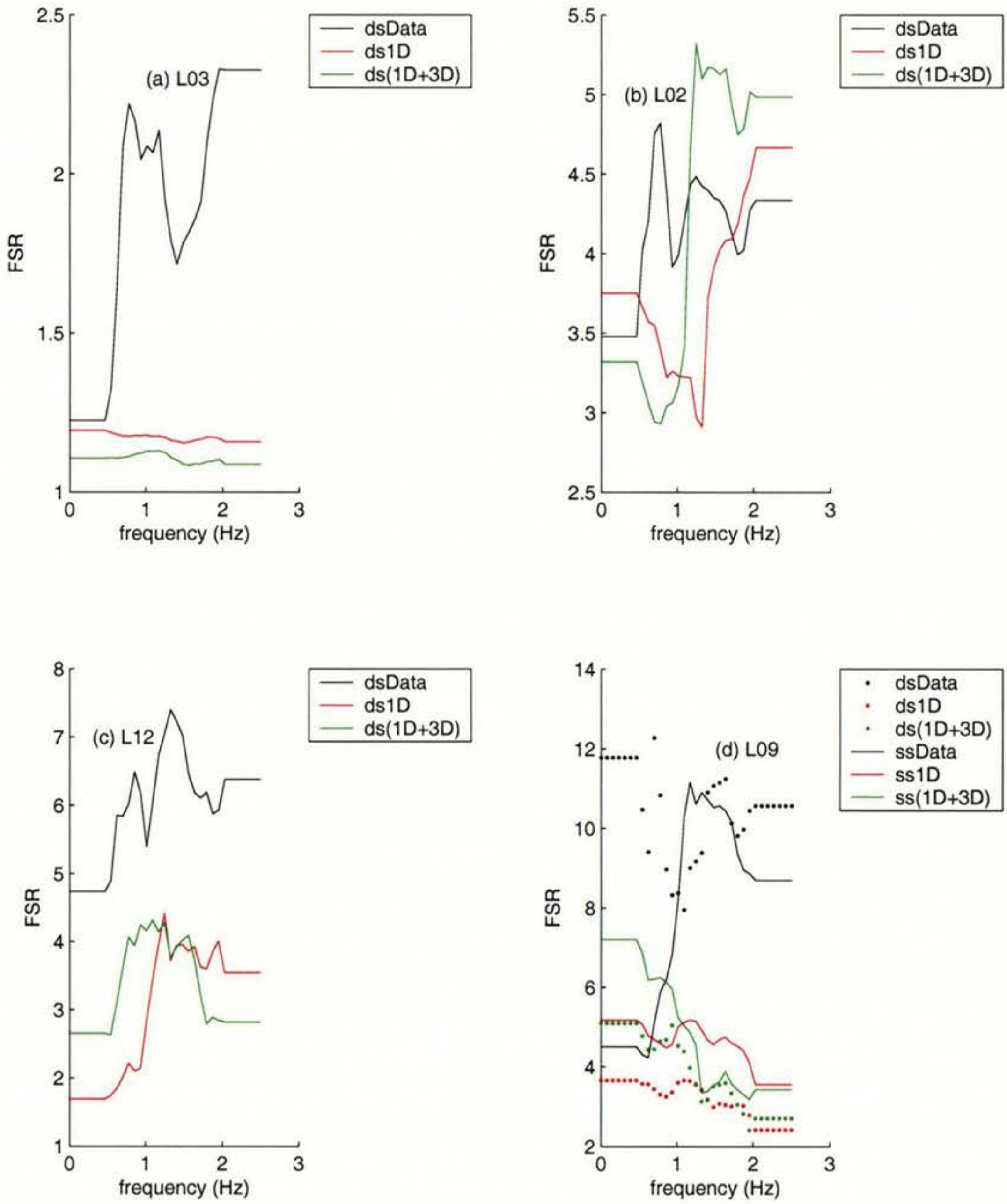

Figure 7.10 *Comparison of FSRs among data, 1D synthetics and (1D+3D) synthetics at L03 (zone 1) for event 4, L02 (zone 2) for the average of event 2, 3 and 4, L12 (zone 3-4) for the average of event 2 and 3 and L09 site (zone 5) for event 2 and event 6 in Table 7.5. The smoothed spectrum of each site is divided by the corresponding smoothed spectrum of reference site L14 respectively. "ds" represents the FSR average of all the dip slip events (event 2, 3 and 4) recorded by each site. "ss" represents the FSR of event 6 recorded by each site, which is a strike slip faulting. L09 recorded two events among the four, the FSR of event 2 is shown in dotted lines (dip slip event). The FSR of event 6 is shown in solid lines (strike slip event).*

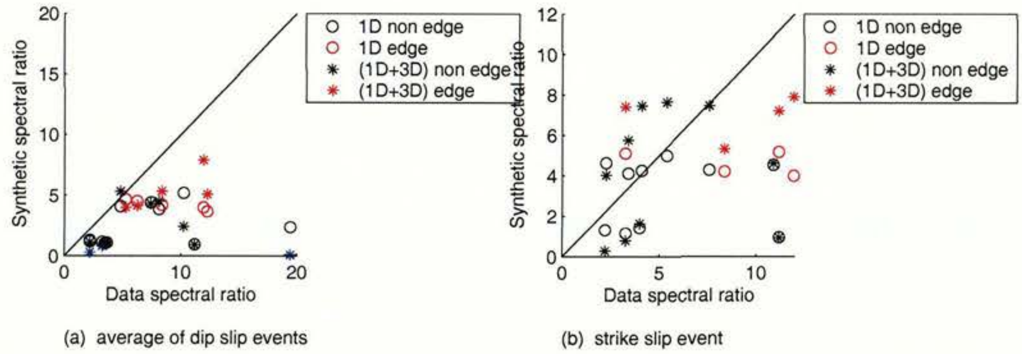

Figure 7.11 *The relationship among the peak FSRs of the data, the 1D synthetics and the (1D+3D) synthetics. A line of y=x is drawn to separate synthetic FSRs that are above or below the data. The red symbols represent the basin edge sites. Generally, the ground motion from (1D+3D) modelling is amplified much more than that from 1D modelling for the sites on the basin edge. The sites with abnormally low (1D+3D) synthetic FSRs are L01, L07 and L17, which fall in the absorbing boundary condition zone (blue symbols) [Figure 2.3]. Only 18 seismographs were in operation in the dip slip events or the strike slip event.*

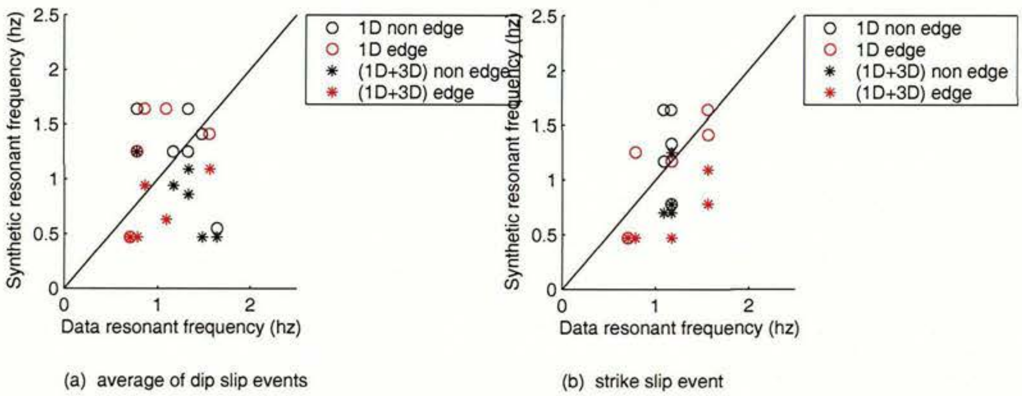

Figure 7.12 *The relationship among the resonant frequencies of the data, the 1D synthetics and the (1D+3D) synthetics. A line of y=x is drawn to separate synthetic resonant frequencies that are above or below the data. The red symbols represent the basin edge sites. The sites falling in zone 1 and absorbing boundary condition area are excluded. Only 18 seismographs were in operation in the dip slip events or the strike slip event.*

the data, 1D synthetics and (1D+3D) synthetics. The resonant frequency from the (1D+3D) synthetics is lower than that from the 1D synthetics. In general, the (1D+3D) synthetics underestimate the observed resonant frequency while the 1D synthetics overestimate the observed resonant frequency.

Figure 7.13 shows the spatial distribution of the maxima of the mean FSRs in the frequency band 0.5-2.0 Hz for all of the data, 1D synthetics and (1D+3D) synthetics. For each site, the average of the maximum mean value of the two horizontal components is plotted at the station location. Plotting the greater of the maxima of the N or E component or simply the maximum of a single component yields essentially the same result. However, for a local earthquake the difference in the response of the north

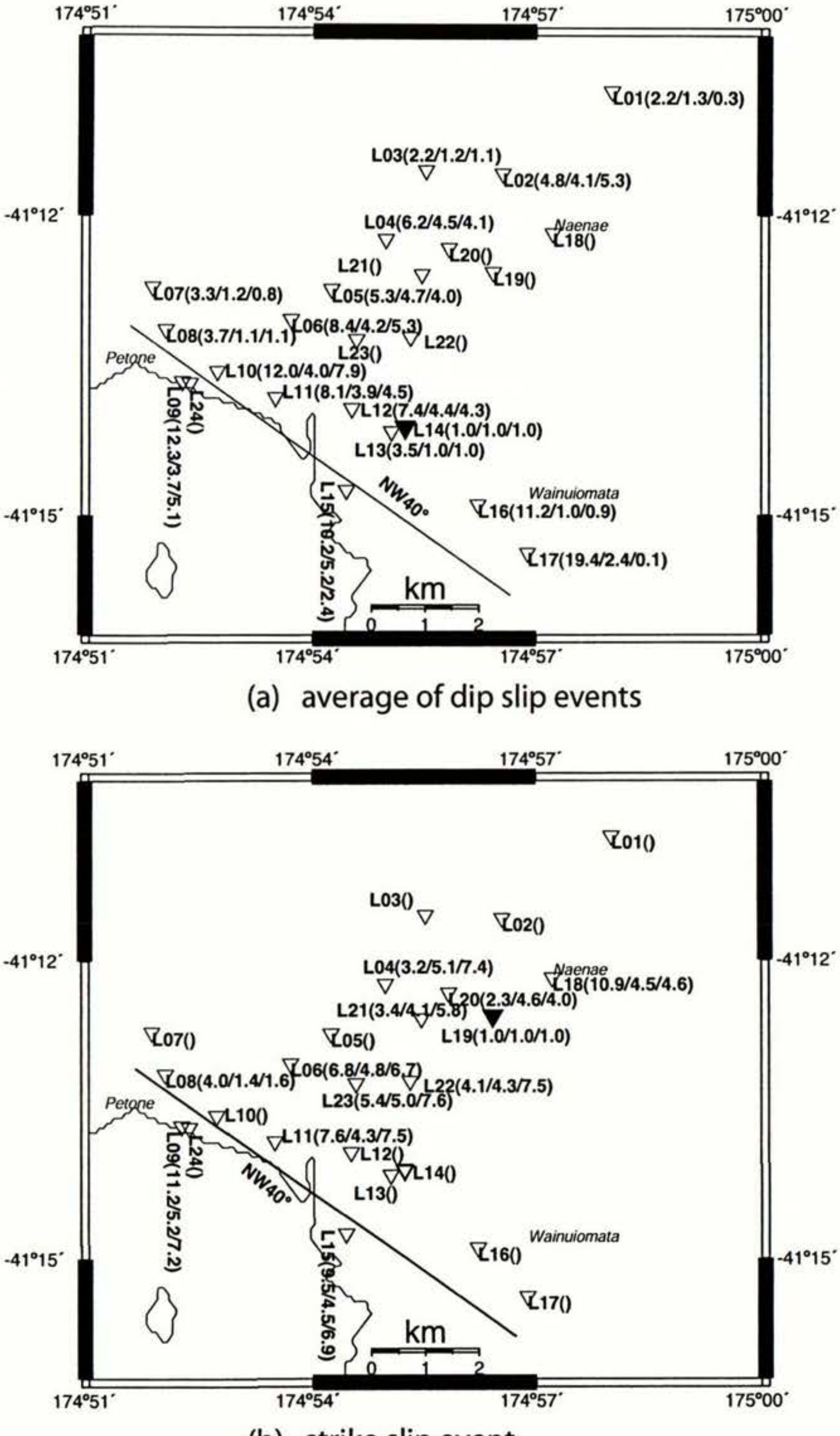

Figure 7.13 *Map of the maximum value of the mean FSR for each site in Hutt Valley (The left value is from the data, the middle is from the 1D synthetic and the right is from the (1D+3D) synthetic). The solid triangle (L14) is the reference site and thus the ratio there is 1.0 by definition. L19 is used as reference site in case L14 failed to record that event. L03, L07, L08 and L19 are the other firm sites. The number plotted is an average of the north and east component. The empty () represents that no value is available due to no observed data available at that site.*

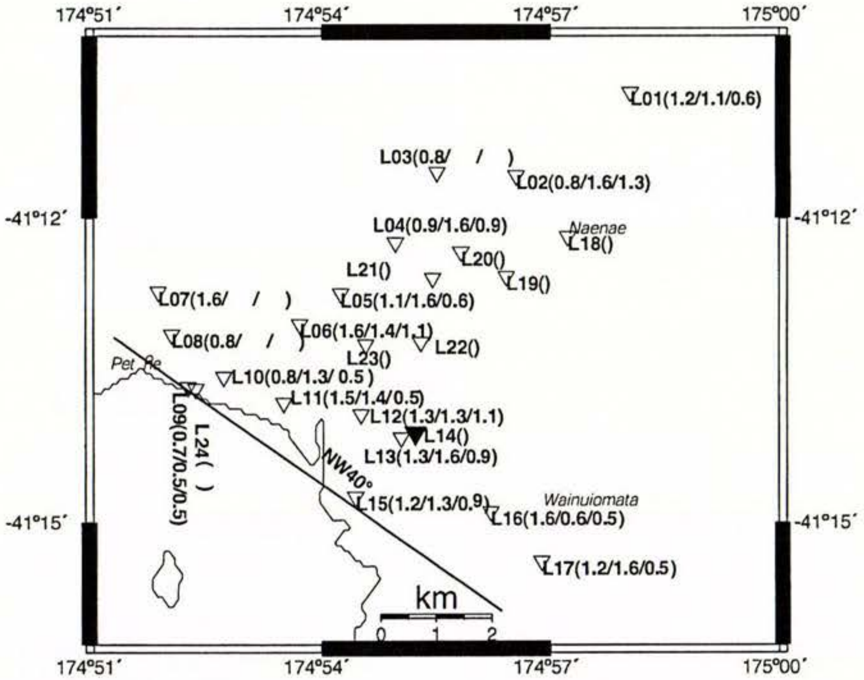

(a) average of dip slip events

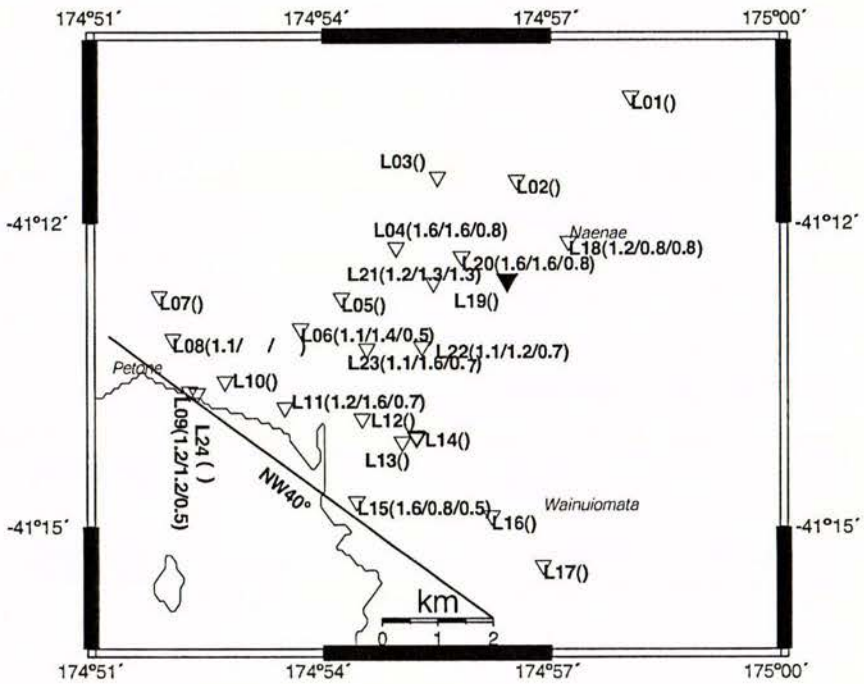

(b) strike slip event

Figure 7.14 *Map of the resonant frequency of the mean FSR for each site in Hutt Valley (The left value is from the data, the middle is from the 1D synthetic and the right is from the (1D+3D) synthetics). The solid triangle (L14) is the reference site. L19 is used as reference site in case L14 failed to record that event. The empty () represents that no values is available due to no observed data available at that site. Note there are no resonant frequencies from the 1D and (1D+3D) synthetics for the stations in zone 1 (L03, L07, L08 and L19).*

and east components can be quite large due to directional effects. The FSR of the reference site (L14 and L19) is defined as 1.0 and is plotted as a solid triangle. Note the increase in amplification over the short distance from L14 to L13 in the data. The figure shows the general increase in FSR from the head of the valley to the foreshore, with higher amplification on the west side of the valley for all of the data, 1D synthetics and (1D+3D) synthetics. This pattern is similar to the variation in sediment thickness in the valley, with the thicker sediments corresponding to the higher amplification (Dellow *et al.*, 1992; Benites and Olsen, 2004). For dip slip events, the highest amplifications were recorded in Wainuiomata valley (L17), but the highest amplification simulated by the local 1D modelling is in Avalon (L15) and that by the (1D+3D) modelling is in Petone (L10). For the one strike slip event, the highest amplifications were recorded in Petone (L09), and the highest amplification simulated by the local 1D modelling is also in Petone (L09) and that by the (1D+3D) modelling is at L06, one of the basin edge sites. Note that L17, L07 and L01 are located in the absorbing boundary condition zone in the 3D Hutt Valley model [Figure 2.3]. This partly answers why the ground motion of (1D+3D) synthetics at L17 is shrunk instead of being amplified compared to that at the rock site (L14). Another factor that accounts for the low amplification in ground motion of 1D and (1D+3D) synthetics for the sites in Wainuiomata valley is that, as discussed in Section 5.7, the actual shear velocity at the top sediment layer there may be as low as 80 m/s (Chávez-García *et al.*, 1999), while in the local 1D models and the Hutt 3D model, it is 175 m/s, a factor of two, too high.

The resonant frequencies of the data, 1D synthetics and the (1D+3D) synthetics are shown in Figure 7.12. Figure 7.14 shows the corresponding spatial distribution of resonant frequency. There is a tendency that (1D+3D) synthetic's resonant frequency is closer to the resonant frequency observed by data compared to the 1D synthetic's for dip slip events [Figure 7.12 (a)].

7.3 Calibration

In this section, I calibrate the local 1D models [Tables 5.1 and 5.2] and the Hutt 3D shaking hazard model by calculating two indices: the average ratio of PVR between data, 1D synthetics and (1D+3D) synthetics, respectively; the average ratio of PSR between data, 1D synthetics and (1D+3D) synthetics, respectively.

1) First, PVR [equations (7.1) and (7.3)] is defined as the ratios of peak partical velocity; PSR [equations (7.4) and (7.6)] is defined as the ratio of peak spectral magnitude. The whole bandwidth

available in the raw spectra is 0.0 Hz to 2.5 Hz, but only 0.5 Hz to 2.0 Hz is valid considering that the smoothed spectra are used in FSR calculation [Figure 7.10]. So the PSR falling beyond 0.5 Hz to 2.0 Hz is not meaningful and excluded.

The recorded data PVR measured at station i for event j is defined as:

$$\begin{aligned} pvrDns(i,j) &= \frac{max(|vDns(i,j,t)|)}{max(|vDns(i0,j,t|)} \\ pvrDew(i,j) &= \frac{max(|vDew(i,j,t)|)}{max(|vDew(i0,j,t|)} \\ pvrDud(i,j) &= \frac{max(|vDud(i,j,t)|)}{max(|vDud(i0,j,t|)} \end{aligned} \tag{7.1}$$

where $vDns(i,j,t)$, $vDew(i,j,t)$ and $vDud(i,j,t)$ are the velocity time history for the NS component, EW component and vertical component respectively and max indicates the maximum value for all time t. || indicate the absolute value. i0 represents the reference rock site (L14 or L19 in the Lower Hutt deployment).

Correspondingly, the 1D synthetic's PVR measured at station i for event j is defined as:

$$\begin{aligned} pvr1ns(i,j) &= \frac{max(|v1ns(i,j,t)|)}{max(|v1ns(i0,j,t|)} \\ pvr1ew(i,j) &= \frac{max(|v1ew(i,j,t)|)}{max(|v1ew(i0,j,t|)} \\ pvr1ud(i,j) &= \frac{max(|v1ud(i,j,t)|)}{max(|v1ud(i0,j,t|)} \end{aligned} \tag{7.2}$$

where $v1ns(i,j,t)$, $v1ew(i,j,t)$ and $v1ud(i,j,t)$ are the velocity time history for the NS component, EW component and vertical component respectively.

Also, the (1D+3D) synthetic's PVR measured at station i for event j is defined as:

$$\begin{aligned} pvr3ns(i,j) &= \frac{max(|v3ns(i,j,t)|)}{max(|v3ns(i0,j,t|)} \\ pvr3ew(i,j) &= \frac{max(|v3ew(i,j,t)|)}{max(|v3ew(i0,j,t|)} \\ pvr3ud(i,j) &= \frac{max(|v3ud(i,j,t)|)}{max(|v3ud(i0,j,t|)} \end{aligned} \tag{7.3}$$

where $v3ns(i,j,t)$, $v3ew(i,j,t)$ and $v3ud(i,j,t)$ are the velocity time history for the NS component, EW component and vertical component respectively.

The PSR for data at station i for event j is defined as:

$$\begin{aligned}
psrDns(i,j) &= max\left[\frac{sDns(i,j,f)}{sDns(i0,j,f)}\right] \\
psrDew(i,j) &= max\left[\frac{sDew(i,j,f)}{sDew(i0,j,f)}\right] \\
psrDud(i,j) &= max\left[\frac{sDud(i,j,f)}{sDud(i0,j,f)}\right]
\end{aligned} \tag{7.4}$$

where $sDns(i,j,f)$, $sDew(i,j,f)$ and $sDud(i,j,f)$ are the FAS of $vDns(i,j,t)$, $vDew(i,j,t)$ and $vDud(i,j,t)$ respectively. And $sDns(i0,j,f)$, $sDew(i0,j,f)$ and $sDud(i0,j,f)$ are the FAS of $vDns(i0,j,t)$, $vDew(i0,j,t)$ and $vDud(i0,j,t)$ respectively, max indicates the maximum value of $\frac{sDns(i,j,f)}{sDns(i0,j,f)}$, $\frac{sDew(i,j,f)}{sDew(i0,j,f)}$ and $\frac{sDud(i,j,f)}{sDud(i0,j,f)}$ for all frequency f.

Correspondingly, the PSR for 1D synthetics at station i for event j is defined as:

$$\begin{aligned}
psr1ns(i,j) &= max\left[\frac{s1ns(i,j,f)}{s1ns(i0,j,f)}\right] \\
psr1ew(i,j) &= max\left[\frac{s1ew(i,j,f)}{s1ew(i0,j,f)}\right] \\
psr1ud(i,j) &= max\left[\frac{s1ud(i,j,f)}{s1ud(i0,j,f)}\right]
\end{aligned} \tag{7.5}$$

where $s1ns(i,j,f)$, $s1ew(i,j,f)$ and $s1ud(i,j,f)$ are the FAS of $v1ns(i,j,t)$, $v1ew(i,j,t)$ and $v1ud(i,j,t)$ respectively, and $s1ns(i0,j,f)$, $s1ew(i0,j,f)$ and $s1ud(i0,j,f)$ are the FAS of $v1ns(i0,j,t)$, $v1ew(i0,j,t)$ and $v1ud(i0,j,t)$ respectively, max indicates the maximum value of $\frac{s1ns(i,j,f)}{s1ns(i0,j,f)}$, $\frac{s1ew(i,j,f)}{s1ew(i0,j,f)}$ and $\frac{s1ud(i,j,f)}{s1ud(i0,j,f)}$ for all frequency f.

Also, the PSR for (1D+3D) synthetics at station i for event j is defined as:

$$\begin{aligned}
psr3ns(i,j) &= max\left[\frac{s3ns(i,j,f)}{s3ns(i0,j,f)}\right] \\
psr3ew(i,j) &= max\left[\frac{s3ew(i,j,f)}{s3ew(i0,j,f)}\right] \\
psr3ud(i,j) &= max\left[\frac{s3ud(i,j,f)}{s3ud(i0,j,f)}\right]
\end{aligned} \tag{7.6}$$

where $s3ns(i,j,f)$, $s3ew(i,j,f)$ and $s3ud(i,j,f)$ are the FAS of $v3ns(i,j,t)$, $v3ew(i,j,t)$ and $v3ud(i,j,t)$

respectively, and $s3ns(i0,j,f)$, $s3ew(i0,j,f)$ and $s3ud(i0,j,f)$ are the FAS of $v3ns(i0,j,t)$, $v3ew(i0,j,t)$ and $v3ud(i0,j,t)$ respectively, max indicates the maximum value of $\frac{s3ns(i,j,f)}{s3ns(i0,j,f)}$, $\frac{s3ew(i,j,f)}{s3ew(i0,j,f)}$ and $\frac{s3ud(i,j,f)}{s3ud(i0,j,f)}$ for all frequency f.

From equations (7.1) and (7.4) we obtained Table 7.3. From equations (7.2) and (7.5) we obtained Table 7.4. From equations (7.3) and (7.6) we obtained Table 7.5.

Tables 7.3, 7.4 and 7.5 demonstrate that in general, the PVR and the PSR are smaller on firm sites and they are bigger on sediment sites for all the recorded data, 1D synthetics and the (1D+3D) synthetics. For the data and (1D+3D) synthetics, the amplifications are caused by the reflections, scattering, interference and resonance of seismic waves in the 3D Hutt Valley; for the 1D synthetics, the amplifications are caused by the reflections, interference and resonance of seismic waves in the local 1D models. It can be found that the 1D synthetic's PVR [Table 7.4] is greater than the (1D+3D) synthetic's PVR [Table 7.5]; however, the 1D synthetic's PSR [Table 7.4] is not greater than the (1D+3D) synthetic's PSR [Table 7.5]. This is from the shaking duration time of the (1D+3D) synthetic being much longer than that of 1D synthetic [Figures 7.4, 7.5 and 7.6].

2) Second, c_{pvr}s (i.e., $cdsns_{pvr}$, $cdsew_{pvr}$, $cdsud_{pvr}$ and $cssns_{pvr}$, $cssew_{pvr}$, $cssud_{pvr}$) are defined based on PVRs (i.e., $pvrDns$, $pvrDew$, $pvrDud$, $pvr1ns$, $pvr1ew$, $pvr1ud$ and $pvr3ns$, $pvr3ew$, $pvr3ud$) for different focal mechanism types; c_{psr}s (i.e., $cdsns_{psr}$, $cdsew_{psr}$, $cdsud_{psr}$ and $cssns_{psr}$, $cssew_{psr}$, $cssud_{psr}$) are defined based on PSRS (i.e., psrDns, psrDew, psrDud, psr1ns, psr1ew, psr1ud and psr3ns, psr3ew, psr3ud) for different focal mechanism types.

$cdsns_{pvr}$, $cdsew_{pvr}$ and $cdsud_{pvr}$ for the local 1D models are defined as equation (7.7):

$$\begin{aligned} cdsns_{pvr} &= \frac{1}{m}\left[\sum_{j=1}^{m}\frac{1}{n}\left(\sum_{i=1}^{n}\frac{pvrDns_{ij}}{pvr1ns_{ij}}\right)\right] \\ cdsew_{pvr} &= \frac{1}{m}\left[\sum_{j=1}^{m}\frac{1}{n}\left(\sum_{i=1}^{n}\frac{pvrDew_{ij}}{pvr1ew_{ij}}\right)\right] \\ cdsud_{pvr} &= \frac{1}{m}\left[\sum_{j=1}^{m}\frac{1}{n}\left(\sum_{i=1}^{n}\frac{pvrDud_{ij}}{pvr1ud_{ij}}\right)\right] \end{aligned} \quad (7.7)$$

and $cdsns_{pvr}$, $cdsew_{pvr}$ and $cdsud_{pvr}$ for the Hutt 3D shaking hazard model are defined as equation

Table 7.3

Maximum ratios of ground motion parameters for the recorded data

Event	comp	L01	L02	L03	L04	L05	L06	L07	L08	L09	L10	L11	L12	L13	**L14**	L15	L16	L17	L18	**L19**	L20	L21	L22	L23	L24*
2	*pvrDns*	-	1.8	-	1.3	-	2.2	1.5	1.8	2.0	1.6	1.6	-	-	1.0	-	2.9	-	-	-	-	-	-	-	-
	pvrDew	-	1.4	-	1.1	-	1.6	0.9	1.0	0.9	1.0	0.9	-	-	1.0	-	1.8	-	-	-	-	-	-	-	-
	pvrDud	-	3.8	-	1.7	-	1.7	2.3	1.6	3.3	1.5	2.4	-	-	1.0	-	1.8	-	-	-	-	-	-	-	-
	psrDns	-	8.5	-	9.2	-	10.8	4.6	5.2	12.3	11.9	12.6	-	-	1.0	-	14.0	-	-	-	-	-	-	-	-
	psrDew	-	1.8	-	2.6	-	3.8	1.0	1.0	4.2	4.3	3.1	-	-	1.0	-	4.6	-	-	-	-	-	-	-	-
	psrDud	-	3.5	-	3.4	-	3.9	1.2	1.9	5.7	4.9	4.3	-	-	1.0	-	3.7	-	-	-	-	-	-	-	-
3	*pvrDns*	1.6	1.3	-	1.3	-	-	0.6	0.9	-	-	0.7	0.8	1.2	1.0	0.7	2.1	2.3	-	-	-	-	-	-	-
	pvrDew	3.2	1.0	-	1.8	-	-	0.8	1.0	-	-	0.9	1.1	1.5	1.0	1.1	2.9	3.9	-	-	-	-	-	-	-
	pvrDud	1.0	0.9	-	1.1	-	-	0.3	0.5	-	-	0.5	0.3	0.5	1.0	0.7	0.7	1.1	-	-	-	-	-	-	-
	psrDns	2.8	3.7	-	7.1	-	-	2.6	3.1	-	-	8.3	7.4	3.5	1.0	10.2	8.5	17.9	-	-	-	-	-	-	-
	psrDew	0.9	2.3	-	2.4	-	-	1.0	1.0	-	-	3.4	2.8	0.8	1.0	4.7	2.8	5.5	-	-	-	-	-	-	-
	psrDud	2.6	4.7	-	4.1	-	-	1.5	2.3	-	-	5.6	4.9	1.4	1.0	4.6	4.7	23.6	-	-	-	-	-	-	-
4	*pvrDns*	0.5	0.5	0.8	0.4	0.4	0.5	-	0.3	-	-	0.7	-	-	1.0	-	1.3	2.1	-	-	-	-	-	-	-
	pvrDew	0.6	0.6	0.6	0.4	0.5	0.6	-	0.3	-	-	0.4	-	-	1.0	-	1.3	0.9	-	-	-	-	-	-	-
	pvrDud	0.5	0.6	0.4	0.3	0.8	1.2	-	0.4	-	-	1.2	-	-	1.0	-	0.8	0.6	-	-	-	-	-	-	-
	psrDns	2.7	4.9	3.0	6.3	7.4	8.8	-	3.8	-	-	10.7	-	-	1.0	-	14.4	31.8	-	-	-	-	-	-	-
	psrDew	1.2	2.2	2.3	3.8	4.6	7.1	-	2.7	-	-	6.0	-	-	1.0	-	8.0	12.7	-	-	-	-	-	-	-
	psrDud	1.4	2.7	2.0	1.9	2.9	3.7	-	1.4	-	-	3.0	-	-	1.0	-	5.5	18.7	-	-	-	-	-	-	-
6	*pvrDns*	-	-	-	1.1	1.8	1.9	-	2.9	2.4	-	2.1	-	-	-	1.8	-	-	1.8	1.0	2.1	1.5	3.5	2.3	-
	pvrDew	-	-	-	0.8	1.4	2.8	-	1.5	1.5	-	1.0	-	-	-	1.7	-	-	1.9	1.0	2.4	1.7	1.7	1.2	-
	pvrDud	-	-	-	2.1	3.3	6.7	-	3.0	6.7	-	4.8	-	-	-	3.8	-	-	1.4	1.0	2.8	1.9	2.2	3.3	-
	psrDns	-	-	-	4.1	8.6	10.2	-	5.8	16.9	-	12.1	-	-	-	14.6	-	-	17.3	1.0	3.1	5.1	6.0	8.1	-
	psrDew	-	-	-	2.4	3.4	4.0	-	3.0	9.4	-	3.3	-	-	-	5.2	-	-	5.8	1.0	1.5	2.3	2.7	3.4	-
	psrDud	-	-	-	2.3	4.8	5.0	-	2.4	7.8	-	3.1	-	-	-	4.9	-	-	6.1	1.0	1.3	4.0	3.6	4.8	-

note: **black station: rock site**, underlined station: other firm sites. - No recorded data. *pvrDns*, *pvrDew*, *pvrDud*: PVR relative to rock site L14 or L19 of ns component, ew component and ud component; *psrDns*, *psrDew*, *psrDud*: PSR relative to rock site L14 or L19 of ns component, ew component and ud component. This table is obtained from equation (7.1) and (7.4). The event number is identical to that in Table 3.2.

Table 7.4

Maximum ratios of ground motion parameters for the 1D synthetic

Event	comp	L01	L02	L03	L04	L05	L06	L07	L08	L09	L10	L11	L12	L13	**L14**	L15	L16	L17	L18	**L19**	L20	L21	L22	L23	L24†
2	*pvr1ns*	-	3.9	-	3.7	-	4.2	1.1	1.2	3.1	3.2	4.1	-	-	1.0	-	1.0	-	-	-	-	-	-	-	-
	pvr1ew	-	2.3	-	4.2	-	3.8	1.2	1.2	3.5	3.3	3.6	-	-	1.0	-	1.0	-	-	-	-	-	-	-	-
	pvr1ud	-	4.1	-	3.3	-	3.5	1.1	1.2	3.6	3.9	3.1	-	-	1.0	-	1.1	-	-	-	-	-	-	-	-
	psr1ns	-	4.8	-	4.7	-	4.2	1.0	1.0	3.7	4.0	3.8	-	-	1.0	-	1.0	-	-	-	-	-	-	-	-
	psr1ew	-	4.2	-	5.2	-	4.3	1.2	1.2	4.5	4.5	3.9	-	-	1.0	-	1.0	-	-	-	-	-	-	-	-
	psr1ud	-	3.7	-	3.4	-	3.2	1.0	1.0	3.4	3.3	3.1	-	-	1.0	-	1.0	-	-	-	-	-	-	-	-
3	*pvr1ns*	0.9	4.0	-	2.6	-	-	1.2	1.4	-	-	3.4	2.2	1.2	1.0	3.3	0.8	1.8	-	-	-	-	-	-	-
	pvr1ew	0.8	2.5	-	3.6	-	-	1.2	1.2	-	-	4.9	4.1	1.2	1.0	3.4	1.1	2.4	-	-	-	-	-	-	-
	pvr1ud	1.1	3.3	-	2.9	-	-	1.3	1.2	-	-	3.1	3.0	1.0	1.0	4.0	1.0	2.0	-	-	-	-	-	-	-
	psr1ns	1.4	3.6	-	4.3	-	-	1.3	1.2	-	-	4.0	4.4	1.0	1.0	5.2	1.0	2.5	-	-	-	-	-	-	-
	psr1ew	0.9	3.0	-	4.3	-	-	1.0	1.0	-	-	3.6	4.3	1.1	1.0	5.2	1.1	2.2	-	-	-	-	-	-	-
	psr1ud	1.4	5.9	-	4.1	-	-	1.3	1.2	-	-	4.6	4.3	1.0	1.0	5.5	1.1	2.7	-	-	-	-	-	-	-
4	*pvr1ns*	1.6	4.1	1.4	4.0	3.6	4.7	-	1.3	-	-	3.8	-	-	1.0	-	0.8	1.4	-	-	-	-	-	-	-
	pvr1ew	1.3	3.7	1.2	3.5	3.3	4.2	-	1.0	-	-	3.9	-	-	1.0	-	1.0	2.0	-	-	-	-	-	-	-
	pvr1ud	1.2	2.8	1.4	3.8	3.5	3.7	-	1.3	-	-	3.1	-	-	1.0	-	0.8	2.0	-	-	-	-	-	-	-
	psr1ns	1.4	5.0	1.3	5.2	5.1	4.5	-	1.2	-	-	4.0	-	-	1.0	-	0.9	2.2	-	-	-	-	-	-	-
	psr1ew	1.2	4.0	1.1	4.2	4.2	3.9	-	0.9	-	-	3.7	-	-	1.0	-	1.0	2.7	-	-	-	-	-	-	-
	psr1ud	1.4	4.4	1.3	4.2	3.4	3.9	-	1.2	-	-	3.5	-	-	1.0	-	0.9	3.4	-	-	-	-	-	-	-
6	*pvr1ns*	-	-	-	3.4	4.2	3.9	-	1.2	3.6	-	3.2	-	-	-	2.2	-	-	2.2	1.0	3.1	2.6	2.7	3.8	-
	pvr1ew	-	-	-	3.1	3.6	3.4	-	1.1	3.2	-	3.4	-	-	-	3.3	-	-	2.3	1.0	3.6	2.7	3.2	3.7	-
	pvr1ud	-	-	-	2.9	3.3	2.7	-	1.1	3.7	-	2.8	-	-	-	4.0	-	-	4.3	1.0	3.7	2.5	3.5	2.9	-
	psr1ns	-	-	-	5.4	6.1	5.1	-	1.6	5.5	-	4.5	-	-	-	4.1	-	-	4.7	1.0	4.8	4.2	4.2	5.3	-
	psr1ew	-	-	-	4.8	4.9	4.5	-	1.3	4.9	-	4.2	-	-	-	4.8	-	-	4.4	1.0	4.4	4.1	4.3	4.7	-
	psr1ud	-	-	-	2.9	3.0	3.6	-	1.0	3.6.	-	3.3	-	-	-	6.3	-	-	6.0	1.0	4.7	2.7	2.7	2.5	-

note: **black station: rock site**, underlined station: other firm sites. - No 1D synthetic calculated due to no corresponding recording. *pvr1ns*, *pvr1ew*, *pvr1ud*: peak partical velocity ratio relative to rock site L14 or L19 of ns component, ew component and ud component; psr1ns, psr1ew, psr1ud: PSR relative to rock site L14 or L19 of ns component, ew component and ud component. This table is obtained from equation (7.2) and (7.5). The event number is identical to that in Table 3.2.

Table 7.5

Maximum ratios of ground motion parameters for the (1D+3D) synthetic

Event	comp	L01	L02	<u>L03</u>	L04	L05	L06	<u>L07</u>	<u>L08</u>	L09	L10	L11	L12	L13	**L14**	L15	L16	L17	L18	**L19**	L20	L21	L22	L23	L24‡
2	*pvr3ns*	-	2.6	-	1.9	-	2.5	0.6	1.1	1.5	2.8	1.9	-	-	1.0	-	0.8	-	-	-	-	-	-	-	-
	pvr3ew	-	1.1	-	1.9	-	1.8	0.4	0.8	1.0	1.4	0.7	-	-	1.0	-	0.9	-	-	-	-	-	-	-	-
	pvr3ud	-	6.8	-	3.0	-	3.6	0.1	0.9	3.9	2.7	4.4	-	-	1.0	-	0.8	-	-	-	-	-	-	-	-
	psr3ns	-	7.3	-	5.3	-	7.4	0.9	1.2	5.1	7.9	6.6	-	-	1.0	-	0.9	-	-	-	-	-	-	-	-
	psr3ew	-	2.5	-	4.1	-	2.9	0.6	0.9	2.7	3.6	2.0	-	-	1.0	-	1.0	-	-	-	-	-	-	-	-
	psr3ud	-	20.6	-	10.8	-	10.6	0.3	1.0	11.4	9.3	9.7	-	-	1.0	-	1.0	-	-	-	-	-	-	-	-
3	*pvr3ns*	0.2	5.0	-	2.0	-	-	0.6	1.4	-	-	2.8	2.4	1.0	1.0	1.6	0.9	0.0	-	-	-	-	-	-	-
	pvr3ew	0.1	0.9	-	1.5	-	-	0.3	1.2	-	-	1.2	1.4	1.1	1.0	1.3	0.9	0.0	-	-	-	-	-	-	-
	pvr3ud	0.1	9.9	-	5.9	-	-	0.2	1.2	-	-	4.9	6.3	0.9	1.0	3.2	1.3	0.0	-	-	-	-	-	-	-
	psr3ns	0.3	6.7	-	3.4	-	-	0.7	1.3	-	-	4.2	4.3	1.0	1.0	2.4	0.9	0.1	-	-	-	-	-	-	-
	psr3ew	0.3	2.4	-	3.4	-	-	0.6	1.1	-	-	2.7	3.2	1.0	1.0	3.4	1.1	0.1	-	-	-	-	-	-	-
	psr3ud	0.1	14.9	-	5.7	-	-	0.2	1.2	-	-	7.5	7.2	1.0	1.0	5.4	1.1	0.0	-	-	-	-	-	-	-
4	*pvr3ns*	0.2	1.3	1.1	1.5	1.7	1.2	-	0.9	-	-	1.2	-	-	1.0	-	1.0	0.0	-	-	-	-	-	-	-
	pvr3ew	0.2	0.9	1.0	0.8	1.0	0.9	-	0.9	-	-	0.7	-	-	1.0	-	1.1	0.0	-	-	-	-	-	-	-
	pvr3ud	0.1	7.1	1.3	3.6	4.0	4.7	-	1.2	-	-	3.5	-	-	1.0	-	0.9	0.0	-	-	-	-	-	-	-
	psr3ns	0.3	3.2	1.2	4.5	4.2	3.8	-	1.0	-	-	3.2	-	-	1.0	-	0.4	0.1	-	-	-	-	-	-	-
	psr3ew	0.3	1.9	1.1	2.5	3.0	2.9	-	0.9	-	-	2.1	-	-	1.0	-	0.3	0.1	-	-	-	-	-	-	-
	psr3ud	0.1	19.0	1.3	11.9	13.5	13.8	-	1.2	-	-	13.3	-	-	1.0	-	0.5	0.1	-	-	-	-	-	-	-
6	*pvr3ns*	-	-	-	3.6	4.3	4.3	-	1.7	3.5	-	4.4	-	-	-	4.2	-	-	4.5	1.0	4.0	4.5	3.5	3.6	-
	pvr3ew	-	-	-	1.1	0.9	1.0	-	1.1	0.7	-	0.7	-	-	-	0.5	-	-	0.3	1.0	0.5	0.8	0.4	0.8	-
	pvr3ud	-	-	-	5.0	5.5	4.5	-	1.0	5.6	-	5.7	-	-	-	2.9	-	-	5.0	1.0	4.9	5.0	4.1	5.3	-
	psr3ns	-	-	-	11.7	16.1	11.2	-	2.1	12.4	-	13.1	-	-	-	12.4	-	-	8.4	1.0	7.3	9.7	13.3	13.2	-
	psr3ew	-	-	-	3.1	2.4	3.0	-	1.2	2.1	-	2.2	-	-	-	1.4	-	-	1.1	1.0	1.1	1.8	1.7	2.1	-
	psr3ud	-	-	-	11.4	12.8	10.1	-	1.0	11.9	-	12.1	-	-	-	5.7	-	-	2.9	1.0	11.5	11.0	5.4	8.8	-

note: **black station: rock site**, <u>underlined station: other firm sites</u>. - No (1D+3D) synthetic calculated due to no corresponding recording. *pvr3ns*, *pvr3ew*, *pvr3ud*: PVR relative to rock site L14 or L19 of ns component, ew component and ud component; psr3ns, psr3ew, psr3ud: PSR relative to rock site L14 or L19 of ns component, ew component and ud component. This table is obtained from equation (7.3) and (7.6). The event number is identical to that in Table 3.2. Note the ratios at L01, L07 and L17 are abnormally small since these three stations are located in the absorbing boundary condition zones [Figure 2.3].

(7.8):

$$\begin{aligned}
cdsns_{pvr} &= \frac{1}{m}\left[\sum_{j=1}^{m}\frac{1}{n}\left(\sum_{i=1}^{n}\frac{pvrDns_{ij}}{pvr3ns_{ij}}\right)\right] \\
cdsew_{pvr} &= \frac{1}{m}\left[\sum_{j=1}^{m}\frac{1}{n}\left(\sum_{i=1}^{n}\frac{pvrDew_{ij}}{pvr3ew_{ij}}\right)\right] \\
cdsud_{pvr} &= \frac{1}{m}\left[\sum_{j=1}^{m}\frac{1}{n}\left(\sum_{i=1}^{n}\frac{pvrDud_{ij}}{pvr3ud_{ij}}\right)\right]
\end{aligned} \tag{7.8}$$

In equations (7.7) and (7.8), $pvrDns_{ij}$, $pvr1ns_{ij}$ and $pvr3ns_{ij}$ are the PVR of observed data, 1D synthetics and (1D+3D) synthetics, respectively for the NS component at ith station, jth dip slip event, and n is the total number of stations that recorded the event in each corresponding area in Table 7.7, m is the total number of events recorded. $pvrDew_{ij}$, $pvr1ew_{ij}$ and $pvr3ew_{ij}$ are for the corresponding EW component, and $pvrDud_{ij}$, $pvr1ud_{ij}$ and $pvr3ud_{ij}$ are for the corresponding vertical component. $cdsns_{pvr}$, $cdsew_{pvr}$ and $cdsud_{pvr}$ are the PGV calibration coefficients for dip slip event in NS component, EW component and vertical component respectively.

and $cdsns_{psr}$, $cdsew_{psr}$ and $cdsud_{psr}$ for the local 1D models are defined as equation (7.9):

$$\begin{aligned}
cdsns_{psr} &= \frac{1}{m}\left[\sum_{j=1}^{m}\frac{1}{n}\left(\sum_{i=1}^{n}\frac{psrDns_{ij}}{psr1ns_{ij}}\right)\right] \\
cdsew_{psr} &= \frac{1}{m}\left[\sum_{j=1}^{m}\frac{1}{n}\left(\sum_{i=1}^{n}\frac{psrDew_{ij}}{psr1ew_{ij}}\right)\right] \\
cdsud_{psr} &= \frac{1}{m}\left[\sum_{j=1}^{m}\frac{1}{n}\left(\sum_{i=1}^{n}\frac{psrDud_{ij}}{psr1ud_{ij}}\right)\right]
\end{aligned} \tag{7.9}$$

and $cdsns_{psr}$, $cdsew_{psr}$ and $cdsud_{psr}$ for the Hutt 3D shaking hazard model are defined as equation (7.10):

$$\begin{aligned}
cdsns_{psr} &= \frac{1}{m}\left[\sum_{j=1}^{m}\frac{1}{n}\left(\sum_{i=1}^{n}\frac{psrDns_{ij}}{psr3ns_{ij}}\right)\right] \\
cdsew_{psr} &= \frac{1}{m}\left[\sum_{j=1}^{m}\frac{1}{n}\left(\sum_{i=1}^{n}\frac{psrDew_{ij}}{psr3ew_{ij}}\right)\right] \\
cdsud_{psr} &= \frac{1}{m}\left[\sum_{j=1}^{m}\frac{1}{n}\left(\sum_{i=1}^{n}\frac{psrDud_{ij}}{psr3ud_{ij}}\right)\right]
\end{aligned} \tag{7.10}$$

In equations (7.9) and (7.10), $psrDns_{ij}$ is the PSR for NS component at the ith site, jth event from the data in each corresponding area in Table 7.7. $psr1ns_{ij}$ and $psr3ns_{ij}$ are the PSR for the NS component at the ith site, jth dip slip event from the 1D synthetics and (1D+3D) synthetics, respectively; n is the the number of stations in that area, m is the total number of events recorded. $psrDew_{ij}$, $psr1ew_{ij}$ and $psr3ew_{ij}$ are for the corresponding EW component, $psrDud_{ij}$, $psr1ud_{ij}$ and $psr3ud_{ij}$ are for the corresponding vertical component. $cdsns_{psr}$, $cdsew_{psr}$ and $cdsud_{psr}$ are the PSR calibration coefficients for dip slip event in NS component, EW component and vertical component respectively.

$cssns_{pvr}$, $cssns_{psr}$, $cssew_{pvr}$, $cssew_{psr}$, $cssud_{pvr}$ and $cssud_{psr}$ are the same indices, but for strike slip faulting.

These final values [Tables 7.6 and 7.7] are the numbers by which one should multiply 1D synthetics or (1D+3D) synthetics to get the expected ratios in a real earthquake. Thus a value greater than 1 for a given index (either $cdsns_{pvr}$, $cdsns_{psr}$, $cdsew_{pvr}$, $cdsew_{psr}$, $cdsud_{pvr}$ and $cdsud_{psr}$ or $cssns_{pvr}$, $cssns_{psr}$, $cssew_{pvr}$, $cssew_{psr}$, $cssud_{pvr}$ and $cssud_{psr}$) implies that the data is higher in amplitude than the (1D+3D) synthetics; vice versa for a value less than 1.0.

Tables 7.6 and 7.7 show that:

1. 1D synthetics from the local 1D models all overestimate the PVR; but all underestimate the PSR.

2. For predominant dip slip earthquakes, on average, the simulated PVR from (1D+3D) forward modelling overestimates the real PVR. But the simulated FSR from (1D+3D) forward modelling underestimates the real FSR in NS component and EW component while it overestimates the real FSR in vertical component.

3. For predominant strike slip earthquake, both the simulated PVR and PSR from (1D+3D) forward modelling overestimates the ground amplification in NS component and vertical component while it underestimates the PVR and FSR in EW component. The PVR and FSR of EW component are quite different from those of the other components, respectively; this phenommena may be caused by the effect of directivity.

The standard deviations in each zone in Table 7.7 are not trivial for both dip slip events and strike slip event. This probably is caused by the fact that even within the same zone, there is still variance

Table 7.6

Calibration indices and standard deviations for the local 1D models

Focus type	number of events used	Parameter	zone 1	zone 2	zone 3-4	zone 5	Basin edge §
dip slip	3	$cdsns_{pvr}$	0.7±0.5	0.5±0.3	0.3±0.1	0.3±0.2	0.3±0.2
		$cdsew_{pvr}$	0.6±0.2	0.6±0.4	0.3±0.1	0.2±0.1	0.3±0.1
		$cdsud_{pvr}$	0.6±0.4	0.5±0.3	0.3±0.2	0.5±0.2	0.4±0.2
		cds_{pvr}	0.6±0.4	0.5±0.3	0.3±0.1	0.3±0.2	0.3±0.2
		$cdsns_{psr}$	3.4±1.2	1.8±1.0	1.7±0.3	2.6±0.6	2.2±0.7
		$cdsew_{psr}$	2.3±0.9	0.9±0.4	1.0±0.4	2.2±0.9	1.9±1.0
		$cdsud_{psr}$	1.6±0.3	0.9±0.3	0.9±0.2	1.2±0.3	1.1±0.4
		cds_{psr}	2.5±0.8	1.2±0.6	1.2±0.3	2.0±0.6	1.7±0.7
strike slip	1	$cssns_{pvr}$	2.4±∽	0.9±0.3	0.6±0.2	0.6±0.1	0.5±0.1
		$cssew_{pvr}$	1.4±∽	0.6±0.1	0.4±0.1	0.5±0.2	0.5±0.2
		$cssud_{pvr}$	2.7±∽	0.7±0.1	0.9±0.2	1.4±0.7	1.5±0.7
		css_{pvr}	2.2±∽	0.7±0.2	0.6±0.2	0.8±0.3	0.8±0.3
		$cssns_{psr}$	3.6±∽	1.1±0.3	2.0±1.2	2.4±0.8	1.8±0.8
		$cssew_{psr}$	2.3±∽	0.5±0.1	0.8±0.2	1.1±0.4	1.0±0.5
		$cssud_{psr}$	2.4±∽	1.0±0.5	1.2±0.5	1.5±0.5	1.5±0.5
		css_{psr}	2.8±∽	0.9±0.3	1.3±0.7	1.6±0.6	1.4± 0.6

The site classification is identical to that in Figure 3.3, the basin edge sites can be found in Figure 2.3. The error bars represent 1 standard deviation. cds_{pvr} and cds_{psr} are the correponding calibration coefficients averaged over the three components for dip slip events. css_{pvr} and css_{psr} are the correponding calibration coefficients averaged over the three components for strike slip event. ∽ denotes that there is only one measurement and the standard deviation is not calculable.

Table 7.7

Calibration indices and standard deviations for the Hutt 3D shaking hazard model

Focus type	number of events used	Parameter	zone 1	zone 2	zone 3-4	zone 5	Basin edge
dip slip	3	$cdsns_{pvr}$	0.8±0.5	0.7±0.3	0.5±0.2	0.6±0.3	0.6±0.3
		$cdsew_{pvr}$	0.7±0.3	1.1±0.3	0.8±0.2	0.8±0.2	0.8±0.2
		$cdsud_{pvr}$	0.7±0.6	0.4±0.2	0.2±0.2	0.4±0.2	0.4±0.2
		cds_{pvr}	0.7±0.5	0.7±0.3	0.5±0.2	0.6±0.3	0.6±0.3
		$cdsns_{psr}$	3.3±0.9	1.7±1.1	2.2±1.0	2.1±0.6	1.8±0.4
		$cdsew_{psr}$	2.6±1.3	1.4±0.7	1.3±0.5	3.4±1.6	2.8±1.6
		$cdsud_{psr}$	1.6±0.3	0.5±0.5	0.6±0.3	0.4±0.2	0.4±0.2
		cds_{psr}	2.5±0.8	1.2±0.8	1.4±0.6	2.0±0.8	1.7±0.7
strike slip	1	$cssns_{pvr}$	1.7±∽	0.6±0.3	0.4±0.1	0.5±0.1	0.4±0.3
		$cssew_{pvr}$	1.4±∽	3.7±1.2	1.9±1.1	2.6±1.7	1.8±0.2
		$cssud_{pvr}$	3.0±∽	0.5±0.1	0.8±0.4	0.8±0.4	0.9±0.2
		css_{pvr}	2.4±∽	0.6±0.2	0.6±0.3	0.7±0.3	0.7±0.3
		$cssns_{psr}$	2.8±∽	0.5±0.0	0.7±0.3	1.1±0.5	0.8±0.4
		$cssew_{psr}$	2.5±∽	1.4±0.1	2.0±1.2	2.6±1.6	2.0±1.6
		$cssud_{psr}$	2.4±∽	0.4±0.2	0.5±0.3	0.8±0.6	0.4±0.2
		css_{psr}	2.6±∽	0.8±0.1	1.1±0.6	1.5±0.9	1.1± 0.7

The site classification is identical to that in Figure 3.3, the basin edge sites can be found in Figure 2.3. The error bars represent 1 standard deviation. L17, L01 and L07 were left out in averaging since they were in the absorbing region [Figure 2.3]. cds_{pvr} and cds_{psr} are the correponding calibration coefficients averaged over the three components for dip slip events. css_{pvr} is the correponding calibration coefficients averaged over the NS and UD components for strike slip event since $cssew_{pvr}$ is much higher, which appears to be caused by the effect of directivity. css_{psr} is the correponding calibration coefficients averaged over the three components for strike slip event. ∽ denotes that there is only one measurement and the standard deviation is not calculable.

in the sediment structures from site to site. Nevertheless, all the standard deviations are less than the corresponding averages.

Note that the PVR and PSR for L17, L07 and L01 in Table 7.5 are small. (1D+3D) synthetics can not match the data at L17 (at Wainuiomata, near the south margin of the 3D model), L07 (nearby the north margin of the 3D model) and L01 (nearby the eastern margin of the 3D model) at all since these three stations are located in the absorbing boundary zone in the 3D model [Figure 2.3]. There is no way for these three stations to keep away from the absorbing boundary zone, because it is limited by the original size of the whole Wellington 3D shaking hazard model. Therefore, we left them out in the calculation of calibration.

A too sharp velocity contrast between Layer 1 and Layer 2 [Table 7.1] in the 1_{st} step of (1D+3D) modelling generates a strong *SP* conversion [Figures 7.6]. This occurs because the replacement layer (Layer 1 in Table 7.1) is too thick. This leads to the reduction of PGV and PAS at each site. However, this will not affect the FSR and resonant frequency much since effects due to the path between the source and the receiver are much reduced through the uses of spectral ratios. A test with a realistic velocity model showed the spectrum changed but the resonant frequency almost remained constant.

The local 1D modelling can remedy one deficiency of the (1D+3D) modelling: (1D+3D) modeling can only simulate to up to 2.5 Hz so far due to the limited knowledge of the heterogeneity structure of Hutt Valley, while 1D modelling can simulate to a higher frequency.

The strong ground motion simulated from an assumed Wellington Fault rupture (Benites and Olsen, 2004) was based on strike slip faulting, so the calibration indices for strike slip in Table 7.7 correspond to the calibration indices for the ground motion simulated from the assumed Wellington Fault rupture (Benites and Olsen, 2004). If we only focus on the NS component and UD component, the PVRs from (1D+3D) modelling really overestimate those from the recorded ground motion, respectively. This result agrees with the result predicted by the simulation from the assumed Wellington Fault rupture (Benites and Olsen, 2004) (see thesis page 4).

Problems lie in the EW component. Unlike the result anticipated by the simulation from the assumed Wellington Fault rupture (Benites and Olsen, 2004), PVR from (1D+3D) modelling underestimates that from the recorded ground motion. This phenomena probably is caused by the effect of directivity in the seismic wavefield propagation, which is quite complicated. I left EW component out in the calibration for css_{pvr}. Note the calibration indices obtained here are for the Hutt 3D shaking model, which is only $\frac{1}{3}$ the size of the whole Wellington 3D shaking model. Therefore, compared to the rock site, the ground motion on sediment sites simulated by the Hutt 3D shaking model is not amplified as much as the whole Wellington 3D shaking model as mentioned in Section 1.2.

CHAPTER 8

CONCLUSIONS AND PERSPECTIVES

I determined the focal mechanisms for the events recorded by the portable deployments, and modelled the 1D synthetics from individual 1D models. I developed a new modelling technique named as *(1D+3D) hybrid technique*, and obtained two indices for calibrating the Hutt 3D shaking model with (1D+3D) synthetics.

8.1 Development of *the (1D+3D) hybrid modelling technique* for studying seismic hazard in sediment valley

A new technique named (1D+3D) hybrid technique for studying seismic response of sediment in 3D heterogeneous structure involving both 1D simulation (Bouchon, 1979) and 3D simulation (Benites and Olsen, 2004; Olsen, 2000; Gottschammer and Olsen, 2001; Olsen, 2001; Marcinkovich and Olsen, 2003) is formed in this study. The ground motions of stress and velocity are first brought to the position of the sediment-bedrock interface in the 3D model by the DWN method (Bouchon, 1979) of 1D modelling, then they are carried on by FD method (Olsen, 2000; Gottschammer and Olsen, 2001; Olsen, 2001; Marcinkovich and Olsen, 2003; Benites and Olsen, 2004) in the 3D model to investigate the behaviour of basins and soft soil during an earthquake. The seismic rays propagate layer by layer before they arrive at the position of the sediment-bedrock interface in the 3D model. Modifying the 1D modelling and 3D modelling programs and combining them together, getting them work on a Linux computer (they originally were run on Unix computer) is my contribution.

To determine how well the technique works, we did the following:

1. We put an independent explosion point source in a 3D test half space model and the corresponding 1D half space model. The velocity synthetics produced by 1D modelling and 3D

modelling are quite similar to each other in the main part for *P* travel time, amplitude, period and waveform. Nevertheless, the 1D synthetics and 3D synthetics created are not totally identical: after the main seismogram stops in the 1D synthetics, there are still some late vibrations in the 3D synthetics, which is noise introduced by the numerical computational nature of FD method. The noise probably can be reduced by cutting the grid size to a smaller value. Computation facilities allowing tests of this idea, or comparisons to full 3D modelling, were not available. As the DWN method (Bouchon, 1979) for 1D modelling and the FD method (Pitarka *et al.*, 1998; Olsen, 2000; Gottschammer and Olsen, 2001; Olsen, 2001; Marcinkovich and Olsen, 2003; Benites and Olsen, 2004) for 3D modelling use completely different methods in simulating seismic waves, comparisons suggest that both the DWN method code and the FD code work properly.

2. We put a double couple point source in the 1D half space model, propagate the motion of wavefield to the position of the sediment-bedrock interface of the Hutt test model by the DWN method (Bouchon, 1979), then propagate the motion wavefield through the rest of the half space medium by FD method (Benites and Olsen, 2004; Olsen, 2000; Gottschammer and Olsen, 2001; Olsen, 2001; Marcinkovich and Olsen, 2003) to compute (1D+3D) velocity synthetics. Note the (1D+3D) test model is still a uniform half space model here. Independently, the 1D velocity synthetics to the free surface are created by the DWN method (Bouchon, 1979). The velocity synthetics produced by 1D modelling and (1D+3D) modelling separately show that they are essentially identical in waveform and amplitude in *P* and the initial *S* stages. This displays that the new developed (1D+3D) hybrid modelling technique works properply. However, there is dispersion error in the synthetics from (1D+3D) modelling. That appears mainly after the *S* phase arrival. The dispersion error amplitude is 10% of the signal amplitude.

The new technique is put into practice in calibrating the Hutt 3D shaking hazard model with four earthquakes of different focal mechanisms.

8.2 Modelling ground motions in the Hutt deployment sites in two different ways

The ground motions in the Hutt deployment sites were synthesized by 1D modelling technique and (1D+3D) modelling technique independently and were used to compare with the observed data.

8.2.1 Modelling ground motions in the Hutt deployment station sites by DWN method

An individual 1D model is derived from the Hutt 3D model for each station in the Hutt deployment, and 1D synthetics are obtained by the DWN method (e.g. Bouchon, 1979; Benites *et al.*, 2002). The results illustrate that the 1D synthetics from the individual 1D models can match the data better than the 1D synthetics from the Robinson (1986) velocity model by a longer duration time and higher peak magnitude at the soft sites.

8.2.2 Modelling ground motions in the Hutt deployment sites by the newly developed (1D+3D) hybrid technique

Before this work, Olsen (1995) simulated the 3D elastic wave propagation in the Salt Lake basin, US; plane waves and Ricker wavelet were used as input in that study. Pitarka *et al.* (1998) simulated the 3D near-fault strong ground motion for the 1995 Hyogo-ken Nanbu (Kobe), Japan earthquake. Olsen (2000) also simulated the site amplification in the Los Angeles Basin; furthermore, Olsen (2001) modelled the 3D ground strong motion for large earthquakes on the San Andreas fault with dynamic and observational constraints. Benites and Olsen (2004) modelled the strong ground motion in the Wellington area by assuming a rupture of the Wellington fault, New Zealand. The rectangular Wellington fault source was implemented in the 3D modelling in that study. Unlike the case of Benites and Olsen (2004), in which both the rupture and the wave propagation in the 3D basin are calculated at time steps by a FD scheme, in (1D+3D) modelling we split the ground motion modelling into two parts:

1. For each earthquake, we first calculated the wavefield at the bottom of Hutt Valley basin due to a point source at the focus of the earthquake using the focal mechanism. This is done by the modified 1D forward modelling algorithm originally developed by Benites *et al.* (2002) based

on the DWN method to represent the source (Bouchon, 1979) and reflectivity (Kennett, 1983) to incorporate the layered medium of the Wellington regional model underneath the basin. Some development is made to obtain all the components of stress tensor and velocity vector in the Cartesian coordinate system.

2. we calculated the wavefield at the free surface of the 3D basin using the Finite Difference scheme (Benites and Olsen, 2004; Olsen, 2000; Gottschammer and Olsen, 2001; Olsen, 2001; Marcinkovich and Olsen, 2003), using as input the time-domain stress and velocity wavefields at Hutt Valley sediment-bedrock interface. Also, the original Finite Difference scheme is adapted for this project by replacing the double couple point source with an *interface source*.

The testing of newly developed (1D+3D) modelling method and analysis and critique of all FSRs (sediment site spectrum divided by rock site spectrum) for the 1D modelling data, (1D+3D) modelling data and recorded data have led to the following conclusions:

8.3 Conclusion

I reached the following points through program testing and ground motion modelling:

1. The 1D synthetics for the alluvium sites underestimate the site effect compared to the data in the temporary deployment.

2. The newly developed (1D+3D) modelling technique works properly at least for *P* and the initial *S* pulses, as confirmed by 1D/3D test and 1D/(1D+3D) test. This is a breakthrough in modelling the real ground motion in an alluvial valley. It should allow future work for the (1D+3D) modelling with the whole Wellington 3D shaking model.

3. Indices for PVR and PSR are obtained to calibrate the local 1D models and the Hutt 3D shaking hazard model. The (1D+3D) synthetics for the alluvium sites overestimate the PVR for strike slip faulting in NS and UD components; this is in agreement with the result predicted by the simulation from the assumed Wellington Fault rupture (Benites and Olsen, 2004). However, the (1D+3D) synthetics for the alluvium sites underestimate the PVR for strike slip faulting in EW component; this is contradictory to what is predicted by the simulation from the assumed Wellington Fault rupture (Benites and Olsen, 2004). It probably can be interpreted by the

effect of directivity in wavefield propagation. The (1D+3D) synthetics for the alluvium sites underestimate the PSR for both dip slip faulting and strike slip faulting.

4. A too sharp velocity contrast between Layer 5 and Layer 6 [Tables 5.1 and 5.2] generates a strong *SP* conversion in the 1D synthetics [Figures 5.11, 5.12 and 5.13]. Similarly, a too sharp velocity contrast between Layer 1 and Layer 2 and a too thick, low velocity replacement layer (Layer 1) [Table 7.1] in the 1_{st} step of (1D+3D) modelling generates a strong *SP* conversion in the (1D+3D) synthetics [Figures 7.6]. This leads to the reduction of PGV and PAS at each site for the 1D synthetics and (1D+3D) synthetics, respectively. However, this will not affect the FSR and resonant frequency much since effects due to the path between the source and the receiver are much reduced through the uses of spectral ratios.

8.4 Perspectives

Several suggestions are made which may aid the direction of this research in the future. They are as the follows:

1. Attenuation (Q factor) was incorporated in neither the 1D DWN method nor the newly developed (1D+3D) method yet. This explains why the simulated PVR and PSR are higher than expected. It should be incorporated for propagation of seismic waves in the upper sediment layers in future study.

2. Originally, we wanted to calibrate the whole Wellington 3D ground shaking model established by Rafael Benites, Kim Olsen and Peter Wood, which is 38.96 km by 9.96 km by 9.6 km. True ground motion data from four portable deployments by John Taber and New Zealand Strong Motion Network for this task were gathered already. The focal mechanisms for all the earthquakes recorded by the four deployments were solved. Unfortunately, it is impossible to calibrate the whole Wellinton 3D ground shaking model because we are limited by the computational power available at GNS. With the Linux computer used in this project, it will take 21 days to get the (1D+3D) modelling result for the whole Wellington 3D model for one event. The Hutt 3D model chosen is only $\frac{1}{3}$ the size of the whole Wellington 3D model. The computer power limits us to work on a smaller model only, so we work on the Lower Hutt 3D ground shaking model only this time. It took 7 days for modelling one event's wavefield in the free

surface of Hutt Valley. Therefore lots of data collected were not used this time. The Wellington array by Dr. John Taber recorded many earthquakes well, but is not exploited this time due to the computer limitation.

3. Even in the calibration of the Hutt 3D shaking hazard model, we have not used all the available data so far. To calibrate it fully, more events representing all sorts of focal mechanisms should be used; all the data assembled (weak motion data, strong motion data, short period data and broad band data) should be used. Only short period weak motion data has been employed by now in this research due to the time limitation set by the project.

4. The conclusion from calibrating the Wellington 3D shaking model as a whole will be more precise than that from calibrating the Hutt 3D shaking model only. The *interface source* works like a "lens" of a camera, the interface of Wellington 3D shaking model is 3 times larger than that of the Hutt 3D shaking model, hence it can receive and pass on more energy from the double couple point source beyond the 3D model.

5. We have compared the synthetics from 1D modelling and (1D+3D) modelling with the short period, weak motion data. For the future research, a Lower Hutt portable deployment of broad band instruments with strong motion recorded data will enable the comparison between the broad band, strong motion observations and the (1D+3D) modelling results. This is necessary for understanding the seismic behaviour of Hutt Valley under long period strong motion shaking.

6. Consideration given to the effect of surface topography surrounding the valley will improve the (1D+3D) modelling.

7. To enhance the accuracy and resolution for higher frequency, an unstructured grid may be built to enable elements of differing sizes and proportions to give a high degree of geometric detail. Node spacing can be tailored in proportion to the local S velocity to give similar numerical accuracy and high computational efficiency throughout the geometry of the problem. To fulfill this proposal, it is necessary to develop the (1D+3D) hybrid method further to handle variable grid size.

REFERENCES

ADAMS, B. (2000), *Basin Edge Effect from SH-wave Modelling with Reference to the Lower Hutt Valley, New Zealand*, Ph.d. thesis, University of Canterbury, Christchurch, New Zealand, 269 pp.

ADAMS, J. C. AND BRAINERD, W. S. (1997), *FORTRAN 95 HANDBOOK COMPLETE ISO/ANSI REFERENCE*, The MIT Press, Cammbridge, Massachusettes, USA, Cammbridge, Massachusettes, USA, 711 pp.

AKI, K. AND RICHARDS, P. G. (1980), *Quantitative seismology theory and methods*, W. H. Freeman and Co., San Francisco, 932 pp.

ANDERSON, H., WEBB, T. AND JACKSON, J. (1993), Focal Mechanisms of large earthquakes in the South Island of New Zealand: implications for the accommodation of Pacific-Australia plate motion, *Geophys. J. Int.* **115**: 1032–1054.

BENITES, R. AND AKI, K. (1994), Ground motion at mountains and sedimentary basins with vertical seismic velocity gradient, *Geophysical journal international* **116(1)**: 95–118.

BENITES, R. AND OLSEN, K. B. (2004), Modeling Strong Ground Motion in the Wellington Metropolitan area, New Zealand. In press, *BSSA* .

BENITES, R., ROBINSON, R., WEBB, T. AND MCGINTY, P. (2002), *Modelling realistic ruptures on the Wellington fault, Client Report 2002/85*, Lower Hutt, New Zealand, 46 pp.

BEN-MENAHEM, A. AND SINGH, S. J. (1981), *Seismic waves and sources*, Springer-Verlag, New York, USA, 1108 pp.

BOAS, M. L. (1966), *Mathematical Methods in the Physical Sciences*, John Wiley & Sons, Inc. USA, Chicago, Illinois, USA, 778 pp.

BORCHERDT, R. D. AND GLASSMOYER, G. (1992), On the characteristics of local geology and their influence on ground motions generated by the Loma Prieta earthquake in the San Francisco Bay region, California, *Bull. Seimol. Soc. Amer.* **82**: 603–641.

BOUCHON, M. (1979), Discrete wave number representation of elastic wave fields in three-space dimensions, *J. Geophys. Res.* **84**: 3609–3614.

BOUCHON, M. AND AKI, K. (1977), Discrete wavenumber representation of seismic souce wave fields, *Bull. Seismol. Soc. Am.* **67**: 259–277.

CAVILL, A., SAVAGE, M. K. AND TABER, J. J. (1997), Source mechanisms for event recorded by a temporary deployment of broadband instruments in the southern North Island, *Institute of Geophysics Report 1997/03, Victoria University of Wellington, 36 pp.* .

CERJAN, C., KOSLOFF, D., KOSLOFF, R. AND RESHEF, M. (1985), A nonreflecting boundary condition for discrete acoustic and elastic wave equations, *Geophysics* **50**: 705–708.

CHÁVEZ-GARCÍA, F. J., STEPHENSON, W. R. AND RODRIGUEZ, M. (1999), Lateral propagation effects observed at Parkway, New Zealand: a case history to compare 1D versus 2D site effects, *Bull. Seismol. Soc. Am.* **89**: 718–732.

CHIN, B. H. AND AKI, K. (1991), Simultaneous study of the source, path and site effects on strong ground motion during the 1989 Loma Prieta earthquake:a preliminary result on pervasive non-linear site effects, *Bull. Seismol. Soc. Am.* **81**: 859–884.

CLAYTON, R. AND ENGQUIST, B. (1977), Absorbing boundary conditions for acoustic and elastic wave equations, *Bull. Seismol. Soc. Am.* **67**: 1529–1540.

COUSINS, W. J. (1998), New Zealand strong-motion data 1965-1997., *Lower Hutt: Institute of Geological & Nuclear Sciences science report 98/04. 1 computer laser optical disk* .

COUTEL, F. AND MORA, P. (1998), Simulation-based comparison of four site-response estimation techniques, *Bull. Seismol. Soc. Am.* **88**: 30–42.

DELLOW, G. D., READ, S. A. L., BEGG, J. G., VAN DISSEN, R. J. AND PERRIN, N. D. (1992), Distribution of geological materials in Lower Hutt and Porirua, New Zealand: a component of a ground shaking hazard assessment, *Bull. of the New Zealand National Society for Earthquake Engineering* **25(4)**: 332–344.

DIXON, W. J. AND MASSEY, F. J. (1969), *Introduction to Statistical Analysis*, McGraw-Hill, Inc., Tokyo, Japan, 638 pp.

DREGER, D. S. AND HELMBERGER, D. V. (1990), Broadband modelling of local earthquakes, *Bull. Seismol. Soc. Am.* **80**: 1162–1179.

DREGER, D. S. AND HELMBERGER, D. V. (1993), Determination of source parameters at regional distances with three-component sparse network data, *J. Geophys. Res.* **98**: 8107–8125.

DREGER, D. S. AND LANGSTON, C. (1995), *1995 IRIS Workshop on Moment Tensor Inversion.*

FIELD, E. H., ANDERSON, J. G., HENYEY, T. L., JACKSON, D. D., JOYNER, W. B., LEE, Y., MAGISTRALE, H., MINSTER, B., OLSEN, K. B., PETERSEN, M. D., STEIDL, J. H., WALD, L. A. AND WILLS, C. J. (2000), Accounting for site effects in probabilisitic seismic hazard analyses of southern California: overview of the SCEC Phase III report, *Bull. Seismol. Soc. Am.* **90**: S1–S31.

GELI, L., BARD, P. AND JULLIEN, B. (1988), The effects of topography on earthquake ground motion: a review and new results, *Bull. Seismol. Soc. Am.* **78**: 42–63.

GLEDHILL, K. R., RANDALL, M. J. AND CHADWICK, M. P. (1991), The EARSS seismograph: system description and field trials, *Bull. Seismol. Soc. Am.* **81(4)**: 1380–1390.

GOTTSCHAMMER, E. AND OLSEN, K. B. (2001), Accuracy of the Explicit Planar Free-Surface Boundary Condition Implemented in a Fourth-Order Staggered-Grid Velocity-Stress Finite-Difference Scheme, *Bull. Seismol. Soc. Am.* **91**: 617–623.

HAINES, A. J. AND YU, J. (1997), Observation and synthesis of spatially-incoherent weak-motion wavefields at Alfredton Basin, New Zealand, *Bull. of the New Zealand National Society for Earthquake Engineering* **30(1)**: 14–31.

HARTZELL, S., CRANSWICK, E., FRANKEL, A., CARVER, F. AND MERMONTE, M. (1997), Variability of site response in the Los Angeles Urban area, *Bull. Seismol. Soc. Am.* **87**: 1377–1400.

HUDSON, J. A. (1963), *SH* waves in a wedge-shaped medium, *Geophys. J. Royal Astr. Soc.* **7(5)**: 517–546.

IRIS (2004), http://www.geonet.org.nz/snzo-drum.html.

KAWASE, H. (1996), The cause of the damage belt in Kobe: "the basin-edge effect", constructive interference of the direct S-wave with the basin induced diffracted Rayleigh waves, *Seis. Research Lett.* **67**: 25–34.

KENNETT, B. L. N. (1983), *Seismic Wave Propagation in Stratified Media, Cambridge Monographs on Mechanics and Applied Mathematics*, Cambridge University Press, Cambridge, UK, 342 pp.

KIM, Y. S. AND ROESSET, J. M. (2004), Effect of nonlinear soil behavior on inelastic seismic response of a structure, *International Journal of Geomechanics* pp. 104–114.

LAY, T. AND WALLACE, T. (1995), *Modern Global Sesimology*, Academic Press, San Diego, USA. 521 pp.

LEVANDER, A. R. (1988), Fourth-order Finite-difference P-SV Seismograms, *Geophysics* **53**: 1425–1436.

LEVANDER, A. R., BLANCH, J. O., ROBERTSON, J. O. A. AND SYMES, W. W. (1999), *VE2D22, 2-D Visco-Elastic Finite Difference Modelling - version 2.2, DOCUMENTATION AND RELATED PROGRAMS*, Rice University, Houston, Texas 77005, USA.

LINES, L. R., SLAWINSKI, R. AND BORDING, R. P. (1998), A recipe for stability analysis of finit-difference wave equation computations, *Crewes Research Report* **10**: 1–6.

MARCINKOVICH, C. AND OLSEN, K. B. (2003), On the Implementation of Perfectly Matched Layers in a 3D Fourth-Order Velocity-Stress Finite-Difference Scheme, *JGR* **108 (B5), 2276, doi:10.1029/2002JB002235**.

MATCHAM, I. (1999), *Source mechanism determination using broadband data in the New Zealand seismic environment*, Master's thesis, Victoria University of Wellington, 183 pp.

MATHWORKS (1996), *Using Matlab*, The Mathworks, Inc, Natick, Massachusetts, US, I-38 pp. http://www.mathworks.com.

MAUNDER, D. E. (1993), *New Zealand Seismological Report, 93/44*, Lower Hutt, New Zealand, 169 pp.

NAGANO, M. (1998), Amplification characteristics of the ground motions in deep irregular underground structure with vertical discontinuity, *Proc. 2nd Intl. Symposium on the Effects of Surface Geology on Seismic Ground Motion, Yokohama*, Yokohama, Japan, pp. 859–866.

NFORMI, S., MAO, W. AND GUBBINS, D. (1996), Seismic source parameters in New Zealand from broad-band data, *Geophys. J. Int.* **124**: 289–303.

OETIKER, T., PARTL, H., HYNA, I. AND SCHLEGL, E. (2003), *The Not So Short Introduction to LATEX* 2_ε, Swiss Federal Institute of Technology, Swizerland, 101 pp.

OLSEN, K. B. (1994), *Simulation of three-dimensional wave propagation in the Salt Lake Basin*, Ph.d. thesis, University of Utah, Salt Lake City, Utah, USA, 157 pp.

OLSEN, K. B. (1995), Simulation of 3D Elastic Wave Propagation in the Salt Lake Basin, *Bull. Seismol. Soc. Am.* **85**: 1688–1710.

OLSEN, K. B. (2000), Site Amplification in the Los Angeles Basin from 3D Modeling of Ground Motion, *Bull. Seismol. Soc. Am.* **90**: S77–S94.

OLSEN, K. B. (2001), Three-dimensional ground motion simulations for large earthquakes on the San Andreas fault with dynamic and observational constraints, *Jour. Comp. Acoust.* **9(3)**: 1203–1215.

OSBORNE, N. M. (1999), *The Basin Edge Effect In The Lower Hutt Valley, Wellington Using Weak Ground Motion Recordings*, Honours Thesis, pp 70.

OSBORNE, N. M. AND TABER, J. J. (1999), Oberservaton of basin edge effects in the Hutt Valley, New Zealand, from weak ground motion recordings, *Proceedings of the Sixth International Conference on Seismic Zonation*, Palm Springs, California (CDROM), US.

PITARKA, A., IRIKURA, K., IWATA, T. AND SEKIGUCHI, H. (1998), Three-dimensional simulation of the near-fault ground motion for the 1995 Hyogo-ken Nanbu (Kobe), Japan earthquake, *Bull. Seismol. Soc. Am.* **88**: 428–440.

ROBINSON, R. (1986), Seismicity, structure and tectonics of the Wellington region, New Zealand, *Geophys. J. R. Astr. Soc.* **87**: 379–409.

SAVAGE, M. K. AND ANDERSON, J. G. (1995), A local magnitude scale for the western Great Basin-Eastern California region from synthetic Wood-Anderson seismograms, *Bull. Seismol. Soc. Am.* **85**: 1236–1243.

SCHWARTZ, S. Y. (1995), Source parameters of aftershock of the 1991 Costa Rica and 1992 Cape Mendocino, California earthquake from inversion of local amplitude ratio and broadband waveforms, *Bull. Seismol. Soc. Am.* **85**: 1560–1575.

SRITHARAN, S. AND MCVERRY, G. H. (1992), Microzone effeces in the Hutt Valley in records from a strong motion accelerograph array, *Bull of the New Zealand National Society for Earthquake Engineering* **25**: 246–264.

TABER, J. J. (2000), Comparison of site response determination techniques in the Wellington Region, New Zealand, *Proceedings of the 12th World Conf. Earthquake Engineering, Auckland, New Zealand*, Auckland, New Zealand (CDROM).

TABER, J. J. AND RICHARDSON, W. P. (1992), *Frequency dependent amplification of weak ground motions in Wellington City and the Kapiti coast*, Victoria University of Wellington, PO Box 600, Wellington, New Zealand. Client report to Wellington Regional Council.

TABER, J. J. AND SMITH, E. G. C. (1992), Frequency dependent amplification of weak ground motions in Porirua and Lower Hutt, New Zealand, *Bull. of the New Zealand National Society for Earthquake Engineering* **25(4)**: 303–331.

TABER, J. J., SRITHARAN, S., MCVERRY, G. H. AND ANSELL, J. H. (1993), *Site effects from seismic shaking: A comparison of strong and weak ground motions in Wellington City and the Hutt valley*, PO Box 600, Wellington, New Zealand. Report to the Earthquake and War Damage Commission, 48 pp.

TAPLEY, W. C., TULL, J. E., MINER, L. AND GOLDSTEIN, P. (1990), *Sac Command reference manual version 10.5d*, Lawrence Livermore National Laboratory, Regents of the University of California,California, USA. http://www.llnl.gov/sac/.

VAN DISSEN, R. J. AND BERRYMAN, K. R. (1996), Surface rupture earthquakes over the last ~1000 years in the Wellington region, New Zealand and implications for ground shaking hazard, *J. Geophys. Res.* **101(B3)**: 5999–6019.

VAN DISSEN, R. J., TABER, J. J., STEPHENSON, W. R., SRITHARAN, S., PERRIN, N. D., MCVERRY, G. H., CAMPBELL, H. J. AND BARKER, P. R. (1992b), *Earthquake ground shaking hazard assessment for the Wellington area, New Zealand, DSIR Geophysics contract report 1992/23*, PO Box 600, Wellington, New Zealand. Client report to Wellington Regional Council.

VAN DISSEN, R. J., TABER, J. J., STEPHENSON, W. R., SRITHARAN, S., READ, S. A. L., MCVERRY, G. H., DELLOW, G. D. AND BARKER, P. R. (1992a), Earthquake ground shaking hazard assessment for the Lower Hutt and Porirua areas, *Bull. of the New Zealand National Society for Earthquake Engineering* **25**: 286–302.

WALD, D. J. AND HEATON, T. H. (1994), Spatial and temporal distribution of slip for the 28 June 1998 Landers, California, earthquake, *Bull. Seismol. Soc. Am.* **84**: 668–691.

WEBB, T. H. AND ANDERSON, H. (1998), Focal mechanisms of large earthquakes in the North Island of New Zealand: slip partioning at an oblique active margin, *Geophys. J. Int.* **134**: 40–86.

WESSEL, P. AND SMITH, W. H. F. (1998), New, improved version of Generic Mapping Tool released, *EOS Trans. Amer. Geophys.* **U. 79(47)**: 579.

ZENG, Y. AND ANDERSON, J. G. (1995), A method for direct computation of the differential seismogram with respect to the velocity change in a layered elastic solid, *Bull. Seismol. Soc. Am.* **85**: 300–307.

APPENDIX A

INSTRUMENT RESPONSE

The instrument responses of the seismometer & recorder used in this project are as the follows:

Mark Products L4-C with EARSS recorder (short period, Velocity Transducer, sampling rate 50 Hz)

CONSTANT 18643681.280

ZEROS 3

0.000000e+00 0.000000e+00

0.000000e+00 0.000000e+00

0.000000e+00 0.000000e+00

POLES 5

-1.0000 0.0000

-66.6432 66.6432

-66.6432 -66.6432

-4.2097 4.6644

-4.2097 -4.6644

Guralp CMG-40T 60s with Quanterra Q4126 recorder (broad band, Velocity Transducer, sampling rate 100 Hz)

CONSTANT 1.1064928E+08

ZEROS 3

0.000000E+00 0.000000E+00

0.000000E+00 0.000000E+00

8.796450E+02 0.000000E+00

POLES 3

-7.401600E-02 7.401600E-02

-7.401600E-02 -7.401600E-02

-3.041060E+02 0.000000E+00

Kinemetrics force-balance accelerometer with EARSS recorder (short period, Accelerometer)

CONSTANT 53477.38

ZEROS 1

0.000000e+00 0.000000e+00

POLES 7

-1.0000 0.0000

-66.6432 66.6432

-66.6432 -66.6432

-220.0 224.0

-220.0 -224.0

-1005.0 0.0

-2010.0 0.0

SNZO (GeoTech KS-36000_I BD seismometer with Quanterra Q680 Datalogger, very broad band, Velocity Transducer)

CONSTANT 6.213803e+13

ZEROS 4

0.000000e+00 0.000000e+00

0.000000e+00 0.000000e+00

0.000000e+00 0.000000e+00

0.000000e+00 0.000000e+00

POLES 6

-89.8500 0.0000

-18.4300 18.9100

-18.4300 -18.9100

-0.0123 0.0123

-0.0123 -0.0123

-0.0042 0.0000

Mark Kinemetrics L4-C with EARSS recorder (short period, Velocity Transducer, sampling rate 100

Hz)

CONSTANT 18643681.280

ZEROS 4

0.000000e+00 0.000000e+00

0.000000e+00 0.000000e+00

0.000000e+00 0.000000e+00

POLES 5

-1.000000e+00 0.000000e+00

-1.332900e+02 1.332900e+02

-1.332900e+02 -1.332900e+02

-3.769900e+00 5.026500e+00

-3.769900e+00 -5.026500e+00

Guralp CMG40T sensor with Nanometrics Orion recorder (broad band, Velocity Transducer, sampling rate 100 Hz (Martha removed 1 zero and changed 1 sign -314.1600 314.1600))

CONSTANT 1.301530e+07

ZEROS 3

999.0260 0.0000

999.0260 0.0000

999.0260 0.0000

POLES 3

-0.1480 0.1480

-0.1480 -0.1480

314.1600 0.0000

The CONSTANT represents the product of sensitivity of the sensor, recorder and gain. Note that the instrument response of Mark Products L4-C with EARSS recorder (short period, Velocity Transducer, sampling rate 50 Hz) which is used in NZSN is different from that of Mark Kinemetrics L4-C with EARSS recorder (short period, Velocity Transducer, sampling rate 100Hz) which is being used in Dr. John Taber's temporaray deployments. Because the sensors are different (One is Mark Products L4-C, another is Mark Kinemetrices L4-C) and the sampling rate of EARSS recorder are different (One is 50 Hz, another is 100 Hz).

APPENDIX B

FOCAL MECHANISMS FOR THE OTHER EVENTS

Originally, we aimed to calibrate the whole Wellington 3D shaking hazard model, which is 38.96 km by 9.96 km by 9.6 km. So I preproccessed the seismic data from all portable ararys available and from New Zealand Strong Motion Network. Besides the data sets I characterized in Section 3.1.4, I also have got the ground shaking data from the Wellington deployment (Oct. 1991- Jan. 1992) (Taber and Richardson, 1992), the Leeds Tararua deployment (Jan. 1991-Sep. 1992) (Nformi *et al.*, 1996), the broad band deployment (Dec. 1997-Jan. 1998) (Taber, 2000), the Alicetown deployment (Jan. 1999) (Osborne and Taber, 1999). The data sets from the Leeds Tararua deployment were used in focal mechanism determination for the events fell in the Wellington deployment period only. The data sets from New Zealand Strong Motion Network were aimed to be used in calibrating the whole 3D model only. All the other data sets from the temporary array were planned to be used in both focal mechanism determination and the 3D model calibration. Unfortunately, limited by time and computational ability, only the Hutt 3D shaking model has been calibrated with the observed data from the Lower Hutt deployment. I will not list the above data sets which was not used in the (1D+3D) hybrid method modelling so far in this thesis. I list the focal mechanisms for the other events I determined or collected from the studies of Webb and Anderson (1998) and Anderson *et al.* (1993) in Table B.1. If the (1D+3D) hybrid simulation method developed in this project works reliablely, we will start to calibrate the whole 3D model when a powerful computer becomes available. The focal mechanisms in Table B.1 will be used in the further research.

Table B.1

Focal mechanisms unused in the calibration of the Hutt 3D shaking hazrad model.

No.	Date	Time	Lat (°)	Lon (°)	Depth (km)	Mag	strike (°)	Dip (°)	Rake (°)	Dist* (km)
1	05/01/73	13:54	-39.04	175.25	149	7.0	142	66	76	235
2	18/01/77	05:41	-41.73	174.30	34	6.0	213	68	251	73
3	28/12/97	16:39	-40.40	174.71	79	4.2	190	60	30	96
4	31/12/97	19:21	-42.05	173.91	21	4.0	30	80	30	128
5	10/01/98	16:28	-40.25	174.95	70	4.3	290	70	35	96
6	03/01/99	07:00	-41.09	174.51	57	5.5	90	35	345	33
7	09/01/99	13:18	-43.38	173.98	12	4.9	300	20	200	226
8	20/01/99	11:29	-41.78	174.61	31	3.6	260	50	340	59
9	21/01/99	14:58	-40.58	174.71	66	3.7	0	90	260	67
10	25/01/99	06:01	-41.47	174.45	24	3.7	110	50	230	63

Dist: epicentral distance from the corresponding array

APPENDIX C

FSRS FOR DATA AND 1D SYNTHETICS AT OTHER SITES

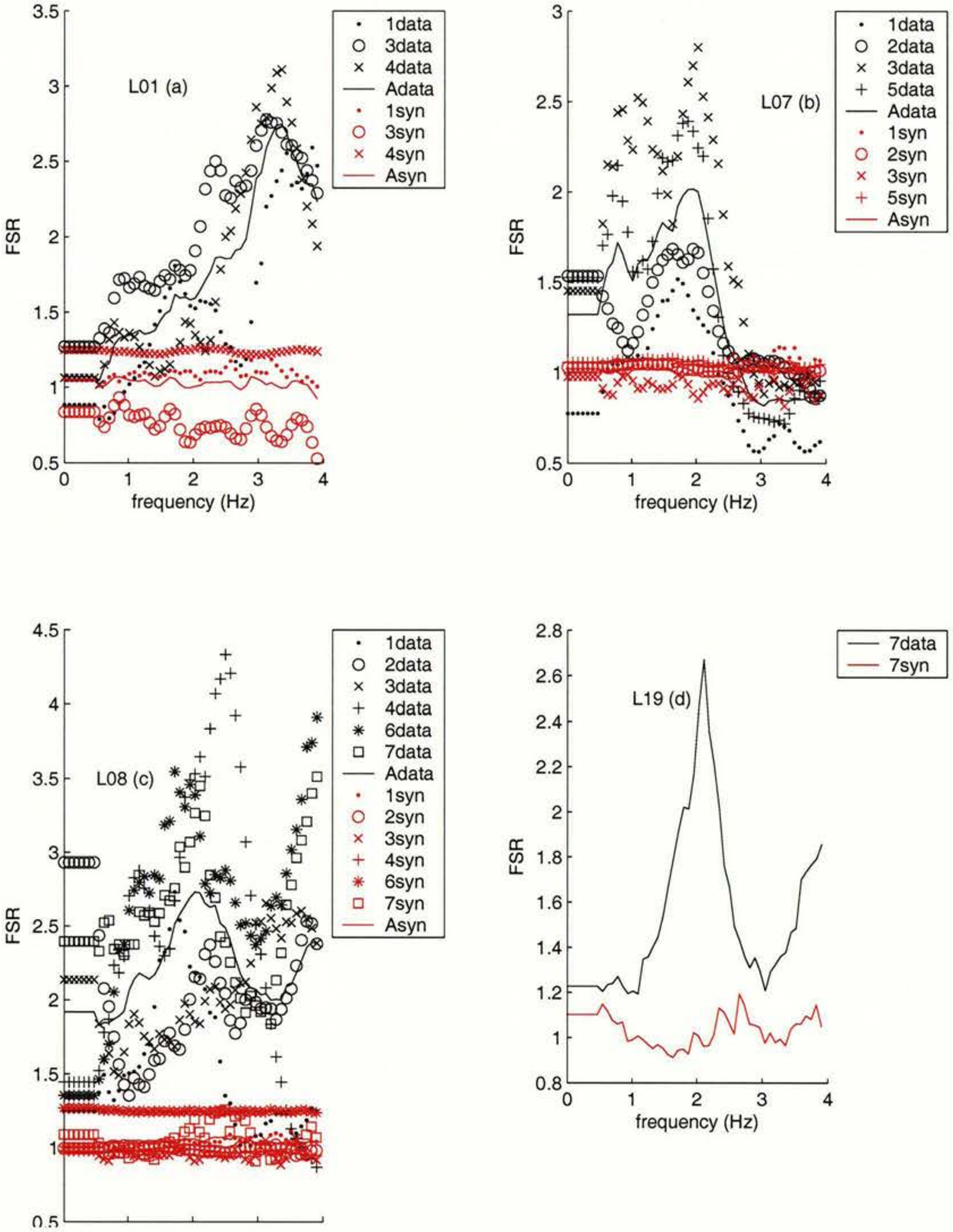

Figure C.1 *Comparison between FSRs of data and synthetic in the horizontal components for all events for site L01, L07, L08 and L19 (zone 1). The solid line is the average over all events. "1data" and "1syn" represent the data and synthetic FSR, respectively for event 1 in Table 3.2. Other symbols are analogous. "Adata" and "Asyn" represent the avearage of data FSR and the avearage of synthetic FSR, respectively.*

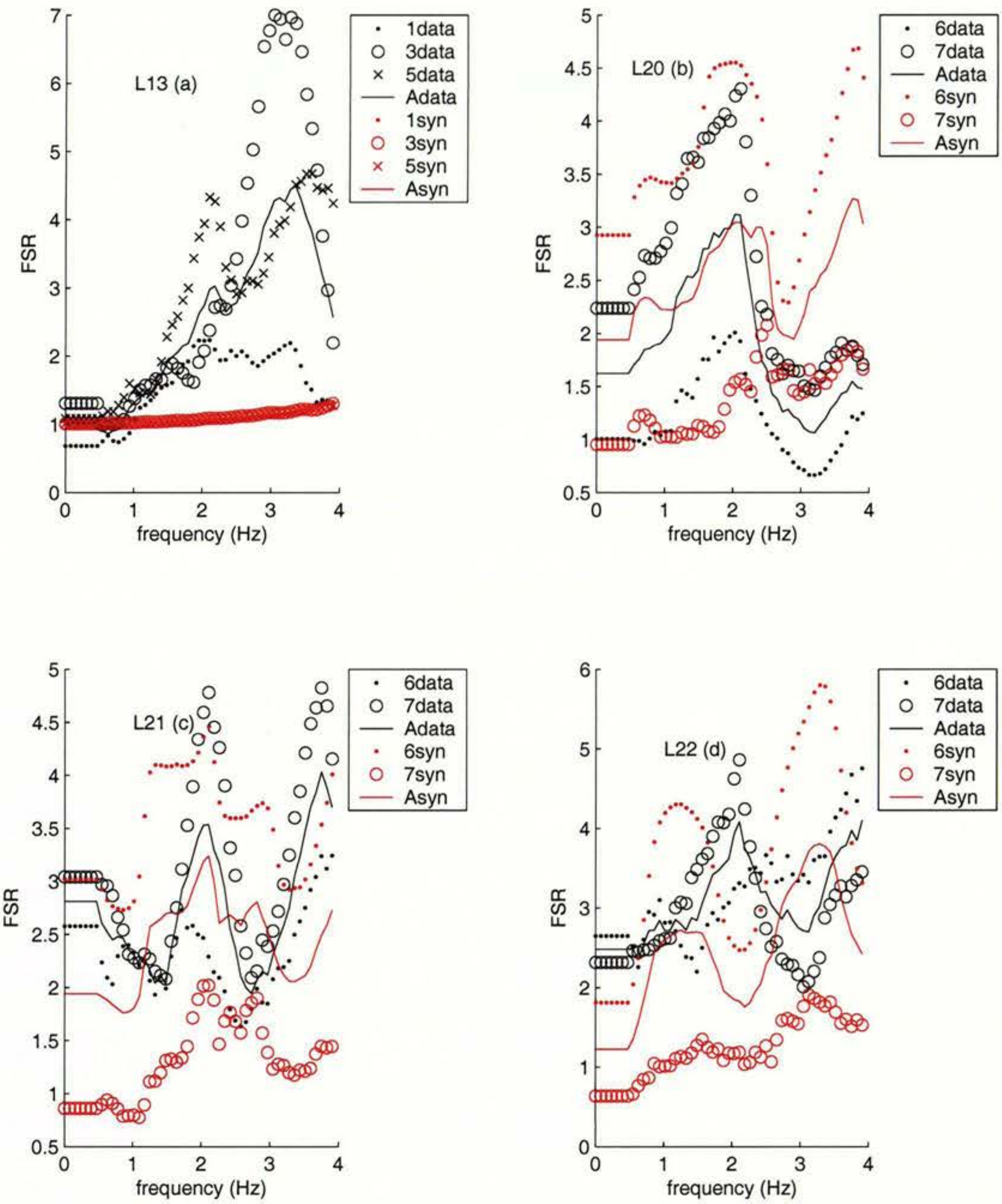

Figure C.2 *Comparison between FSRs of data and synthetic in the horizontal components for all events for site L13, L20, L21 and L22 (zone 2). The solid line is the average over all events. "1data" and "1syn" represent the data and synthetic FSR, respectively for event 1 in Table 3.2. Other symbols are analogous. "Adata" and "Asyn" represent the avearage of data FSR and the avearage of synthetics FSR, respectively.*

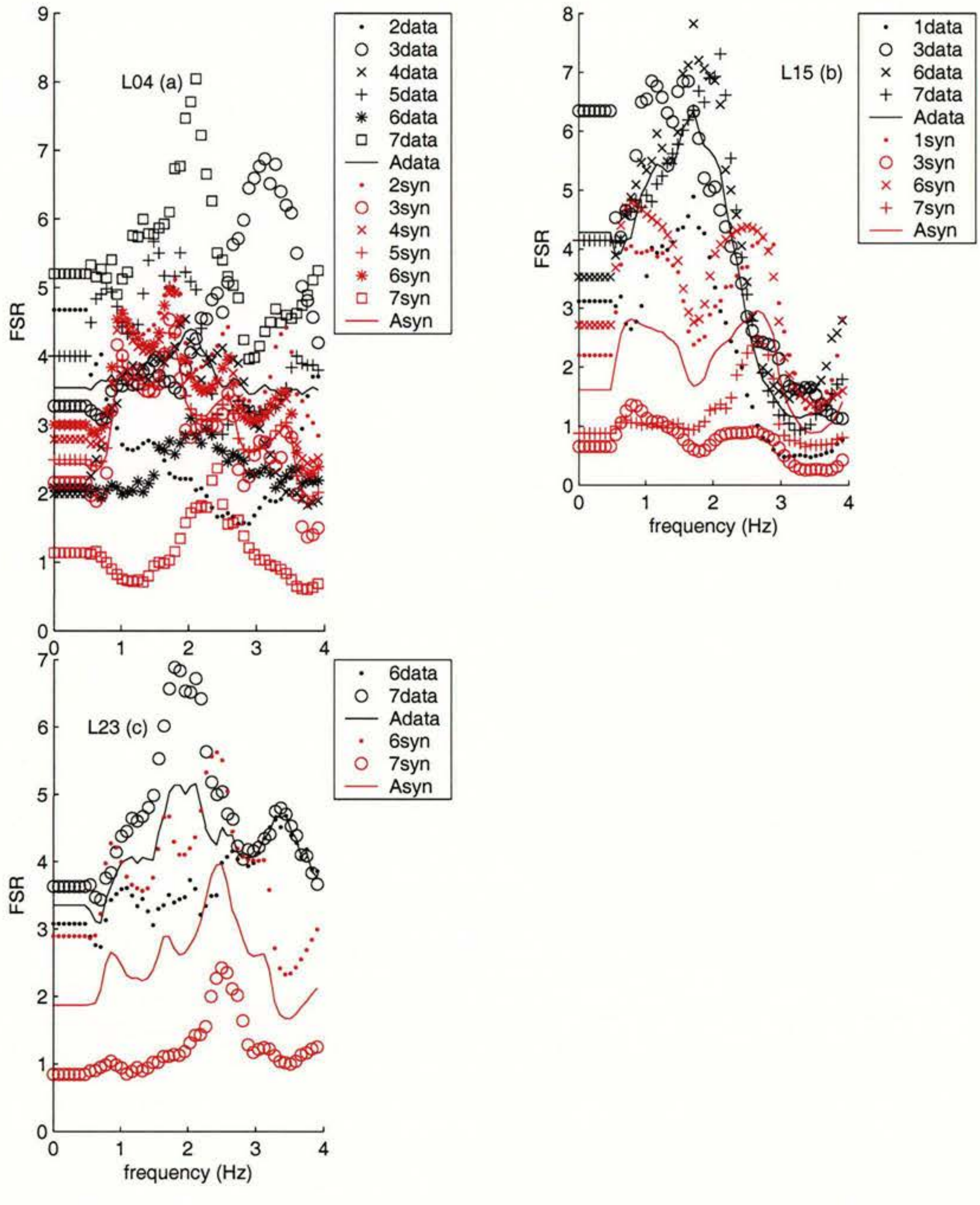

Figure C.3 *Comparison between FSRs of data and synthetic in the horizontal components for all events for site L04, L15 and L23 (zone 3-4). The solid line is the average over all events. "2data" and "2syn" represent the data and synthetic FSR, respectively for event 2 in Table 3.2. Other symbols are analogous. "Adata" and "Asyn" represent the avearage of data FSR and the avearage of synthetics FSR, respectively.*

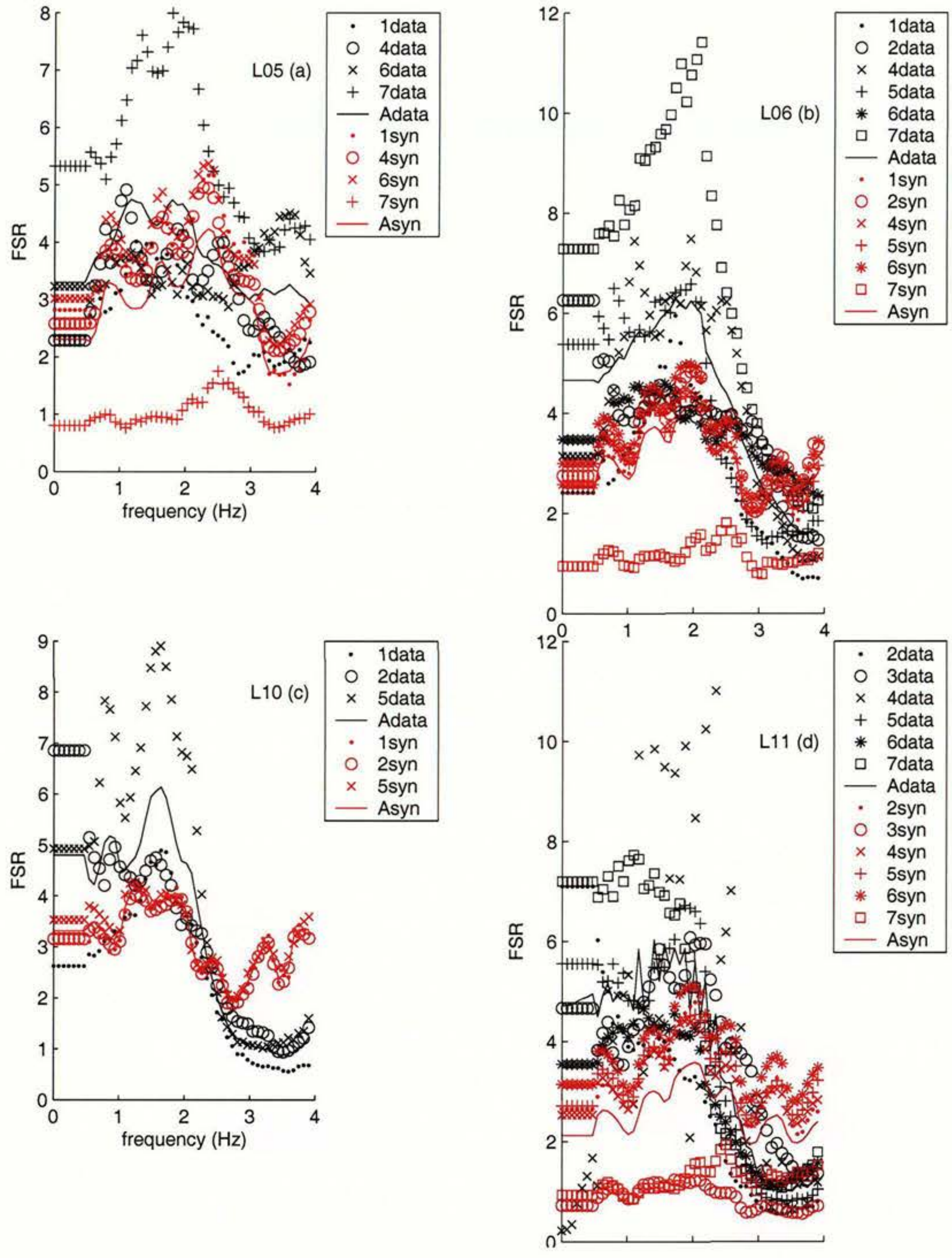

Figure C.4 *Comparison between FSRs of data and synthetic in the horizontal components for all events for site L05, L06, L10 and L11 (zone 5). The solid line is the average over all events. "1data" and "1syn" represent the data and synthetic FSR, respectively for event 1 in Table 3.2. Other symbols are analogous. "Adata" and "Asyn" represent the avearage of data FSR and the avearage of synthetics FSR, respectively.*

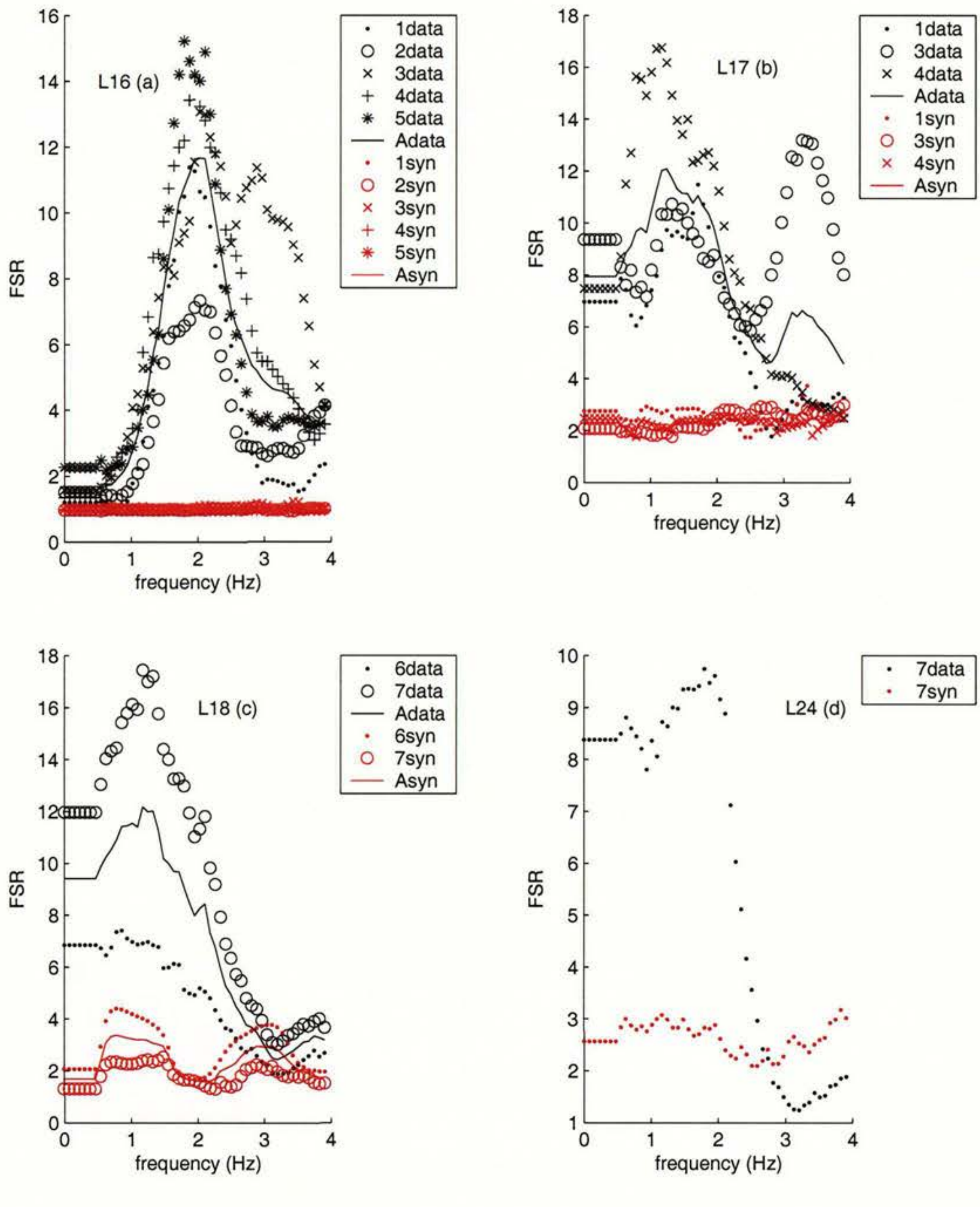

Figure C.5 *Comparison between FSRs of data and synthetic in the horizontal components for all events for site L16, L17, L18 and L24 (zone 5). The line is the average over all events. Note that the ground motion at L16 is amplified greatly from observed data but is not amplified from the 1D synthetics, this is caused by that L16 was actually located at sediment site but in the Hutt 3D shaking hazard model L16 is located at firm site. "1data" and "1syn" represent the data and synthetic FSR, respectively for event 1 in Table 3.2. Other symbols are analogous. "Adata" and "Asyn" represent the avearage of data spectral ratio and the avearage of synthetics spectral ratio, respectively.*

APPENDIX D

FSRS FOR DATA, 1D SYNTHETICS AND (1D+3D) SYNTHETICS AT OTHER SITES

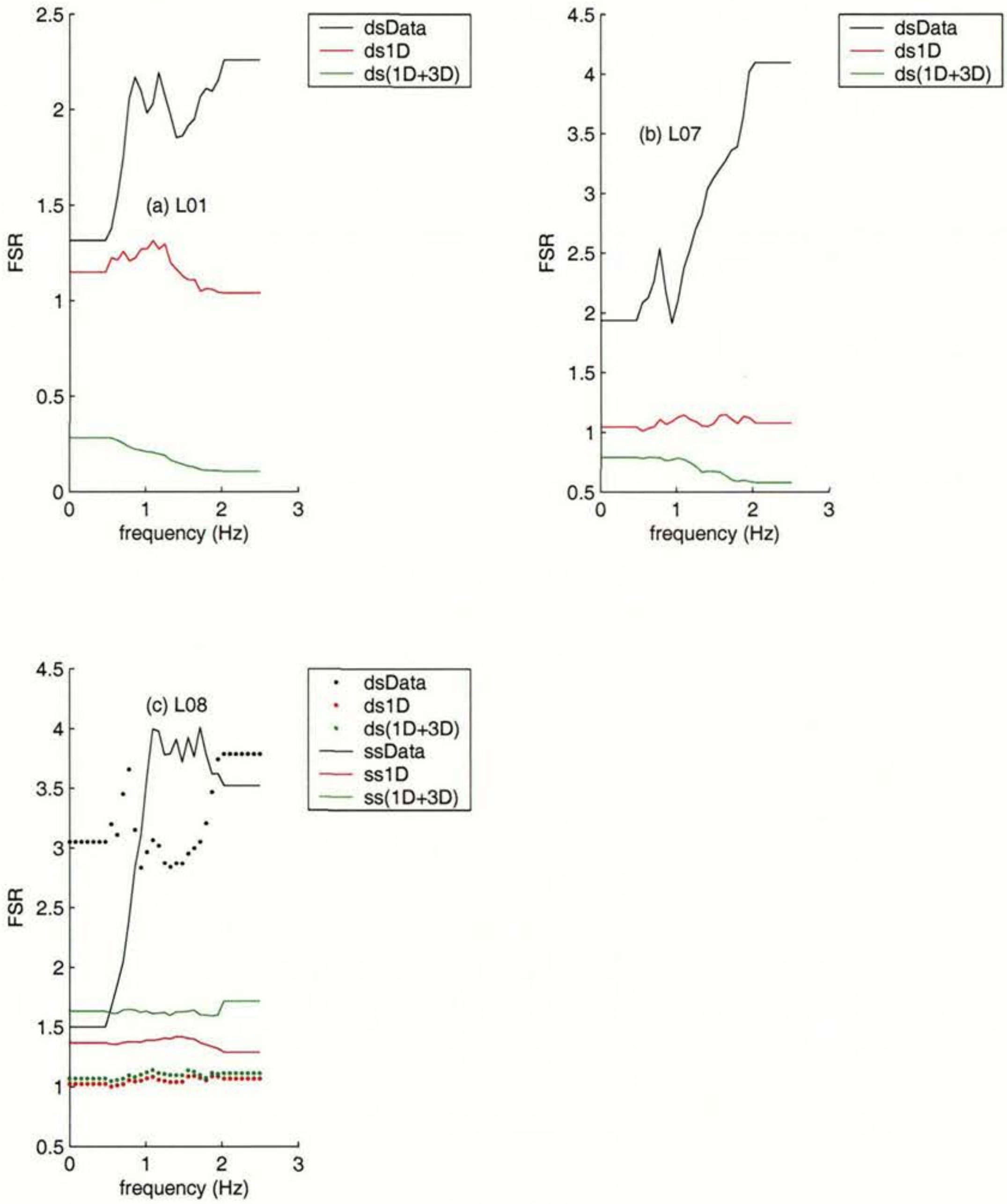

Figure D.1 *Comparison between FSRs of data, 1D synthetics and (1D+3D) synthetics in the horizontal components for all events for site L01, L07, L08. "ds" represents dip slip faulting; "ss" represents strike slip faulting. Note ground motion amplifications from (1D+3D) synthetics at L01 and L07 are below 1.0 because L01 and L07 are situated in absorbing boundary condition zone [Figure 2.3].*

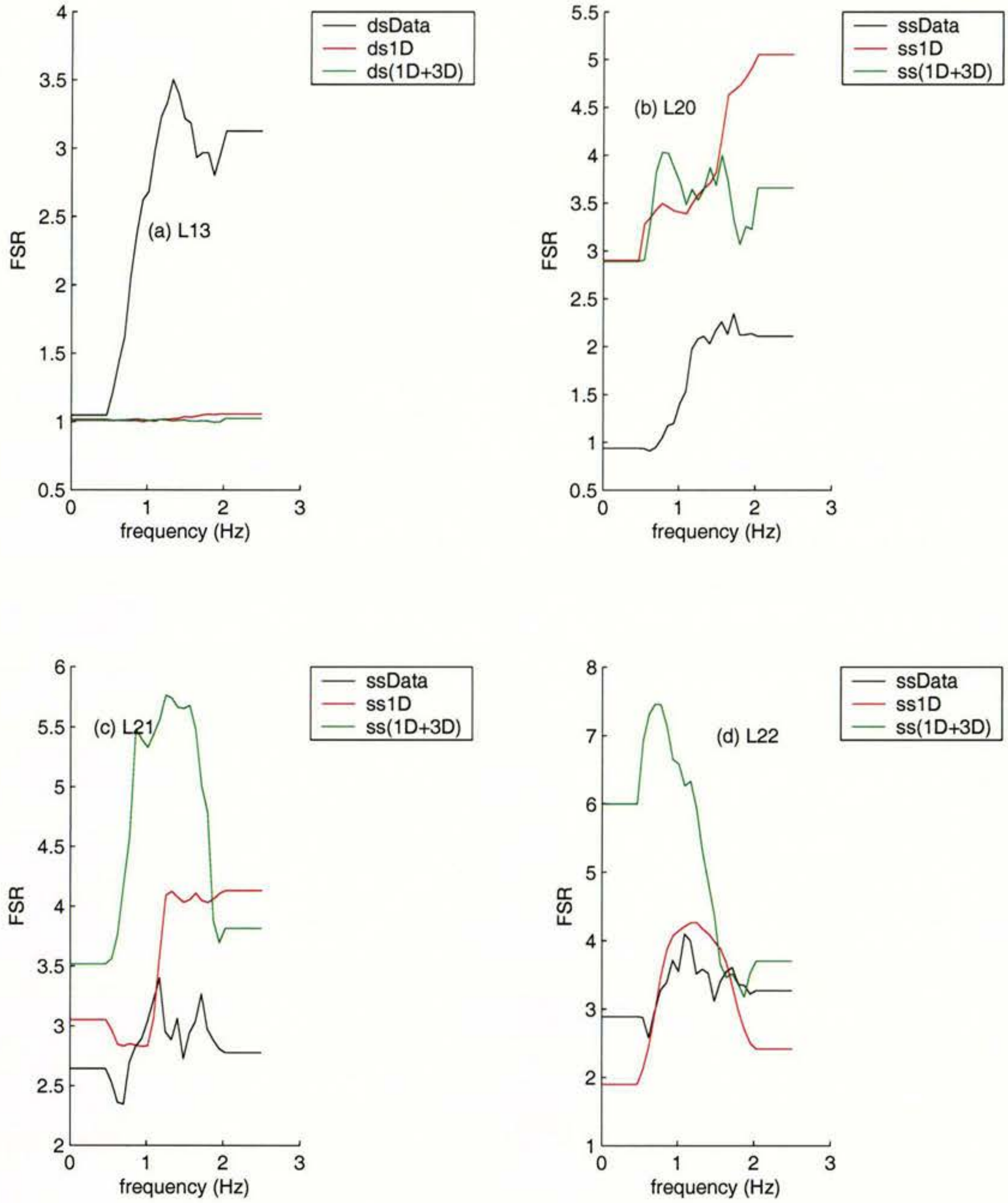

Figure D.2 *Comparison between FSRs of data, 1D synthetics and (1D+3D) synthetics in the horizontal components for all events for site L13, L20, L21 and L22 (zone 2). "ds" represents dip slip faulting; "ss" represents strike slip faulting.*

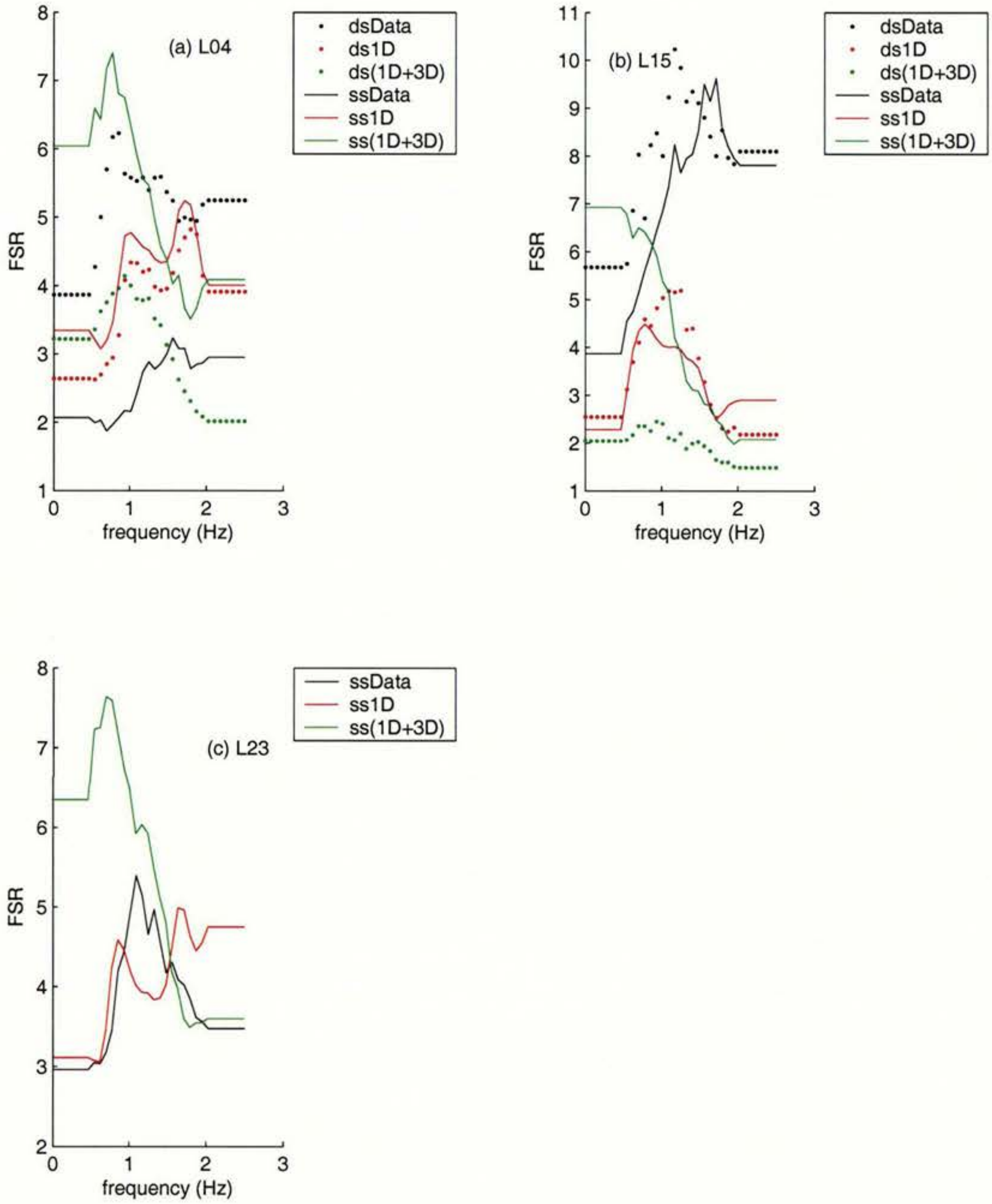

Figure D.3 *Comparison between FSRs of data, 1D synthetics and (1D+3D) synthetics in the horizontal components for all events for site L04, L15 and L23 (zone 3-4). "ds" represents dip slip faulting; "ss" represents strike slip faulting.*

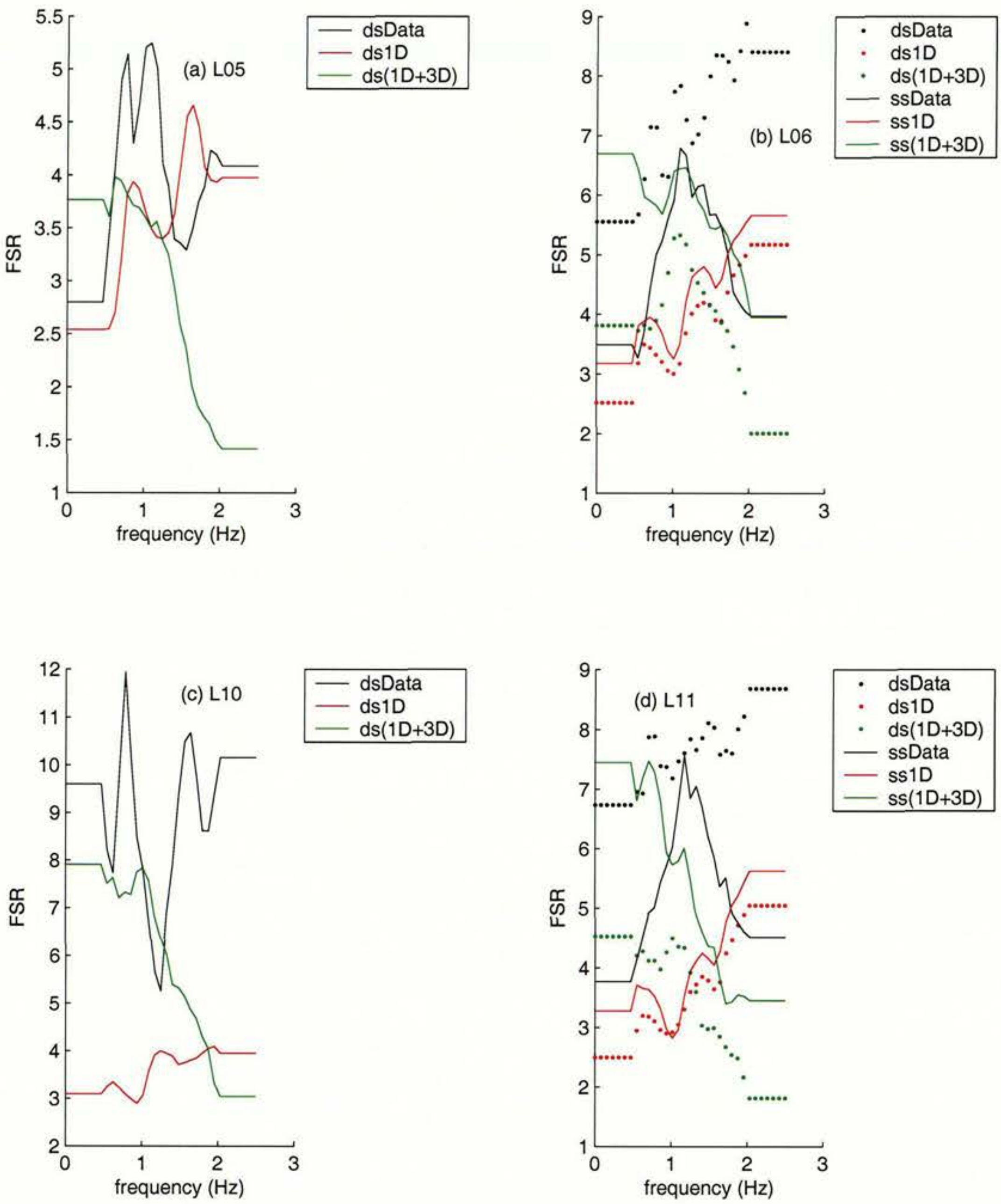

Figure D.4 *Comparison between FSRs of data, 1D synthetics and (1D+3D) synthetics in the horizontal components for all events for site L05, L06, L10 and L11 (zone 5). "ds" represents dip slip faulting; "ss" represents strike slip faulting.*

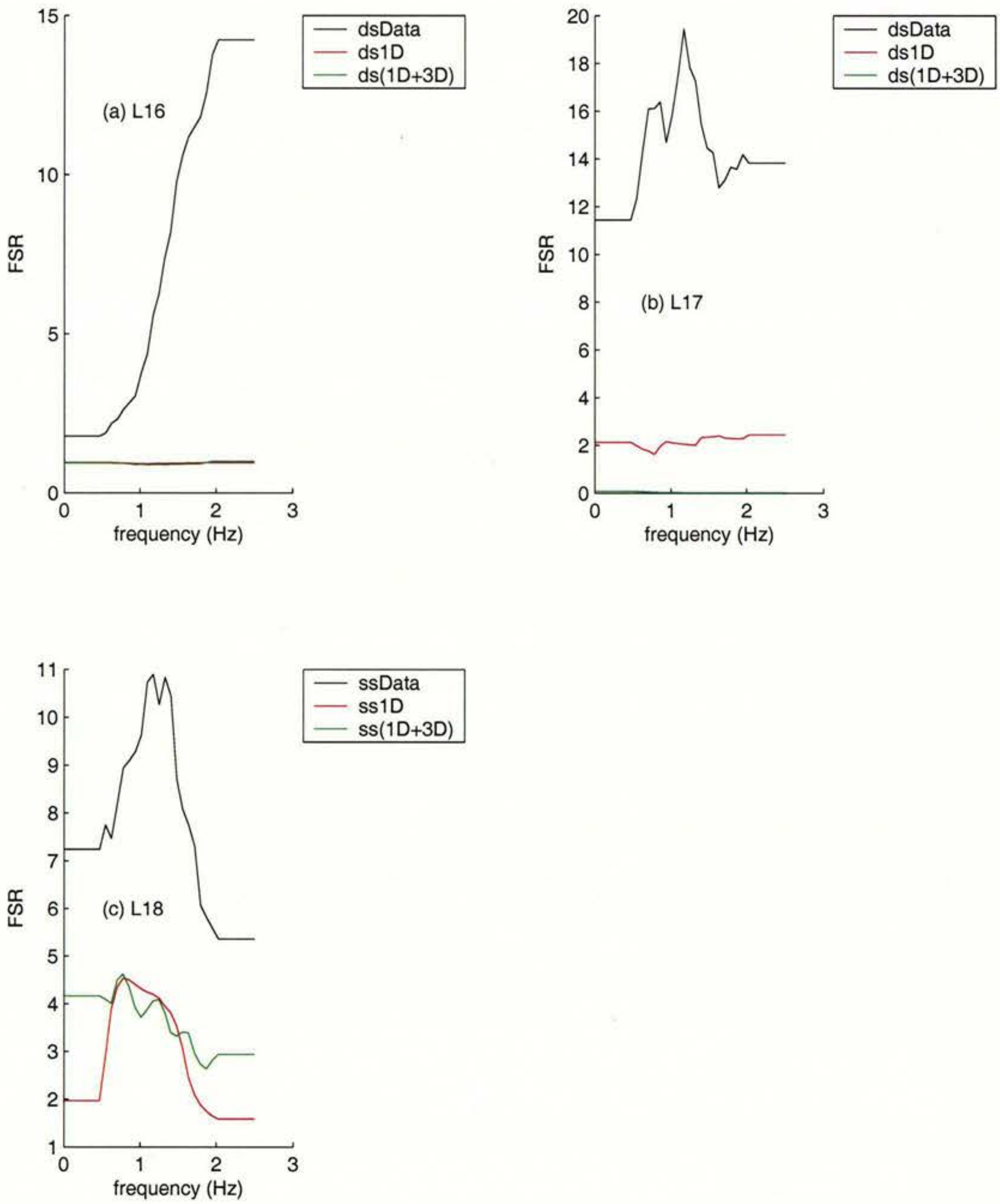

Figure D.5 *Comparison between FSRs of data, 1D synthetics and (1D+3D) synthetics in the horizontal components for all events for site L16, L17, L18 and L24 (zone 5). "ds" represents dip slip faulting; "ss" represents strike slip faulting. Note ground motion amplifications from (1D+3D) synthetics at L17 is nearly 0.0 because L17 is situated in absorbing boundary condition zone [Figure 2.3]. At L16 site, the FSR from 1D synthetics and (1D+3D) synthetics are nearly identical, both are much smaller than that from the observed data, this phenomena is caused that L16 is actually located on sediment site in the Lower Hutt deloyment, but no sediment layer exists in the 3D Hutt shaking hazard model and the corresponding 1D individual model for L16.*